UNIVERSITÀ DEGLI STUDI DI MILANO

Scuola di Dottorato in Fisica, Astrofisica e Fisica Applicata
Dipartimento di Fisica

Corso di Dottorato in Fisica, Astrofisica e Fisica Applicata
Ciclo XXXIII

Nuclear fragmentation cross sections measurements for hadrontherapy: implementation and optimization of a beam monitoring system

Settore Scientifico Disciplinare FIS/04

Supervisore: Professor Giuseppe BATTISTONI

Cosupervisore: Professor Franco CAMERA

Coordinatore: Professor Matteo PARIS

Tesi di Dottorato di:
Yunsheng DONG

Anno Accademico 2019/2020

Commission of the final examination:

External Referee:
Eugenio Paoloni, Eugenio Scapparone

External Member:
Francesca Ballarini, Alessio Sarti

Internal Member:
Angela Bracco

Final examination:

Date ??

Università degli Studi di Milano, Dipartimento di Fisica, Milano, Italy

Contents

Introduction

Particle therapy is a form of radiotherapy that adopts charged ions, mainly protons and ^{12}C, to treat solid tumours. The main advantages of particle therapy with respect to conventional radiotherapy are given by the higher precision in the localization of the dose, the better sparing of healthy tissues and the higher biological effectiveness of charged hadrons over X-rays. For these reasons, in the last few years both the number of particle therapy treatment centers and the number of patients are increasing. At the moment, there are 109 operative particle therapy facilities all over the world and other 37 structures are under construction. From 1994 to 2018 about 27905 people have been treated with carbon ion beams and 190036 people with protontherapy [1]. Nowadays, even if it is a well established technique in the treatment of certain type of cancers, the research for the improvement of the current methods and the development of new strategies are still ongoing.

One of the aspects currently under study is related to the effects of the nuclear inelastic interactions within the particle therapy treatments. Indeed, in the case of heavy ion therapy ($Z \geq 2$), the nuclear interactions can lead to the fragmentation of the projectile. The secondary particles are emitted mostly in the same direction and with similar kinetic energy per nucleon of the projectiles, but, having a lower mass with respect to the primary, they have a longer range. Thus, the final effect of the fragmentation is a dose deposition outside the tumour volume that can be particularly relevant for the healthy tissues, or possible organ at risk, placed along the beam direction, beyond the tumour site.

A similar effect is present also considering the consequences of the nuclear inelastic interactions in protontherapy treatments. In this case, the secondary particles are produced from the target atom nuclei. They have a range of the order of few µm and they lead to a non negligible dose deposition along the beam entrance channel.

Both the effects derived from the nuclear inelastic interactions are taken into account in the current treatment planning systems. However, as pointed out by different studies [2, 3], the accuracy of the dose deposition calculation caused by the nuclear fragmentation needs to be improved. In particular, the state of the art points out a lack of experimental data of nuclear differential cross sections ($d^2\sigma/d\Omega \cdot dE$) relevant for particle therapy applications. These data are required to improve the treatment planning systems both in protontherapy and heavy ion therapy and to benchmark the MC simulation tools, especially in view of the use of new ions species which are considered as very promising for the development of particle therapy, such as ^{4}He and ^{16}O [4].

A similar situation is present also in the framework of the space radioprotection field. The future space missions include a new lunar landing with a crew of astronauts and

the exploration of Mars with rovers [5]. Both the expeditions will have a long duration and they will be far from Earth. In this kind of missions, a long exposure to the galactic cosmic radiation, or the solar particle events generated by a solar flare, could be lethal for the crew and harmful for the equipment. As in particle therapy, also in this case there is a lack of differential cross section measurements about the nuclear inelastic interactions of the particles involved in space radiations. In this framework, the measurements are fundamental both to evaluate the health hazard derived form the radiation fragments and to develop a new shielding design suitable for the future space missions.

Since the same particles and similar necessities are present both in particle therapy and in space radioprotection, the FOOT (FragmentatiOn Of Target) experiment is designed to measure the differential cross sections ($d^2\sigma/d\Omega \cdot dE$) of fragments produced in nuclear interactions relevant for both the fields. In particular, FOOT aims to measure this process for ^{4}He, ^{12}C and ^{16}O beams at 250-700 MeV/u of kinetic energies impinging on targets composed of ^{12}C, C_2H_4 and PMMA ($C_5O_2H_8$). In order to study the fragmentation of the target material relevant for protontherapy, FOOT adopts an inverse kinematic approach and a subtraction of cross section method, measuring the differential cross sections ($d\sigma/dE$) of ^{12}C and ^{16}O beams at 200 MeV/u on targets of ^{12}C and C_2H_4.

In the FOOT experiment there are two different experimental setups. One of the setups is an apparatus derived from the nuclear emulsion technology developed and adopted in the OPERA experiment [6]. The main component of the emulsion setup is a compact detector composed of different layers of nuclear emulsions and absorbing materials, developed for the detection of light ($Z \leq 3$) fragments. The second setup is an apparatus composed of different sub-detectors optimized to detect heavy ($Z \geq 3$) fragments. In this case, the electronic spectrometer is composed of a beam monitoring system, different tracking detectors working in a magnetic field provided by two permanent magnets, a time of flight measurement system, an energy loss detector and a calorimeter.

In both the experimental setups there is a drift chamber called Beam Monitor that is adopted to measure the incoming beam direction and position. In addition, the detector is exploited to recognize and reject the events in which the projectile undergoes a nuclear inelastic interaction in the material upstream of the target. The Beam Monitor reconstructed tracks are particularly important for the data collected in the framework of the protontherapy measurements. Indeed, in this case, the projectile track is employed to retrieve the parameters of the Lorentz boost adopted to perform the inversion of the kinematics.

The present Ph. D. project has been proposed in order to contribute to the design, optimization, construction and first operation of the FOOT experiment, focusing on the beam monitoring system and, in particular, on the drift chamber. The aim of the project is to develop a reconstruction algorithm to be included in the FOOT data analysis code, to manage and optimize the acquisition software and the hardware settings of the detector during the test beams, to experimentally calibrate and characterize the Beam Monitor and to study the performances of the drift chamber in the framework of the FOOT experiment requirements.

In details, a multi-track reconstruction software has been developed and optimized combining the advantages provided by the properties of the Legendre polynomials with a χ^2 minimization algorithm. Then, a calibration and performance assessment of the Beam Monitor has been conducted at the Trento protontherapy facility with proton beams at 228 and 80 MeV of kinetic energy. In particular, the characterization of the drift chamber has been carried out by means of an external tracking telescope composed of different layers of micro-strip silicon detectors. In this occasion, the detector efficiency, spatial resolution and active area have been measured experimentally. In addition, the

space-time relations of the Beam Monitor have been calibrated by means of the telescope tracks. The results have been adopted as benchmark of a self-calibration algorithm developed to estimate the space-time relations using only the hits and tracks of the drift chamber. Finally, the Beam Monitor chamber has been successfully operated in the first data takings of FOOT. These data acquisition runs were conducted with both the experimental setups at the GSI accelerator facility (Germany), with ^{16}O and ^{12}C beams at different energies. In the framework of the emulsion apparatus measurements, the drift chamber has been employed to measure the spatial distribution of the irradiation pattern and to count the total number of particles delivered. In the test conducted with the electronic spectrometer, the Beam Monitor measured the transverse beam spot size. In addition, a characterization of the GSI 700 MeV/u carbon ion beam has been conducted by the Beam Monitor, measuring the beam rate, the transverse spot size and the angular spread. Finally, the measured performances of the drift chamber have been studied to verify the compatibility of the detector with the FOOT experiment requirements. In particular, in order to evaluate the capability of the Beam Monitor to identify and reject the events in which the projectile fragments in the material upstream of the target, different selection criteria based on the detector hits and tracks have been studied by means of MC simulations. Furthermore, since the Beam Monitor track is exploited to perform the inversion of the kinematics in the framework of the protontherapy measurements, a calculation of the impact of the detector spatial resolution on the cross section estimates has been conducted by means of MC simulations.

In Chapter 1 an overview of the physics and the biological aspects underlying the interactions of hadrons with matter will be presented. In addition, a focus on the role of the nuclear inelastic interactions in particle therapy and in space radioprotection will be reported. Chapter 2 is dedicated to describe the FOOT experiment, showing the aims, the strategy of measurements, the experimental setups and the software aspects. The principle of operations of the gaseous detectors will be presented in Chapter 3, together with a detailed description of the goals and the software aspects related to the FOOT drift chamber. Chapter 4 will illustrate all the experimental measurements performed with the Beam Monitor. In particular, the methods and the results of the detector calibration and performance assessment will be shown, followed by the presentation of the drift chamber measurements collected within the FOOT emulsion and electronic spectrometers. Finally, the study of the Beam Monitor performances in the framework of the FOOT experiment is illustrated in Chapter 5. The selection criteria developed to recognize the pre-target fragmentation events will be discussed. The systematic uncertainty of the cross section measurement derived from the Beam Monitor spatial resolution will be shown.

CHAPTER 1

Nuclear Physics and Biology

1.1 Introduction

The scientific research in modern age is increasingly extended and specialized in each field in order to expand our knowledge and develop new technology. In the framework of interaction of radiation with matter, which is a multidisciplinary physics branch, medical physics is one of the applications emerged in the last century. Among the different topics covered by medical physics, one of the new scientific research field born from the multidisciplinary interactions of physics, biology and medicine is Particle Therapy (PT).

The goal of PT is to treat cancer tumours with hadrons, exploiting their physics properties in the interaction with matter and the biological response of the irradiated tissues. Differently from conventional radiotherapy that adopts photon beams, the particles currently employed in PT are mainly protons and ^{12}C, but other ions such as ^{4}He and ^{16}O are under study. The main advantages in the use of hadrons with respect to photons in the cancer treatment are given by the higher precision in the localization of the dose and the better sparing of healthy tissues. In addition, the biological effectiveness of treatments is enhanced in case of PT conducted with ions.

The charged ions radiation effects relevant in PT are of great interest also in the framework of radioprotection in space. Indeed, the particles adopted in PT are also involved in the galactic cosmic radiations, even if with a completely different energy range.

In both fields the nuclear inelastic interaction plays an important role and it cannot be neglected: in the former case it can modify the results of the treatments if not properly considered. In the latter case, the fragmentation of cosmic rays on the spacecraft material contributes to the damaging dose absorbed by the astronauts that can lead to carcinogenesis and degenerative tissues.

In this chapter the fundamentals of charged particles interaction with matter are presented in Sec.(1.2), followed by an overview of the biological aspects involved in PT in Sec.(1.3). The state of the art of the Particle therapy is shown in Sec.(1.4), focusing on the role of the nuclear inelastic interaction. The space radioprotection aspects and the requirements needed for the future long term space missions will be presented in Sec.(1.5).

1.2 Interaction of charged particles with matter

Different phenomena occur when a charged particle passes through a material. Focusing on the particles involved in PT, the main interaction of an incident hadron is the Coulomb force that occurs with the orbital electrons of the target material atoms. The effect of this interaction is an excitation or a ionization of the absorber atom nuclei with the consequent energy loss of the incident particle. In addition, the projectile initial direction is tilted as described by the multiple Coulomb scattering theory.

Besides the collisions with electrons, the incident particle could interact with a lower probability directly with the absorber atom nucleus through elastic and inelastic scatterings. The former contributes to the multiple Coulomb scattering with relevant effects at large angles. The latter is more difficult to be modeled and it may cause the fragmentation of the projectile and/or of the target nucleus, leading to the formation of new particles. The physics and the details about all these phenomena will be presented in the following.

1.2.1 Stopping power

The energy loss of a charged particle traversing a given absorber material is described by the *Stopping power*, defined as the particle energy lost (dE) per unit path length (dx):

$$S = -\frac{dE}{dx} \tag{1.1}$$

The stopping power depends on the properties of both the incident particle and the absorber material. The first formulation about the interaction of the projectile with the electrons of the target material atoms was given by Niels Bohr with an approach based on classical physics. Then, Bethe and Bloch improved the Bohr model including the quantum mechanical theory, giving the following *Bethe and Bloch formula* [7]:

$$-\frac{dE}{dx} = 2\pi\, N_a\, r_e^2\, m_e\, c^2\, \rho\, \frac{Z}{A}\, \frac{z^2}{\beta^2} \left[\ln\left(\frac{2m_e\, \gamma^2\, v^2\, W_{max}}{I^2} \right) - 2\,\beta^2 - \delta - 2\,\frac{C}{Z} \right] \tag{1.2}$$

$r_e =$ classical electron radius
$m_e =$ electron mass
$N_a =$ Avogadro constant
$Z =$ atomic number of absorbing material
$A =$ atomic weight of absorbing material
$\rho =$ density of absorbing material
$z =$ charge of incident particle
$\delta =$ density correction relevant at high energies
$C =$ shell correction relevant at low energies
$W_{max} =$ maximum energy transfer in a single collision for a incident particle with mass M [8] $= \frac{2m_e c^2 \beta^2 \gamma/2}{1+2\gamma m_e/M+(me/M)^2}$
I= mean excitation potential [9] $= \begin{cases} 12\,\mathrm{Z}+7, & \text{eV if } Z \leq 13 \\ 9.76\,\mathrm{Z}+58.8\,\mathrm{Z}^{-0.19} & \text{eV if } Z > 13 \end{cases}$

The Eq.(1.2) is valid for particles with $0.1 \leq \beta\gamma \leq 1000$ and materials with intermediate charge [8]. In order to reach deep-seated tumours at a maximum of 30 cm in the human body, the highest kinetic energies available at the PT treatment centers are about 250 MeV for protons and 450 MeV/u for carbon ions, corresponding to a particle velocities of the order of $\beta \sim 0.6$ and $\beta \sim 0.7$ respectively. An example of the stopping power of protons in water at energies relevant for PT is shown on the left panel of Fig.1.1. In this energy region, excluding the constant terms (e.g.: m_e, N_a, $Z/A \sim 0.5$) and the negligible variables (e.g.: δ), the energy loss in the Bethe-Block formula essentially depends on the absorber material density and mean excitation potential ($\rho \cdot \ln(1/I^2)$) and the square of the incident particle charge and velocity (z^2/β^2), without any dependence on the incident particle mass. The main source of energy loss is given by the excitation or ionization of electrons in target material and the stopping power is commonly defined as *electronic stopping power*.

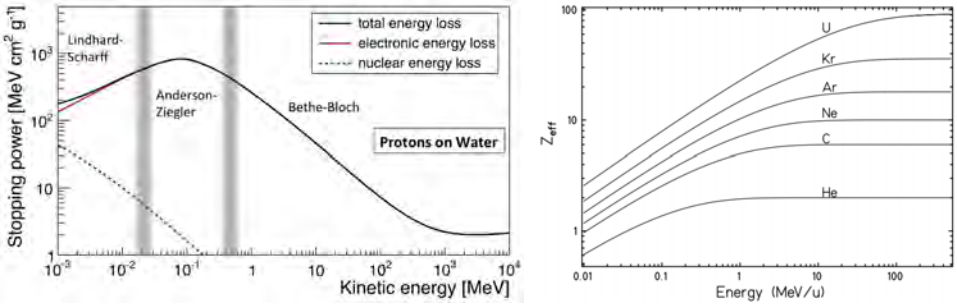

Figure 1.1: On the left: Stopping power for protons in water as a function of the kinetic energy [10]. On the right: examples of effective charges Z_{eff} calculated with the Barkas formula [11].

Due to the $1/\beta^2$ factor in Eq.(1.2), the projectile will release most of its energy only close to the end of its path in the medium. Here, the particle velocity is comparable to the orbital velocity of the bounded electrons and the shell correction (C/Z) comes into play. In the low kinetic energy region (below about 10 MeV/u for light ions) the Bethe-Block formula fails to describe all the different phenomena and the energy loss can be represented by the Anderson and Ziegler model [12]. In this energy range, the stopping power reaches a maximum in the *Bragg peak*, that occurs when particle velocity v_p is:

$$v_p \sim z^{2/3} v_0 \tag{1.3}$$

where v_0 is the Bohr velocity ($v_0 = e^2/\hbar$). For ^{12}C ions, the Bragg peak results to be at about 350 keV/u.

After the maximum energy loss, the sum of ionization and recombination processes reduces the effective charge of the incident particle, lowering its energy loss. In order to take into account this effect, the projectile charge (z) in equation (1.2) has to be replaced by an effective charge Z_{eff}. Different higher order of correction exists to describe this quantity, one of them is the empirical formula derived from W.H. Barkas [13]:

$$Z_{eff} = Z[1 - \exp(-125\,\beta\,Z^{-2/3})] \tag{1.4}$$

As shown in the right panel of Fig.(1.1), the Barkas correction regarding the ions adopted in PT is relevant only for particles at energies below 1 MeV/u.

For projectiles with a kinetic energy $\leq$ 100 keV/u, in the Lindhard-Scarff region, the energy loss is proportional to β and it can be modelled as [14]:

$$\frac{dE}{dx} \sim 8\,\pi\,\rho\,\frac{N_a\,\hbar^2}{m_e}\,\frac{z^{7/6}\,Z}{z^{2/3}+Z^{2/3}}\,\frac{\beta}{\beta_0} \tag{1.5}$$

where $\beta_0 = \frac{e^2}{4\,\pi\,\epsilon_0\,\hbar\,c}$ is the electron velocity of the classical Bohr hydrogen atom model. In this kinetic energy region, the Coulomb interactions with the target nuclei dominate the energy loss mechanism. This phenomena is known as *nuclear stopping power* and it occurs only at the very end of the particle path (last few µm). It leads to a negligible effect in the PT treatments since the spatial range is of the order of the diameter of a single cell nucleus [15].

1.2.2 Energy and range straggling

The particle range is defined as the total distance that a particle travels inside a medium before lose all its energy and come to rest. In a theoretical approach, the range should

consider all the small angular deviations given by the elastic Coulomb scatterings that occurs between the projectile and the target material nuclei. However, in the PT clinical regime, the electromagnetic stopping power is the dominant source of energy loss and the angular deviations on the range evaluation are negligible.

Assuming a straight line for the projectile path, the mean range (R) can be computed as a function of the particle energy (E_0) in the Continuous Slowing Down Approximation (CSDA) with the following expression:

$$R(E_0) = \int_0^{E_0} \left(\frac{dE}{dx}\right)^{-1} dE \tag{1.6}$$

In the integration of the Bethe-Block formula in Eq.(1.6), the mean excitation potential (I) is the main source of uncertainty for the stopping power and the range evaluation. It is defined as the first energy weighted moment of the dipole oscillator strength distribution of the target system. The approximation given by Bloch $I(eV) = 10 \cdot Z$ is reasonable only if $Z > 20$, thus inadequate for light materials. Various methods have been adopted to evaluate the mean excitation potential with different results. In principle, it is a well-defined function of the electronic excitation properties of the target and it does not depend on the projectile. Indeed, it can be consistently determined theoretically, but the experimental measurements are difficult to perform and they can lead to distinct results. Typically, the mean excitation potential is evaluated from the stopping power or the range measurements, but the results depend considerably on the initial assumptions made concerning the method of extraction and on the projectile properties [16]. As an example, for water the values ranges between 74.6 eV and 81.8 eV, with an average value of $I = 79.2 \pm 1.6$ eV [17].

The effect of this parameter on the range evaluation is shown in Fig.(1.2): on a proton beam of 200 MeV, varying the mean excitation potential with the values found in literature, the beam range fluctuates of millimeters.

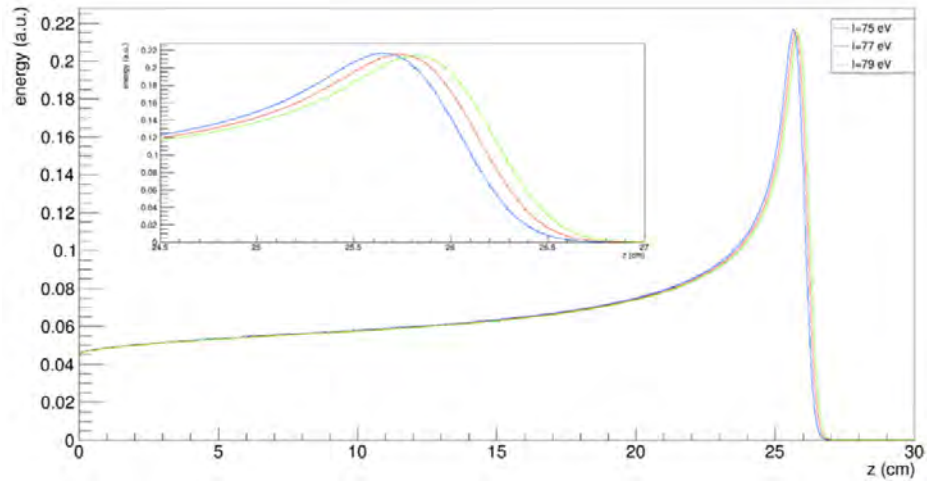

Figure 1.2: Bragg peak profiles of a 200 MeV proton beam in water calculated with a change in the mean ionization potential of $\pm 2.5\%$ [18].

The integration of the Bethe-Block formula in Eq.(1.2) is complex and different approximations can be adopted. As an example, the Bragg-Kleeman formula provides a

practical range relationship:

$$R(E_0) \sim \alpha E_0^p \tag{1.7}$$

where $R(E_0)$ is the range in cm, E_0 is the particle kinetic energy expressed in MeV, p and α are constant parameters. For protons at therapeutic energies (0-200 MeV), it has been found that $p \sim 1.77$ and $\alpha \sim 2.2 \cdot 10^{-3}$ cm/MeV^p [19].

In order to evince the range correlation with the incident particle properties, Eq.(1.6) can be modified expressing the Bethe-Block formula in Eq.(1.2) as $dE/dx = z^2 f(\beta)$. Since $E = m\gamma c^2$, differentiating the energy with respect to the particle velocity, it is possible to obtain $dE/d\beta = m\, g(\beta)$. Thus the range definition of Eq.(1.6) can be expressed as:

$$R(E_0) = \frac{m}{z^2} h(\beta) \tag{1.8}$$

where $h(\beta)$ is a universal function that depends only on the initial velocity of the particle. Equation (1.8) permits to scale the range of different ions easily. An example of the mean range of the particles adopted in PT is shown in Fig.(1.3).

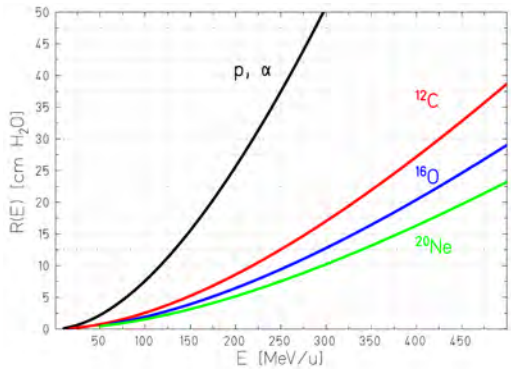

Figure 1.3: Mean range of heavy ions in water [20].

Generally, the range and the stopping power are estimated interpolating the range-energy tables validated and accepted by the scientific community [21]. However, tables can differ each other of $1-2\%$ due to a different evaluation of the mean excitation potential in Eq.(1.2). Since 1% of the range of protons at 180 MeV in water corresponds to a non negligible distance of 2 mm, in clinical practice the treatment planning relies on the experimental measurements of the ranges in water frequently performed by means of a dosimeter and a water tank yielding the Bragg curve. The measurements are specific of each facility due to the unique machinery properties.

Since the stopping power expressed in Eq.(1.2) is a mean value, a large number of collisions in the slowing down process can cause a broadening of the Bragg peak, leading to the energy and range straggling effect. In details, considering a charged particle passing in a thin material layer, the energy loss distribution is asymmetric with a tail on the high energy region. This is due to the production of high energetic electrons called $\delta - rays$, which are generated by the collisions of the projectile with a large amount of energy transfer.

The Vavilov distribution describes the energy loss fluctuations [22], but in the limit of many collisions in which the central limit theorem can be applied, the energy loss distribution can be approximated by a Gaussian with the standard deviation σ_E defined

as:

$$\sigma_E = 4\,\pi\,Z_{eff}\,Z\,e^4\,N_A\,\Delta x\left(\frac{1-\beta^2/2}{1-\beta^2}\right) \tag{1.9}$$

The energy loss straggling is the cause of the range straggling and, given Eq.(1.6), the two respective variance σ_E and σ_R are correlated:

$$\sigma_R^2 = \int_0^{E_0}\left(\frac{d\sigma_E}{dx}\right)\left(\frac{dE}{dx}\right)^{-3} \tag{1.10}$$

In a practical context, σ_R is a nearly constant fraction of the range and it can be described as:

$$\frac{\sigma_R}{R} = \frac{1}{\sqrt{m}}\,f\left(\frac{E}{m}\right) \tag{1.11}$$

where E and m are the energy and the mass of the incident particle and f is a slowly varying function that slightly depends on the absorber. A plot of the σ_R/R ratio for protons in different materials is shown in Fig.(1.4). Range straggling for PT protons in water is about 1.2% and it is of the order of 10^{-3} for ^{12}C ions due to the $1/\sqrt{m}$ factor in Eq.(1.11) [23]. An example of the Bragg peak broadening of protons and carbon ions is shown on the bottom panel of Fig.(1.5). In an experimental framework, considering the range straggling, the measured range is defined as the depth of the distal 80% point of the Bragg peak and it is commonly denoted as d_{80}.

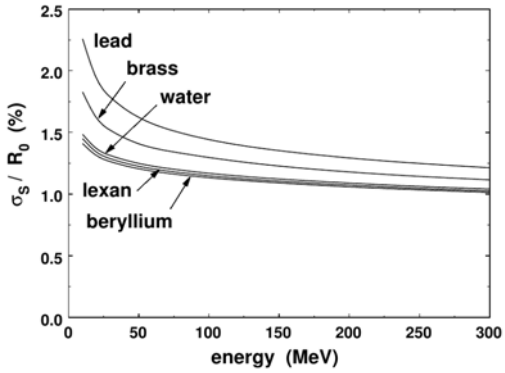

Figure 1.4: Range straggling as a function of the energy for proton beams in different materials [23].

1.2.3 Multiple Coulomb Scattering

In addition to the range straggling that occurs along the incident particle direction, the elastic Coulomb scatterings between the projectile and the target material nuclei lead to a lateral deviation of the incident particle direction. A full description of the Multiple Coulomb Scattering (MCS) cumulative effect on the lateral beam spread is given by the Moliére theory [24].

For small angles and thin materials, the net angular deflection can be approximated by a Gaussian with a width σ_θ derived by Highland [25]:

$$\sigma_\theta = \frac{14.1\,\text{MeV}}{\beta\,p\,c}\,z\sqrt{\frac{d}{X_0}}\left[1+\frac{1}{9}\,\log_{10}\left(\frac{d}{X_0}\right)\right] \tag{1.12}$$

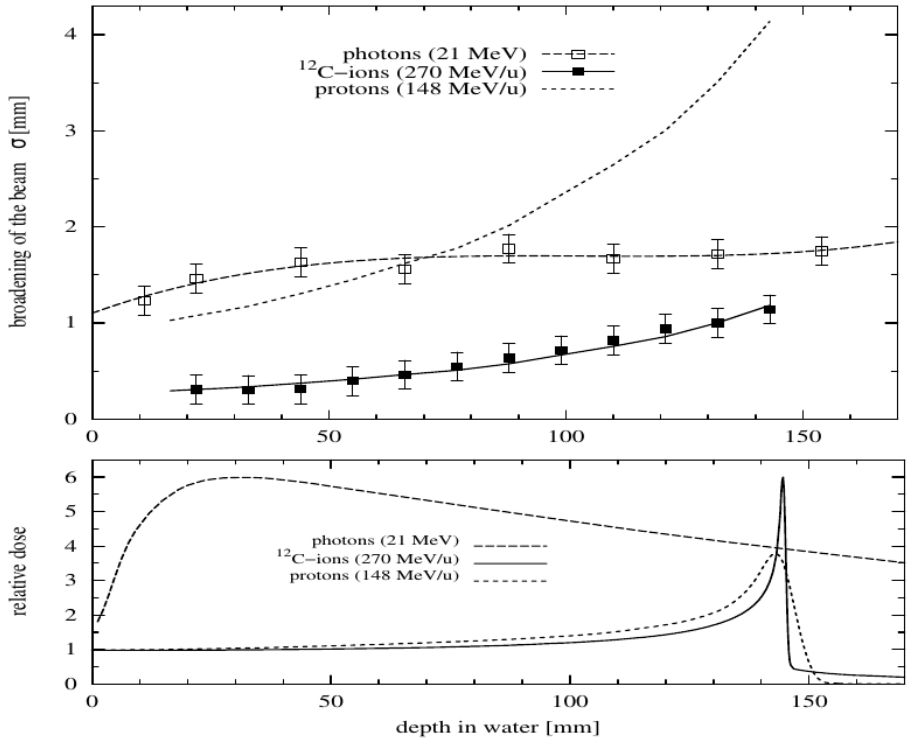

Figure 1.5: Lateral spread of photon, proton and carbon ion beams as a function of the penetration depth (top) and the depth dose correlation (bottom) [11].

where p and β are the particle momentum and velocity respectively, d and X_0 are the thickness and the radiation length of the absorbing material. Values of X_0 for common materials can be calculated and they are present in different databases [26]. For mixtures or compound materials the radiation length can be evaluated as:

$$\frac{1}{X_0} = \sum_j \frac{w_j}{X_j} \tag{1.13}$$

where w_j and X_j are respectively the fraction by weight and the radiation length of the j^{th} element. Since the radiation length decreases with the increase of the element charge $X_0 \sim 1/z^2$, targets constitute of heavier elements with higher charges lead to higher angular spread (e.g.: water $\sim 36.08\,\text{g/cm}^2$; Fe $\sim 13.83\,\text{g/cm}^2$; Pb $\sim 6.37\text{g/cm}^2$).

Considering incident particles with the same ranges, the MCS effect on the heavy charged particles is smaller with respect to the light particles due to the mass contribution included in the $\beta\, p\, c$ denominator of Eq.(1.12). This effect is clearly shown in the first panel of Fig.(1.5). Indeed, considering a proton beam at 148 MeV and a carbon ion beam at 270 MeV/u having the same range of about 15 cm, the former final angular spread is about four times larger than the latter.

Equation (1.12) is valid only for thin materials. Indeed, the particle velocity changes as a function of its position in the target and the $\beta\, p$ term at the denominator of Eq.(1.12) is not constant. A generalization of the Highland approximation to be adopted for the

thick target materials has been proposed in [27] with the following equation:

$$\sigma_\theta = 14.1\,\mathrm{MeV}\,z\,\left[1+\frac{1}{9}\,\log_{10}\left(\frac{d}{X_0}\right)\right]\times\left(\int_0^d\left(\frac{1}{\beta\,p\,c}\right)^2\,\frac{dx'}{X_0}\right)^{\frac{1}{2}} \tag{1.14}$$

Another limit of the Highland approximation of Eq.(1.12) is shown in Fig.(1.6): the angular distribution of a proton beam has a Gaussian core and about 99% of the protons are inside the $\pm 2.5\,\sigma$ region, but due to nuclear interactions that can produce a large angle deviation even with a single collision, the Highland approximation fails at large angles. As an example, in Fig.(1.6) at $5\,\sigma$ the Moliére distribution is 100 times higher than the Highland approximation.

A possibility to include the nuclear interactions contributes is to add a Cauchy-Lorentz distribution to the Gaussian electromagnetic core distribution [28, 29]. However, for the majority of the proton radiotherapy problems Eq.(1.12) is enough precise. Furthermore, in an experimental framework, the MCS is usually evaluated by means of Monte Carlo (MC) simulations. Thus, the MCS effect is estimated with a combination of different methods based on Moliére or Lewis theory [30], including the possibility of single scatterings at large angles.

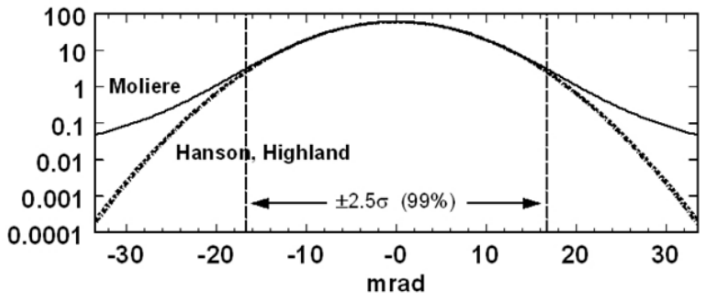

Figure 1.6: Angular distribution for 158.6 MeV protons traversing 1 cm of water [31].

1.2.4 Nuclear Interactions

Nuclear interactions can be divided in elastic and inelastic collisions. In the former case the kinetic energy is conserved and it contributes to the lateral beam spread above all at large angles. In the latter case, only the total momentum is conserved and it could lead to the production of secondary particles. The fragments can be derived from the incident ion due to the *projectile fragmentation* effect and from the target material atoms, leading to the *target fragmentation* effect.

Nuclear inelastic interaction is a many-body problem and the fundamental theory that describes this phenomenon is the quantum chromodynamics (QCD), which application with a non perturbation theory is not feasible for the energy of interest of PT.

At the moment, there are different semi-empirical models developed to describe the data. A simple initial method to evaluate the reaction cross section σ_R is to adopt a geometric approximation in which the nucleus is assumed to be a "black" sphere with radius a:

$$\sigma_R = \sigma_T - \sigma_{el} = \pi(A_p + A_T)^2 \tag{1.15}$$

where σ_T and σ_{el} are the total and the elastic cross section, and A_p and A_T are the projectile and the target nucleus radius. Starting from Eq.(1.15), different models has been developed to parametrize the nuclear reactions:

- $\boldsymbol{\sigma_R(E) = \pi\, r_0^2\, (A_p^{1/3} + A_T^{1/3} - b)^2}$
  where r_0 is the nucleon radius, A is the number of nucleons and b a correction factor. This is the Bradt-Peters formula [32] and it is a good approximation only for particles at very high energy (> 1.5 GeV/u), not suitable for PT applications.

- $\boldsymbol{\sigma_R(E) = \pi\, r_0^2\, c_1(E)\, (A_p^{1/3} + A_T^{1/3} - c_2(E))^2}$
  in which $c_1(E)$ and $c_2(E)$ are energy dependant parameters [33]. This parametrization is exploited in the NASA transport code HZETRN [34] for cosmic radiation both for heavy and light ions [35, 36].

- $\boldsymbol{\sigma_R(E) = \pi\, r_0^2\, [1 + A_T^{1/3} - b_0(1 + A_T^{-1/3})]^2 \cdot f(E, Z_T)}$
  where Z_T is the charge of the target nucleus, $f(E, Z_T)$ is an energy and target dependant function relevant at low energy ($E < 200$ MeV) and b_0 is the transparency parameter of the Bradt-Peters formula, which can be considered as an expansion of the target nucleons number: $b_0 = 2.247 - 0.915(1 + A_T^{-1/3})$. This formula is adopted to describe the proton-nucleus interactions in the HIBRAC code [37] that has been developed specifically for PT applications. At energy below 200 MeV, the function $f(E, Z_T)$ is required to include the cross section enhancement. It has different shape and parametrization depending on the projectile charge and energy range. The resulting cross section calculation is in good agreement with data, as shown in Fig.(1.7).

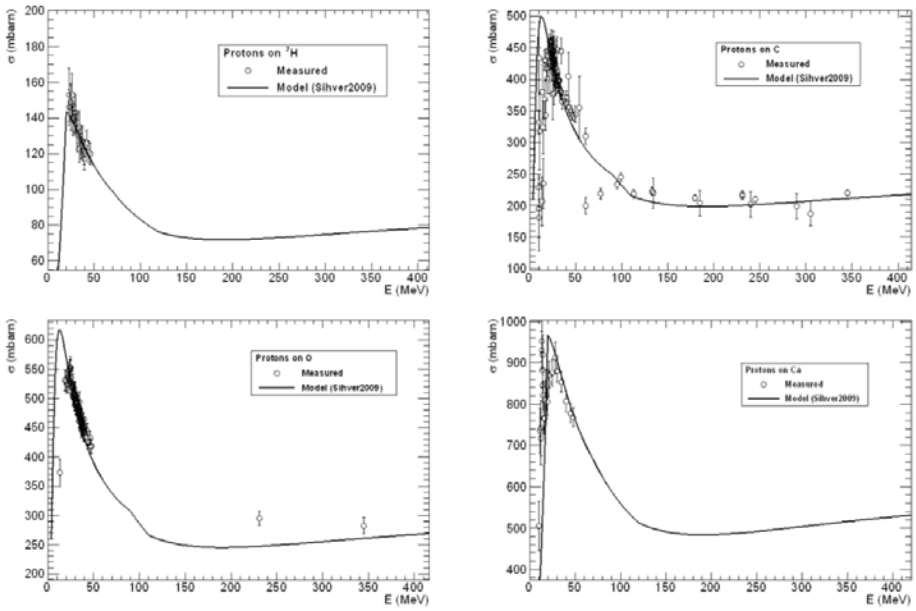

Figure 1.7: Measured and simulated fragmentation cross sections of protons on different targets of interest for PT. MC simulation by means of the HIBRAC code [18].

Different models have been developed over the years to include the nuclear interactions in the MC simulation tools. A lot of them are based on the two-step *abrasion-ablation* or *cascade-evaporation* model [38], that describes the nucleus-nucleus collisions adopting a geometrical approach.

In the first dynamic abrasion stage, which occurs with a time scale of about $10^{-22} - 10^{-23}$ s, the projectile interacts with the overlapping nucleons of the target nucleus. The result is the formation of an excited projectile pre-fragment with almost the same initial velocity, direction and the ratio of mass over nuclear charge of the incident particle ($(A/Z)_f \sim (A/Z)_i$), together with the isotropic production of light particles and a slowly recoiled quasi-target fragment. In proton therapy the projectile cannot fragment. Thus, the abrasion process leads only to the production of fragments derived from the target nuclei.

The following abrasion stage occurs with a time scale of about $10^{-18} - 10^{-16}$ s. It consists in the de-excitation of the fragments and the light nuclei mainly by means of nuclear evaporation, leading to the production of γ-rays, protons, neutrons and light fragments with a kinetic energy of few MeV.

Examples of the nuclear models commonly adopted in the MC simulation codes to evaluate the first dynamic stage of the interaction are [10]:

- **Intra-Nuclar Cascade (INC) model [39, 40]:** it is adopted in a lot of modern MC codes to describe the nuclear interactions of particles with energies from 100 MeV/u up to hundreds of GeV/u. The collision between the incident particle and the target material atom is modeled as the incoherent sum of the results of independent incident nucleon interactions with the target nucleus. Each of them are described as a series of two-body interactions, in which the target nucleons are considered as a cold Fermi gas with a proper nuclear density distribution and nuclear potential wall. The conditions for the validity of the model are related to the incident particle De Broglie wavelength λ_H. In particular, it has to be negligible with respect to the average distance between the target nucleons d and with respect to the mean free path λ_N inside the nucleus. These conditions are necessary to apply the target nucleons hypothesis and the independent incident nucleons approximation:

$$\lambda_H = \frac{2\pi\hbar}{p} << d = \left(\frac{3}{4\pi\rho_N}\right)^3 \; ; \; \lambda_H = \frac{2\pi\hbar}{p} << \lambda_N = \frac{1}{\sigma\rho_N} \tag{1.16}$$

  where σ and ρ_N are respectively the proton-nucleon cross section and the intranuclear density. For protons at clinical energies (e.g.: up to 250 MeV), the first Eq.(1.16) is not satisfied since $\lambda_H \sim d \sim 1$ fm. However, due to quantum effects, the effective mean free path of nucleons in the nuclear media is increased and the validity of the INC model is extended also to low energy protons down to 50 MeV.

- **Quantum molecular dynamics (QMD) model [41, 42]:** it is developed to describe the nucleus-nucleus interactions with projectiles at 50-400 MeV/u. In this case each nucleon of the projectile and of the target material is represented by a Gaussian wave function. The dynamics is simulated according to the Fermi kinetic energy inside the potential wall generated by the other surrounding nucleons. The collision process is simulated minimizing the nucleon-nucleon Hamiltonian equation of motions, considering all the nucleons presented in the projectile and target overlapping region. Due to the increase of complexity, MC simulations performed with this model are much more slow than using the normal INC model.

- **Boltzmann-Master-Equation (BME) model [43]:** as the QMD model, it is adopted only for nucleus-nucleus interactions of incident particles with energies up to 100 MeV/u. At this energy, the main process to be taken into account is the complete fusion of the projectile with the target nucleus, or the incomplete fusion between the quasi-projectile and the quasi-target fragments produced by a break-up process. In particular, the BME model describes the thermalization of composite nuclei by means of two-body interactions and secondary particles emissions.

The results of the first interaction stage with the intranuclear cascade process is the production of protons, neutrons and, through the coalescence mechanism, also light fragments.

If the incident particle is a proton (nucleon-nucleus interaction), the dynamic stage is composed also by a pre-equilibrium stage simulated according to the exciton model [44, 45]. In particular, the excitons are particles above the Fermi level or holes in the Fermi sea. In the pre-equilibrium stage, given a compound nucleus excitation energy E_{tot}, the excitons are emitted by means of nucleon-nucleon interactions until E_{tot} is below any emission threshold.

The second de-excitation phase is equal both for nucleon-nucleus and nucleus-nucleus interactions and, depending on the energy and the target nucleus mass, it consists of:

- **Nuclear evaporation:** emission of light fragments ($Z \leq 2$) with a kinetic energy of few MeV, similar to the evaporation of a hot system.
- **Fermi break-up:** the nucleus breaks into lighter fragments if the excitation energy exceeds the binding energy of the fragmentation channels. This effect occurs only for light nuclei with $A \leq 16$, which is the typical scenario in PT.
- **Fission:** The heavy ($Z \geq 65$) excited nucleus can break into two fragments. Since in the human body such heavy nuclei are not present, this is not relevant for PT.
- **Gamma emission:** The last stage of the de-excitation process is given by the emission of γ rays in order to reach a final configuration only with stable nuclei.

1.3 Biological effects of ionizing radiation

The biological effect of the ionizing radiation exploited in PT is the ionization of the molecules contained in the cells. In particular, after a rapid cascade of chemical reactions, the molecules are damaged or converted into highly reactive particles with unpaired electrons known as *free radicals*.

An overview on the damages involved by hadrons adopted in PT is presented in the next subsection, followed by a summary of the definitions and the parameters adopted in PT.

1.3.1 DNA damage

As verified by experimental measurements [47], the main goal of PT treatments is to damage the DNA. Indeed, it is the largest molecule in the cell, it is present only in two copies with a very limited turnover and it is central to all the cellular functions.

The DNA can be damaged both *directly* and *indirectly* by the incident radiation as described by the *oxygen-fixation hypothesis* depicted in Fig.(1.8). In details, the free radicals produced by the ionizing particles can damage the target molecules directly breaking a DNA bond, or indirectly if other participants are involved. In the latter case, a free

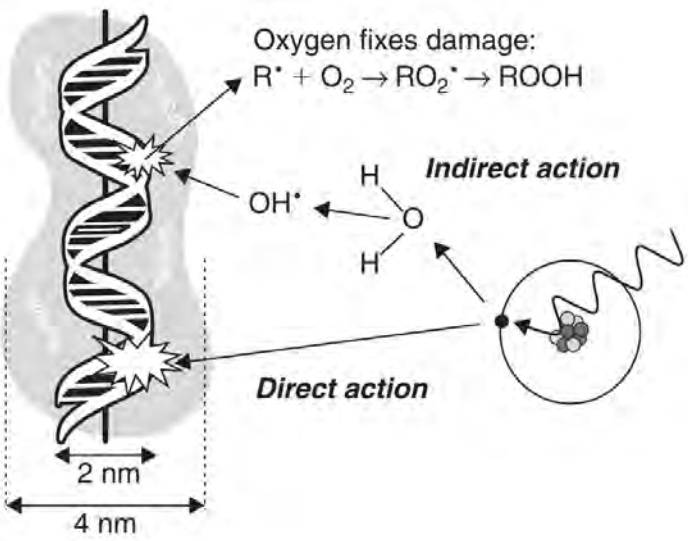

Figure 1.8: Picture of the oxygen fixation hypothesis [46].

radical produced in water (R*) is unstable and, reacting with oxygen, it leads to the production of RO_2^*. After further reactions, this particle can generate ROOH in the target molecule. In this way, it leads to a stable change in the chemical composition of the target molecule and the damage is said to be chemically *fixed*. In the absence of oxygen, the unstable R* molecule has a longer half-life and it can react with H^+ chemically restoring its original form, not damaging the target molecule.

Natural DNA damages are common events since each human cell is subject to about 70000 lesions per day, classified as [48, 49]:

- **Base damages:** this is a very common type of genomic damage consisting of a chemical modification to a base of a nucleotide. It includes different effects such as: cytosine deamination, depurination, depyrimidination and 8-oxoG damage. About 25% of the spontaneous lesions are base damages.

- **Single Strand Breaks (SSB):** it occurs when one of the two DNA helix structure is damaged. Spontaneous SSBs are very frequent, estimated to be about 55000 per cell per day ($\sim 75\%$ of the total lesions).

- **Double Strand Breaks (DSB):** if two SSB affect the same DNA molecule on both the helix, the damage is more severe with respect to SSB and it is defined as DSB. The estimated frequency of DSB per cell per day is about 25/70000.

- **Clustered lesions:** referred to complex lesions or locally multiplied damaged sites. It is defined as the case in which two or more lesions are located within 10 or 20 base pairs ($\sim$1-2 helical turns of the DNA). This category has great variability due to the multiplicity of the type of lesions and the number of lesions per cluster. Due to its complexity, clustered lesions are the most difficult to be repaired, showing a great level of damage and mutability due to inaccurate repair. It is very rare in nature if not induced by ionizing radiations or chemicals [49].

The effectiveness of ionizing radiations are various depending on the different DNA repair systems that contrast the diverse forms of damages caused by different agents. The main goal of PT is to produce permanent damages in the tumorous tissues by means of clustered DSB lesions. On the contrary, the aim of the space radiation protection is to limit the more damaging lesions induced by the space radiations as much as possible. In both cases, the biological effects of the ionizing radiations have to be estimated properly. A general trend of the reparability, mutagencity, cytotoxicity and damage complexity is shown in Fig.(1.9).

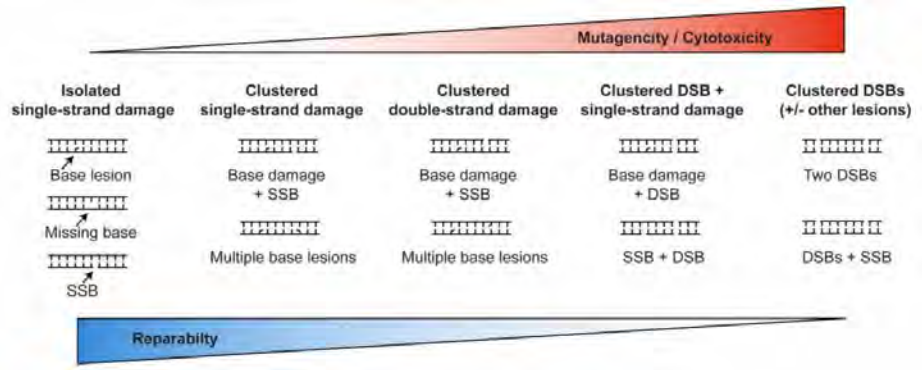

Figure 1.9: Classification of DNA damages. The damage complexity increase from left to right, corresponding to an increase of mutagencity and cytotoxicity and a decrease of the reparability [49].

1.3.2 Dose and LET

In order to evaluate the radiation effectiveness, the ionizing particle energy release must be quantified. In radiotherapy and space radioprotection it is measured by means of the *Absorbed dose* (D), defined as the energy deposited in matter (dE) by the ionizing radiation per unit mass (dm) and measured in Gray (Gy=Joule/Kg):

$$D = \frac{dE}{dm} \tag{1.17}$$

typical dose values adopted in protontherapy are of the order of 60-70 Gray divided in 30-35 fractions and delivered to the tumor in 6-7 weeks.

Distinct types of radiations leading to the same amount of absorbed dose can have very different biological effectiveness. A parameter that can take into account and evaluate this diversity is the Linear Energy Transfer (LET), defined as the amount of energy (dE) locally transferred from an ionizing particle to the material traversed per unit distance (dl):

$$\mathrm{LET}_\Delta = \left(\frac{dE}{dl}\right)_\Delta \tag{1.18}$$

The Δ is an upper threshold for the energy of secondary electrons, adopted to consider only the amount of energy deposited close to the primary particle track. The LET defined in (1.18) is usually referred as *restricted* LET and it is closely related, but different from the stopping power due to the Δ threshold. If no upper limit is considered, the *unrestricted* LET (LET_∞) is equal to the electronic stopping power. LET values for particles adopted in clinical treatments are shown in Tab.(5.2).

The relevance of the DNA damages that a ionizing particle can produce in a cell is directly related to the LET. X-rays and γ-rays adopted in conventional radiotherapy are considered as low LET radiation. At the energy of interest for the medical treatments, their interactions with matter is based on the Compton scattering and the photoelectric effect. They provides only sparse ionizations leading to a low biological effectiveness. On the contrary, the heavy charged particles adopted in PT are considered as high LET particles. In particular, due to their enhanced energy deposition density along the track path, they tend to create more DSB and clustered lesions, as shown in Fig.(1.10).

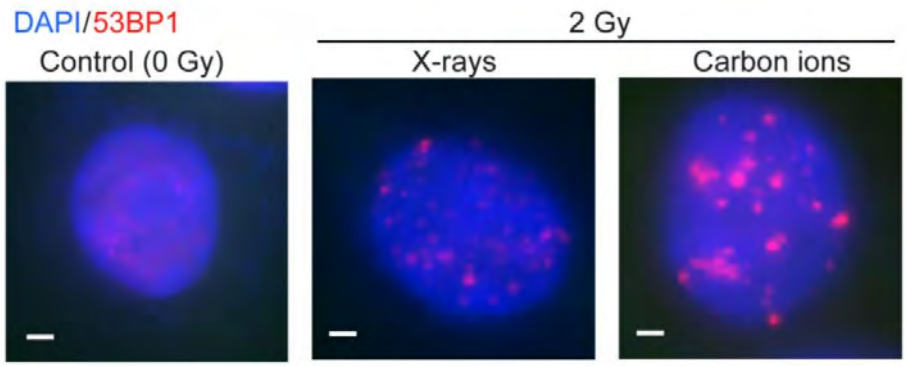

Figure 1.10: RKO colon carcinoma cells irradiated with 2 Gy of X-rays (center) and Carbon ions (right). Cell nuclei are stained in blue with DAPI and DSB damages are stained in red with 53BP1. White scale bars are 1nm [49].

Table 1.1: Average LET values of different radiations in water [50].

Radiation	Cut off energy Δ (eV)	LET_Δ (keV/µm)
^{60}C gamma rays	Unrestricted	0.239
	100	0.229
22 MeV X-rays	100	0.19
2 MeV electrons (whole track)	100	0.20
^{3}H β particles	100	4.7
50 kV X-rays	100	6.3
5.3 MeV α particles (whole track)	100	43

1.3.3 Survival curve

In order to quantify the biological enhanced effectiveness of charged hadrons over the electrons and photons adopted in classical radiotherapy, different parameters have to be introduced.

The first one is the *cell survival curve* which represents the fraction of surviving cells with reproduction capability as a function of the absorbed dose. Figure (1.11) shows examples of survival curves related to particles with different energy and LET values. At high doses, all the survival curves tend to have a linear evolution, but in the low dose region, only the particles associated with a low LET values have a shoulder with a non linear tendency.

The conventional parametrization of the survival curves is the *Linear Quadratic model*:

$$S(D) = e^{-\alpha D - \beta D^2} \tag{1.19}$$

where S is the survival fraction, D is the absorbed dose, α and β are experimentally fitted parameters. In particular, α is related to the slope of the linear component of the curves shown in Fig.(1.11) and β is related to the non linear part.

The ratio α/β describes the shoulder of the survival curves at low doses and it gives indications related to the reparability of the damages. It depends primarily on the features of the target tissues and secondarily on the incident particle properties. In particular, high α/β ratio is associated to particles with high LET and it corresponds to radiations that can provide more severe and irreparable damages to the target cells. Given the same type of radiation, particles with lower energies are associated with higher values of LET and higher values of α/β ratio due to the LET dependency on the particle velocity (LET$\sim \beta^{-2}$).

Considering Fig.(1.11), this fact is true except for the curve associated with the 2.5 MeV α particles that has the highest LET values, but not the highest α/β ratio. This is given by the combination of the *overkill* effect and the stopping power behaviour at low energies. In particular, in the former case the projectile delivers more energy than the necessary to kill a cell, wasting the dose release. In the latter case, given an absorbed dose value, the enhancement of the energy loss at low energy range leads to the reduction of the incident particle fluence with the consequent reduction of the number of damaged target cells. This effect is shown also in the left figure of Fig.(1.12).

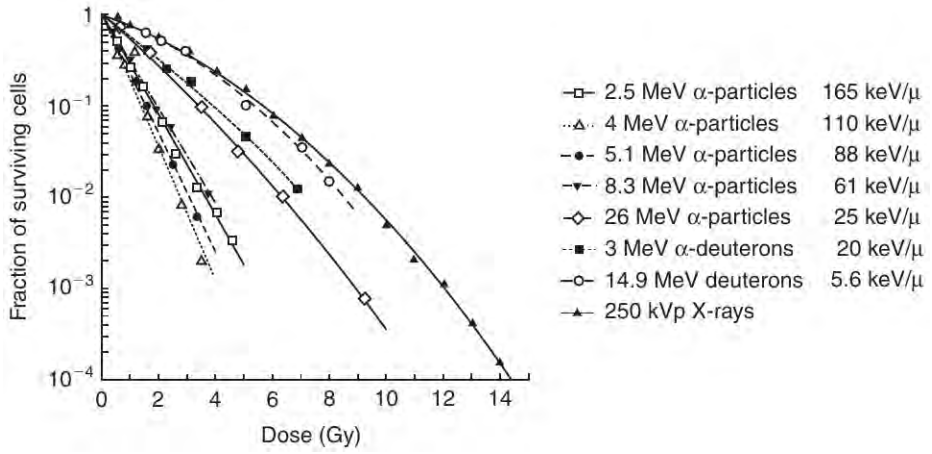

Figure 1.11: Survival curves of human kidney cells exposed *in vitro* to different radiations with different LET values [46].

1.3.4 Relative Biological Effectiveness

The α/β ratio is a parameter strictly related to the linear quadratic model and it is not sufficient to fully take into account the different biological effectiveness aspects. A more comprehensive parameter is the *Relative Biological Effectiveness* (RBE) defined as the ratio of a reference radiation dose (D_{ref}) and the dose of the interested radiation (D_{test}) that

produces the same effect (isoeffect):

$$\mathrm{RBE} = \left.\frac{\mathrm{D_{ref}}}{\mathrm{D_{test}}}\right|_{\mathrm{iso}} \tag{1.20}$$

The reference radiation commonly adopted is the 250 kVp X-rays or the ^{60}Co γ rays, since they are low LET radiation sources regularly available in clinical or experimental facilities. Typically, the RBE is determined from cell survival curves and the isoeffect is set to be the 10% of the survival fraction.

The RBE depends on different parameters and it is related both with biology and physics aspects. As an example, in the former case it depends on the type of the target cells and on the cell oxygenation level. In the latter case, it depends on the dose and the incident particle species.

The first picture in Fig.(1.12) shows the RBE evolution for the human kidney cells featured in Fig.(1.11) evaluated at a survival fraction level of 0.8, 0.1 and 0.001. In all the cases, the RBE increases with the increase of LET up to a maximum of about 100 keV/µm. Then it drops for higher values of LET due to the overkill effect. The optimum LET value varies depending on the cell type and the radiation beam. the general trend is that heavy particles are associated with higher values of optimum LET and maximum RBE. Typical RBE values for the particles involved in PT are of the order of 1.5-5 for ^{12}C ions and about 1.1 for protons, depending on the particle energy and LET.

The main goal in PT is to maximize the damage to the tumour sparing the surrounding healthy tissues. To achieve this purpose, the RBE has to be maximized in the Bragg peak region and minimized in the entrance channel. As shown in Fig.(1.13), heavy ions have similar maximum RBE at the Bragg peak, but only the ^{12}C ion has a low RBE value of about 1 in the entrance channel. This is one of the reasons why carbon ion has been selected as the preferred heavy particle adopted in PT. Regarding protontherapy, in clinical facilities the proton RBE is assumed to be 1.1 along all the particle path, but different studies indicate a wide range of measured proton RBE values close to the Bragg peak.

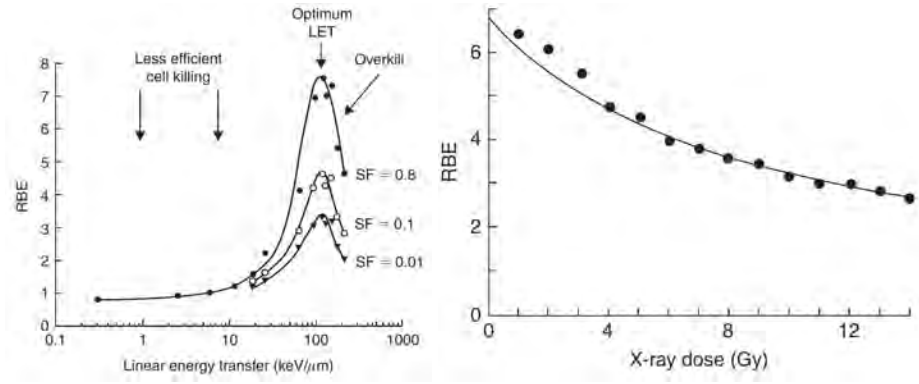

Figure 1.12: On the left, RBE values as a function of LET, calculated from Fig.(1.11) at cell survival fraction (SF) levels of 0.8, 0.1 and 0.01. On the right, measurements (black dots) of RBE values of 4 MeV α particles impinging on cell lines irradiated *in vitro*. The theoretical RBE calculated with Eq.(1.21) is shown with the line [46].

The RBE is a fundamental parameter adopted in clinical facilities to prepare the treatment planning, since the dose deposition evaluation strictly relies on this parameter. A first analytic parametrization of the RBE can be performed exploiting the linear

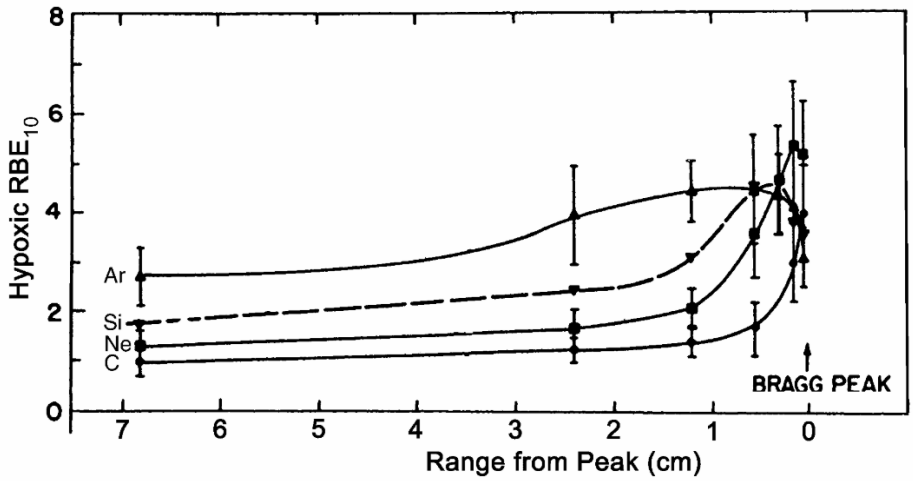

Figure 1.13: RBE for different heavy ions as a function of the penetration depth [11].

quadratic formula (Eq.(1.19)) to model both the tested and the reference radiation survival curves. The resulting RBE value calculated as a function of the reference dose (d_r) or the test dose (d_t) is:

$$\begin{aligned} RBE &= \frac{K \, + \, \sqrt{K^2 + 4Kd_r(1 + d_r/V)/C}}{2(1 + d_r/V)} \\ RBE &= \frac{-V \, + \, \sqrt{V^2 + 4VDd_t(1 + d_t/C)}}{2d_t} \end{aligned} \tag{1.21}$$

where $K = \alpha_t/\alpha_r \, , \; V = \alpha_r/\beta_r \, , \; C = \alpha_t/\beta_t$ with α and β given by the linear quadratic model for the test (t) and the reference (r) radiations. An example of measured and calculated RBE values as a function of the dose is shown on the right panel of Fig.(1.12). In this case, the RBE has been measured with in vitro experiments and it increases with the decrease of the dose. The tendency has been verified also with *in vivo* experiments [46].

At the moment, a comprehensive RBE model does not exist yet and different theories have been developed and exploited in different clinical facilities. A list of the most common RBE models is presented below [51]:

- **Local Effect Model (LEM):** it has been developed at GSI in Germany [52]. The basic hypothesis is that the local biological effect is given only by the expected local energy deposition, independently from the radiation type. Thus, given a fixed biological target, the different radiation track structures are the cause of the different RBE values. The last version of this model is LEM IV [53] developed in 2010. In this version, the biological response is directly related to the local DSB density, including a parametrization for isolated and clustered DSB.

- **Microdisimetric Kinetic Model (MKM):** it is developed by Hawkins [54, 55] relying on the theory of Dual Radiation Action [56] and it is adopted mostly in Japan. In this model, the cell killing depends on the energy distribution spread over a sub-nuclear region called *domain*. Assuming the nucleus as a cylinder with a given

radius R composed of different domains of radius r, the RBE of a given radiation can be evaluated as a function of R, r and the slope of the specific survival curve in the limit of LET=0.

- **NIRS approach:** it is based on the linear quadratic model and it is developed and adopted at Chiba, in Japan [57]. In this model, the dose is calculated using the α and β parameters of the linear quadratic model derived from empirical tables. Then, the RBE is computed measuring the dose of the test radiation at different depths for different energies by means of *in vitro* measurements conducted on human salivary gland tumor cells. Finally, the RBE values adopted for the treatment planning systems are computed scaling the *in vitro* RBE values according to the RBE observed in previous clinical experience with fast neutrons.

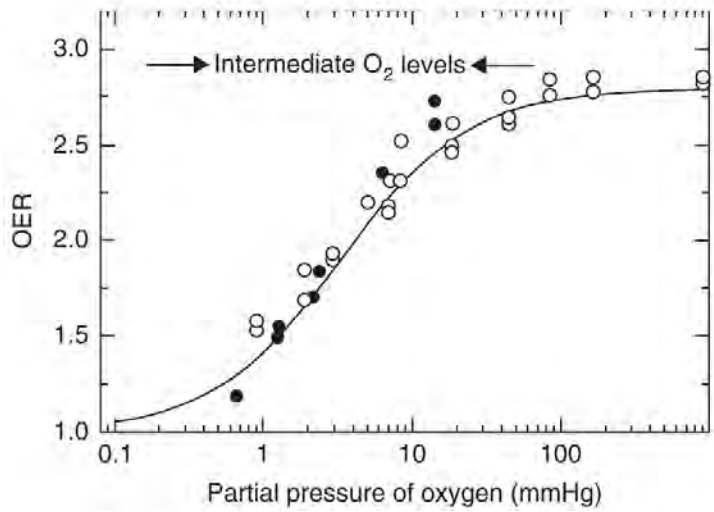

Figure 1.14: OER values measured at different oxygen partial pressure levels [46].

1.3.5 Oxygen Enhancement Ratio

A confirm of the different damage mechanisms related to low and high LET particles is given by the dependency of the radiation effectiveness on the oxygenation level of the target tissues. Most solid tumours need to develop their own blood supply system, but this angiogenesis process usually lags behind the faster increase of the number of neoplastic cells. This leads to the development of hypoxic microregional tumorous areas that are nutrient deprived and with a lack of oxygen. The presence of oxygen atoms in a target material can remarkably modify the biological effectiveness of a radiation [58] and this effect is quantified by the *Oxygen Enhancement Ratio* (OER), defined as the ratio between the radiation dose in hypoxia condition (D_{hyp}) over the radiation dose in an aerobic condition (D_{air}), for the same biological effect (isoeffect):

$$OER = \left.\frac{D_{hyp}}{D_{air}}\right|_{iso} \tag{1.22}$$

The dependence of the radiobiological effectiveness on the degree of oxygen concentration is shown in Fig.(1.14): cells with an oxygen partial pressure level below 0.15

mmHg are the most radioresistant, while the OER rises remarkably for the cells with an oxygen partial pressure level of about 0.5-20 mmHg. Further increase of the oxygen concentration enhances the radiosensitivity slightly.

The rise of the radiation damage due to the oxygenation is described by the oxygen-fixation hypothesis presented in Sec.(1.3.1). The overall effect of the oxygenation on the biological effectiveness is clearly shown on the left of Fig.(1.15), in which the same cells exposed to the same radiation have two completely different survival curves due to different oxygenation levels. Contrary to tumorous tissues, normal tissues are considered to be well oxygenated, thus more sensitive to the radiation effects. However, for the high ionizing particles adopted in PT, the OER is close to 1 due to their different cell killing mechanism, mainly based on clustered direct damages and without the need of mediators like free radicals. This effect is illustrated in the right picture of Fig.(1.15), in which the OER decreases with the increase of the LET. The sharp reduction of OER occurs over the same range of the optimum LET values shown in Fig.(1.12).

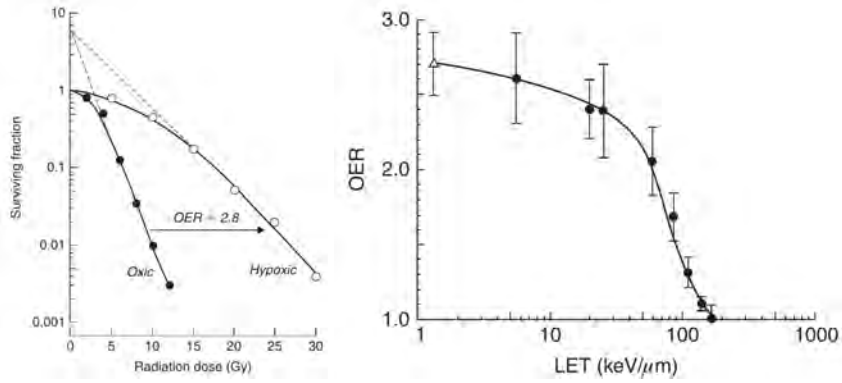

Figure 1.15: On the left, survival curves for cultured mammalian cells exposed to X-rays under hypoxic and oxic conditions. On the right, OER as a funtion of the LET for monoenergetic α and deuteron particles (circles) and 250 kVp X-rays (triangle) [46].

1.4 Particle Therapy

According to the World Health Organization report [59], the global cancer burden is significant and increasing. The number of cancer cases per year was of 18.1 million in 2018 and it is expected to be about 29.4 million in 2040. In this framework, radiotherapy is an essential and inseparable component for a comprehensive cancer treatment and care. In high-income countries, it is adopted in more than 50% of all cases of cancer, often combined with surgery or chemotherapy or both.

The aim of radiotherapy is to deliver a sufficient amount of dose to the tumorous tissues achieving local control and sparing the surrounding healthy tissues as much as possible. In order to quantify the damages on the carcinogenic and the healthy cells caused by a a given dose of radiation, two quantities are employed. The *Tumour Cure Probability* (TCP) is defined as the probability to obtain tumor control, killing the carcinogenic cells. The *Normal Tissue Complication Probability* (NTCP) is defined as the probability to experience complications and side effects on the healthy tissues of an organ or structure. Both of them can be visualized on a dose-response curve in order to differentiate among treatment plans. As shown in Fig.(1.16), the best radiotherapy treatment is the one that

enhances the separation region among the two curves defined as the *therapeutic window*.

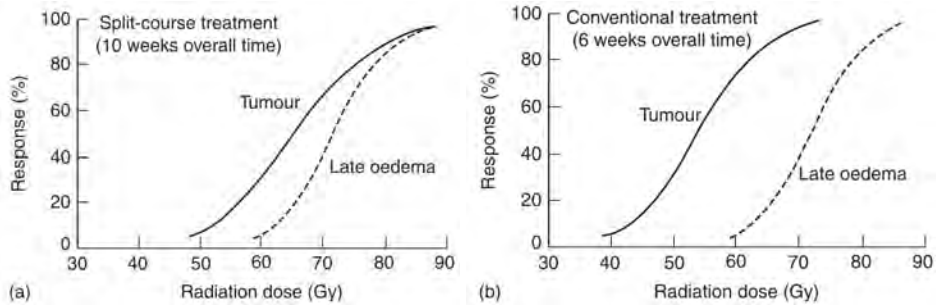

Figure 1.16: Dose–response curves for local control of laryngeal carcinoma (solid lines) and late laryngeal oedema (dotted lines) for split-course treatment (left) and conventional treatment (right). In this case, the latter treatment is preferred since the protraction of the overall treatment time narrows the therapeutic window [46].

The first tentative of radiotherapy has been performed in 1896 using X-rays on a breast cancer [60]. Since then, the technology improvement and the research results lead to the spread and the development of radiotherapy as a well established technique for cancer treatments.

Nowadays, different hospitals have a linac accelerator adopted for the conventional radiotherapy. In particular, it is performed with X-rays at few MeV delivered in multiple beams with different directions and entrance positions to spare the healthy tissues as much as possible.

In order to determine the treatment, different computer algorithms, defined as *Treatment Planning System* (TPS), are exploited to model the interactions between the radiation beam and the patient's anatomy. In details, TPS are adopted to simulate the spatial distribution of the radiation dose over all the volumes, evaluating the dose deposited both in the target tumour region and the healthy tissues. They are useful instruments that help the clinicians to determine the optimum treatment parameters matching the prescribed dose and constraints.

The state of the art for the photon radiation therapy is the *Intensity Modulated Radiation Therapy* (IMRT), in which the intensity of the radiation beam is modulated in small volumes, conforming the radiation dose to the three dimensional shape of the tumor and decreasing the dose deposition in the healthy tissues [61].

Differently from the conventional radiotherapy, PT is conducted exploiting charged hadrons, implying the use of cyclotrons and synchrotrons for the beam acceleration process. Since the first PT treatment performed with protons in 1954, more than 100000 patients have been treated with protons and more than 10000 with carbon ions [62].

The advantages of this technique over the conventional radiotherapy is given both by biology and physics properties. The former is given by the enhanced biological effectiveness presented in Sec.(1.3). The latter is represented by the different dose deposition profile of the charged particles, as illustrated in Sec.(1.2) and shown in Fig.(1.17). Due to the presence of the Bragg peak in the charged hadrons depth-dose profile and the consequent enhanced peak-to-plateau ratio, the dose conformation to the tumour volume can be achieved with higher precision. As shown in Fig.(1.18), PT adopts a minor number of beam entrance positions and it better preserves the healthy tissues with respect to the conventional radiotherapy.

In order to cover the tumour volume along the beam longitudinal coordinate, a single

beam with a given energy is not sufficient since the Bragg peak is too narrow. Thus, different beams with slightly different energies are superimposed to obtaining a broad irradiation profile called *Spread Out Bragg Peak* (SOBP), as shown in Fig.(1.19).

In clinical practice, the SOBP is created smearing the beam energy with *passive* or *active* modulations. In the former case, it is performed placing passive material layers with grooves called *ridge filters*. The filters are developed to produce a constant biological effect, taking into account the variation of RBE as a function of depth. In the latter case, the target volume is divided into layers with an equal beam energy and each layer is composed of a grid of points called voxels. Then, a pencil beam is delivered by means of a magnetic scanning system to each voxel, modifying the beam energy between the layers.

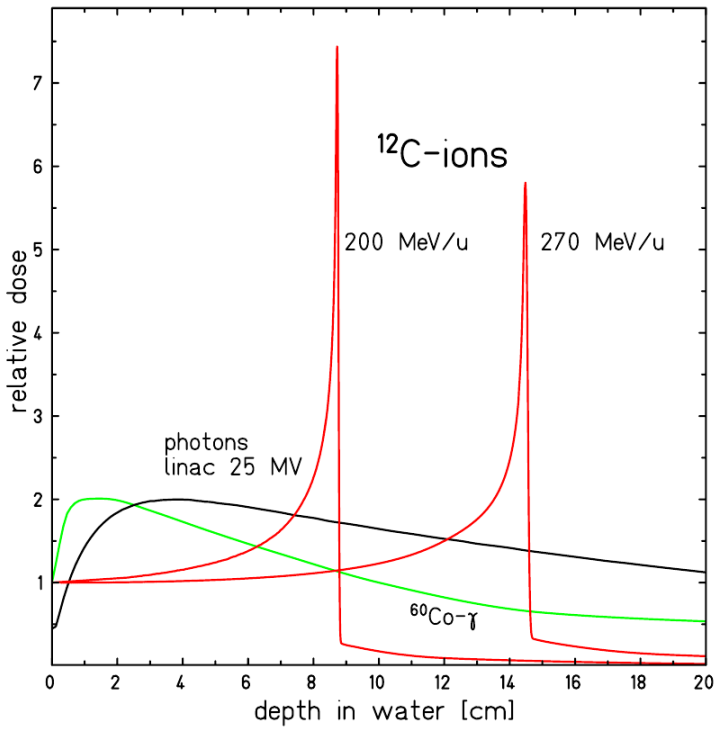

Figure 1.17: Depth-dose profiles of $^{60}Co - \gamma$ radiation, photons and ^{12}C ions at different energies in water [20]

The development of techniques and technologies in this field is still in progress mainly to explore new radiation approaches, to enhance the range monitoring devices and to improve the current TPS. At the moment, all the hadrontherapy centers spread over the world adopt proton and/or carbon ion beams for the clinical treatments. However, the use of other species of ion beams are still under study, focusing the efforts on the possibility to exploit helium and oxygen particles [4].

Regarding the range monitoring, the nuclear reactions in PT lead to the production of secondary particles that can be exploited to measure the beam range in the patients, due to their correlation with the Bragg peak position. In the last years different devices have been developed aiming to perform a monitoring of the treatments, with the purpose to take into account the range uncertainty due to patient positioning, anatomic changes,

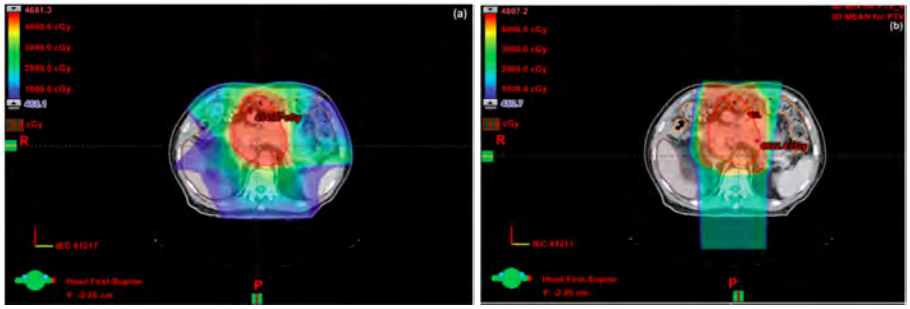

Figure 1.18: Example of a typical dose distribution achievable with X-rays (left) and protons (right) [63].

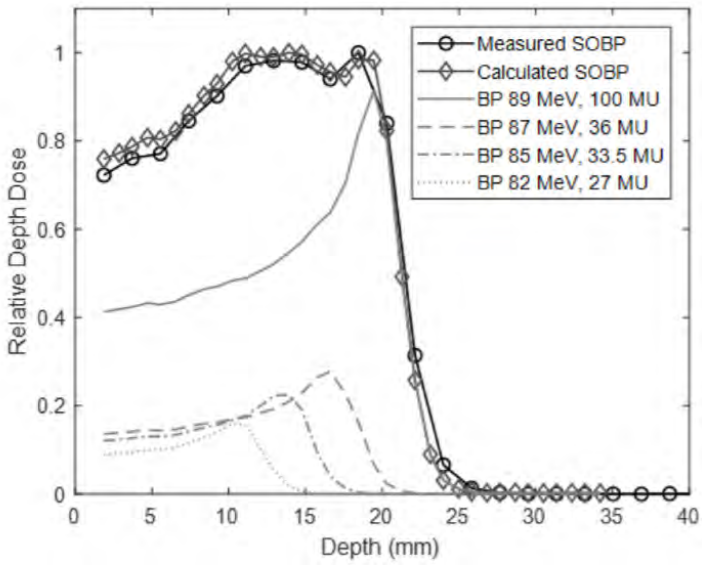

Figure 1.19: Example of measured and calculated SOBP curves obtained with protons at different energies [64].

beam delivery and dose deposition calculation [65]. As an example, the INSIDE project recently installed in CNAO (Italy) measures the secondary protons and the PET photons to provide an online monitoring for both carbon ion and proton therapy treatments [66].

At present, one of the open questions in PT is related to the effect of the nuclear inelastic interactions on the dose deposition and how to include them in the current TPS. As described in Sec.(1.2.4), there are two distinct outcomes from the nuclear inelastic interaction: the fragmentation of the projectile in case of heavy ion therapy and the fragmentation of the target nuclei both in proton and heavy ion therapy. The two cases and their relative relevance in PT will be discussed in detail in the next subsections.

1.4.1 Projectile Fragmentation in Particle Therapy

At the therapeutic energies, a fragmentation of the incident particle can occur only for projectiles with A>1, thus excluding protons. The bulk of the resulting heavy secondary particles have almost the same velocity and direction of the primary, but with a lower

mass. Instead, light fragments are emitted with a wide angular spread, up to 90°. The result is a build up of lower Z fragments with longer range and larger angle spread. The overall effect is the creation of a halo of projectile fragments that smears out what would otherwise be a sharp beam edge, releasing undesired dose beyond the Bragg peak and at larger angles.

The build-up curves of the secondary fragments produced by a 400 MeV/u ^{12}C ion beam in water is shown in Fig.(1.20). All the fragments are progressively produced with increasing depth, until a maximum reached at the Bragg peak. Beyond this peak, the amount of secondaries is reduced since all the primary carbon ions are stopped. In this region only light fragments can be produced from the secondary particles, leading to a long dose deposition tail after the Bragg peak.

The main contribution of the secondaries is given by proton and helium particles. All the other heavier fragments have an yield with one order of magnitude lower. In particular, the beryllium isotopes yield is even more reduced due to the prompt break up of ^{8}Be into two α particles.

Regarding the angular distribution of the fragments, as shown in Fig.(1.21), all the particles are produced focused in the beam forward direction, with an increasing width for the particles with a smaller charge. The FWHM ranges from the 3° of Boron fragments to the 10° of hydrogen particles. In particular, at the Bragg peak depth, the fraction of secondaries emitted with an angle $> 10^\circ$ is of about 40% for protons and of 7% for helium fragments. No relevant differences are observed between the two angular distributions at the two different depth of Fig.(1.21). Thus, the angular spread is mainly caused by the fragmentation process itself and only slightly influenced by the multiple Coulomb scattering.

All these effects should be considered in the TPS simulations in order to estimate the whole dose deposition correctly. A comparison between the measured heavy fragments build-up data with the simulations is shown in Fig.(1.22). The MC code adopted is based on TRiP98 [67], which is the computational kernel for the TPS developed and adopted for the ^{12}C ion therapy at GSI. The mismatch between experimental data and simulation results for the heavy ion fragments build up curves has a maximum of about 20-30%. There is also a contribution to the dose deposition from secondary neutrons, that has been estimated to be ten times smaller than the dose given from the charged fragments [3].

In order to improve the current TPS, more experimental data are necessary to study the nuclear interaction models and to improve the MC simulation codes. In particular, measurements performed on thick targets as done in [68] are not appropriate to test the nuclear reaction models with sufficient details. Experiments performed with thin targets that adopt large acceptance and high resolution spectrometers are needed.

1.4.2 Target Fragmentation in Proton Therapy

Both in protontherapy and in heavy ion therapy, the fragmentation of the target nuclei occurs along all the beam direction from the entrance channel to the Bragg peak depth. The secondary particles are isotropically produced and they include evaporated neutrons, protons and recoiled heavy target nuclei. The latter has a short range of the order of few μm and leads to an additional non negligible dose deposition. Due to their limited range values, the detection of target fragments is very difficult, establishing an arduous technological challenge. For this reason there are few data about target fragmentation and this effect is not considered in the current TPS.

A recent study performed with CR-39 plastic nuclear track detectors [69] measured

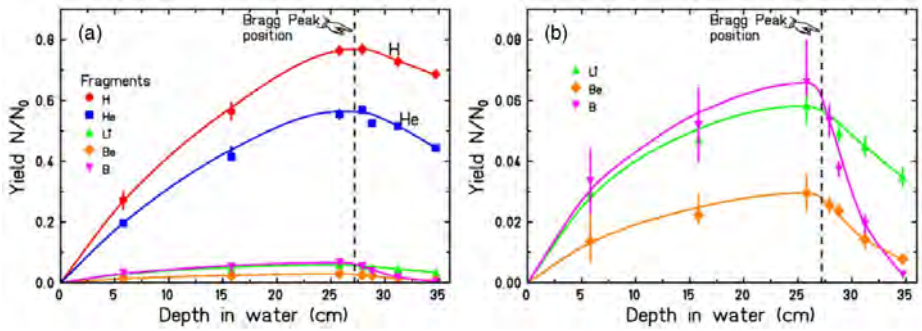

Figure 1.20: Build-up curves of secondary fragments produced by 400 MeV/u ^{12}C ions in water for all the fragments (a) and with an expanded view for the heavy particles (b). The yields were obtained integrating the measured angular distribution for all the particles emitted in a forward cone of 10° with respect to the beam axis [68].

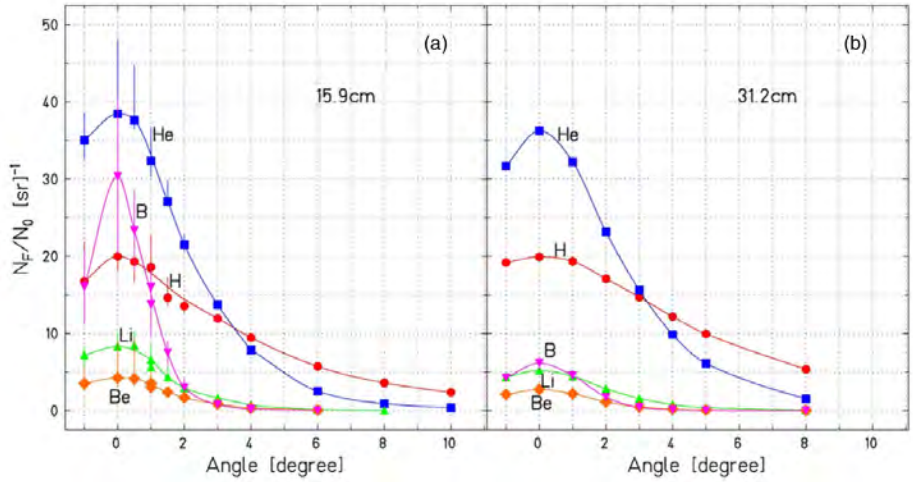

Figure 1.21: Angular distribution of charged fragments produced by 400 MeV/u ^{12}C ions in water targets of 15.9 cm(a) and 31.2 cm (b) [68].

the secondary target fragments fluence and dose contribution generated from PT projectiles at the Bragg peak plateau. The left panel of Fig.(1.23) shows the secondary fragments fluence distribution as a function of LET. Each LET spectrum follows a power-law curve with different shoulders due to the different fragment composition. The absolute fragments fluence from the carbon ion beam is four times higher then the proton beam due to its higher nuclear cross section. However, due to the enhanced LET of the heavy ion particles (10.9 keV/µm for ^{12}C and 0.53 keV/µm for protons), the required primary carbon ion fluence is smaller than the primary proton fluence to deliver the same amount of dose. The results of these two competing effects are shown in the right panel of Fig.(1.23), in which the secondary fragments fluence spectra are normalized to the primary beam dose. As expected, the stopping power dependence on Z^2 wins over the $A^{2/3}$ dependence of the nuclear cross section. The proton normalized fluence is 5.4 times larger than the carbon ion and 1.6 larger with respect to the helium ion normalized fluence.

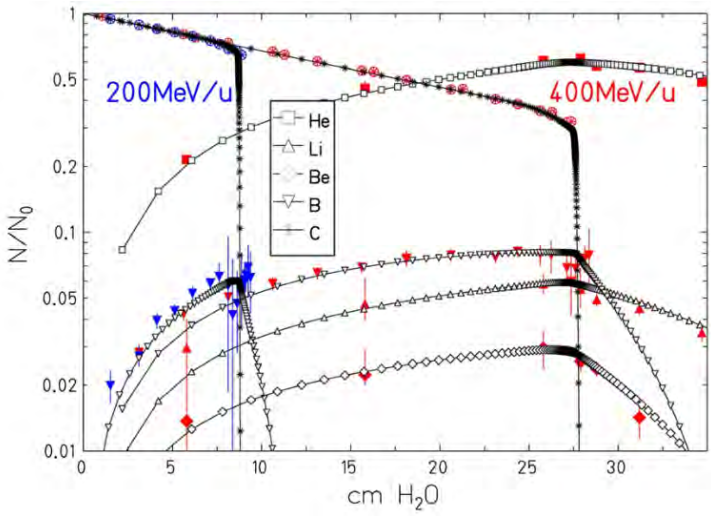

Figure 1.22: Measured (full symbols) beam loss of ^{12}C ion particles at 200 MeV/u (blue) and 400 MeV/u (red) in water with the heavy fragments build up curves, together with the TRiP98 simulated results (open symbols). Correction factors between 0.8 and 1.3 have been applied on the simulated build-up curves of the heavier fragments (B, Be, Li) to achieve agreement between measurements and calculations [68].

Table 1.2: Dose and fluence measurements for target fragments produced by different primary ion beams with the same initial fluence (F_p) of about $1.7 \cdot 10^{10}$cm^{-2} [69].

Beam	Energy [MeV/u]	Primary dose (D_p)[Gy]	Fragments dose (D_s)[Gy]	D_s/D_p $[\cdot 10^{-3}]$	Fragments fluence (F_s) $[\cdot 10^6$cm$^{-2}]$	F_s/F_p $[\cdot 10^{-4}]$
Proton	157	14.86	0.18 ± 0.01	12.19 ± 0.38	1.93 ± 0.04	1.10 ± 0.03
Helium	145	62.80	0.47 ± 0.01	7.43 ± 0.12	4.75 ± 0.07	2.73 ± 0.04
Carbon	383	302.7	0.68 ± 0.01	2.25 ± 0.04	6.62 ± 0.08	3.99 ± 0.05

From the LET spectra, the fragments absorbed dose contribution can be calculated and the overall results are summarized in Tab.(1.2). As for the fluence, also in this case the target fragments produced by carbon ion beams release a higher amount of absorbed dose with respect to the proton beam, but the relative dose contribution with respect to the primaries is lower. The results show that in the Bragg peak plateau, the target fragments produced in proton therapy release about 1.2% of the total absorbed dose with a relative fluence of $1.1 \cdot 10^{-4}$. The contribution for the helium and carbon ion beams are lower, but not negligible. In all the cases, the nuclear interactions make a significant contribution to the dose deposition at the plateau of the Bragg curve that should be considered in the TPS.

As resulted from a study performed with MC simulations [2], the target fragments dose deposition ahead of the Bragg peak is even more relevant. Fig.(1.24) shows the expected number of cells killed by ionizations and from secondary fragments along the primary beam path, assuming that each cell hit by a secondary particle die. Both the numbers of ionization and fragmentation events increase approaching to the Bragg peak, but in the entrance channel the target fragments contribution is about 10% and it reduces to about 2% at the Bragg peak. The previous experimental measurements and this MC simulation results are in agreement about the target nuclear inelastic contribution at the Bragg peak. However, further measurements are required to improve the target frag-

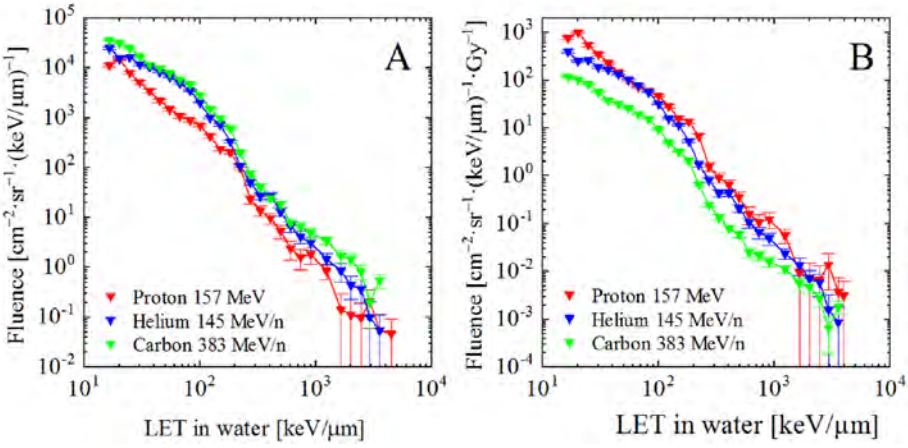

Figure 1.23: Measured absolute fluence (A) and fluence normalized to primary beam dose (B) as a function of LET for target fragments produced by different primary ion beams [69].

mentation models and to be adopted as benchmark for the MC tools.

Furthermore, in the current TPS the proton RBE is assumed to be 1.1 along all the LET range, but different studies show the inaccuracy of this approximation measuring different values of RBE, even up to 3.5, as shown in Fig.(1.25). The motivations of this fluctuation are still under studies, but nuclear interactions are one of the possible causes. Even if no clinical data reported about severe side effects due to the use of a fixed proton RBE value, a more complete RBE model that includes also the fragmentation effect is necessary to improve the current treatments.

In conclusion, nuclear inelastic interactions are not yet properly considered in the current TPS leading to possible relevant underestimate of dose calculation both in heavy ion and in protontherapy. In order to improve the current TPS, to enhance the present nuclear reaction models and to check the MC simulation output, new measurements on the fragmentation cross sections of the particles at the energies adopted in PT are required.

1.5 Radioprotection in Space Missions

Since the last century, one of the main space endeavors is the exploration of planets and satellites close to the Earth. The National Aeronautics and Space Administration (NASA) planned different long term missions, including a new lunar exploration with the landing of astronauts on the Moon by 2024, and a long term mission on Mars with a rover and a helicopter [5]. One of the most critical aspect of these missions is the health of the crew and the radiation hardness of the involved detectors. Once the astronauts leave the Earth with its protective environment provided by the magnetosphere, they are subject to space radiations composed of different particles at different energies. For the long term missions, the two main radiation hazards are:

- **Galactic Cosmic Radiation (GCR)**: it is composed of ionized particles from the entire element table with energies up to 10^{20} eV. In details, the GCR consists of electrons ($\sim$ 1-2%) and baryons ($\sim$ 98-99%). The latter composition is given by about 85-90% of protons, 10-14% of helium and $\sim$ 1% of heavy nuclei (Z>2), depending

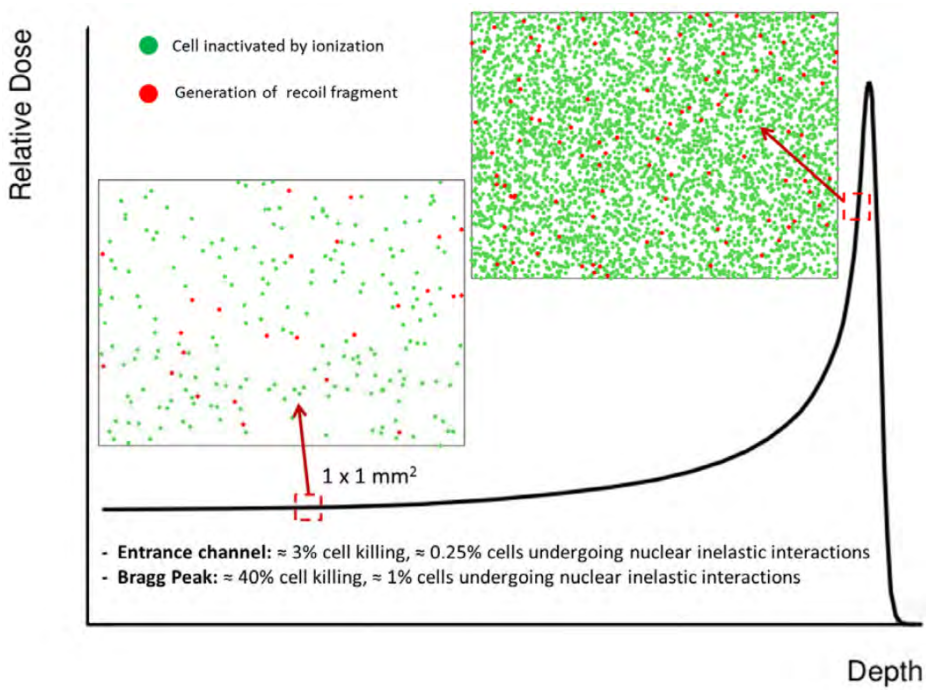

Figure 1.24: Schematic view of cells killed by primary ionization (greed dots) and fragmentation effect (red dots) at the entrance channel and close to the Bragg peak [2]. The depth is of the order of centimeters and the dose is in arbitrary units.

on the solar modulation. The detailed proton and heavy ion nuclei energy spectra is illustrated in Fig.(1.26). All the spectra are influenced by the solar activity. However, they are characterized by a peak at few hundreds of MeV/u followed by a long tail of high energetic particles.

- **Solar Particles Events (SPE)**: they are particles generated during the solar flares. The SPE are composed of protons $\sim 90\%$, helium $\sim 10\%$ and heavy (Z>2) ions $\sim 1\%$ with typical energies between 1 MeV/u up to several hundreds of MeV/u. They have great variability both in particle flux and energy spectra, as shown in Fig.(1.27).

  The SPE can be further divided into *impulsive* and *gradual* events. The former has a short duration (< 1 day) and it is characterized by a high proton content. Due to the limited fluence, it does not represent a serious radiation hazard. The latter has a duration of the order of few days. It has a higher flux and a wider longitudinal spread. In this case, the proton flux has a typical steep rise up to a maximum with a time scales of tens of minutes to an hour, followed by a second intensity peak at energies below 50 MeV that could also be higher than the first peak.

  Differently from the impulsive events, the gradual SPE represent a significant radiation hazard that the space missions must take into account carefully. One of the difficulty for the radioprotection from SPE is given by their unpredictable frequency and intensity. As an example, no anomalous large solar flares occurred during Solar Cycle 21 (1975-1986), but six large events had been detected in the Solar Cycle 22 only in five months between August and December 1989. In general,

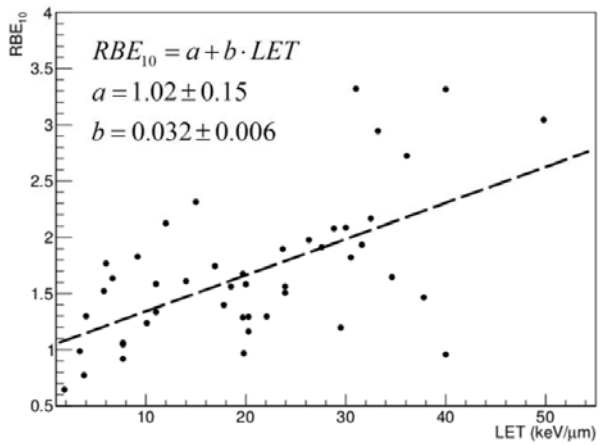

Figure 1.25: Proton RBE values for 10% survival fraction, extracted from database independent of α/β ratio. [2].

particles from SPE have lower energies compared to the GCR barions and they occur only in a limited time window, representing a minor hazard in the long term space missions.

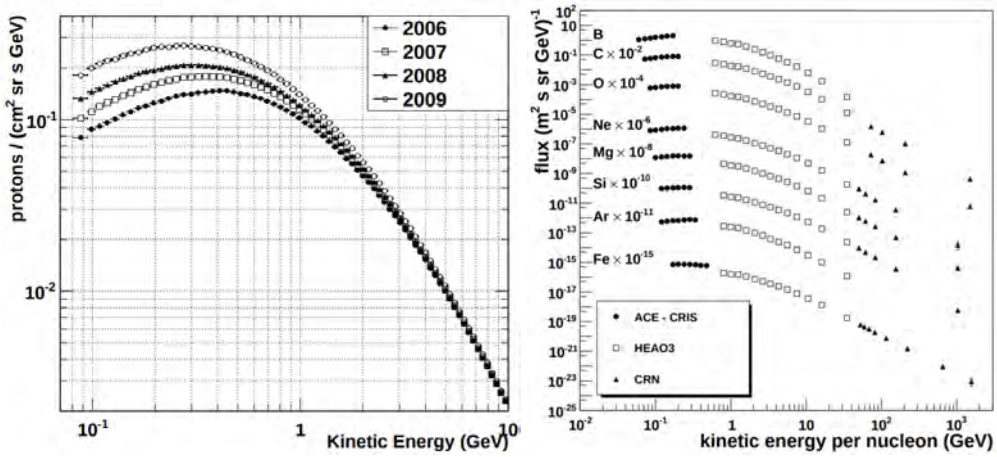

Figure 1.26: GCR Energy spectra for proton (left) measured by PAMELA experiment from 2006 to 2009 and for heavy ion (right) measured by CRN, HEAO-3 and ACE-CRIS experiments. In the latter case, the elements spectra are shifted on the vertical axis to avoid overlap [70].

Even if protons are the most abundant particles both in SPE and in GCR, their contribution to the absorbed dose is limited due to the energy loss dependency on the projectile charge (dE/dx$\sim z^2$). In addition, they have poor radiobiological effectiveness (proton RBE$\sim$1.1) compared to heavy ions (e.g.: carbon ion RBE$\geq$3). The 1% of heavy particles in GCR flux is responsible of about 60% of the overall dose equivalent deposition in unshielded space. In particular, the largest dose equivalent contribution in free space is given by the iron ions, due to its high charge (Z=26) and high LET value (155 keV/μm in water). A summary of the particles contributions to dose equivalent, cell

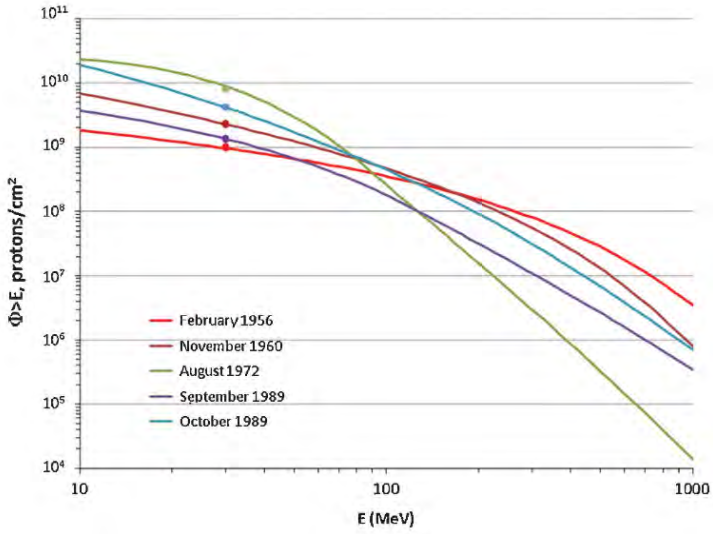

Figure 1.27: Integral energy spectra of some intense SPE happened in the last century [33].

death, neoplastic transformation and mouse tumors is shown in fig(1.28).

For the common people living in Europe, the annual effective dose absorption is between 2 and 5.5 mSv. On the Mars surface, the measured annual GCR effective dose rate is of 232 mSv and the SPE dose equivalent per event is of 0.025 mSv/event. A common way to mitigate both the effects of SPE and the heavy ion GCR is the use of passive shielding materials.

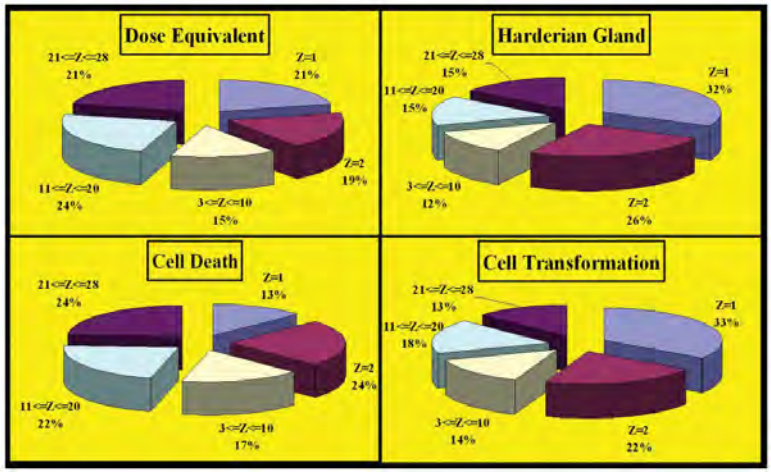

Figure 1.28: Contribution from different GCR charge groups to different radiation quality factors [33].

In case of SPE, the more dangerous events are those with a high fluence ($> 10^7$ protons·cm^{-2}) of protons with energy grater than 30 MeV. For a mission of 120 days, the probability to deal with at least one of such large SPE is of about 80%. For a mission of 540 days, there is almost no chance to avoid a large SPE, making the shielding from

SPE an essential part of the space missions.

Considering the models based on the past SPE data, the amount of material required to be shielded from the most dangerous solar events has been estimated to be of the order of 20 g/cm^2. Since the typical thickness of spacecrafts is of the order of 5 g/cm^2, the required shielding is usually reached in localized areas called *storm shelters* placed within the spacecrafts. In case of large SPE, an alarm is triggered and the astronauts can take cover in the storm shelters for the whole event duration.

In order to develop an efficient warning system to foresee the arrival of the SPE particles, different studies are focused on the detection and the correlation of the relativistic solar electrons with the SPE. In particular, the electrons could be detected up to one hour before the subsequent proton arrival and they could be related to the proton integral flux, providing a useful alarm system for the large SPE [33].

Also for the GCR, a passive material can be adopted to protect the astronauts exploiting the nuclear inelastic interactions to break up the incident high Z and high LET projectile into a shower of lower charge and lower LET fragments. One of the suitable spacecraft shielding material is aluminum because, depending on its thickness, it can trigger nuclear fragmentations without the production of too many neutrons. The same happens also with heavier materials such as steel or lead. As an example, 20 $g{\cdot}cm^{-2}$ of aluminum can attenuate ^{56}Fe and ^{12}C flux of a factor 0.617 and 0.423 respectively. Other projectiles with intermediate atomic number have in between attenuation factors [71].

However, the overall effect of the shielding material is a complex balance between the advantages and the harmful effects due to the different LET, RBE and energy deposition of the various projectile species and fragmentation products. As an example, the fragmentation of carbon and oxygen ions can increase the radiation hazard leading to the production of α particles of few MeV that are near to the maximum RBE value. The same results occur when oxygen and carbon ions do not undergo nuclear inelastic reaction, since their initial LET and RBE values are in the overkill region and they will increase the biological effectiveness losing energy in the shielding material. On the contrary, heavy ions with high LET close to the RBE peak such as iron nuclei can take advantages of the shielding material even without the fragmentation effect, since the energy loss will decrease their LET and RBE values.

At the moment, there are different studies aiming to improve the passive shielding material choice and also to develop new protection techniques both for SPE and GCR. As an example, polyethylene has been identified to be a valuable shielding material due to its high concentration of hydrogen atoms. Indeed, different experiments have already been conducted to test this material [72]. An other promising technique for the protection from GCR is the active shielding. It consists in the deflection of the radiations by means of electromagnetic fields created by superconductive magnets. The AMS experiment [73] helped to produce different ideas for the active shielding techniques. However, the effectiveness, the power and mass requirements, the device failure probability and also the biological effects of strong magnetic field on humans have to be evaluated properly to develop this new shielding approach.

In order to research new shielding materials, to improve the current MC transport codes and to develop new stochastic based risk models for the future long term space missions, new cross section measurements are required. Up to now, many integral cross section data have already been taken, but there is a significant lack of double-differential cross section measurements about light particles production and with new materials of interest [33].

CHAPTER 2

The FOOT experiment

2.1 Introduction

The FOOT (FragmentatiOn Of Target) experiment is a nuclear physics experiment inserted in the framework of PT and radioprotection in space. The main goal of the project is to measure the fragmentation differential cross sections ($d\sigma/d\Omega \cdot dE$) of the particles involved both in PT and in space radiations at different energies.

The experiment has been approved in 2017 and it is funded by the Italian National Institute for Nuclear Physics (INFN). At the moment, the collaboration is composed of about a hundred physicists from Italy, France, Germany and Japan.

In the project, two different experimental setups have been developed for the detection of heavy ($Z \geq 3$) and light ($Z \leq 3$) fragments, due to the different measurement requirements. The first one is an *electronic spectrometer* that is composed of different subdetectors, each one with a specific goal. The second setup is an *emulsion spectrometer* which is a compact detector based on the nuclear emulsion technology.

In order to optimize the detector parameters and to perform preliminary studies by means of MC data, the FLUKA code has been adopted for the simulation of both the apparata. The analysis of the MC and the experimental data is conducted by means of a dedicated reconstruction software developed within the FOOT experiment.

Details about the goals, the strategy of measurement and the experimental plan are illustrated in Sec.(2.2). A comprehensive presentation of both the apparata is shown in Sec.(2.3), followed by the description of the experimental requirements in Sec.(2.4). Finally, a general description of the FLUKA simulation code and the reconstruction software is presented in Sec.(2.5).

2.2 Aims and strategy of measurement

Nuclear inelastic interactions play an important role both in PT and space radiation protection. As point out in Sec.(1.4) and Sec.(1.5), the current MC simulation codes and the semi-empirical models cannot properly take into account all the aspects related to the nuclear inelastic interactions. One of the reasons is the lack of data on the fragmentation cross sections of particles at typical energies relevant for PT and space radiation protection. In particular, no data are present for the target fragmentation differential cross section $d\sigma/dE$ of protons at 60-250 MeV impinging on ^{16}O and ^{12}C target materials. In the case of projectile fragmentation, a double differential cross section measurement has been performed by the GANIL experiment (France), measuring the fragmentation of ^{12}C ions at 50 and 95 MeV/u on targets of C and C_2H_4 materials [74, 75]. However, no data are available at higher energies typical of PT (up to 450 MeV/u) or radiation protection

in space (on average around 700 MeV/u - 1 Gev/u). A similar scenario is present also for oxygen data, in which most of the measurements are collected with a projectile energy below or equal to 280 MeV/u.

The FOOT experiment aims to fill the gap and provide measurements of the double differential cross sections with respect to kinetic energy and angle, for both target and projectile fragmentation effects involved in PT and space radiation protection. Details about the goals and the strategy of measurements adopted to fulfill all the requirements are presented below.

2.2.1 Motivations and experimental program

The FOOT experiment double differential cross section data taken in the framework of PT will be exploited by the MoVe-IT (Modeling and Verification for Ion beam Treatment planning) experiment [76] to improve the current treatment planning systems. The aim is to properly take into account the biological effects caused by the nuclear inelastic interactions, developing a variable proton RBE model and exploring the hypothesis to extend the current pool of particles adopted in PT.

In the framework of PT projectile fragmentation, FOOT will measure the cross sections of ^{4}He, ^{12}C and ^{16}O beams with kinetic energies in the range 200-400 MeV/u, on targets made of ^{12}C, C_2H_4 and PMMA ($C_5O_2H_8$). In particular, ^{4}He and ^{16}O beams measurements aim to evaluate the possibility to introduce these ions in the current PT pool of particles. For the target fragmentation and the proton RBE studies, FOOT will measure the cross sections of ^{12}C and ^{16}O at 200 MeV/u on ^{12}C and C_2H_4 targets, adopting an inverse kinematic approach.

The same primary beams used in PT are of great interest also for the space radiation protection field, since they are present in the galactic cosmic radiation with higher energies. As shown in Fig.(1.26), the fluxes of different heavy ions included in the galactic cosmic radiations are peaked at about 700 MeV/u. For this reason, FOOT will perform a set of measurements dedicated to the space radiation protection needs, with the same pool of particles (^{4}He, ^{12}C and ^{16}O) at 700 MeV/u and impinging on the same target materials (^{12}C, C_2H_4 and PMMA).

In addition, all the FOOT experiment data will be exploited as benchmark for the current MC simulation tools, leading the possibility to improve the current nuclear interaction models and giving benefits to other physics fields.

The first two FOOT data takings have been conducted at the GSI experimental facility (Germany) with oxygen ions at 200 MeV/u and 400 MeV/u and with carbon ions at 700 MeV/u. The next tests will be conducted at CNAO (Italy) and GSI. These two structures, together with the HIT (Germany) accelerator, are the facilities where FOOT will take data, since they can provide the requested primary particles with the energies of interest.

2.2.2 Target material

The choice of the FOOT experiment targets is driven by the necessity to replicate the human body composition that is mainly given by oxygen (61%), carbon (23%) and hydrogen (10%) atoms [77]. Only in the second case, a carbon ion target can be made and adopted in experimental rooms without any complication. For the oxygen and hydrogen cases, the handling of a pure gaseous and inflammable material prevents the use of such kind of targets in the accelerator facilities for safety reasons. In addition, the gas low density would deeply drop the interaction rate, making the experiment unsustainable.

In order to overcome all the complications, the FOOT experiment adopts carbon targets enriched with oxygen and hydrogen particles, i.e.: PMMA and C_2H_4. The collected measurements will be subtracted with the pure carbon target data in order to retrieve the cross sections on pure oxygen and hydrogen targets. As an example, the calculation of the hydrogen cross section measurement is expressed in Eq.(2.1) and the results from a previous experiment conducted at Ganil [74] is shown in Fig.(2.1).

$$\sigma(\mathrm{H}) = \frac{1}{2}(\sigma(\mathrm{CH_2}) - \sigma(\mathrm{C})) \tag{2.1}$$

With this method, a solid target with a thickness of few millimeters can be used avoiding

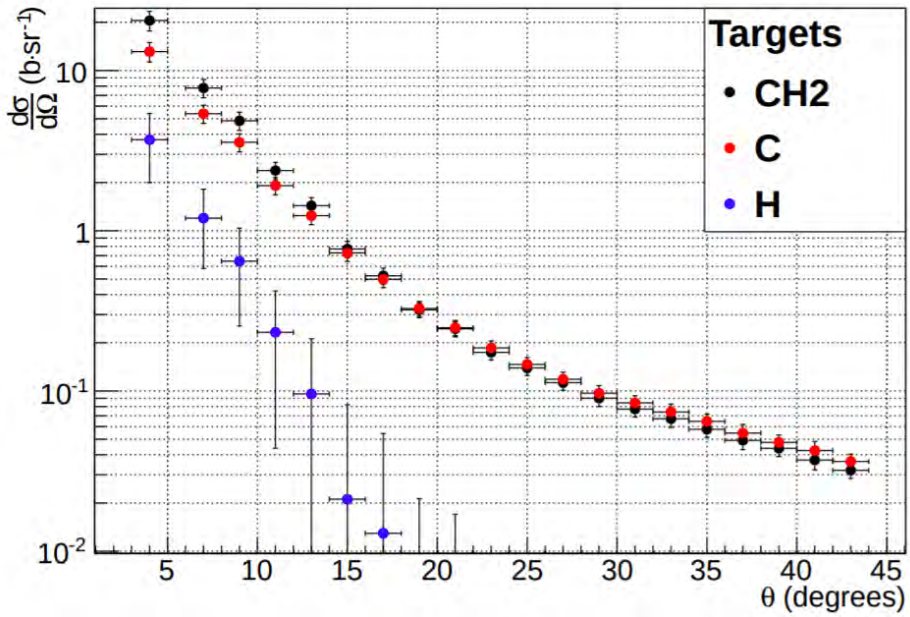

Figure 2.1: Differential cross section measurements of α fragments produced by 95 MeV/u carbon ions on targets of CH_2 and C. The angular distribution for the hydrogen target is derived by the difference between both, divided by two [74].

the handling difficulties and enhancing the nuclear interaction probability.

The main constraints about an excessive target thickness are given by the necessity to limit the probability of secondary fragmentation and the multiple Coulomb scattering. In addition, the particle energy lost within the target cannot be measured and it lowers the precision of the results. The main unavoidable drawback of this method is given by the large uncertainties on the final cross section results. Indeed, the two cross section measurements in the right part of Eq.(2.1) have similar values and the subtraction results are an order of magnitude smaller with respect to the initial measured values. This effect is clearly visible in Fig.(2.1).

2.2.3 Inverse kinematic approach for the target fragmentation measurements

The target fragments produced by protons in PT have energies of the order of few MeV and ranges of the order of tens of µm. The detection of such particles is not a simple

task since the fragments can leave the target only if they are produced close to the exit window, in the last few micrometers of material. Avoiding the use of thick targets, the development and the handling of a target with a thickness of few micrometers is not an easy operation. Moreover, the nuclear inelastic interaction rate in such thin target would be strongly reduced and the initial kinetic energy of the fragments cannot be measured with high accuracy due to a non negligible energy loss in the target material.

In order to overcome all the difficulties, the FOOT experiment adopts an inverse kinematic approach to study the target fragmentation effect. The direct kinematic would imply to measure the fragments produced by a proton beam impinging on a tissue-like target made of oxygen or carbon ion. On the contrary, in the inverse kinematic approach the tissue-like atoms are shot against a target made of protons, switching the role of projectile and target. In this way, the produced fragments have boosted energies and longer ranges making their detection simple. In addition, the target can be created with a thickness of the order of millimeters, rising the nuclear inelastic interaction probability and not relevantly modifying the fragment initial kinetic energy.

In order to recover the original system of reference and retrieve the cross section data of protons on carbon and oxygen targets, all the four momenta components of the fragments and the projectile must be measured accurately. This leads to different experimental requirements on the FOOT apparatus performances, but, in this way, the Lorentz transformation matrix can be reconstructed.

Finally, due to the complications reported in Sec.2.2.2 about the management of a gaseous target only made of hydrogen atoms, the FOOT experiment will adopt two targets of ^{12}C and C_2H_4, exploiting the subtraction of cross sections techniques also for the target fragmentation studies.

2.2.4 Radiobiology requirements

Different studies have been conducted by means of MC simulations with the current treatment planning systems to estimate the required accuracy on the FOOT experimental measurements. Among the FOOT experiment goals, the most stringent requirements are those given by the PT necessities evaluated by the MoVe-IT experiment. In order to improve the current treatment planning systems, the maximum uncertainty tolerated on the differential cross section measurements ($d\sigma/dE$) for the target fragmentation process is of 10%. For the projectile fragmentation studies, the angular and energy double differential cross section ($d^2\sigma/d\Omega \cdot dE$) have to be measured with an accuracy at least of 5%. In order to fulfill the radiobiological desiderata, the capability of charge and isotopic identification of fragments have to be of about 2-3% and 5% respectively.

2.3 Experimental setup

The FOOT experiment designed and developed two distinct experimental setups to measure the differential cross sections. The reason of this choice is given by the different properties of light ($Z \leq 3$) and heavy ($Z \geq 3$) fragments. As resulted from a simulation performed by means of FLUKA MC code shown in Fig.(2.2), the angular distribution of light particles are widely spread. On the contrary, heavy fragments are mainly emitted inside a cone of 10° with respect to the initial particle direction.

Due to the distinct angular distributions and the different requirements to detect the particles, an *electronic spectrometer* has been designed to detect the heavy fragments. Instead, an *Emulsion Cloud Chamber* (ECC) detector has been developed to measure the cross sections of light particles with a wide angular range. The lithium (Z=3) fragments

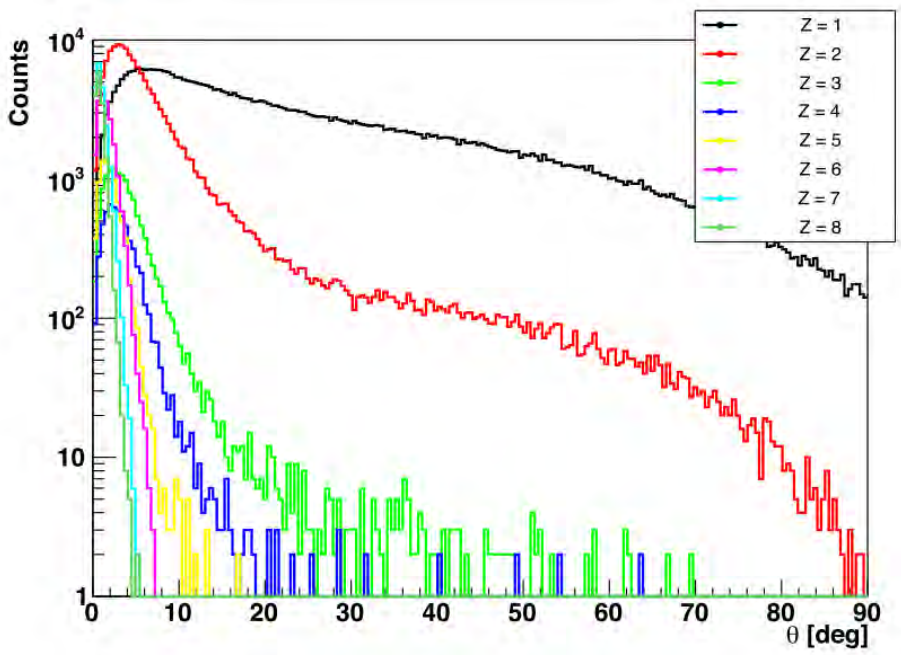

Figure 2.2: Angular distribution of fragments produced by an oxygen beam at 200 MeV/u impinging on a 2 mm thick target made of C_2H_4. Data simulated by means of FLUKA.

will be detected by both the setups and the results will be adopted as cross check between the two apparata.

2.3.1 Electronic spectrometer

The FOOT electronic spectrometer has been developed to detect the fragments with $Z \geq 3$. The setup has an angular acceptance of about 10° to contain and detect all the interested particles. The total longitudinal length is limited by the space availability of the experimental facilities which can provide the required primary beams. In addition, FOOT will take data in different structures, so the setup portability is a non negligible aspect to be taken into account. The total length of the apparatus varies between 1.5 and 3.5 meters according to the energy of the beam. A schematic view of the electronic spectrometer is shown in Fig.(2.3).

The whole apparatus can be divided in three parts:

- **Upstream region:** is composed of a *Start Counter* plastic scintillator and a *Beam Monitor* drift chamber. These detectors are adopted in the event trigger system, in the Time Of Flight (TOF) measurement system and to reconstruct the incoming primary particle track.
- **Magnetic spectrometer:** two permanent magnets and a set of tracking detectors (*Vertex detector, Inner Tracker* and *Microstrip Silicon Detector*) are placed just beyond the target to reconstruct the fragments tracks and momenta.
- **Downstream region:** is composed of a *Tof-Wall scintillator* and a *Calorimeter*. The former is exploited to measure the fragment energy loss $\Delta E/\Delta x$ and, combined

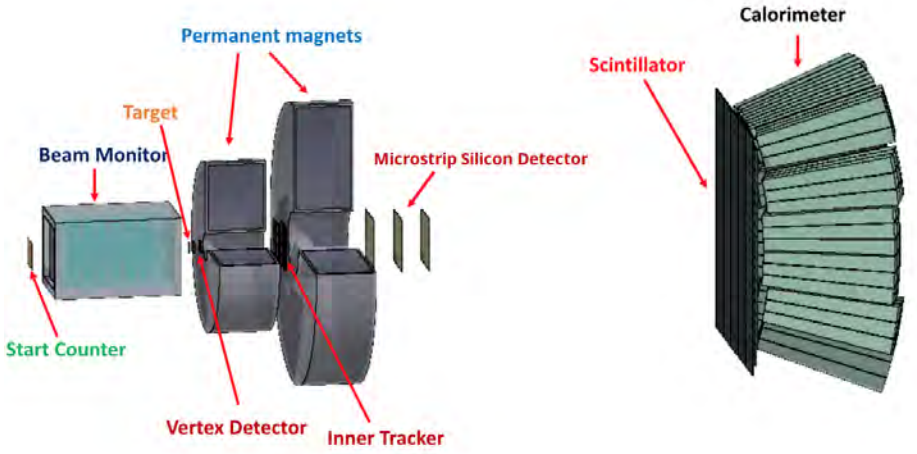

Figure 2.3: Schematic view of the FOOT electronic spectrometer detectors.

with the Start Counter scintillator, to provide the particle TOF values. The latter is adopted to measure the kinetic energy.

The longitudinal position of the downstream region detectors depends on the incident particle beam energy. In details, for the PT measurements conducted with primaries with a kinetic energy below or equal to 400 MeV/u, the scintillator and the calorimeter are placed at about 1 meter from the target. For the high energy particle beams with kinetic energies of about 700-800 MeV/u dedicated to the space radiation protection data, the downstream detectors are placed at about 3 meters from the target position, increasing the accuracy of the TOF measurement.

A complete description of the different detectors is presented in the next paragraphs, including the presentation of the data acquisition system and the trigger logic tested in a data taking performed at GSI.

Start Counter

The Start Counter (SC) detector is a plastic scintillator adopted to measure the beam rate, to provide the trigger for the acquisition system and to determine the start time of the TOF measurement performed with the downstream scintillator.

It consist of a 250 µm thick and $5 \times 5\,\mathrm{cm}^2$ large squared foil of EJ-228 scintillator [78, 79] mounted in an aluminium frame and contained in a black 3D printed box. Two squared windows made of 4 µm of aluminized mylar are placed in the black box corresponding to the beam entrance and exit positions. The scintillation light is collected laterally by 48 SiPMs bundled in 8 channels. A picture of the SC detector is shown in Fig.(2.4).

The SiPM waveforms are read by a WaveDAQ system [80] that provides also the SiPMs power supply. The maximum signal sampling rate is of 5 Gsamples/s and the dynamic range is of 1 V. The incoming signals can be amplified by a factor of 0.5-100 before the digitization in order to have the possibility to exploit the detector for different projectile species and energies.

The acquired data are analyzed offline with a constant fraction discriminator technique to extract a precise measurement of the event time. This information is exploited by the drift chamber detector as reference time and by the downstream scintillator for the TOF measurement.

The detector has been tested at CNAO and GSI with carbon and oxygen ion beams at different energies. A time resolution of the order of 60 ps has been achieved for ^{12}C ion beam with a kinetic energy of 700 MeV/u.

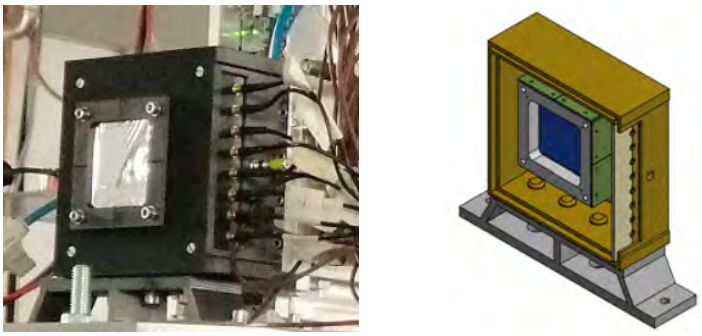

Figure 2.4: A picture (left) and a technical draw (right) of the SC detector.

Beam Monitor

The Beam Monitor (BM) is a drift chamber originally developed in the FIRST experiment [81] and adopted both in the electronic and the ECC setups. It is placed above the target aiming to measure the incoming beam direction and the impinging point position of the primaries on the target. In addition, for the electronic spectrometer purpose, the BM multi-track reconstruction capability is exploited to reject the events in which the projectile interacts inelastically with the SC or the BM itself.

The detector consists of six planes of vertical and horizontal layers of cells, enclosed by two films of mylar with a thickness of 100 µm placed at the beam entrance and exit. Each plane is composed of two layers of cells for the vertical and horizontal view, both perpendicular with respect to the beam line. Each layer is made of three cells and two consecutive layers of the same view are staggered by half a cell to solve left-right ambiguities in the track reconstruction. The cells have a rectangular shape (1.6 cm $\times$ 1 cm) with the longer side perpendicular to the incoming beam direction. Eight aluminium field wires with a diameter of 90 µm delimit the cell area. Two adjacent cells of the same plane and same layer, share three field wires. A gold-plated tungsten sense wire with a diameter of 25 µm is placed at the cell center. It is connected to the BM high voltage and to the readout electronics. A scheme of the BM detector with a detailed view of an internal cell is illustrated in Fig.(2.5).

Twelve dedicated front-end electronic boards are adopted to read all the sense wire signals. The BM output waveforms are connected to a VME leading edge discriminator which output is read by a VME TDC module integrated in the FOOT experiment DAQ system.

The detector active area is of about $4 \times 4\,\mathrm{cm}^2$ and the total length is 21 cm. The active length, defined as the distance along the beam direction between the sense wire positions on the first and the last layer of the same view, is of 13 cm. A picture and the technical draw of the BM is shown in Fig.(2.6).

The BM operates at about 0.9 bar with a gas mixture made of Ar/CO_2 at 80/20% and with a gas flow rate of about 1 l/h.

The calibration and the performance assessment of the detector has been conducted at the Trento protontherapy facility with protons at 228 MeV and 80 MeV. The spatial resolution of the detector is of about 100 µm in the central part of the cell and the related angular resolution is of the order of few mrad. The hit detection efficiency has been found to be about 90%.

The detector has already been successfully adopted in two ECC setup data takings and in the first FOOT electronic spectrometer test, both conducted at the GSI facility with oxygen and carbon ion beams at different energies. Details on the detector functioning are illustrated in Sec.(3.3) and the results of the calibration and the performances of the detector are shown in Chap.(4).

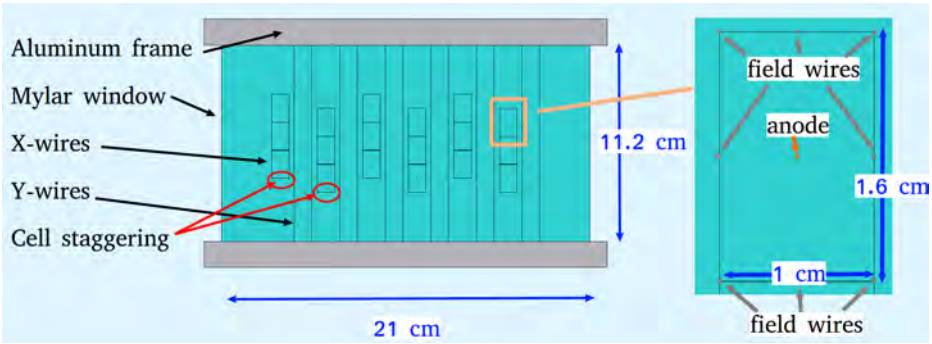

Figure 2.5: Schematic view of the BM detector with a detailed sketch of a BM cell structure.

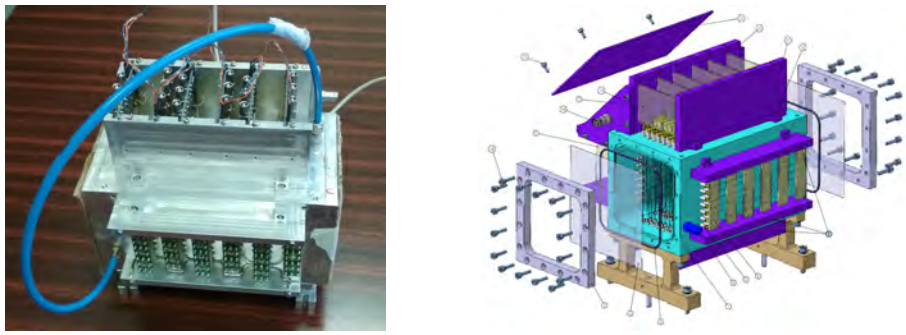

Figure 2.6: A picture (left) and a technical draw (right) of the BM detector.

Vertex detector

As shown in Fig.(2.7), the vertex detector (VTX) is composed of four layers of silicon pixel detectors placed at few millimeters beyond the target, achieving a geometrical acceptance of about 40°. This detector is adopted to reconstruct the track and the momentum of the particles, together with the other tracking detectors of the magnetic spectrometer. In addition, it is exploited to identify the projectile interaction position in the target material matching the BM track.

Each layer of the VTX is composed of 928×960 MIMOSA-28 (M28) Monolithic Active Pixel Sensors (MAPS). The pixels have a pitch of 20.7 µm for a total transverse active area of $2.022 \times 2.271\,\mathrm{cm}^2$. The thickness of the epitaxial layer is of 15 µm on a high resistivity substrate of about $400\,\Omega\cdot$cm. The total thickness of a single layer is of 50 µm and the distance between the layers is of 2-3 millimeters.

Each pixel includes an amplification and a Correlated Double Sampling (CDS) circuit that is read out with a 185.6 µs frame readout time. The overall maximum rate capability of the detector is of the order of 1-2 kHz to avoid excessive pile up. This corresponds also to the FOOT electronic spectrometer maximum rate capability, since the VTX is the slowest detector in the acquisition chain.

A previous version of the detector with a former version of MIMOSA-26 sensors has been adopted in the FIRST [81] experiment reaching a spatial resolution of the order of 5 µm [82].

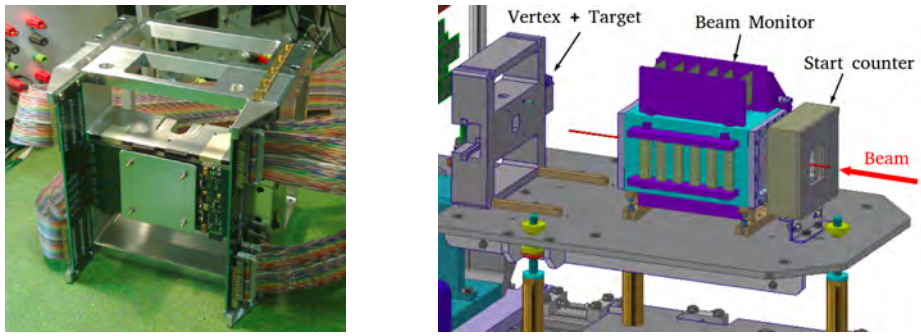

Figure 2.7: On the left, picture of the target and VTX detector setup; on right, a schematic view of the upstream region detectors together with the target and vertex container.

Magnetic system

Beyond the target and the vertex detector, two permanent magnets (PMs) in a Halbach configuration provide the requested magnetic field to bend the fragments initial directions making the particles momentum detection possible. The choice of the type and the configuration of the magnets have been driven by the necessity to match the portability of the apparatus with the momentum resolution requirement. In particular, a magnetic dipole in vacuum could satisfy the latter condition, but it cannot be easily moved and installed in the different accelerator facilities. In addition, the Halbach configuration allows the installation of a tracking station also in the middle of the magnetic system, improving the momentum resolution capability.

Each PM is composed of twelve blocks of magnets arranged in an annular configuration, as shown on the left panel of Fig.(2.8). Since the magnetic field increases with the external radius and decreases with the gap radius, the two PM have been designed with two different dimensions, in order to provide the required magnetic field maintaining an angular acceptance of 10° for the fragments.

The first PM, close to the vertex detector, has an internal diameter of 5 cm and it provides a maximum magnetic field of 1.4 T. The second PM, close to the downstream region, has a gap diameter of 10.6 cm and the maximum magnetic field is of 0.9 T. Between the two PMs there is a gap of 50 cm where the Inner Tracker detector is installed.

Both the PMs provide a magnetic field with a Gaussian shape along the Y axis, perpendicular with respect to the beam direction, as shown on the right panel of Fig.(2.8).

The Sm_2Co_{17} has been chosen as PMs material due to its capability to maintain the magnetic properties also in a high radiation environment.

A dedicated mechanical structure has been developed to enclosure and support the PMs, managing the total weight of about 250 Kg and the repulsion force of about 2000 N present in the gap between the two PMs. In order to allow the installation and the alignment of the magnetic spectrometer detectors, the mechanical support provides the possibility to lift the magnets, as shown in Fig.(2.9).

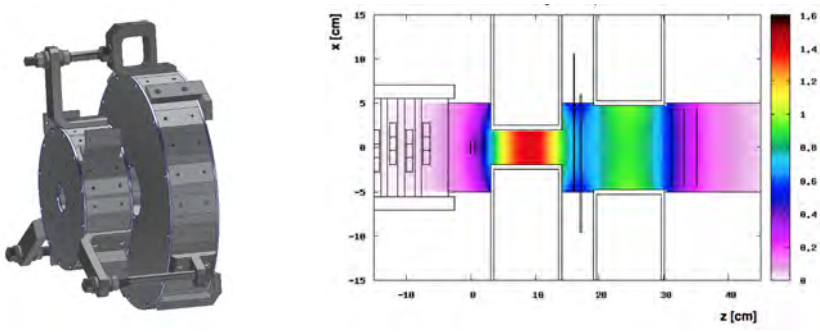

Figure 2.8: On the left, technical draw of the two magnets containing structure; On the right, the computed magnetic field map.

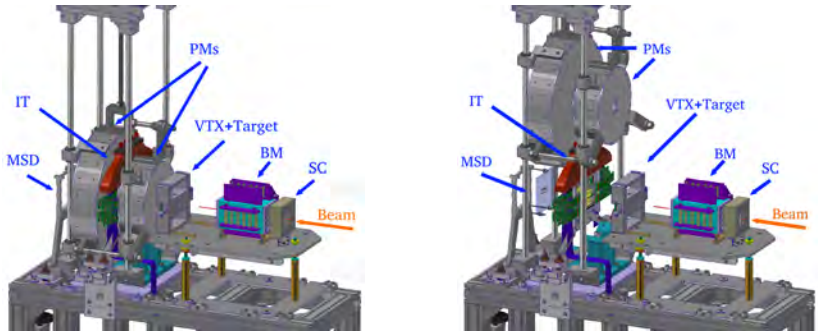

Figure 2.9: The FOOT mechanical structure adopted to contain all the upstream detectors and the magnetic spectrometers during the data taking (left) and during the detectors alignment configuration (right), with the PMs lifted up.

Inner Tracker

The Inner Tracker (IT) detector is composed of two layers of silicon pixel detectors placed in the two PMs gap and used as the second station of the magnetic spectrometer.

The IT adopts the same M28 sensor as the VTX detector simplifying the DAQ readout system. The magnetic field effect on the M28 should be negligible [83].

In order to maximize the active area resulted to be about $8 \times 8\,\mathrm{cm}^2$, the M28 sensors are arranged in ladders, as in the PLUME project [84] (see Fig.(2.10)). Each IT plane is composed of two ladders supported by a mechanical frame as illustrated in Fig.(2.11). Each ladder has eight M28 sensors, four on each side, glued on a 2 mm thick support structure made of low density silicon carbide (SiC) foam. On each ladder side, the four

M28 sensors are glued and bonded on a kapton-metal flex cable that provides the communication with the outside world. The dead area between two consecutive sensors on the same ladder side is of 30 µm and the overall material budget of an IT ladder is $x/X_0 \sim 0.3\%$.

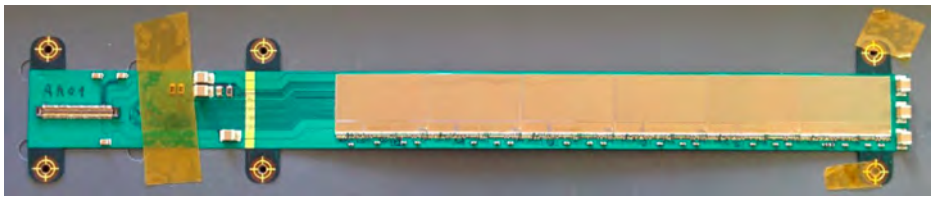

Figure 2.10: Picture of a PLUME ladder.

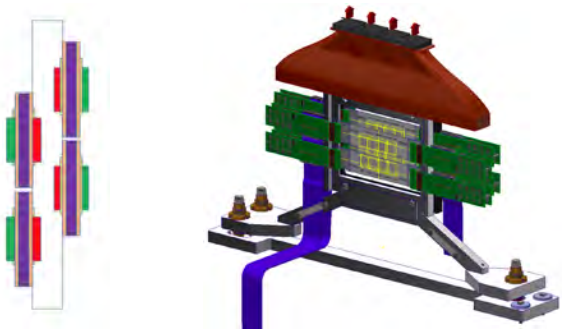

Figure 2.11: Scheme of the IT detector from a perpendicular view (left) and along the beam line (right).

Microstrip Silicon Detector

The Microstrip Silicon Detector (MSD) is the last station of the FOOT magnetic spectrometer. It is composed of three layers of silicon microstrip detectors placed beyond the two PMs at about 35 cm far from the target.

The MSD is adopted to reconstruct the position of the fragments with the possibility to measure also the energy release (ΔE) of the particles. In the former case, in addition to the momentum measurement, the detector is fundamental to match the reconstructed tracks with the downstream scintillator and calorimeter hits. In the latter case, the redundant independent measurement of ΔE is complementary to the one performed by the Tof-Wall scintillator which is necessary for the fragments charge identification.

The three MSD layers are separated by a gap of about 2 cm. Each layer has an active area of $9.6 \times 9.6\,\mathrm{cm}^2$ and it is composed of two perpendicular Single-Sided Silicon Detector (SSSD) sensors glued on a hybrid Printed Circuit Board (PCB) that provides the mechanical support. The light shielding is achieved exploiting the metallized sensors backplane, as shown in Fig.(2.12).

Each sensor has a thickness of 150 µm and the strip pitch is of 50 µm. The read out of each SSSD is performed by means of ten VA1140 chips with a read out pitch of 150 µm, for a total of 640 channels. The expected spatial resolution provided by the digital read out is of about 40 µm.

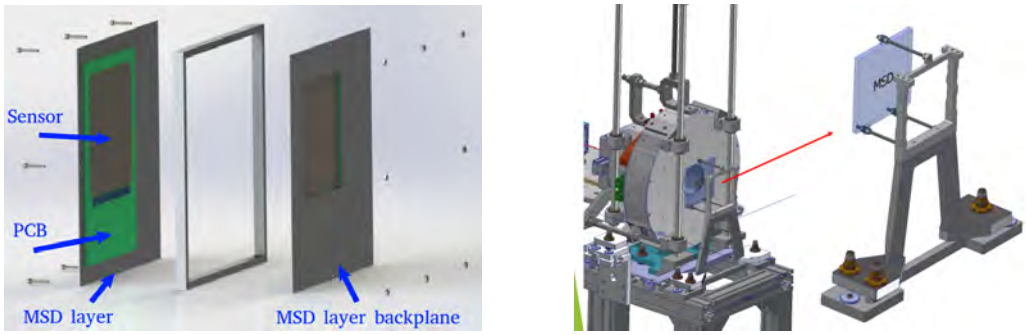

Figure 2.12: On the left, scheme of two layers of the MSD detector; On the right, the MSD arrangement in the mechanical support designed for the FOOT experiment.

Tof-Wall Scintillator

The Tof-Wall detector (TW) is composed of two layers of plastic scintillator bars (EJ-200) [79] adopted to measure the fragments ΔE, position and the last TOF time stamp.

The two layers are arranged along the vertical or the horizontal coordinate, both perpendicular with respect to the beam line. Each layer is composed of 20 parallel bars wrapped with a reflective aluminum and darkening black tape. The detector active area is of 40×40 cm^2 that corresponds to an angular aperture of 10° at 1 m from the target. Each bar has a dimension of $40\,\text{cm} \times 2\,\text{cm} \times 2\,\text{mm}$, ensuring a fragments pile-up frequency at the level of $\leq 1\%$. The thickness of the bar has been chosen as a compromise between the requirements given by the ΔE resolution on one hand, and the necessity to reduce the secondary fragmentation probability on the other hand. A picture of a TW bar and of the whole detector is shown in Fig.(2.13).

The read out of each bar is performed by four SiPMs placed at both the extremities to allow the reconstruction of the hit position along the bar. Each SiPM has an active area of 3×3 mm^2 and a microcell pitch of 25 µm, for a total of 4×14400 pixels coupled at each bar edge. The channels are digitized at 3-4 Gsamples/s by a WaveDAQ shared with the SC detector. The read out dynamic range is extended over a factor of 100 allowing the simultaneous measurement of signals from protons to oxygen ions.

The detector has already been tested in different facilities with different primary beams [85]. As shown in Fig.(2.14), the obtained energy loss resolution $\sigma(\Delta E)/\Delta E$ is of about $\sim 6 - 14\%$ and $\sim 5 - 7\%$ and the time resolution is of 120-180 ps and 30-40 ps for proton and carbon ion beams, respectively. Finally, the precision on the time measurement allows a hit position reconstruction resolution along the bar of $\sigma_{\text{pos}} \leq 8$ mm.

Calorimeter

The last downstream detector in the FOOT electronic spectrometer is a calorimeter placed just beyond the TW and adopted to measure the kinetic energy of the fragments.

The detector is inherited from the L3 experiment conducted at CERN [86] and it is composed of 320 $Bi_4Ge_3O_{12}$ (BGO) crystals. Each crystal has a truncated pyramid shape with a length of 24 cm, a front area of about $2 \times 2\,\text{cm}^2$ and a base area of about $3 \times 3\,\text{cm}^2$. The geometrical configuration of the detector is still under study. At the moment, the hypothesis is to arrange the crystals in modules of 3×3 elements building a spherical cap configuration as shown in fig(2.15).

The signal of each crystal is collected by a matrix of 25 SiPMs with an active surface

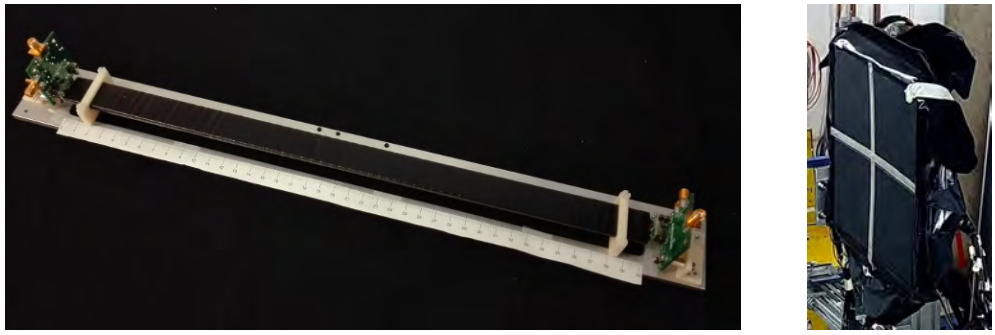

Figure 2.13: Pictures of a crystal of the TW (left) and the whole detector (right) during a test performed at GSI.

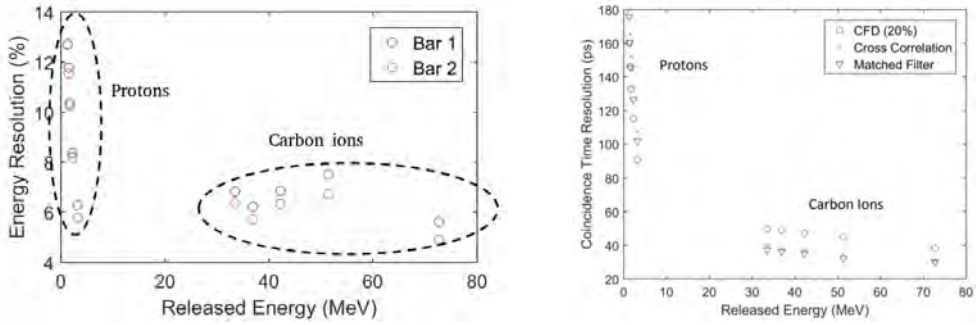

Figure 2.14: Energy resolution $\sigma(\Delta E)/\Delta E$ (left) and coincidence time resolution (right) as a function of the energy released (ΔE) in two bars of the TW detector. Data taken at Trento and CNAO with protons at 60-230 MeV and carbon ions at 115-400 MeV/u.

of $2 \times 2\,\mathrm{cm}^2$ and a microcell pitch of 15 µm that provides a linear response in the energy range up to 10 GeV. Each SiPM matrix signal is read out by a board specifically designed to match its dimensions and to read out also the SiPM temperature. In this way, the signal variations due to temperature changes can be compensated offline. Finally, the crystal signals are collected and sampled at 62.5 MSamples/s by a CAEN waveform digitizer V1740.

Different data takings have been conducted at CNAO and GSI and others are foreseen in 2021 to test various SiPM models, digitizer boards and BGO wrapping. The energy resolution has been evaluated exploiting both the signal amplitude (*amplitude analysis*) and its integral (*charge analysis*).

As an example, Fig.(2.16) shows the signal integral distributions of the data taken at CNAO with carbon ions at different energies. Each distribution has a Gaussian shape with a tail on the left caused by the neutrons produced in the crystals that cannot be contained and detected. This effect leads to an underestimation of the particle energy. However, the detector resolution is estimated considering the parameters of a Gaussian fit performed only in the peak region. Similar distributions are collected also with the amplitude analysis and, as illustrated in Fig.(2.17), the preliminary results obtained with proton, carbon and oxygen ion beams in the energy range of 70-400 MeV/u, show an energy resolution $\sigma(E_{kin})/E_{kin}$ below 2% for the heavy particles ($Z \geq 2$), fulfilling the FOOT experiment requirements for the PT measurements.

Indeed, in the low energy range ($E_{kin} \leq 200$) relevant for PT, the calorimeter reaches its best performances since the energy loss of the fragments is mainly due to the electromagnetic interaction of the incident particles with the target electrons and nuclei. However, the neutron production sets a systematic intrinsic limit on the detector energy resolution.

At the energies relevant for the space radiation protection measurement ($E_{kin} \sim 700\,\mathrm{MeV/u}$), the calorimeter cannot fully contain all the fragments and different phenomena including pion production and hadronic showering occur, degrading the detector performances.

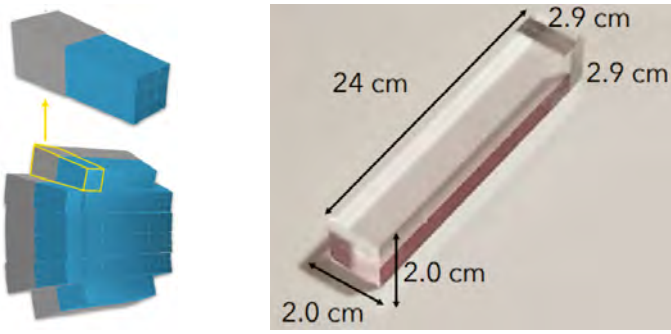

Figure 2.15: On the left, schematic view of the FOOT calorimeter arrangement; on the right, picture of a BGO crystal.

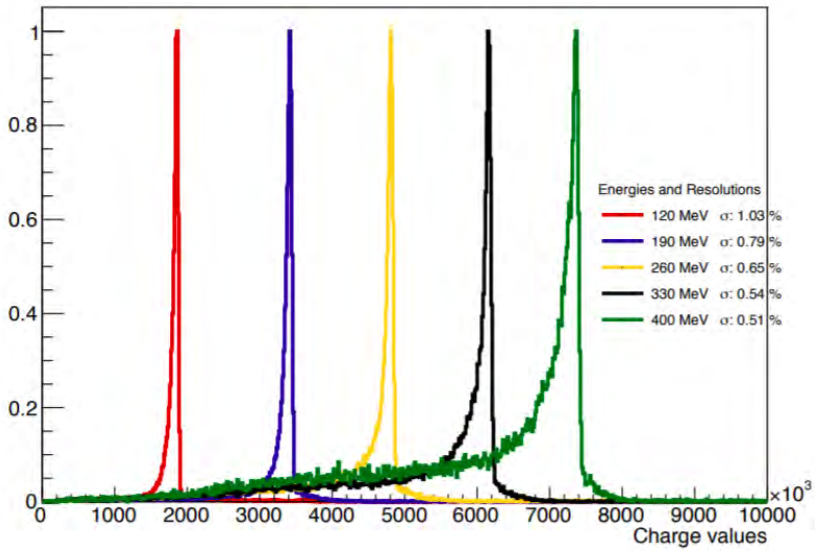

Figure 2.16: Calorimeter charge analysis distributions for measurements taken at CNAO with carbon ion beams at different energies. The distributions are normalized to the maximum peak height.

Data Acquisition System

A dedicated Data Acquisition (DAQ) system has been developed to handle the entire

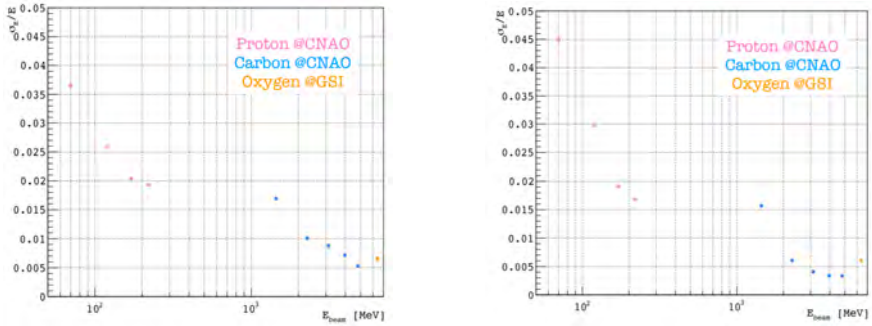

Figure 2.17: Preliminary energy resolution of a single crystal of the FOOT calorimeter evaluated with an amplitude analysis (left) and charge analysis (right) technique. The tests have been performed at CNAO and GSI with different particles at different energies.

FOOT electronic spectrometer data stream derived from all the detectors. The DAQ scheme is shown in Fig.(2.18). It is based on the simultaneous use of different computers and specific detector read out systems that communicate through optical fibers and ethernet cables.

The head of the DAQ is the control PC that is adopted to launch the GUI interface to start/stop the data acquisition, configuring and controlling all the other DAQ components. During the acquisition phase, different computers are adopted for a monitoring purpose, showing histograms about the general acquisition process and the detectors status (e.g.: detector occupancy, particle energy loss etc.) with a rate of the order of seconds.

A storage PC is used during the data taking to collect all the detectors data on a SSD disk at a maximum rate of 400 MB/s. The data are sent in a second phase to a dedicated NAS system exploited to store all the FOOT experiment measurements. The data size is expected to be of the order of 30 kB per event with the main component given by the SC and TW waveforms ($\geq 75\%$). However, the DAQ can handle a maximum data size of the order of 100 kB per event.

The FOOT maximum acquisition rate is set by the slowest detector of the setup represented by the VTX and IT. The M28 chip has a read out time of 185.6 µs that sets an upper limit on the rate of about 5 kHz. However, in order to reduce the pile-up effects in the M28 chip, the actual acquisition rate is of the order of 1 kHz.

Trigger

The SC detector, which is the fastest detector of the whole apparatus, is adopted to set a minimum bias trigger for the data acquisition, avoiding possible sources of systematic uncertainty given by the trigger selection. In particular, it is a majority trigger fired when a minimum number of SC channels signals exceeds a given threshold.

Since the expected rate of nuclear inelastic interactions in the target is of the order of 1% and the acquisition rate is of the order of 1 kHz, the amount of time necessary to acquire a significant sample of fragmentation data ($\sim 5 \cdot 10^4$) would be of about 13 hours, collecting about $5 \cdot 10^7$ events. Considering that the time availability in the accelerator facilities is limited, a trigger for the fragmentation events is required to increase the amount of interesting data reducing the collection of events without any nuclear inelastic interaction and avoiding a waste of time and resources.

For this purpose, the FOOT electronic spectrometer uses the TW since it is a scintil-

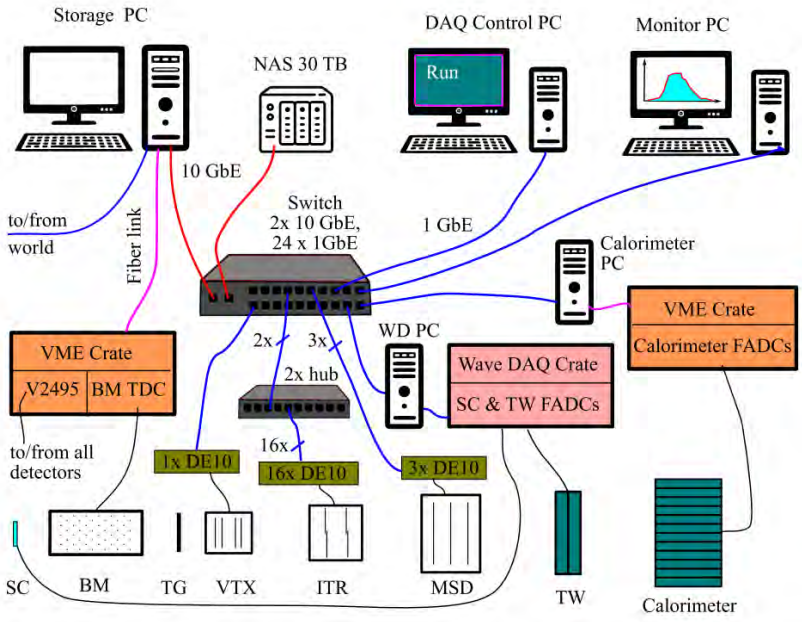

Figure 2.18: The FOOT DAQ scheme.

lator with a fast time response placed in the downstream region after the target. The scheme of the fragmentation trigger adopted during a test performed at GSI is shown in Fig.(2.19). In details, the TW bars placed outside the incident beam direction are discriminated with a low threshold value. In order to fire the trigger, at least two hits of these bars on one or the other view are requested together with the minimum bias trigger signal derived from the SC. A veto is set by the AND of the two TW central bars that are hit when no secondary particles are produced.

2.3.2 Emulsion Cloud Chamber setup

In order to measure the differential cross sections of light fragments ($Z \leq 3$), the FOOT experiment adopts a setup based on the nuclear emulsion layer technology, reaching an angular acceptance of about $70°$.

Details about the emulsion film structures and working principles will be presented in the subsequent paragraph, followed by the description of the ECC detector and the experimental setup.

Nuclear emulsion film

The use of nuclear emulsion films in the framework of physics experiments started in the half of XX^{th} century [88], but the spread in the use of this technology for experimental purposes occurred only between the end of the last century and the beginning of this century with the DONUT [89], CHORUS [90] and OPERA [91] experiments. In particular, the OPERA emulsion films needed to be developed in a large scale quantity, allowing the first industrial production of nuclear emulsions. This led to the possibility to obtain emulsion films with high sensitivity combined with a low unit cost.

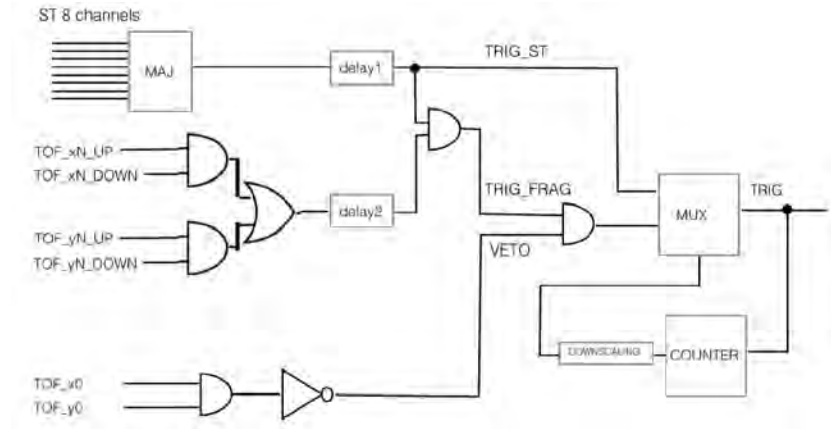

Figure 2.19: The FOOT fragmentation trigger scheme.

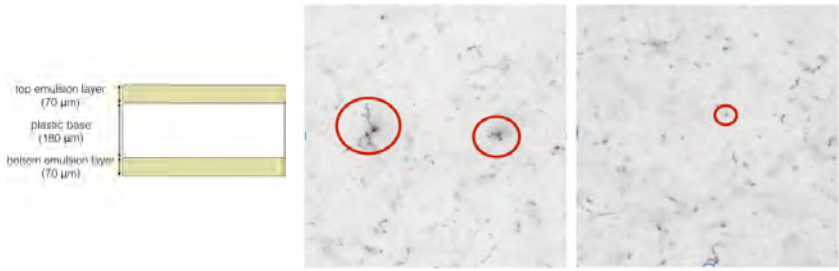

Figure 2.20: On the left, the schematic view of a nuclear emulsion film; At the center and on the right, a picture of the tracks generated by carbons (center) and protons (right) impinging perpendicularly on the emulsion layer. In the former case, the delta rays are also visible. The view size is 300×300 µm [87].

The FOOT experiment nuclear emulsion films are derived from those of the OPERA experiment, but with differences in technical specifications. In particular, the FOOT emulsions are composed of two sensitive layers of gel with interspersed AgBr crystals of 0.2 µm diameter deposited on the two side of a plastic base, as shown in the left panel of Fig.(2.20). The layer surface is of $12 \times 10\,\mathrm{cm}^2$, the overall thickness is of 320 µm and the sensitive thickness is of 140 µm.

When a charged particle crosses a nuclear emulsion film, it ionises the medium along its path leaving a latent image of the track given by a sequence of sensitized sites. After a complex chemical process known as *development*, each site becomes a crystallization nucleus for metallic Ag and black-silver grains with a diameter of 0.6 µm are impressed on the particle track, as shown in Fig.(2.20).

Subsequent to the development, a fully automated optical microscope is adopted to obtain an optical tomography of each field of view of the emulsion layers. Adjusting the focal plane of the objective lens within the thickness of the films, the three dimension position of the black-silver grains are reconstructed and digitized. Once the scanning procedure is finished, a dedicated software has been developed to reconstruct the aligned grains on a sensitive layer of a film producing *micro-tracks*. Two aligned micro-tracks identified on the two layers of the same emulsion film form a *base-track* and different aligned base-tracks from adjacent films define a full particle track with an associated

volume and density. The position resolution of the reconstructed track is of 0.3 µm and the associated angular resolution is of the order of 1.2 mrad.

The density of a track in an emulsion layer is proportional to the ionization of the particle. This gives the possibility of a charge identification within the dynamical range allowed by the detector. For the FOOT emulsions, a minimum ionizing particle leaves a track with a density of the order of 50 grains/100 µm. In order to overcome the saturation effect that occurs for highly ionizing particles, a *refreshing* procedure is adopted to extend the detector dynamical range. In details, the refreshing exploits the progressive oxidation of the latent image centers (called *fading*) that leads to a decrease of the number of recorded grains along the track. Since fading is enhanced in conditions of high temperature and humidity, the refreshing procedure exploits this phenomenon to partially or totally erase the tracks of the less ionizing particles. This can done keeping the emulsion films for an appropriate time (e.g.: 24 hours) in a high relative humidity of 95-98% and at a fixed temperature. Combining the different volumes of the same track reconstructed after different refreshing stages performed with increasing temperatures, it is possible to achieve an accurate particle identification [87]. As an example, analyzing the data taken with the ECC setup at GSI with oxygen beams at 200 and 400 MeV/u, the refreshing procedure has been conducted at $28°, 34°$ and $36°$. Scanning the emulsion films after each refresh, the deleted tracks are respectively mainly from cosmic rays, protons and helium ions. The choice of the refreshing temperatures needs to be tuned properly by means of specific calibration data takings conducted with particles at well known energies delivered on the emulsion layers. The main drawback of the refreshing procedure is given by the *fog*, which consists of random background grains created by thermal excitation and that are enhanced in high temperature environments. For this reason, the refreshing cannot be performed at too high temperatures in order to maintain the purity of the collected data. On the other hand, the charge identification is more challenging at lower temperatures. Thus, different methods have been developed to perform the particle identification and, in the framework of the FOOT experiment, new methods based on machine learning techniques are under studies.

Emulsion Cloud Chamber detector

The emulsion cloud chamber is a compact detector composed of different layers of emulsion films and passive material. The former are adopted to reconstruct the particle position and energy loss. The latter are exploited as target material and absorber layers. As shown in Fig.(2.21), there are three main sections in this detector:

- **Target and vertexing section:** the first ECC section is composed of emulsion films alternated with layers of C or C_2H_4 target material which have a thickness of 1 or 2 mm, respectively. In this part, the emulsion films are adopted mainly as vertex detector to reconstruct all the charged fragments tracks. In order to reach a statistically significant number of interaction events, the overall length of this section is defined by the target material and the incident particle charge and energy.

- **Charge identification section:** the central section is completely composed of emulsion films, aiming to measure the fragments charge with the refreshing procedure.

- **Momentum measurement and isotope identification section:** the last ECC section is composed of emulsion films interleaved with absorber layers made of passive high-Z material. The particle momentum and mass can be evaluated measuring the length of the entire track and the angles between the base-tracks caused by the MCS effect. Indeed, in Eq.(1.8) and Eq.(1.12) all the variables can be measured

directly except the particle mass (m) and velocity (β). Different absorber material with different thickness are adopted to enhance the dynamical range of the momentum measurement. As for the target and vertexing section, also in this case the length and the composition of the absorber layers depends on the incident particle energy and charge. The passive layers with lower Z are placed at the beginning.

The length of the sections are evaluated by means of MC simulations performed with the FLUKA software. For the data taking performed at GSI with oxygen ions with kinetic energies of 200 MeV/u and 400 MeV/u, the ECC detector composition is shown in Fig.(2.21). The length of the vertexing section is of 39 mm and 69 mm for the C and C_2H_4 targets, respectively. The central charge identification part is long 7.8 mm and the last momentum measurement section length is of 55 mm and 81 mm for the 200 MeV/u and 400 MeV/u particle beams, due to the different number of final lead layers (20 and 40). The total length ranges between 11.2 cm and 16.8 cm.

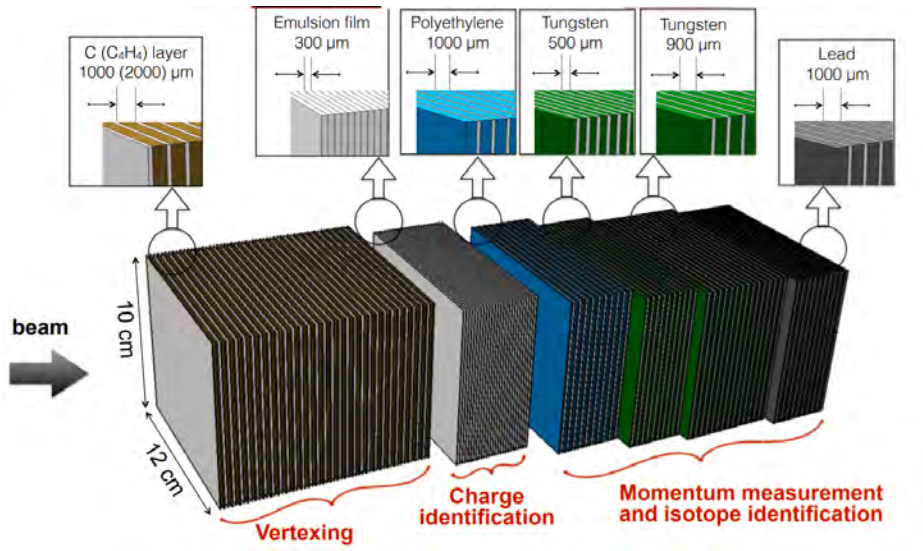

Figure 2.21: Schematic view of the emulsion spectrometer.

Experimental setup

For each ECC exposure, the total number of particles and the irradiation pattern need to be studied and optimized previously by means of MC studies. Indeed, on one hand, an excess of the incident particles would increase the tracks pile-up worsening the reconstruction algorithm efficiency and lowering the detector overall performances. On the other hand, an insufficiency in the number of particles would decrease the statistics without the possibility to fully exploit the detector. Since the beam monitoring systems presented in the accelerator facilities do not always have a precise particle counter detector, the experimental setup adopted for the ECC data taking includes a plastic scintillator First Start Counter (FSC) and the Beam Monitor adopted also in the FOOT electronic spectrometer.

The FSC is a scintillator developed in the framework of the FIRST experiment. It is a 250 μm thick disc of plastic scintillator with a radius of 26 mm. The detector light output

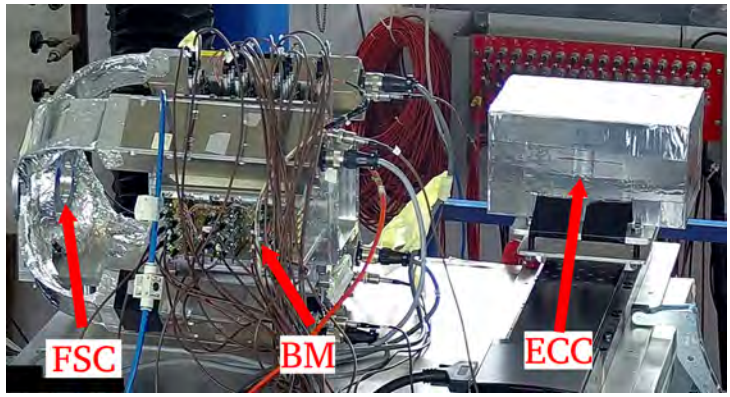

Figure 2.22: A picture of the whole ECC setup with FSC, BM and ECC during a data taking performed at GSI.

is collected by 160 optical fibers placed at the disc border and grouped in four bundles, each read by a fast photomultipliers with about 40% quantum efficiency [92].

The two additional detectors are placed above the ECC as shown in Fig.(2.22). In particular, the scintillator is adopted to count the total number of delivered particles, to provide the trigger for the data acquisition and the time reference for the BM detector. The BM is exploited to measure the incident particle direction and impinging point position on the ECC detector.

During a data taking, the irradiation pattern designed for the ECC is delivered many times only on the BM and FSC detectors to check the beam properties and stability before the ECC exposure. If the reconstructed beam profile and the counting results satisfy the ECC requirements among different repetitions, the emulsions are placed along the beam line for the exposure. A detailed example of a data taking conducted at the GSI facility with an oxygen ion beam at 200 MeV/u and 400 MeV/u is described in Sec.(4.3).

Data acquisition system

Since the BM and the FSC need to take data in a stand alone mode both to perform the ECC data takings and the BM test beams, a dedicated data acquisition system based on VME and NIM modules has been developed to couple the two detectors. In details, each of the BM output channel is connected to a leading edge discriminator and then to a TDC. Instead, the FSC readout channels are connected to a QDC adopted to measure the integral of the signals and to a discriminator followed by a coincidence module. The majority given by three out of four FSC channels with a signal is considered as the evidence of an incoming projectile. Thus, the output of the coincidence module is propagated to a scaler to count the total number of projectiles and to a dual timer. This last component is adopted to propagate the trigger signal among the other VME modules, setting a veto until the event acquisition is completed. The interface between the acquisition computer and all the VME modules is handled by a VME bridge. When the trigger is delivered from the dual timer to the bridge, it takes care to collect and send to the computer the scaler, the QDC and the TDC information. Once all the data of an event have been written on the hard disk, the bridge sends a signal to the dual timer to reset the veto and the whole acquisition system is ready for the next event.

The acquisition program is a custom c++ code derived from the FIRST experiment. It is a flexible software capable to handle different VME modules communicating through

the VME bridge. In the framework of the FOOT experiment, the program is used to set the threshold of the BM discriminators and the TDC settings. In addition, it is adopted to read, pack and save the data collected from the VME bridge. Due to the customization of the code, it can be easily modified to satisfy the specific requirements of each data taking..

2.4 Experimental requirements

In order to fulfill the FOOT experiment goals satisfying the radiobiological desiderata shown in Sec.(2.2.4), different methods are adopted to estimate the fragments charge and mass. For the light fragments ($Z \leq 3$), the ECC refreshing procedure and the high tracking precision well satisfy all the required performances, as shown in [87]. Regarding the heavy fragments ($Z \geq 3$) detected by the electronic spectrometer, the particle energy loss (ΔE), kinetic energy (E_{kin}), velocity (β) and momentum (p) measurements are combined with different methods to identify the charge and mass, to perform the inverse kinematic approach and to evaluate the double differential cross section.

Details about the electronic spectrometer detector measurements, the required performances evaluated by means of FLUKA MC studies and the preliminary results obtained from the tests are shown below, followed by the presentation of the techniques involved for the fragments charge and mass identification.

2.4.1 Electronic detector required performances

In order to measure the differential cross sections and to perform the charge and mass identification, the fragments ΔE, E_{kin}, β and p have to be measured with a sufficient precision. Different detectors have already been tested and by means of MC simulations, the expected and the required performances have been evaluated with the following results:

- **Energy loss ($\boldsymbol{\Delta E}$):** is measured by the MSD and the TW detectors. This measurement is fundamental for the charge identification and the preliminary detector performances show a resolution of the order of $\sigma(\Delta E)/E \sim 3 - 10\%$, as presented in Fig.(2.14). In particular, the energy resolution of the TW detector can be modelled as:
$$\sigma(\Delta E) \sim a + \frac{b}{\Delta E}$$
where $a = 0.904\,\text{MeV}$ and $b = 18.6\,\text{MeV}$.

- **Kinetic energy ($\boldsymbol{E_{kin}}$):** is given by the sum of the energy depositions of the particle in the magnetic spectrometer detectors and the calorimeter. The latter gives the main contribution to the measurement, setting also the resolution that for an electromagnetic calorimeter can be evaluated as:
$$\frac{\sigma(E_{kin})}{E_{kin}} = \frac{a}{\sqrt{E_{kin}}} \oplus \frac{b}{E_{kin}} \oplus c$$
where $a/\sqrt{E_{kin}}$ indicates the stochastic term related to the fluctuations in the sampling of the electromagnetic shower development, b/E_{kin} is the noise term given by the electronic noise of the readout circuit and c is the constant contribution related to the calibration uncertainties. As shown in Fig.(2.17), the initial tests show a resolution of $\sigma(E_{kin})/E_{kin} \leq 2\%$ for the oxygen and carbon ions with energies of

80-400 MeV/u. Further tests and data takings are foreseen in the near future. However, a systematic error affects the calorimeter measurements due to the neutrons produced and escaped from the detector.

- **Velocity (β):** the particle velocity is evaluated from the particle path length and TOF measurements with the following formula:

$$\beta = \frac{L}{c \cdot TOF} \tag{2.2}$$

where L is the fragment path length from the production position to the TW detector, whose, combined with the SC initial timestamp, provides the TOF measurement. The particle total travelled distance L is given by the global reconstruction algorithm based on a Kalman filter. It includes the bending due to the magnetic field and its resolution is of the order of few millimeters, considering also the detector position measurement resolution.

Regarding the TOF resolution, it is evaluated as $\sigma_{TOF} = \sqrt{\sigma_{SC}^2 + \sigma_{TW}^2}$. Different tests have been conducted with the SC and TW detectors in CNAO and GSI facilities with 115-400 MeV/u carbon and 400 MeV/u oxygen ions. The results are shown in Fig.(2.23): for carbon and oxygen ions in the PT energy range, the overall TOF resolution is of the order of 70 ps. For protons, as shown in Fig.(2.14), the TW time resolution is between 100 and 180 ps and the consequent TOF resolution is expected to be about 140-250 ps, due to their less ionizing effect. However, since the electronic spectrometer is designed for the detection of heavy fragments ($Z \geq 3$), the overall results fulfill the experimental requirements of a TOF resolution $\lesssim 100$ ps. The resolution on the particle velocity is mainly given by the TOF contribution $\sigma(\beta) \sim \frac{L}{c \cdot TOF^2} \cdot \sigma(TOF)$ and it is of the order of $\sim$0.006.

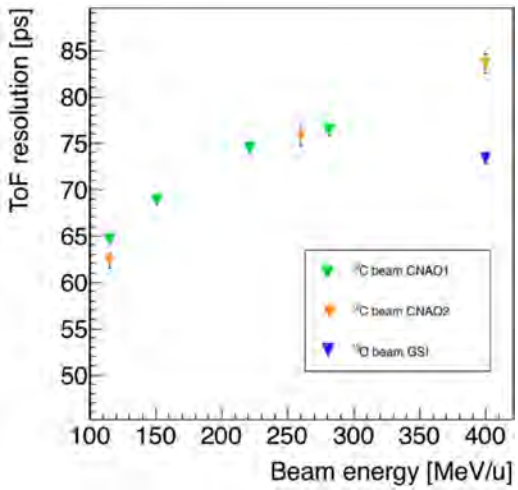

Figure 2.23: TOF resolution evaluated as a function of the incident particle type and energy. Data taken at CNAO and GSI with the SC and TW detectors.

- **Momentum (p):** is evaluated by means of the FOOT magnetic spectrometer. Each detector provides different hits that are elaborated by a global reconstruction algorithm based on a Kalman filter. In the FOOT software, two different Kalman

filter codes have been developed and, at the moment, both the algorithms are in a optimization stage. The preliminary results show that the required momentum resolution is of $\sigma(P)/P \sim 5\%$ and it is achievable.

2.4.2 Charge and mass identification

In order to optimize the FOOT electronic spectrometer performances, a detailed MC simulation has been developed including all the detectors parameters and materials. By means of simulations, different methods has been developed for the particle charge and mass identification.

Charge identification
For the emulsion spectrometer, the fragment charge is evaluated using the refreshing procedure, exploiting the particle energy loss dependence on the atomic number. The same physics phenomenon is used also in the electronic spectrometer for the charge identification with two different methods. The first one involves the MSD and the TW detectors consisting in the estimate of the Bethe-Bloch energy loss formula shown in Eq.(1.2) and simplified as:

$$\frac{dE}{dx} \sim z^2 \cdot f(\beta) \tag{2.3}$$

where dE/dx is the energy loss, z is the particle charge and $f(\beta)$ is a function of the particle velocity (β), which is expected to be similar to that of the primary particle. In particular, both the detectors measure the particle energy release ΔE, while the path length Δx is considered roughly equal to the detector thickness. The ratio $\Delta E/\Delta x$ is an estimate of the energy loss that combined with the β measurement provides a charge identification. An example is shown in the left panel of Fig.(2.24).

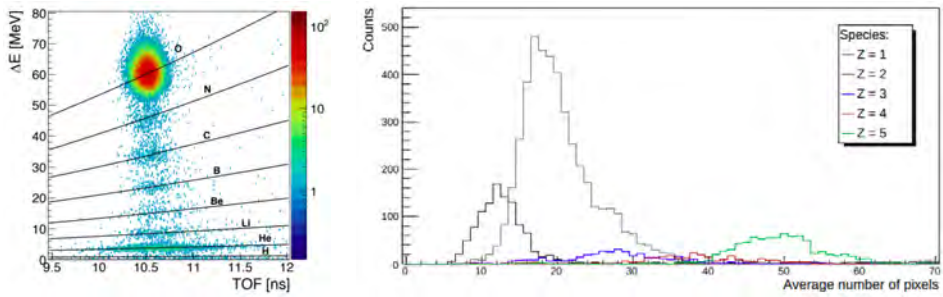

Figure 2.24: On the left, preliminary results of the charge identification performed on the fragments detected by the TW using the energy release ΔE and the TOF measurements. The data has been collected at GSI with an incident oxygen ion beam at 400 MeV/u. On the right, the cluster size distribution of the M18 sensors produced by the fragments originated from carbon ion beams at energies between 400 MeV/u and 1000 MeV/u impinging on different materials [82].

The second method employs the VTX and the IT detectors. In details, when a charged particle crosses a layer of silicon pixel detector, it fires different adjacent pixels that can be grouped in a cluster. The number of the fired pixels defines the *cluster size* and it depends on the particle energy loss and, consequently, on the incident particle charge. Considering the results obtained from the data taking conducted in the framework of the FIRST experiment on the M18 and M26 sensors, which are the previous version of the

FOOT VTX M28 sensors, an empirical model has been developed to describe the cluster size as a function of the energy loss [82]:

$$n_p = 2\pi\, r_s\, \log\left(\frac{\Delta E}{2\pi E_g T_s}\right) \tag{2.4}$$

where n_p is the mean number of pixels, ΔE is the energy loss, E_g is the mean energy for the creation of charge carriers (e.g.: $E_g = 3.6\,\text{eV}$ for silicon material), r_s and T_s are two free parameters. Combining Eq.(2.4) and Eq.(2.3), it is possible to extrapolate the particle charge from the cluster size and the TOF measurements. Since the cluster size is related to the energy loss logarithmically, with this method the charge identification capability is decreased for the high-energy loss and high charged particles, as shown in the right panel of Fig.(2.24).

The best charge identification performances are obtained by the TW detector. Given the ΔE resolution of the order of 3-10%, the fragment charge mis-identification level evaluated by means of MC simulation is below 4%. However, the VTX cluster size method can be adopted to cross-check the TW results and it can be employed in the VTX track reconstruction algorithm.

Mass identification

The particle isotopic measurement is a more challenging goal compared to the charge identification. For this reason, the particle mass is evaluated combining the TOF, momentum and kinetic energy measurements in three different ways:

1. **TOF and momentum:**

$$p \;=\; m\,\gamma\,\beta \;=\; \frac{m\,\beta}{\sqrt{1-\beta^2}} \;\Rightarrow\; m \;=\; \frac{p\sqrt{1-\beta^2}}{\beta}$$

$$A_1 = \frac{m}{u} = \frac{1}{u}\frac{p\sqrt{1-\beta^2}}{\beta}$$

   where $u = 931.494\,\text{MeV}/c^2$ is the atomic mass unit, p is the particle momentum, γ is the Lorentz factor and β is the particle velocity.

2. **TOF and kinetic energy:**

$$p^2 = E_{tot}^2 - m^2 \quad\Rightarrow\quad m^2\,\gamma^2\,\beta^2 = (E_{kin}+m)^2 - m^2$$

$$A_2 = \frac{m}{u} = \frac{E_{kin}}{u}\,\frac{1+\sqrt{1+\gamma^2\,\beta^2}}{\gamma^2\,\beta^2}$$

   where E_{kin} is the kinetic energy.

3. **Momentum and kinetic energy:**

$$E_{tot}^2 = p^2 + m^2 \quad\Rightarrow\quad (E_{kin}+m)^2 = p^2 + m^2$$

$$A_3 = \frac{m}{u} = \frac{E_{kin}^2 - p^2}{2E_{kin}}$$

Since the calorimeter suffers for the neutron production, the best mass identification evaluation is obtained with the combination of TOF and momentum measurements. However, all the three methods are adopted to reduce the systematic uncertainty and to achieve the best possible results. The redundancy of the mass determination techniques is an important key factor in the FOOT experiment to reach the goal. Finally, two methods are employed to combine the different mass estimates:

- **Standard $\boldsymbol{\chi^2}$ minimization algorithm:** is based on the minimization of the following function:

$$\chi^2 = f(\overrightarrow{x}) + \boldsymbol{A^T}(\boldsymbol{C}\boldsymbol{C^T})^{-1}\boldsymbol{A} \tag{2.5}$$

  where

$$f(\overrightarrow{x}) = \frac{(TOF - \overline{TOF})^2}{\sigma^2(TOF)} + \frac{(p - \overline{p})^2}{\sigma^2(p)} + \frac{(E_{kin} - \overline{E_{kin}})^2}{\sigma^2(E_{kin})} \tag{2.6}$$

  TOF, p and E_{kin} are the reconstructed values, $\sigma(TOF)$, $\sigma(p)$ and $\sigma(E_{kin})$ are the respective uncertainty and $\overline{TOF}$, $\overline{p}$ and $\overline{E_{kin}}$ are the fit output parameters. $\boldsymbol{A} = (A_1 - \overline{A},\, A_2 - \overline{A},\, A_3 - \overline{A})$ is the mass estimate vector, where A_1, A_2 and A_3 are the mass estimated values and $\overline{A}$ is the fitted output mass. The matrix $\boldsymbol{C}$ is the correlation matrix:

$$C = \begin{bmatrix} \frac{\partial A_1}{\partial TOF} \cdot \sigma(TOF) & \frac{\partial A_1}{\partial p} \cdot \sigma(p) & 0 \\ \frac{\partial A_2}{\partial TOF} \cdot \sigma(TOF) & 0 & \frac{\partial A_2}{\partial E_{kin}} \cdot \sigma(E_{kin}) \\ 0 & \frac{\partial A_3}{\partial p} \cdot \sigma(p) & \frac{\partial A_3}{\partial E_{kin}} \cdot \sigma(E_{kin}) \end{bmatrix}$$

- **Augmented Lagrangian Method (ALM):** is based on a iterative procedure of minimization of the Lagrangian function $\mathcal{L}$:

$$\mathcal{L}(\overrightarrow{x}, \boldsymbol{\lambda}, \mu) = f(\overrightarrow{x}) + \sum_{i=1}^{3} \lambda_i c_i(\overrightarrow{x}) + \frac{1}{2\mu} \sum_{i=1}^{3} c_i^2(\overrightarrow{x})$$

  where $f(\overrightarrow{x})$ is the function to minimize shown in Eq.(2.6), $c_i(\overrightarrow{x}) = (A_i - \overline{A})$ are the constraints, A_i are the mass values estimated with the previous methods, $\overline{A}$ is the fitted mass output parameter, λ_i are the Lagrange multipliers and μ is a positive penalty parameter that, multiplied with $c_i^2(\overrightarrow{x})$, constitutes the augmentation factor.

The results obtained with both methods are similar. As shown in Fig.(2.25), considering the expected values of $TOF \sim 70$ ps, $\sigma(p)/p \sim 3.7\%$ and $\sigma(E_{kin})/E_{kin} \sim 1.5\%$, the ^{11}C, ^{12}C and ^{13}C peaks are visible and the mass identification can be performed.

The impact of the different measurements to the mass identification is shown in Fig. (2.26). The most relevant effect is given by the TOF measurement precision, whose also influences the charge identification performances. Furthermore, in the space radiation measurements, the calorimeter performances are reduced since it cannot fully contain the high energy particles. In this scenario, the mass identification performed with TOF and momentum measurements is even more relevant. For these reasons, different efforts have been spent to optimize the SC and the TW detectors. In addition, for the space radiation measurements, the downstream detectors has been shifted far from the target at about 3 meters to increase the TOF distance and to enhance its resolution.

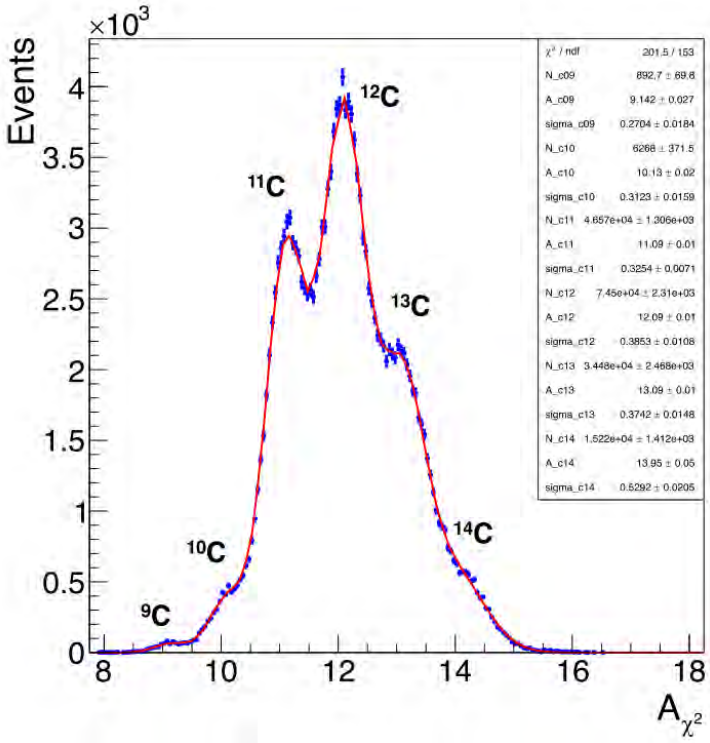

Figure 2.25: Example of mass identification performed with the χ^2 method on MC simulated data. The resolution of the measurements has been set to their expected values: $TOF \sim 70\,\text{ps}$, $\sigma(p)/p \sim 3.7\%$ and $\sigma(E_{kin})/E_{kin} \sim 1.5\%$.

2.5 Simulation and reconstruction

In order to perform the preliminary studies on the FOOT electronic spectrometer, the FLUKA MC simulation tool has been adopted to generate simulated data. In addition, a dedicated software has been developed to read and elaborate both real and simulated data. The FOOT analysis software performs the reconstruction of the detector measurements (i.e.: time stamps, ΔE, detector hits and tracks etc.) and the subsequent analysis (i.e.: charge and mass identification, cross section measurement etc.).

A brief introduction to the FLUKA simulation tool adopted for the MC data production is presented in this section, followed by the illustration of the FOOT reconstruction software.

2.5.1 Simulation: the FLUKA Monte Carlo code

The MC simulation tool adopted in the FOOT experiment is FLUKA (FLUktuierende KAskade) [93, 94, 95]. It is a general simulation tool widely employed in different physics branches for the calculations of particle transport and interactions with matter. One of the field in which FLUKA is particularly suitable is PT since different specific simulation features have been developed for the clinical research. The code is continuously updated with the latest modern physics models, adopting the microscopic models whenever possible and checking the latest experimental data as benchmark for the simulation output.

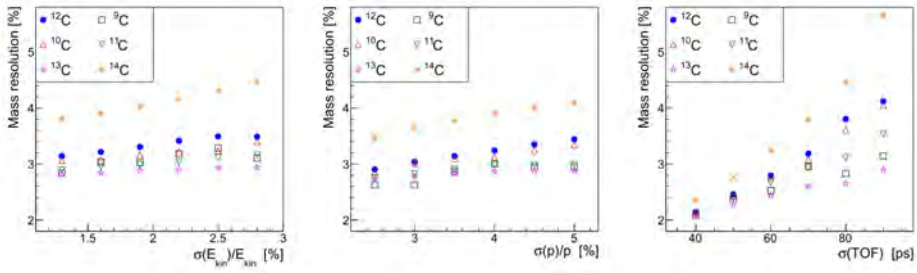

Figure 2.26: Mass identification resolution dependencies for the carbon ion isotopes performed on MC simulated data. The resolution of the measurements has been set to their expected values($TOF \sim 70$ ps, $\sigma(p)/p \sim 3.7\%$ and $\sigma(E_{kin})/E_{kin} \sim 1.5\%$) varying, from left to right, the E_{kin}, p and TOF resolutions.

The main models adopted in FLUKA for the description of the principal physics phenomena are shown below, followed by the presentation of the simulation output scheme specifically developed in the framework of the FOOT experiment.

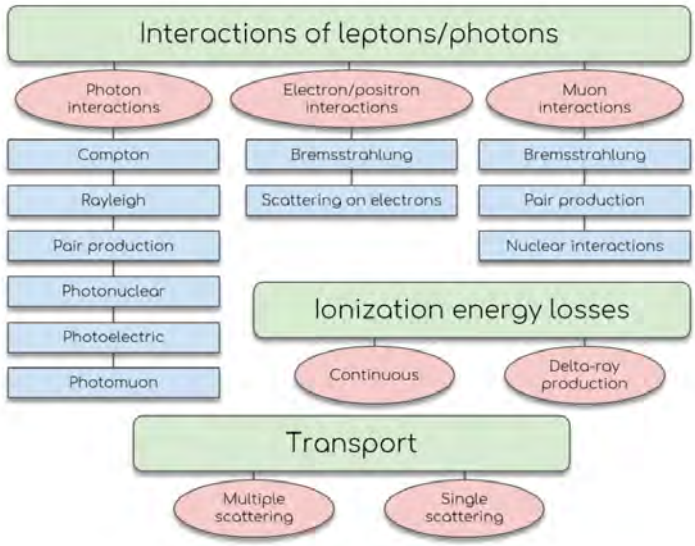

Figure 2.27: Scheme of the electromagnetic interactions models developed in FLUKA [96].

Charged particle transport

FLUKA can simulate all the interactions summarized in the schematic view of Fig.(2.27). The charged particles are propagated into materials by means of an original algorithm based on the Moliére theory. It gives the correct lateral displacement due to the Multiple Coulomb Scattering and it handles some demanding challenges such as the electron backscattering effect and the energy deposition in thin layers, even in the few keV energy range.

The energy loss mechanism is simulated according to the Bethe-Bloch theory described in Sec.(1.2), considering also the Barkas, Bloch and Ziegler corrections. Optional Δ-ray production and transport can be activated taking into account also for spin effects

and ionisation fluctuations.

The leptons-photons interactions are simulated in a wide energy range of about 12 energy decades, ranging from 1 keV up to 1 PeV. In particular the Bremsstrahlung effect is based on the differential cross section data published by Seltzer and Berger [97] [98] interpolated to obtain a finer energy mesh and extended to 1 PeV. It includes also the Landau-Pomeranchuk-Migdal suppression effect [99] and the Ter-Mikaelyan [100] polarization effect. All the other leptons-photons interactions simulated in FLUKA are listed in Fig.(2.27). However, for the FOOT experiment purposes, the most interesting interactions are the nuclear reactions since the FOOT data will be adopted to benchmark the FLUKA MC outputs.

Hadron-nucleon interactions
The FLUKA hadron-nucleon interactions are described by the resonance production and decays for energies below 5 GeV and by a model based on the Dual Parton Model (DPM) for energies from 5 GeV up to tens of TeV. The DPM is a phenomenological model of particle production in hadronic and nuclear collisions. It is based on the large-N expansion of non-perturbative QCD and the Reggeon field theory [101], allowing to describe also the soft collision process for which the QCD perturbation theory cannot be applied.

Hadron-nucleus interactions
The hadron-nucleus interaction initial stage is simulated in FLUKA with two models:

- **PreEquilibrium Approach to NUclear Thermalization (PEANUT):** this model is adopted for particles with momenta below 3-5 GeV/c. It is based on a detailed Generalized Intra-Nuclear Cascade (GINC) model for the initial hadron-nucleus non-elastic interaction stage. Then, after the emission or absorption of heavy particles, the subsequent pre-equilibrium stage model is adopted to describe the de-excitation of the hot nuclear components, by emission of nucleons and light nuclei (A$<$5) until thermal equilibrium is reached.
- **Glauber-Gribov cascade:** is a field theory formulation of the Glauber model [102] adopted in FLUKA for particles with momentum higher than 5 GeV/c. In this model the inelastic interactions are modelled as multiple interactions of the projectile with the target nucleons with the interaction rate obtained from free handron-nucleon cross sections. As for the PEANUT model, also in this case a subsequent de-excitation phase is described by nuclear evaporation, fission, Fermi break-up and γ de-excitation process, depending on the energy and the target-nucleus mass.

For the FOOT experiment, the PEANUT model is the most relevant since the energy of the particles involved in the measurements is below 5 GeV/c.

Nucleus-nucleus interactions
Depending on the energy, three different models are adopted in FLUKA to describe the nucleus-nucleus interactions:

- For energy below 0.1 GeV/u and between 0.1 and 5 GeV/u, FLUKA adopts a Boltzmann-Master Equation model and a Relativistic Quantum Molecular Dynamics (rQMD) model respectively (see section (1.2.4)). The transition energy range between the two models (100-150 MeV/u) is of great interest for PT and different efforts have been spent in the last years to smooth the transition, developing an extended version of the rQMD code [103].

- at higher energies ($\geq$ 5 GeV/u), a Dual Parton Model and JETs (DPMJET-II or DPMJET-III) model is adopted to simulate the nucleus-nucleus interactions. In details, this model is based on the DPM in connection with the Glauber formalism and it is generally used for the cosmic ray studies.

Details about the different nuclear interaction models are presented in (1.2.4).

FLUKA output
For the FOOT electronic spectrometer, a dedicated simulation output of the FLUKA code has been developed by the FOOT team completely modifying the FLUKA standard output by means of user routines libraries. Since the FLUKA standard output does not include an event per event data structure, the customized output is necessary to make possible the reconstruction of each event, with all the detectors information particle by particle and event per event.

In particular, the custom output is an *ASCII* file that contains all the simulated data and, by means of a program specifically developed, it is converted into a *root* file organized in blocks as following:

- **Particles block:** In this part, the information related to all the particles produced during the simulation are stored. Here, one can retrieve the particle mass, charge, barionic number, position and momentum at the production and at the death. It is also possible to retrieve the pointer to the parent particle.

- **Detector block:** a dedicated block is reserved to store each FOOT detector output, collecting all the hits information relevant for a given device. For each hit, the energy release, the position and momentum values and all the other quantity of interest for the specific detector is saved. As an example, when a particle enters and releases energy in a BM cell, in the BM block a hit is registered with the information about the cell coordinates, the particle entrance and exit position and momentum, the energy deposition and an index that points to the particle block.

- **Crossing block:** each time a particle crosses a region defined in the FLUKA geometry, the information about the crossing position, the particle momentum and a pointer to the particle block is saved.

In order to perform MC studies, the FOOT data analysis software is developed to produce the input files adopted by FLUKA to generate the simulated dataset, considering all the geometry parameters of the FOOT detectors. After the event by event simulation, the FLUKA output contains all the detectors simulated hits and measurements and it is returned as input to the analysis software to perform the MC study. In this way, all the geometry parameters and the projectile properties among the simulation and the analysis software are consistent.

2.5.2 Data analysis

The analysis software developed in the framework of the FOOT experiment is called SHOE (Software for Hadrontherapy Optimization Experiment). It has been developed to read both simulated and real data of all the detectors performing firstly a local and then a global reconstruction procedure. In the former case, the simulated hits or the raw measurements are elaborated to reconstruct the physics quantities relevant for each detector. Then, in the latter case, a global reconstruction algorithm processes all the

information from the detectors to reconstruct the whole event and extract the fragment tracks and properties, performing also the particle charge and mass identification.

The main tasks of the local reconstruction are:

- **SC and TW:** On the real data, it process the waveforms with a virtual constant fraction discriminator algorithm to retrieve the time measurements. In addition, the TW measures also the energy release of each hit applying a signal amplitude analysis. In case of MC studies, FLUKA provides directly a simulated time stamp and the energy release of each particle in each detector.

- **BM:** On the real data, it combines the time measurements with a given space-time relation to extract the distance measurements. With the MC simulations, the distances are directly extracted from the input file. Then, the software performs a track reconstruction procedure to extract the projectile track parameters from the BM hits. Further details about the BM operations are presented in Sec.(3.3).

- **VTX, IT and MSD:** each detector performs a local track reconstruction with the hits positions read from the real data or the MC file. In addition, the energy releases are directly measured by the MSD detector and evaluated by means of the cluster sizes by the pixel detectors.

- **CALORIMETER:** in case of real data, the signals from each crystal are read and processed applying an amplitude, charge and shape analysis to retrieve the energy deposition measurements. Otherwise, FLUKA provides directly the information. In both cases, a clustering algorithm is performed to take into account the particles that cross more than one crystal.

In order to take into account the resolution, efficiency, pile-up and the other specific effects of each detector that cannot be simulated directly by FLUKA, SHOE reproduces the detector resolutions, it eliminates the simulated hits according to the efficiencies and it adds the pile-up and the noise hits in order to make the simulation similar to a real scenario as much as possible.

After the local reconstruction, in the global reconstruction stage all the information from the detectors are combined to finalize the analysis. At this level, there are no differences in the elaboration of MC or real data. In details, the following main tasks are completed:

- **Global track reconstruction:** all the tracks and hits reconstructed by the detectors placed beyond the target are collected and processed to reconstruct the whole particle track. Two different algorithms based on Kalman filters have been developed to complete the task. The first one relies on the GENFIT code [104], which is an open source and experiment-independent set of libraries developed for the track fitting in nuclear and particle physics. The second algorithm, called TOE (Tracking Of Ejectile) is a Kalman filter specifically developed in the framework of the FOOT experiment. It is a lightweight package and it adopts a simplified approach with respect to GENFIT.

  After the track fitting, the particle momentum can be retrieved form the Kalman filter reconstruction algorithm and the TOF, energy release and kinetic energy measurements can be associated to the reconstructed particle.

- **Charge and mass identification:** combining the particle energy loss, kinetic energy, TOF and momentum measurements, the fragment charge and mass identification can be performed with the aforementioned methods.

- **Cross section analysis:** in the final stage, all the information about the particles measurements and the detectors efficiencies are employed to determine the differential cross section measurements.

At the moment, the local reconstruction code is completed for almost all the detectors. Indeed, it has been successfully adopted during the first FOOT electronic spectrometer test performed at GSI with about half of the whole apparatus.

Since it was not possible to write the global analysis code before the completion of the local reconstruction part, the global reconstruction is in a development and optimization phase. In details, all the particle identification and cross section measurement algorithms have been developed with different independent codes that have to be imported in SHOE. After this task, SHOE will be able to process and analyze all the data that the FOOT experiment will collect in next years.

CHAPTER 3

The beam monitoring system of the FOOT experiment

3.1 Introduction

The work of my Ph.D. thesis is focused on the BM detector adopted in the FOOT experiment. I managed both the hardware settings during the test beams and the software aspects related to the acquisition and reconstruction codes.

In this chapter, an overview on the principles of operation of the gaseous detectors will be presented in Sec.(3.2), focusing on the drift chambers. Concerning the FOOT BM, the aims and a detailed description of the detector will be presented in Sec.(3.3), showing the detector electric field studies performed by means of Garfield++ simulation code. In the end, the software developed for the data acquisition and the track reconstruction algorithm will be described.

3.2 Drift chambers principles of operation

Since the first gaseous detector invented in 1908 by E. Rutherford and H. Geiger consisting of a single wire proportional counter [105], the technology improvement and the science progress lead to the development of different types of gaseous detectors. The main examples of the generations of gaseous detectors are: multi-wire proportional chambers (1968) [106], drift chambers (1971) [107], time projection chambers (1978) [108], microstrip gas chambers (1988) [109], micro-pattern gas detectors (e.g. gas electron multipliers (1997) [110], micro-mesh gaseous structures (1996) [111]) and many others. At present, the state of the art is represented by the micro-pattern gas detectors due to their high spatial resolution, high rate capability, large sensitive area, operational stability and radiation hardness [112]. The gaseous detectors are still widely used and the technological development is still ongoing.

Despite the spread of gaseous detector types, all of them are based on three main processes: gas ionization, electrons and ions drift and amplification of ionization. All these phenomena and the specific functioning of drift chambers are illustrated in the following subsections.

3.2.1 Gas ionization

The first step for the particle detection by means of gaseous detectors is the ionization process. The primary ionization occurs when a charged particle (p) enters into the detector sensitive area and collides with a gas molecule (X) producing an ion (X^{n+}) and one or more electrons (ne^-) called *ionization cluster*:

$$p + X \rightarrow p + ne^- + X^{n+} \tag{3.1}$$

The generation of ionization clusters is a random process and the number of primary ionization clusters varies according to a Poisson distribution:

$$P(L/\lambda, k) = \frac{(L/\lambda)^k}{k!} \exp(-L/\lambda) \tag{3.2}$$

where L is the track length, k is the number of clusters and $\lambda = 1/(N\sigma_I)$ is the mean free flight path between the ionizing encounters defined by the density of electrons (N) and the electron ionization cross section (σ_I).

Besides the primary ionization, the majority of the clusters produced along a particle track are given by secondary ionizations generated by means of intermediate excited states:

$$\begin{gathered} p + X \rightarrow p + X^* \ ; \ e^- + X \rightarrow e^- + X^* \\ X^* + Y \rightarrow X + Y^+ + e^- \end{gathered} \tag{3.3}$$

where Y is a molecule of the quenching gas necessary for the functioning of the detector and X^* is the metastable state of a noble gas. The last reaction shown in Eq.(3.3) occurs only if the excitation energy of the noble gas X^* is above the ionization potential of the quenching gas Y [113].

The overall number of electrons created by a particle in a gaseous medium can be evaluated with the following formula:

$$W < N_T >= L \left\langle \frac{dE}{dx} \right\rangle \tag{3.4}$$

where N_T is the average number of total ionization electrons generated along a particle trajectory with a length L, dE/dx is the energy loss described by the Bethe-Bloch formula shown in Eq.(1.2) and W is the mean energy required for the creation of a free electron that depends both on the gas and the particle properties [113].

The experimental measurements of W are performed indirectly since the energy deposition of a relativistic particle is too small to be detected as difference between the initial and the final energy. An example of W measurements is shown in Fig.(3.1). Experimentally, W depends only slightly on the initial energy for α particles above few MeV and electrons above few keV.

Typical values of W, dE/dx, number of primary ionizations (N_P) and total number of electron-ion pairs (N_T) generated in the commonly adopted gases are shown in Tab.(3.1). In case of gas mixtures, a composition law can be used to calculate N_P and N_T. E.g.: considering an Ar/CO_2 gas mixture at 80/20%, the number of electron-ion pairs created by a minimum ionizing proton is:

$$\begin{aligned} \mathrm{N_P} &= 25 \cdot 0.8 + 35 \cdot 0.2 = 27\,\mathrm{pairs/cm}; \\ \mathrm{N_T} &= 2530/26 \cdot 0.8 + 3350/34 \cdot 0.2 \sim 97.6\,\mathrm{pairs/cm} \end{aligned}$$

δ-rays

In case of interactions with high energy transfers, the primary electron may cause secondary ionization clusters. In this case, the electron can be considered as a new charged particle referred as *δ-ray* and it is a source of background for the detection of the incident primary particle. Electrons with an energy above few keV are considered as δ-rays and the number of electrons with an energy equal or above E_0 can be computed as:

$$N_\delta(E_0) = W \left(\frac{1}{E_0} - \frac{1}{E_{max}} \right) \sim \frac{W}{E_0} \quad (\text{if } \ E_0 \ll E_{max}) \tag{3.5}$$

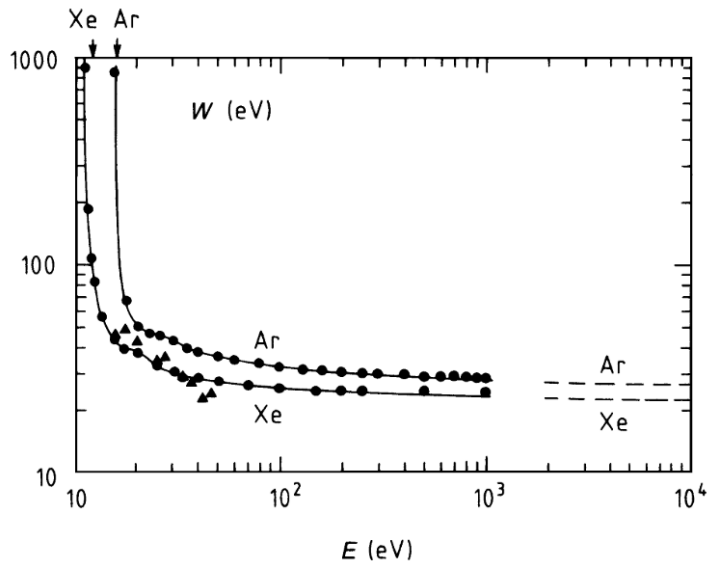

Figure 3.1: Average energy spent for the generation of a ionization electron as a function of the incident particle energy for argon and xenon gases [113].

where E_{max} is the maximum energy transfer allowed in each interaction that can be computed with a two body relativistic kinematics:

$$E_{\text{max}} = \frac{2mc^2\beta^2}{1-\beta^2} \tag{3.6}$$

where m is the electron mass and β is the projectile velocity in units of the speed of light c. As an example, protons at 1 GeV/c have $\beta \sim 0.73$ and $E_{\text{max}} = 1.2$ MeV. Due to the stochastic nature of the ionization process, the fluctuations of the particle energy loss distribution can be described by a Landau function with its characteristic tail towards high energies, up to E_{max}. Figure (3.2) shows the expected number of δ rays as a function of E_0 in case of protons at 1 GeV in argon gas at normal conditions.

The angular distribution of δ-rays as a function of their energy E can be evaluated

Gas	W (eV)	$dE/dx\|_{\text{min}}$ (keV)	N_P (cm^{-1})	N_T (cm^{-1})
He	41.3	0.32	3.5	8
Ne	37	1.45	13	40
Ar	26	2.53	25	97
Xe	22	6.87	41	312
CH_4	30	1.61	28	54
C_2H_6	26	2.91	48	112
CO_2	34	3.35	35	100
CF_4	54	6.38	63	120

Table 3.1: Average energy per ion pair (W), energy loss (dE/dx), primary (N_P) and total (N_T) number of electron-ion pairs per cm created by unit charge minimum ionizing particles in noble and molecular gases at normal temperature and pressure conditions [112].

with a free-electron approximation and the result is:

$$cos^2\theta = \frac{E}{E_{max}} \tag{3.7}$$

Since typically $E_{max} \gg E$, δ-rays are mostly emitted perpendicularly with the respect to the incident particle track. However, due to the large mass difference between projectile and target, the electron directions are completely randomized after just few collisions with large scattering angles and large momentum transfers. In order to have an idea about the quantity and the paths of δ-rays, Fig.(3.3) shows a drawing of the δ-rays produced by the superposition of 10 simulated tracks of protons, helium and carbon ions traversing a drift chamber filled with an Ar/CO_2 gas mixture at standard conditions. As one can notice, the number of δ-rays strongly depends on the dE/dx of the incident particle, as described in Eq.(3.5) and (3.4). The irregular path of the electrons is caused by the collisions with the gas molecules. In addition, the total path length of a δ-ray can be of the order of different centimeters, being a non negligible source of background.

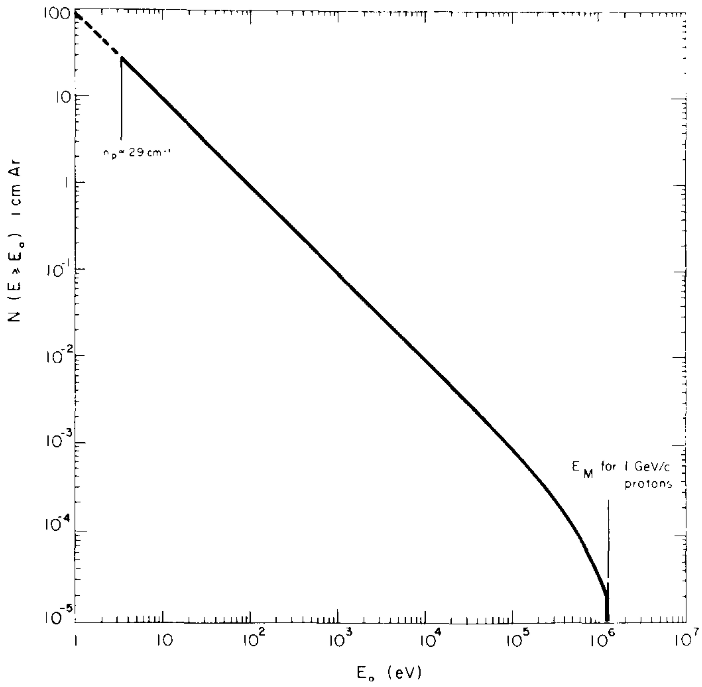

Figure 3.2: Number of electrons with an energy greater or equal to E_0 as a function of E_0, calculated for 1 GeV protons in argon gas at normal conditions [110].

3.2.2 Electrons and ions drift

Once an electron-ion pair has been created, both the particles drift through the gas and scatter on the gas molecules, randomizing their direction at each collision. The particles instant velocity between the collisions is of the order of c, but if an electric field is applied across the gas volume, electrons and ions will drift with a net movement in opposite directions towards the electrodes with an average drift velocity u, which is much smaller

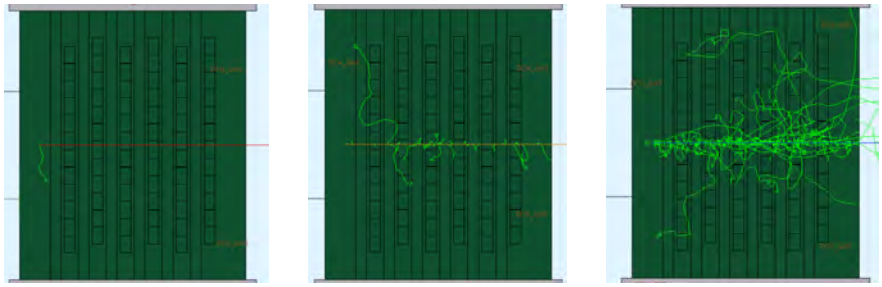

Figure 3.3: Examples of the delta rays (green tracks) produced by 10 tracks of protons (left), helium ions (center) and carbon ions (right) in a drift chamber filled with a gas mixture of Ar/CO_2 at 80/20%. The pictures are derived from simulations performed by means of the FLUKA software.

with the respect to the particle instant velocity. In addition, the collisions with the gas molecules lead to the diffusion process that worsens the detector spatial resolution.

Electrons drift velocity

Considering the electrons, they are accelerated faster with respect to the ions and they lose only a small fraction of energy due to the elastic collisions with the target atoms. In this way they reach energies much grater than the thermal motion energy that can be neglected and their momentum direction is randomized at each collision. Applying an electric field across the gas volume, the electrons are accelerated towards the anode. However, part of the kinetic energy is lost due to the scatterings on the gas molecules. The final balancing effect due to the combination of these two phenomena is a net movement of the electrons towards the anode with a drift velocity computed as [113]:

$$u^2 = \frac{eE}{mN\sigma}\sqrt{\frac{\lambda}{2}} \tag{3.8}$$

where E is the electric field, N is the number density of the gaseous medium, λ is the average fractional energy loss per collision, e and m are respectively the electron charge and mass. Both λ and N depend strongly on the electron energy and the exact gas composition since they are subject to complex quantum-mechanical processes in the scattering with the electron shells of the gas molecules.

Given a fixed gas composition and pressure, the electron velocity depends only on the electric field. In addition, for a certain range of electric field that depends on the gas properties, the drift velocity is only slightly related to the electric field becoming almost constant. This is the best condition for the applications that use the drift times of the electrons to get spatial information (e.g.: drift chambers and time projection chambers).

Examples of electron drift velocities for different concentrations of Ar/CO_2 mixtures are shown in the left panel of Fig.(3.4). Typical values of the electron drift velocities are of the order of $\sim 10^6$ cm/s, which is order of magnitude higher with respect to the drift velocity of the ions $\sim 10^4 - 10^5$ cm/s.

Ions drift velocity

The kinetics of ion movements in gaseous medium is completely different with respect to electrons. Colliding with gas molecules, ions are not scattered isotropically due to their heavier mass. In addition, on one mean-free path, an ion acquires an amount of energy similar to that of the electrons, but a great part of it is lost in the next collision.

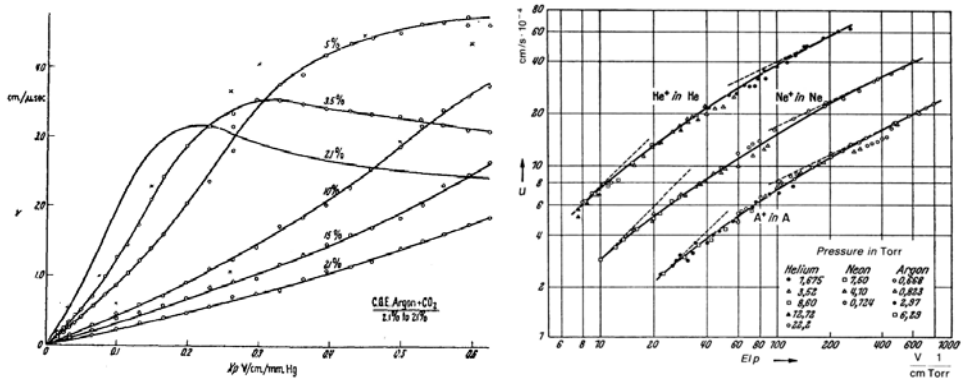

Figure 3.4: On the left: drift velocities of electrons as a function of the reduced electric field (E/P) in Ar/CO_2 mixtures with different concentrations [110]. On the right: drift velocities of different positive noble gas ions in their own gases as a function of the reduced electric field (E/P). The limiting cases at low ($u \propto E$) and high ($u \propto \sqrt{E}$) fields are represented by dashed lines [113].

With the typical electric field intensities adopted in drift chambers and other common gaseous detectors, the ion energy is mainly due to the thermal motion and only a small contribution is given by the external electric field.

The drift velocity u is directly proportional to the electric field (E) and inversely proportional to the gas pressure (P). In order to take into account the reduced electric field (E/P) dependence and considering a constant pressure working point, u can be written as:

$$u = \mu \cdot E \tag{3.9}$$

where μ is the gas *mobility* related to the ion and the gas composition properties, but without a dependence on the electric field up to very high field intensities. Examples of μ values are shown in Tab.(3.2).

Table 3.2: Experimental mobilities values of different ions in different gases [113, 110]

Gas	Ions	Mobility ($cm^2V^{-1}sec^{-}1$)
Ar	Ar^+	1.535
Ar	CH_4^+	1.87
Ar	CO_2^+	1.72
CO_2	CO_2^+	1.09
CH_4	CH_4^+	2.26

If a large external E field is applied, the ion thermal motion can be neglected and the resulting drift velocity is proportional to the square of the reduced field, as in case of electrons [113]. Examples of the ion drift velocities with the two E field limiting cases are shown in the right panel of Fig.(3.4).

3.2.3 Ionization and excitation by means of high electric fields

Drifting towards the positive electrode, the electrons are subject to an increasing electric field. If it is above few kV/cm, the electrons have enough energy to interact with the gas molecules with different processes such as ionization, excitation and also inelastic

phenomena. In this phase, the electron and ion movements induce a current on the electrodes that can be read. The output pulse amplitude depends on the detector shape, the sizes of the wire, the electric field intensity and the gas composition and pressure.

As shown in Fig.(3.5), given a fixed geometry and gas property, a gaseous detector operates in different modalities depending on the intensity of the electric field:

- **Very low electric field voltage:** the electric field is too weak and the electron-ion pairs created by the incident radiation recombine before to reach the electrodes, losing the original signal. No gaseous detector can work in this regime.
- **Ionization chamber:** is the operation modality in which the electric field across the gas volume is high enough to avoid the recombination process, leading to a full collection of the initial electron-ion pairs. In this operation mode, since the signal is generated only by the gas ionizations caused by the incident radiation, the number of ions collected and the pulse amplitude is constant for a certain high voltage range.
- **Proportional counter:** if the electric field beside the electrodes exceeds a certain threshold value, a multiplication process can take place close to the anode wires, leading to the creation of the so-called *avalanche*. In this case the number of secondary electron-ion pairs is proportional to the original ionization. This is the typical regime in which a drift chamber operates.
- **Limited proportionality:** enhancing the electric field, the multiplication process leads to the creation of a great amount of secondary electron-ion pairs that modifies the electric field, giving rise to a *space-charge effect*. In this case, the proportionality between the signal amplitude and the original ionization is lost, since the pulse and the number of collected ions are proportional both to the first and the second ionizations.
- **Geiger-Müller counter:** if the electric field is high enough, several discharges can occur in the gas volume due to the de-excitation of the gas molecules. Indeed, the excited particles release energy emitting photons that can extract electrons by the electrodes. In this way, the full length of the anode wire is enveloped by electrons and ions. This is the operation mode of the Geiger-Müller counter. In this case the proportionality is completely lost and the detector is used to count the number of incident radiations.

Details about the multiplication process, the space-charge effect, the gas atoms excitation and the output signal of the detector are shown in the next paragraphs.

Amplification of ionization

As the energy is above the first ionization potential of the gas molecules, the electrons can create new electron-ion pairs causing a great amount of ionizations. This phenomenon is usually referred as avalanche.

The *Townsend coefficient* (α) is defined as the inverse of the mean free path introduced in Eq.(3.2) and it quantifies the number of pairs produced (dN/N) per unit length of drift (ds):

$$\frac{dN}{N} = \alpha ds \tag{3.10}$$

The Townsend coefficient is determined by the excitation and ionization cross sections of the electrons. It depends on the electric field and it is directly proportional to the

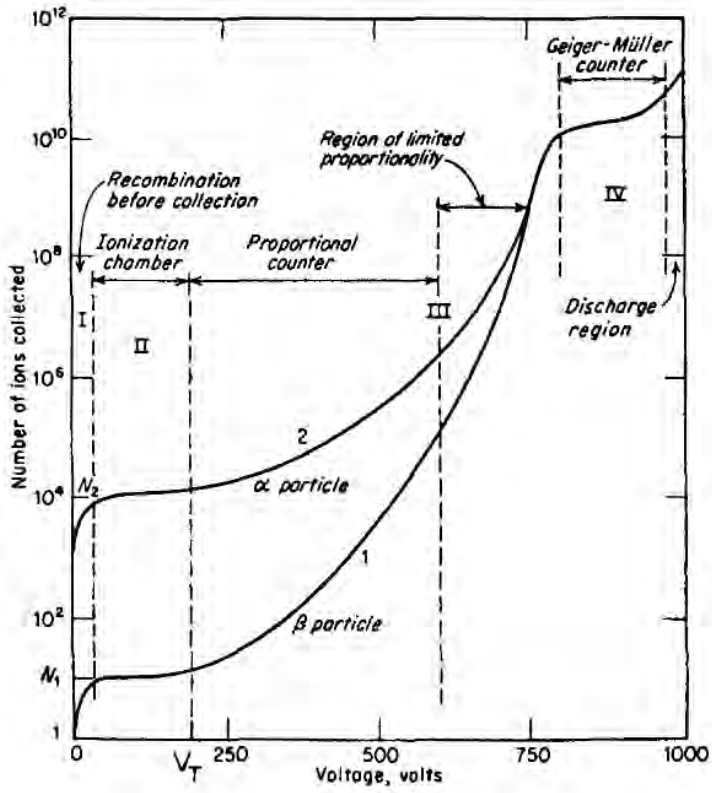

Figure 3.5: The different regions of operation of the gaseous detectors are shown on the gain-voltage plot of a proportional counter [110].

gas density. Due to its complexity, a fundamental formula of α does not exist yet, but it can be approximated with analytic expressions valid for different regions of electric field [114]. Examples of measured Townsend coefficients in different noble gases can be found in the left panel of Fig.(3.6).

Considering a proportional chamber or the cell of a drift chamber with an anode wire set at a positive high voltage, the number of electron-ion pairs created in the high electric field region close to the wire can be computed integrating Eq.(3.10):

$$G = \frac{N}{N_0} = \exp \int_{s_{min}}^{a} \alpha(s) ds = \exp \int_{E_{min}}^{E(a)} \frac{\alpha(E)}{dE/ds} dE \tag{3.11}$$

where N and N_0 are the final and initial number of electrons in the avalanche, s_{min} is the distance from the wire center where the electric field is high enough to start the avalanche, a is the wire radius and dE/ds is the electric field gradient. The N/N_0 ratio defined in Eq.(3.11) is called *gain* (G). Typical values of G for the detectors working in the proportional counter regime is of the order of $10^3 - 10^5$ depending on the electric field, the gas density ($dG/G \propto d\rho/\rho$) and many other parameters.

Space-charge effect

For the correct functioning of a gaseous detector, the gain should be kept constant as

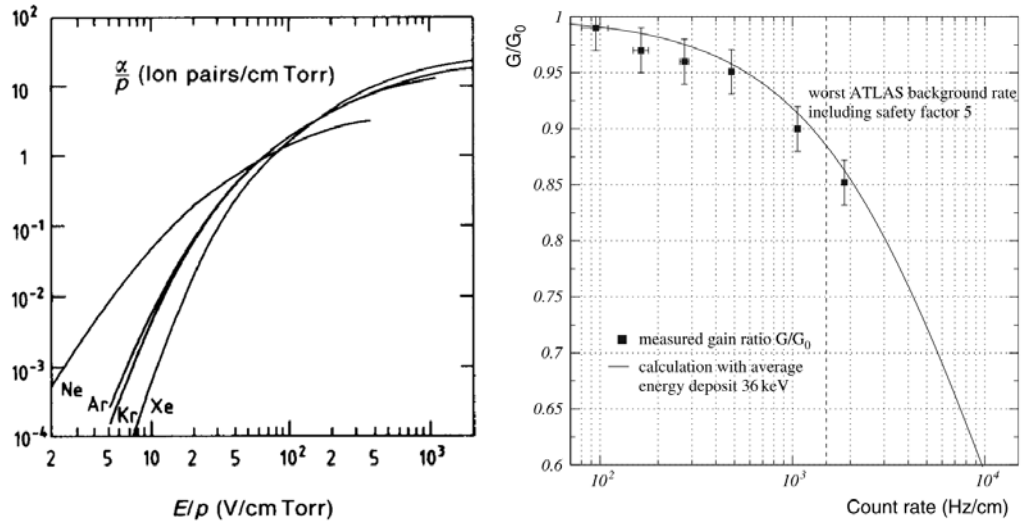

Figure 3.6: On the left: measured Townsend ionization coefficient (α) over the pressure (P) as a function of the reduced electric field for different noble gases [113]. On the right: calculated and measured gain drop in the drift tubes of the ATLAS muon spectrometer [113].

much as possible. One of the source of gain drop that limits the gaseous detector performances is the space-charge effect due to the ion charges. In details, after the creation of an avalanche, all the electrons are collected on the anode while the positive ions start to move towards the negative cathode at a relatively slow speed (few cm/s per V/cm) modifying the electric field across the detector. This leads to a limitation on the rate capability and to a decrease of the detector efficiency. Indeed, considering a scenario with a high incident particle rate, the travelling ions can generate a stationary space-charge density in the gas volume that reduces the electric field with the consequent decrease of the gain factor and of the detector efficiency. An example of the gain drop effect as a function of the incoming particle rate is shown in the right panel of Fig.(3.6).

Gas molecules excitation

During the avalanche process, the excited and ionized noble gas atoms can return to the ground state only by means of radiative processes emitting photons. In addition, also the neutralization of positive ions can be achieved extracting an electron from the cathode with the emission of photons or secondary electrons to reach the energy balance. In both cases, the photons emitted from noble gas atoms usually have energies above the ionization potential of the metal atoms constituting the cathode. In this way, the photo-electrons can be ejected from the metal and they can start new avalanches. This would induce a permanent regime of discharge not allowing a correct functioning of the detector. As an example, considering the common case of argon gas molecules, the minimum energy of the emitted photons is of 11.6 eV [110], while the ionization potential of the aluminum or copper atoms usually adopted as sense or field wire materials is of 5.99 eV and 7.73 eV respectively.

In order to avoid the continuing creation of avalaches, small quantities of polyatomic molecules referred as *quenching gas* are added in the gas medium. These particles allow the absorption of photons in a wide energy range due to their different rotational and

vibrational excited states. In addition, the polyatomic molecules dissipate the energy in excess by means of elastic collisions or dissociating into simpler radicals.

Signal creation and readout electronics
The signal generated in a gaseous detector that works in the proportional regime is derived from the induced currents generated by the movements of electrons and ions produced in avalanches. In the former case, the electrons are produced close to the anode wire and they reach the electrode within a time typically much less than a nanosecond, generating a short signal pulse. In the latter case, the ions are produced far from the cathode where they are collected and, with respect to electrons, they have a reduced drift velocity that decreases further as they start to move. The ion induced signal is the main component of the total signal and it is characterized by a long tail [113]. For this reason, the pulse shape is fundamental to permit a correct signal detection procedure and to increase the rate capability of the gaseous detectors.

The raw signal derived from the sense wire of a gaseous detector that works in a proportional regime can be modeled with the following formula:

$$V(t) = i_0 R_L \cdot \begin{cases} 1 - e^{-t/\tau} & 0 \leq t \leq t_- \\ e^{-(t-t_-)/\tau} - e^{-t/\tau} & t > t_- \end{cases} \tag{3.12}$$

where i_0 is the current collected on the sense wire, t_- is the time related to the charge collection and $\tau = R_L \cdot C_d$, in which R_L is the resistance placed in series to the sense wire to set it at the desired high voltage and C_d is the detector capacity. The gaseous detectors based on the time measurements usually adopt a preamplifier circuit composed of a current amplifier. In particular, the sense wire is connected to an amplifier used in a negative feedback with a capacitor (C_f) and a parallel resistance (R_f), acting as a current integrator. Then, if the time constant ($\tau = C_f \cdot R_f$) is small with respect to the typical duration of the raw signal expressed in Eq.(3.12), the integration do not relevantly change the signal shape and the circuit acts as a current amplifier. In this way, the time measurement of the signal leading edge is not relevantly modified by the readout electronics. An example of a readout scheme adopted for a prototype of the FOOT BM detector is shown in Fig.(3.7). In the picture, the current amplifier components are pointed out in the two light blue boxes. An example of a signal read from the BM front-end board is shown in Fig.(3.8).

3.2.4 Principle of operations of drift chambers

A drift chamber is a gaseous detector that works in a proportional regime. The principle of operation of a drift chamber is based on the timestamps collected by the cells of the detector and the reference timestamp provided by an external apparatus, that is usually represented by a scintillator with a fast and precise time response. With these measurements and knowing the drift velocities of the specific gas composition and working point, it is possible to convert the timestamps into spatial measurements. Then, employing a reconstruction algorithm, the incident particle track parameters can be retrieved.

The different passages required to obtain the spatial measurements are presented in the following paragraphs.

Drift chamber time measurements
Considering a charged particle crossing a drift chamber cell as depicted in Fig.(3.9), different electron-ion clusters are generated along its track and they all drift towards the

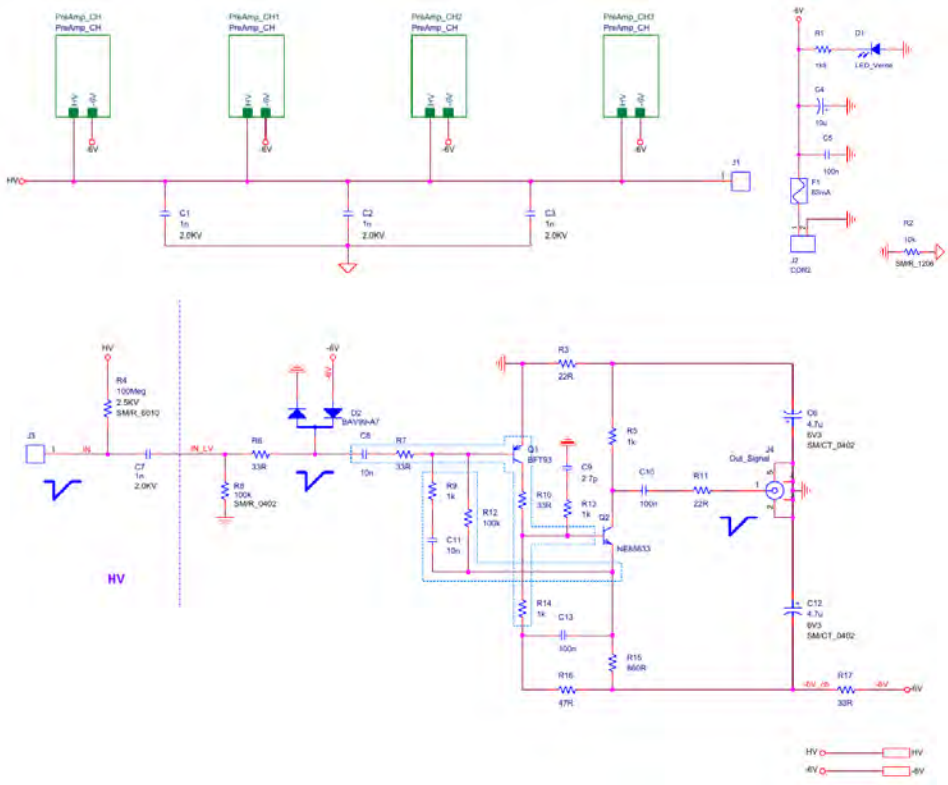

Figure 3.7: Scheme of a readout board adopted for a prototype of the FOOT drift chamber [115]. The current amplifier components are pointed out in the two light blue boxes. The BM has a similar readout electronic scheme.

anode wire or the cathode plane. Among the electrons, the first that reach the destination and start the rise of the signal are those placed at the Point Of Closest Approach (POCA). This is the space position along the particle track in which the distance with respect to the anode wire is minimized. The electronic signal is then read by a Time to Digital Converter (TDC) in order to obtain a measurement timestamp T_M associated with the POCA position. The TDC is adopted also to provide a timestamp of the particle when it crosses an external scintillator, measuring a reference time T_R. The difference between these two timestamps ($T_M - T_R$) is the time required by the particle to travel from the POCA to the scintillator (T_0), plus the drift time required by the electrons to migrate from the POCA to the anode wire (T_F):

$$T_M - T_R = T_0 + T_F \tag{3.13}$$

T_0 is a fixed time that depends only on the geometry of the drift chamber cell and the scintillator position, while T_F is the target of the measurement since it depends only on the drift velocity and the POCA position.

T_0 evaluation

In order to retrieve the T_F measurements, T_0 needs to be estimated for each cell and

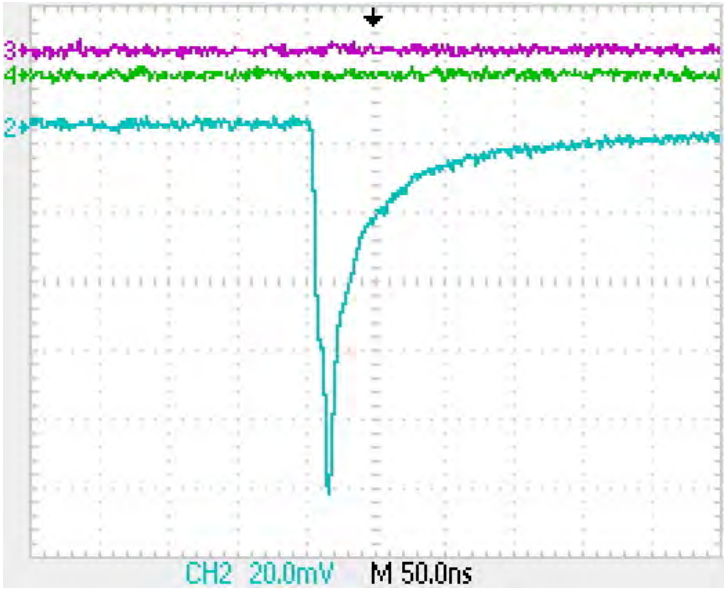

Figure 3.8: The blue signal of channel 2 is an example of a BM output signal from the readout front-end board collected during a data taking performed with a proton beam at 80 MeV.

each dataset. To reach this aim, the T_0 values can be evaluated from the $T_M - T_R$ measurements. As shown in Fig.(3.10), the $T_M - T_R$ distribution is characterized by a steep rise in the left part of the plot where the difference between the two time measurements is minimized. The time values in this region correspond to T_0, since they are the hits in which the projectile crossed or passed close to the anode wire and the associated T_F is equal to 0. Indeed, considering Eq.(3.13), the right part of the equation can be minimized only setting T_F to zero since T_0 is fixed for a given cell and a given experimental setup. However, due to the stochastic nature of the ionization process, T_0 can slightly vary among the events in which it is minimized, leading to a non perfect straight rise in the left part of the plot shown in Fig.(3.10).

As an example, in the FOOT experiment the T_0 values are evaluated as the mean time between the start and the peak of the $T_M - T_R$ distribution. For instance, in Fig.(3.10) the T_0 value is evaluated to be -85.5 ns. The negative value is because in this case $T_M < T_R$ due to the cables of different length that introduce different time delays.

Drift chamber space measurements

Once T_0 is determined, the T_F values are accessible inverting the terms in Eq.(3.13). Since T_F represents the time adopted by the electrons to drift from the POCA to the anode wire, the corresponding drift distance can be measured if the drift velocity map between the anode and the cathode is a known parameter. Indeed, if the last condition is satisfied, it is possible to convert all the T_F times into space measurements (or *hits*) that represent the distances between the incident particle track and the anode wire positions of the crossed cells. This conversion map is generally referred as *Space-Time Relations*. Since the drift velocity is related to a lot of parameters that can also be run dependant (e.g.: gas composition, pressure, electric field etc.), in an experimental context the space-time relations is evaluated by means of iterative algorithms, simulations

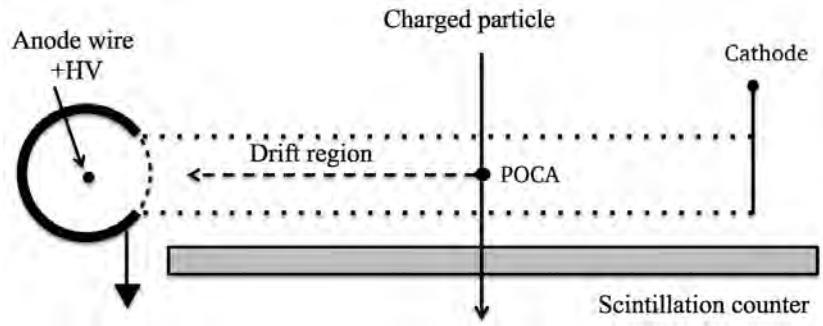

Figure 3.9: Principle of operation of a single cell drift chamber. Picture adapted from [116].

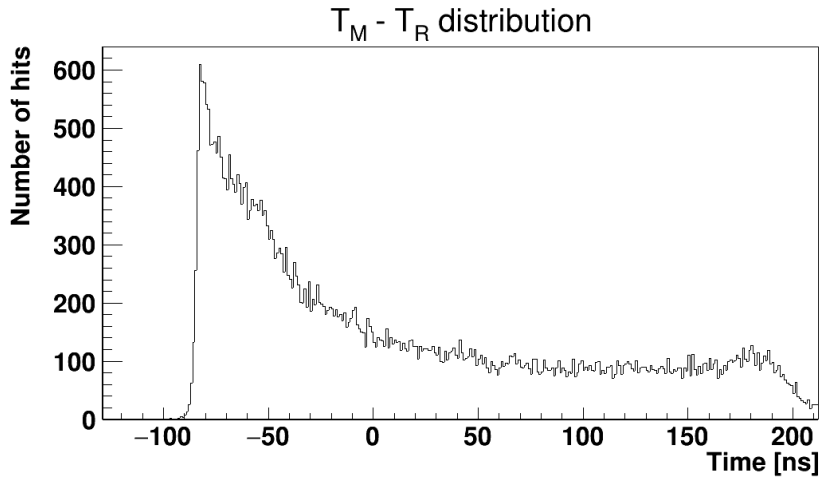

Figure 3.10: $T_M - T_R$ distribution of a given cell of the FOOT BM detector from data taken at Trento with protons at 80 MeV.

or external calibrations.

3.2.5 Drift chamber spatial resolution

Considering an optimal estimate of the space-time relations, the spatial resolution of a drift chamber is determined by different phenomena related to the accuracy of the drift time measurements. The main contributions are given by the primary ionization statistics, the electronics and the diffusion effect. The consequence of these phenomena varies as a function of the drift distance, as shown in Fig.(3.11). In addition, there are a lot of other effects that can play a role (i.e.: multiple Coulomb scattering, energy loss fluctuations, the sense wire position uncertainty etc.).

Details about the main aspects related to the spatial resolution of the drift chambers are shown in the following paragraphs.

Primary ionization statistics

Given a particle that generates k electron-ion pairs along its track in the gaseous medium, one can compute the space distribution of each pair j ($1 < j < k$) along a normalized

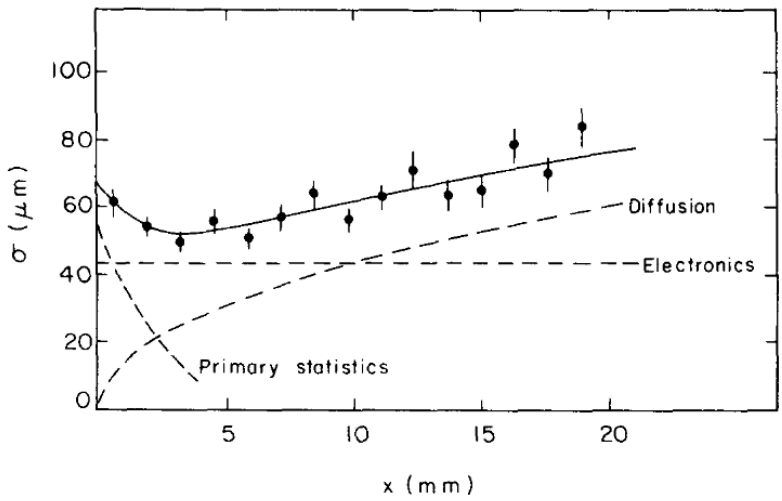

Figure 3.11: Measured space resolution of a drift chamber as a function of the drift distance. The expected contribution derived from different sources of uncertainties are depicted with dotted lines [110].

coordinate $d\,(0 < d < 1)$ with the following expression:

$$D_j^k(d) = \frac{k!}{(k-j)!(j-1)!}(1-d)^{k-j}d^{j-1} \tag{3.14}$$

Considering N as the average number of ionizations per unit length and combining Eq.(3.14) with the number of primary ionization clusters distribution expressed by the Eq.(3.2), the general formula to evaluate the space distribution of the pair j can be computed as [110]:

$$A_j^N(d) = \sum_{k=j}^{\infty} P(N,k)\, D_j^k(d) = \frac{x^{j-1}}{(j-1)!}\, N^j\, e^{-Nd} \tag{3.15}$$

Thus, in the case of a particle that crosses the anode wire, the distribution of the closest electron-ion pair is $A_1^N(d) = N\, e^{-Nd}$. The average minimum distance between the wire and the nearest pair can be computed as:

$$\delta x_0 = < d_{\text{min}} > = \int_0^{\infty} x e^{-Nx} dx = \frac{1}{N} \tag{3.16}$$

Considering the case illustrated in Fig.(3.12) in which a particle crosses a drift chamber cell at a distance x from the anode wire, the drift time and the associated drift distance measured by the detector is given by the electron-ion pair created closest to the POCA position. As calculated in (3.16), the mean distance between the POCA and the nearest ionization cluster is $\delta x_0 = 1/N$. Thus, the detector resolution, defined as δx can be computed as:

$$\delta x = \sqrt{x^2 + (\delta x_0)^2} - x = x\left(\sqrt{1 + \left(\frac{\delta x}{x}\right)^2} - 1\right) \sim \frac{x}{2}\left(\frac{\delta x_0}{x}\right)^2 = \frac{1}{2N^2}\frac{1}{x} \tag{3.17}$$

The $1/x$ dependence of the resolution indicates that the effect of the primary ionization statistics on the spatial resolution is more relevant for the particles passing close to the anode wires.

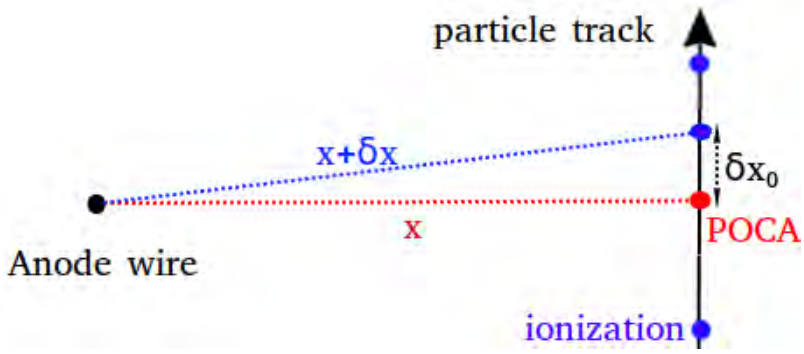

Figure 3.12: A schematic view of a particle that crosses a drift chamber cell at a distance x from the anode wire. The ionization clusters are drawn as blue points and the POCA position is drawn in red. The $x + \delta x$ length is the measured drift distance.

Electronics
The contribution of the electronics on the detector spatial resolution is given by the accuracy of different components adopted for the signal discrimination, shaping and readout. Each stage of the signal propagation can have an effect on the detector performances. As an example, a leading edge discriminator can get the resolution worse since each time measurement depends on the amplitude of the electronic signal. An other example of source of uncertainty is given by the precision of the TDC adopted to sample the output of the discriminators. If in the former case a constant fraction discriminator could resolve the obstacle, in the latter case the only way to improve the detector performances is to get a TDC with a better time resolution. However, except some special cases given by the specific condition of a detector, the general overall contribution on the space resolution given by the electronics is a constant value that does not depends on the specific track position.

Diffusion effect
Considering the simple case in which no external electric or magnetic field is applied, a localized point-like cloud distribution of ions or electrons diffuses in the gas medium through multiple collisions following a Gaussian law [110]:

$$\frac{dN}{N} = \frac{1}{4\pi Dt} \exp -(x^2)/4Dtdx \tag{3.18}$$

where dN/N is the fraction of particles found after a time t in the element dx at a distance x from the origin. D is the diffusion coefficient related to the standard deviation of the distribution:

$$\sigma_L = \sqrt{2Dt} \; ; \;\; \sigma_V = \sqrt{6Dt} \tag{3.19}$$

where σ_L is referred to the linear and σ_V to the volume diffusion. Examples of diffusion coefficients are: 0.04, 0.06 and 0.26 cm^2/sec respectively for argon, oxygen and helium gases [110].

Combining Eq.(3.9) and Eq.(3.19) it is possible to evaluate the diffusion effect as a function of the electric field and the particle travelled distance L:

$$\sigma_L = \sqrt{\frac{2DL}{\mu E}} \tag{3.20}$$

Equation (3.20) states that the spatial resolution gets worse for the particles detected far from the anode collection region. An increase of the electric field can compensate the effect limiting the diffusion, but it would increase also the production of δ-rays. In addition, usually the stability of the gaseous detectors places an upper limit on the electric field.

Considering the case of ions subject to a low electric field ($E/N\sigma \ll KT$) that are typical of drift chamber regions not in proximity of the high voltage wires, the diffusion coefficient can be related with the mobility by the *Einstein formula*:

$$\frac{D}{\mu} = \frac{kT}{e} \tag{3.21}$$

where k is the Boltzmann constant, T is the temperature and e is the elementary charge. In this way the σ_L in Eq.(3.20) can be rewritten eliminating the dependencies on the gas and ion properties, pointing out the relations with the particle travelled distance (L) or the particle velocity (u) and time (t):

$$\sigma_L = \sqrt{\frac{2kTL}{eE}} \;\; ; \;\; \sigma_T = \sqrt{\frac{2kTut}{eE}} \tag{3.22}$$

Examples of the ion diffusion effects described in Eq.(3.22) are shown in Fig.(3.13).

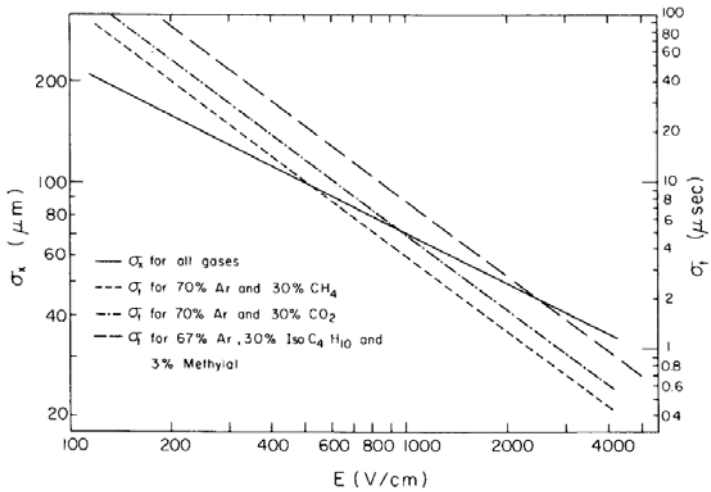

Figure 3.13: Positive ion diffusion coefficient in space (σ_x) and in time (σ_t) as a function of the electric field, considering a drift length of 1 cm in different argon gas mixtures at normal conditions [110].

3.3 The Beam Monitor in the FOOT experiment

The description of the FOOT BM mechanical structure is illustrated in Sec.(2.3). In this part, all the studies and the works carried out prior to the start of the experimental tests

and data acquisition campaigns are illustrated. In particular, details about the detector aims and the required performances is presented in the next subsection. Then, the results of the MC simulation studies performed by means of Garfield++ software to estimate the detector electric field are shown. The last subsection is dedicated to the description of the BM track reconstruction software developed and included in SHOE.

3.3.1 Detector aims and required performances

The FOOT BM is a drift chamber detector adopted to measure the incoming beam direction, the projectile impinging position on the target and to recognize the events in which the projectile interacts inelastically before arriving to the target.

The rationale in the choice of such type of detector for these goals relies mainly on two general properties of the drift chambers: the low material density and the high spatial resolutions that can be obtained. The former detector characteristic is required by the FOOT experiment to minimize the nuclear inelastic interactions prior the target and the multiple Coulomb scattering effect introduced by the detector itself. The latter is necessary to perform the inverse kinematic approach, which requests a spatial resolution of the order of few hundreds of μm.

Indeed, even if the silicon based detectors could easily reach a higher resolution performances, the necessity to measure also the beam direction implies the request to use at least two layers of scintillator that would strongly increase the amount of material budget. This would lead to an enhancement of the probability of an undesired fragmentation of the projectile prior the target and, consequently, an increase of the background within the collected data. The low gas density ($\sim 10^{-}3\,\mathrm{g/cm^3}$) compared to the plastic scintillator material density ($\sim 1\,\mathrm{g/cm^3}$) allows the use of a detector that provides redundant measurements, reaching the required performances.

3.3.2 Electric field studies by means of Garfield++ MC simulation tool

The MC simulation tool Garfield++ [117] has been adopted to estimate the electric field distribution across the BM cells. Garfield++ is a toolkit developed in the framework of the CERN organization [118] for the detailed simulation of gaseous and semiconductor based detectors. It can interface with different external programs to calculate the electric field, to simulate the transport of electrons and ions in gas mixtures and the relative ionization parameters.

For the BM detector, the electric field is evaluated by means of a semi-analytic calculation technique implemented within the Garfield++ software. Once the detector geometry and the material parameters are implemented, the software can evaluate the electric field map if the sense wires high voltage and the field wire potentials are set.

Considering a high voltage of 2200 V, corresponding to the conditions of the BM during the calibration data taking conducted at Trento with protons, the electric field map of a BM cell is shown in Fig.(3.14). As expected, the electric field absolute maximum is located on the sense wire set at the high voltage and placed at the center of the cell. The other relative maxima are situated in the positions corresponding to the field wires, that are set to the ground potential.

The most interesting aspect is related to the electric field minima positions placed between the field wires close to the border of the cell. Since in these regions the electric field is lower, incomplete charge collection and recombination processes can take place reducing the detector efficiency. The last three plots of Fig.(3.14) show the values of the electric fields projected on three different planes perpendicular with respect to the beam

line and placed at different depths corresponding to the cell center (Z=0 cm), between the center and the border (Z=0.25 cm) and at the cell border (Z=0.5 cm). The electric field in the former and the last projections has a minimum of about 0.55 kV/cm and 0.29 kV/cm respectively at about 0.6 and 0.5 cm from the cell center. At the same distance from the sense wire position, the electric field projection at z=0.25 cm shows the start of a steeper decrease of the field intensity from few hundreds of V/cm up to tens of V/cm.

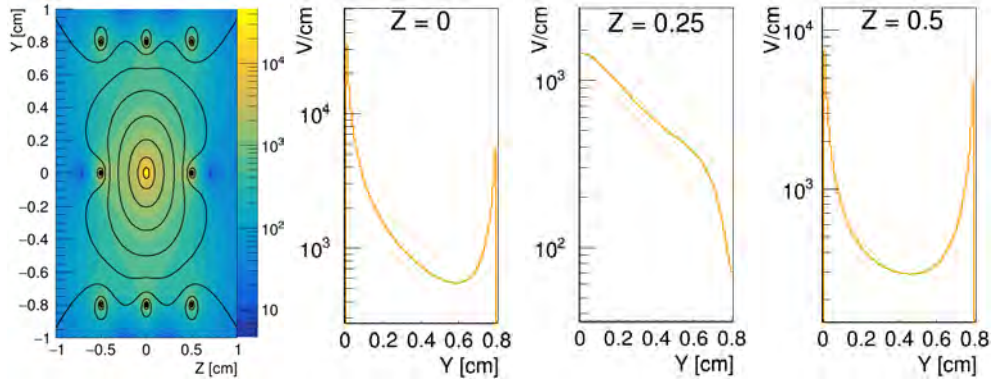

Figure 3.14: The BM electric field intensity of a BM cell evaluated by means of Garfield++ simulation toolkit. On the left, the overall electric field is shown on a 2D plot with the superimposition of the potential field contour plot (black lines). The projections of the electric filed calculated on different planes placed at different depths are shown in the subsequent plots. The beam direction is along the Z coordinate and the sense and field wires are along the X direction.

These evaluations suggest that the detector could be affected by inefficiencies in the hit detection due to the presence of regions with low electric field intensity. Indeed, the BM cell has a simple geometry and the number of field wires per cell is limited. In addition, all the field wires of the detector are set to 0 V, without the possibility to scale the potential of the wires that would increase the electric field uniformity across the cell. However, as shown in Fig.(2.5), the border of a cell corresponds to the centers of the cells placed on the two adjacent layers. Thus, considering a particle crossing the BM with a straight track, the possible inefficient cell region that it can traverse on a given layer is compensated by the areas with a high electric field that it crosses on the adjacent layers. The cell staggering and the redundancy of layers are two fundamental properties of the BM that reduce the effects caused by the low electric field intensity.

3.3.3 Reconstruction software

After the procedure described in Sec.(3.2.4) to obtain the drift chamber space measurements, a reconstruction algorithm is required to fit the drift distances and retrieve the track parameters.

Generalities on drift chamber reconstruction algorithms
Since a hit of a drift chamber represents the distance between the particle track POCA and the sense wire, a simple and efficient method to understand the working principle of a drift chamber reconstruction algorithm consists to draw a circle around the positions of each sense wire with the radius given by the space measurement value. Figure (3.15) illustrates the six layers of the BM Y-Z view cells with the drift measurements given from

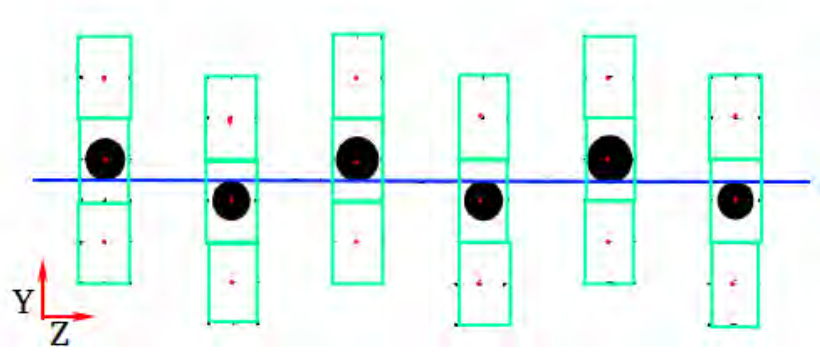

Figure 3.15: A schematic pictures of a fitted track on the Y-Z view of the BM. The cells are drawn in green, the sense wires are the red dots, the drift distances are represented by the black circles and the track is the blue line. Since this is the Y-Z view, all the wires are along the X direction.

a MC simulated event. The goal of a reconstruction software consists to find a line that is tangent to the circles, as shown by the blue line.

Due to the peculiarity of the drift chamber hits and tracking algorithm, the reason for the staggering of the BM layers is evident: if all the layers of Fig.(3.15) are placed at the same Y coordinate, all the circle centers would be aligned and there would be two possible tracks both tangent to all the circles. With the staggering, the left-right ambiguity is resolved and there could be only one track associated with all the hits.

Beam Monitor reconstruction algorithms

The most challenging aspects of a drift chamber reconstruction algorithm are given by the complications in the first estimate of the track parameters and the association of the hits with the track. In addition, these operations should be performed considering the multi-track cases and the background hits.

In the framework of the FOOT experiment, different reconstruction algorithms have been developed for the BM. The previous versions are:

- The first one is a reconstruction software based the GENFIT Kalman filter [119] employed also in the FOOT global event reconstruction code. The track initial seed is given by the position of the first cell with a measurement and the initial direction is set to be along the Z direction. The hit selection is conducted by an algorithm that firstly considers all the single-hit layers and, after a Kalman filter iteration, it adds the more suitable hits from the multiple-hit layers, deleting the outliers.

- GENFIT is an external toolkit realized to be exploited in a wide range of experiments, independent of the specific event topology, detector type or magnetic field arrangement. Since the BM is not influenced by the magnetic field and the event signature does not change a lot among the data, the complexity and the time performance of the Kalman filter provided by GENFIT forced us to find a different solution. The second BM reconstruction algorithm has been developed with a χ^2 minimization technique, exploiting the ROOT [120] framework and the Minuit2 packages [121]. The track initial seed and the hit selection are performed with the same methods as the previous reconstruction algorithm.

The Legendre transform and the final version of the Beam Monitor reconstruction algorithm

The main drawback of the previous algorithms is given by the computational speed. The substitution of the χ^2 minimization method over the GENFIT based Kalman filter speeds up the reconstruction procedure, but the track initial seed and the hit selection algorithm are still not fast and they are not optimized to handle the multi-track events. In order to increase the software velocity developing an algorithm with the multi-track reconstruction capability, a new hit selection algorithm has been developed exploiting the Legendre polynomials.

The Legendre transform is a mathematical operation adopted above all in the framework of thermodynamics and analytical mechanics [122].

Considering a convex function $f(x) : \mathbb{R} \rightarrow \mathbb{R}$ ($\mathrm{d}^2 f/\mathrm{d}x^2 > 0$) and a line equation of the form $y(x) = px + a$, for a value p of the line slope the Legendre transform $F(p)$ of the function $f(x)$ is defined as:

$$F(p) = sup_x[px - f(x)] \tag{3.23}$$

where sup_x indicates the maximization of the function $[px - f(x)]$ with respect to x for constant p. In order to find the maximum of Eq.(3.23), the condition found setting the derivative to zero is:

$$p = \mathrm{d}f(x)/\mathrm{d}x \tag{3.24}$$

Inverting Eq.(3.24), the relation $x(p)$ can be obtained and the Legendre transform of Eq.(3.23) can be written as $F(p) = px(p) - f(x(p))$. The graphical representation of the Legendre transform is shown in the left panel of Fig.(3.16). Basically, given a value p, the transform $F(p)$ finds the x_0 of the initial function $f(x)$ where the tangent line of $f(x)$ in x_0 has a slope p and an interception on the y-axis at $-F(P)$.

For a concave function ($\mathrm{d}^2 f/dx^2 < 0$), the Legendre transform is defined as:

$$F(p) = sup_x[f(x) - px] \tag{3.25}$$

and it maintains the same properties as the previous case. The only difference is the intercept on the y-axis that lacks of the minus sign and it is $F(P)$. Thus, giving a differentiable function $f(x)$, the Legendre transform maps $f(x)$ into a two dimensional space called *Legendre space* $(p, F(p))$ in which the coordinates of the mapped points represent the parameters of the tangent line equations of $f(x)$ [122].

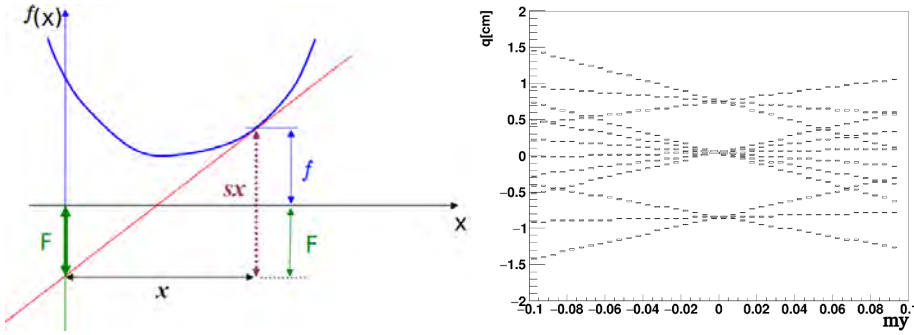

Figure 3.16: On the left, the graphical representation of the Legendre transform $F(p)$ of a function $f(x)$. On the right, the results of the Legendre transform shown in Eq.(3.27) on the BM hits drawn in Fig.(3.15).

As shown in Fig.(3.15), each hit of a track in a drift chamber can be represented by a circle centered in the anode wire of the fired cell, while the particle trajectory is a line

that is tangent to all the associated circles. Thus, mapping the drift chamber circles into the Legendre space, the hits associated to the same track will be clustered and the cluster coordinates will correspond to the track parameters. Considering the Y-Z bi-dimensional space, each circle drawn in Fig.(3.15) can be represented by a set of two equations:

$$\begin{aligned} f_1(x) &= y_0 + \sqrt{R^2 - (x - x_0)^2} \\ f_2(x) &= y_0 - \sqrt{R^2 - (x - x_0)^2} \end{aligned} \tag{3.26}$$

where f_1 refers to the concave and f_2 to the convex part of the circle, R is the circle radius (i.e.: the space measurement), x_0 and y_0 are the anode wire position coordinates. Employing the Legendre transform to the set of equations in Eq.(3.26) and adding a minus sign to the $f_1(x)$ equation to compensate for the minus sign of the intercept value on the y-axis, the final equations to map the BM hits into the Legendre space are:

$$\begin{aligned} F_1(p) &= x_0 p - y_0 - R\sqrt{p^2 + 1} \\ F_2(p) &= x_0 p - y_0 + R\sqrt{p^2 + 1} \end{aligned} \tag{3.27}$$

Applying this set of equations on all the Y-Z view hits of an event, the measurements are mapped into the Legendre space and, exploiting its properties, a hit association procedure can be performed smoothly retrieving also a first estimate of the track parameters.

As an example, the Legendre space plot of the hits displayed in Fig.(3.15) is shown on the right panel of Fig.(3.16). There are two lines drawn for each hit and the plot shows three clusters with almost the same slope (my$\sim$0) and different intercept values: q~ 1, q~ 0 and q~ -1. The first and the latter clusters corresponds to two tangent lines each associated to three hits. Checking in Fig.(3.15), it is evident that the first cluster with $q \sim 1$ is given by a possible track associated with the hits placed in the odd planes and with the tangent points situated on the opposite sites of the actual blue track. The same effect is present also for the last cluster with $q \sim -1$, since it is associated with the three hits placed on the even planes. The cluster with $q \sim 0$ is the actual track of the primary particle shown in blue in Fig.(3.15), indeed it is associated with all the six hits.

For the BM reconstruction algorithm, the first step consists in the mapping of the hits into the Legendre space employing the equations calculated in Eq.(3.27). Then, an iterative algorithm has been developed for the hit association procedure. In details, it finds the cluster with the highest number of hits, flag the associated hits, clean the Legendre space plot and re-apply the entire procedure on the remaining hits until no cluster with a minimum of three hits is present. Since the track parameters obtained from the cluster positions are still not optimized, the χ^2 minimization algorithm based on ROOT and Minuit2 packages is adopted to refine the reconstructed parameters. All the described operations are applied independently on both the BM views.

CHAPTER 4

Beam Monitor calibration and data taking

4.1 Introduction

In the first part of this chapter, the calibration and performance assessment of the BM conducted at the Trento protontherapy facility will be illustrated. In particular, all the detector parameters (e.g.: efficiency, spatial resolution etc.) have been measured experimentally using an external independent tracking telescope. In addition, the space-time relations required to interpret and use the BM measurements have been calibrated both by means of the external tracking detector and by means of a self calibration algorithm.

In the second part of the chapter (Sec.(4.3)), the BM measurements performed in the framework of the FOOT experiment are shown. In details, the methods and the results obtained during both the emulsion and electronic spectrometer data takings will be presented, together with the characterization of the 700 MeV/u carbon ion beam of the GSI accelerator facility.

4.2 Beam Monitor performance assessment at test beams

Even if the BM was adopted in the FIRST experiment and different performance evaluation data takings had been conducted in the past [92, 123], a complete BM characterization performed by means of an external tracking detector has never been accomplished. For this reason, a full performance evaluation of the detector has been conducted in the Trento protontherapy center with proton beams at 228 MeV and 80 MeV of initial kinetic energy. The former beam energy is adopted to characterize the BM and calibrate the detector space-time relations since it minimizes the multiple Coulomb scattering effect. The latter proton beam energy is used to evaluate the detector response with respect to a higher ionizing particle beam, reproducing as much as possible the conditions presented during the FOOT data taking in which the BM is exposed to more ionizing particles such as ^{4}He, ^{12}C and ^{16}O. In this occasion, a micro-strip silicon tracking detector has been adopted as an external independent tracking telescope to ensure a reliable BM calibration and performance assessment.

The experimental setup, the methods adopted to find a proper working point and the data selection are presented in Sec.(4.2.1). Then, the studies about the detector efficiency and spatial resolution are presented in Sec.(4.2.2) and Sec.(4.2.3), followed by the performances of the beam transverse profile measurements shown in Sec.(4.2.4) and the measurement of the BM sensitive area illustrated in Sec.(4.2.5).

In addition to the performance assessment, the micro-strip detector has been adopted also to perform a calibration of the BM space-time relations. Details about the calibration procedure and the results are shown in Sec.(4.2.6). The new performance evaluation and

the results about the calibration of the BM obtained by means of the external tracking detector has been published in [124].

However, as described in Sec.(3.2.4), the drift velocity of drift chambers depends on the reduced electric field applied to the detector. Considering that the BM HV needs to be tuned properly for a given particle species and energy, in principle, the space-time relations require to be optimized for each experimental data taking. Since a proper calibration is not always feasible due to the time availability at the accelerator facilities, a self calibration algorithm has been developed to estimate the space-time relations using only the BM hits and tracks. The performance of this algorithm has been studied both by means of MC simulations and with experimental data. The method and the results of the self calibration algorithm are illustrated in Sec.(4.2.7).

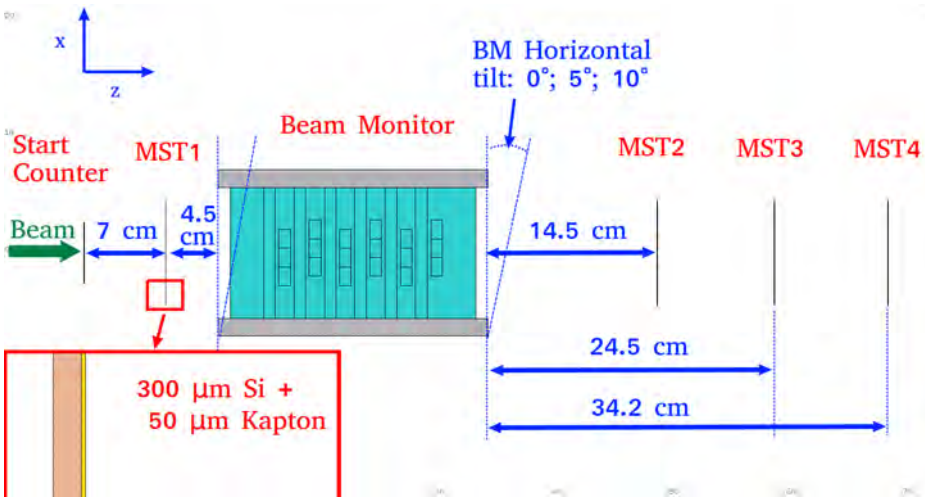

Figure 4.1: Schematic view of the experimental setup adopted for the BM calibration and performance assessment data taking. The bottom-left insert illustrates the mechanical structure of a MST layer.

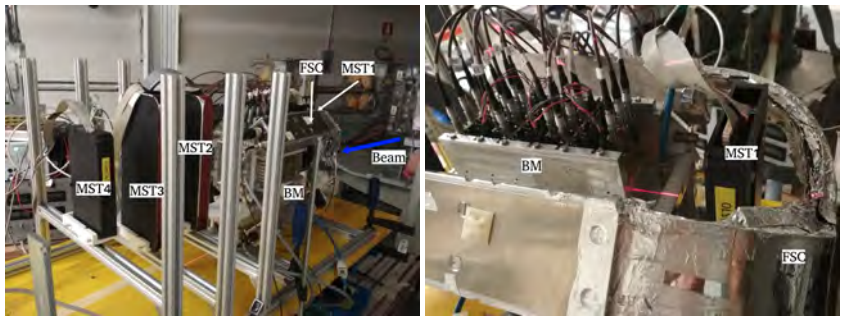

Figure 4.2: General picture of the experimental setup and of the detectors employed for the BM calibration data taking (left). A detailed photo of the first layer of MST placed between the FSC and the BM is shown on the right.

4.2.1 Experimental setup

The experimental setup of the BM calibration data taking is shown in Fig.(4.1) and Fig.(4.2). In details, it is composed of the FSC start counter system (see Sec.2.3.2), the BM and four layers of Micro-strip Silicon Tracker (MST). The FSC is the same detector adopted also for the emulsion spectrometer data taking. The BM, who is the detector to be characterized, has been placed after the first MST layer, followed by the other three layers of MST. The MST is a micro-strip silicon detector. It is composed of 300µm (0.0307 g/cm^2) thick double sided silicon micro-strip sensors with either one or two daisy-chained modules derived from the AMS-02 experiment [125] and updated with a new readout chip. Each side of a MST layer provides the measurement of the X or the Y coordinates of the particles, both perpendicular with respect to the incident beam direction. The detector sensitive area is of $4 \times 7\,cm^2$ and $8 \times 7\,cm^2$ for the two sides. In addition to the sensitive area and the measured coordinate, the other differences between the two sides is the readout pitch, the number of readout channels and chips. In details, each module provides 640 readout channels for the visible junction p-side with a pitch of 104 µm and 384 channels for the reverse ohmic n-side with a readout pitch of 208 µm. The detector overall mean point resolution along a reconstructed track is of 45 µm.

The MST detector was optimized for the measurement of high energy space radiation particles ($E \geq 10\,GeV$) where the multiple Coulomb scattering has only a slight effect on the track reconstruction resolution. On the contrary, this effect is not negligible for the detection of protons at 80 or 228 MeV adopted for this test beam. Indeed, as verified by means of a simulation of the whole experimental setup performed by means of the FLUKA code, the beam spread due to the multiple Coulomb scattering caused by the detectors is of the order of milliradians. This is the reason why the micro-strip silicon detector adopted within the FOOT electronic spectrometer has a thickness of 150 µm, that is the half of the MST detector adopted for the BM calibration. However, in order to minimize the MST resolution worsening due to the multiple Coulomb scattering, only the first and the second layers of MST have been adopted to reconstruct the MST tracks employed in the BM calibration. In this way, the multiple Coulomb scattering effect is of the order of ~ 3 and $\sim 5\,mrad$, respectively for the 228 and the 80 MeV proton beams, as shown in Fig.(4.3).

The beam provided by the Trento protontherapy facility in the experimental room has a Gaussian profile with a transverse spot size that depends on the projectile energy [126]. In the case of a 228 MeV proton beam, the sigma of the beam transverse profile is of the order of 3 mm. Since such a spread is not enough to reach all the area of a BM cell, the BM was rotated at 0, 5 and 10 degrees around the y axis, moving the detector on the horizontal plane. The tilt avoided also the overlap of the cell anodes on one layer with the field wires of the adjacent layers. In this way, the two cell area with the lowest spatial resolution are not overlapped.

The BM and the FSC already have a VME stand alone acquisition chain with a C++ program developed for the FOOT emulsion spectrometer data taking, as described in the last paragraph of Sec.(2.3.2). Since also the MST has a stand alone acquisition program and the integration of the two codes was too time consuming, both the detectors acquired the data separately. The synchronization of the BM and the MST events was ensured by a dedicated hardware trigger-veto system realized with different NIM modules (dual timer, coincidence module etc.). The acquisition rate was of about 200-300 Hz and about $6 \cdot 10^5$ events have been successfully collected during the whole test beam. In the analysis phase, also the track reconstruction procedure has been executed separately for the BM and the MST data. In particular, in the former case the algorithm illustrated

in Sec.(3.3.3) has been employed to reconstruct the BM tracks. In the latter case, the reconstruction algorithm was developed in the framework of the AMS-02 experiment and it was based on a minimization of χ^2 technique. Finally, a dedicated analysis software has been created to combine the tracks and the measurements of both the detectors, performing the calibration of the BM.

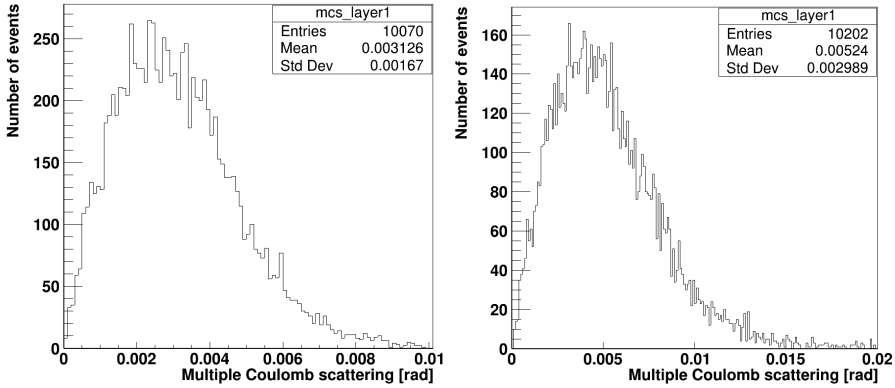

Figure 4.3: Multiple Coulomb scattering effect on the second MST layer calculated from a simulation performed by means of the FLUKA software with a proton beam at 228 MeV (left) and 80 MeV (right) of initial kinetic energy.

Beam Monitor working point

During the data taking, the BM was continuously flushed with an Ar/CO_2 gas at 80/20%, with a flow rate of about 1 l/h and with the pressure fixed at about 0.9 atm over the atmospheric pressure. In order to set the BM channels threshold values adopted in the VME discriminators, both the noise and the signal levels have been measured with an oscilloscope. In the former case, the noise has been detected to be at the level of few mV/50 Ω. In the latter case, the BM signal has been measured to be of the order of hundreds of mV/50 Ω. Thus, for the calibration data taking, the threshold on the BM channels has been set to 20 mV/50 Ω.

After the channel threshold, also the BM High Voltage (HV) needs to be properly tuned prior the beginning of the data acquisition. The rationale for the HV choice is given by different aspects that have to be considered. As an example, the drift chamber is a gaseous detector that operates in a proportional regime, as shown in Sec.(3.2). Thus, the output signal of the BM depends on the ionization of the incident particles, the gas composition, the pressure and the electric field applied on gaseous volume. The stopping power (dE/dx) of the protons in the BM gas medium is of 3.13 MeV·cm^2/g and 6.44 MeV·cm^2/g respectively for the 228 MeV and 80 MeV particles. Once all the other parameters except the last one are already properly set, the amplitude of the output signal of the BM strictly depends on the HV value. Thus, on one hand, if the HV is too low the gain factor defined in Eq.(3.11) that gives rise to the amplification of the signal would be too low and the detector would become inefficient. On the other hand, if the HV value is too high, the amplification of the signal would be too enhanced and the detector readout board would saturate. In addition, the increase of HV would lead to an increase of δ-rays and cross talks. The former are the secondary electrons (δ-rays) that causes further ionization clusters, as described in Sec.(3.2.1). In the latter case, the electrons may escape from cell to an adjacent one, giving rise to background signals. The

optimal HV values is a compromise between all these effects: it has to be high enough to ensure a good hit detection efficiency, but low enough to prevent the saturation of the readout signal and to avoid an excessive production of $\delta-$rays and cross talks.

In order to determine the optimal HV value for the calibration data taking, different datasets with at least 10^5 events per dataset have been collected exploiting a proton beam of 80 MeV and modifying the BM HV from 1800 V up to 2300 V. The signals measured in this range of HV values did not show any saturation of the readout signal, as verified with the oscilloscope. On the contrary, the other effects related to the efficiency, $\delta-$rays and cross-talks have been detected considering the mean and the peak values of the number of hit distribution. Indeed, the expected number of hits for a particle that crosses the whole detector is equal to twelve, that corresponds to the total number of BM layers considering both the views. However, on one hand the BM not perfect hit collection efficiency lowers the number of hits detected per event, and, on the other hand, the effect of δ-rays and cross talks is to enhance the number of observed hits. The BM hit distribution is the result of the sum of these effects and it is spread with a tail along the higher values, as shown in the left panel of Fig.(4.4). The hit distribution mean value is slightly higher than the peak value and both of them depend on the HV setting. The right panel of Fig.(4.4) represents the mean and the peak values of the hit distribution as a function of the HV. The minimum HV required to measure the 80 MeV protons is 1900 V. As expected, the number of BM hits increases with the enhancement of the HV. The final setting of HV has been chosen to be 2200 V since the corresponding mean number of hits is 13 and the peak of the hit distribution is 12. In this way, the hit detection efficiency is high enough to ensure the track reconstruction capability and both the $\delta-$rays and the cross talks are limited. The HV setting has been kept constant during the data taking also with the 228 MeV protons, since no relevant differences in the hit distributions have been detected.

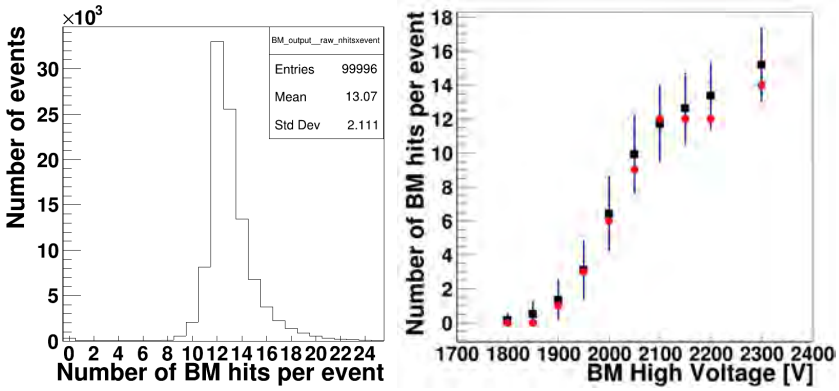

Figure 4.4: On the left, the BM hit distribution of 10^5 protons at 80 MeV collected with the BM HV set at 2200 V. On the right, the mean value (black) and the peak value (red) of the BM hit distribution as a function of the HV. The error bars are the standard deviation of each hit distribution.

Data selection and detector alignment

Different selection criteria have been implemented to reject the background hits and select a clean dataset. In details, a first cut is performed on the time measurements rejecting all the hits with a time $\geq$ 320 ns that corresponds to the expected maximum drift distance. Then, for each event a second selection is applied on the total number of BM

hits that must be ≥ 10 and ≤ 14. This reduces the events that contains hits derived from cross talks and δ-rays. Once the BM hits and events are selected, the space-time relation derived from the FIRST experiment [81] has been adopted to convert the BM time measurements into drift distances permitting the track reconstruction procedure. When the tracks are reconstructed applying the algorithm explained in Sec.(3.3.3), a further selection has been applied rejecting the BM tracks with $\chi^2_{\text{red}} > 10$.

Regarding the MST tracks, since this detector is composed of different layers of sensors, a first internal layer alignment procedure is conducted by means of an iterative algorithm that minimizes the residual distributions. In particular, the alignment of the MST layers is performed on a random sub-sample of the 228 MeV events to minimize the MCS contribution. In addition, the events are required to have a single hit reconstructed in each detector layer to avoid the ambiguities related to the track multiplicity.

Then, the BM and the MST alignment parameters are evaluated exploiting an iterative algorithm based on the minimization of the residuals between the two detector tracks. Finally, the calibration and the performance assessment of the BM has been conducted combining the MST tracks with the BM measurements.

4.2.2 Efficiency

Hit detection efficiency

In order to measure the BM efficiency during the data acquisition preparation phase, a method based on "pivot" and "probe" counters technique is adopted. In details, given a BM view, the events with three aligned hits detected on the three odd (or even) planes are marked as "pivots". On this subset of data, the events in which also the two even (or odd) planes in midst of the pivots planes contain one or two aligned hits are tagged as "probes". Finally, the hit detection efficiency is defined as the ratio of probes over pivots. A schematic view of the pivot-probe method is shown in Fig.(4.5).

The main advantages of this technique are given by the velocity of the calculation and the independence of both the BM reconstruction algorithm and the space-time relations. Indeed, it can be adopted during the setting of the detector working point to have a quick measurement of the efficiency, avoiding the track reconstruction procedure with all its requirements (e.g.: space-time relations, data selection criteria etc.).

The evaluation of the hit detection efficiency as a function of the HV is shown in the left panel of Fig.(4.6). The data are taken with a fixed 80 MeV proton beam and each dataset is composed of 10^5 events collected with a specific HV. The efficiency strictly depends on the HV values and, as expected, it increases with the rise of the HV. The minimum HV necessary to ensure an efficiency ≥ 0.9 is 2150 V and the working point chosen for the data acquisition is 2200 V.

In order to have a better measurement of the efficiency, different datasets of 10^5 events had been taken varying the proton beam energy from 80 MeV to 220 MeV with steps of 20 MeV. The overall mean hit detection efficiency results to be 0.929 ± 0.008. Since the BM is composed of six planes of cells per view, this efficiency value is high enough to ensure a good reconstruction capability. Indeed, the minimum number of hits per view required to reconstruct a track is three and in this case the mean number of hits per view is of 5.58 ± 0.06.

Efficiency as a function of the drift distance

In order to measure the detector efficiency as a function of the drift distance, a different "pivots-probes" method that combines the MST tracks with the BM hits has been developed, thanks to the availability of an external tracking detector. In details, for a given

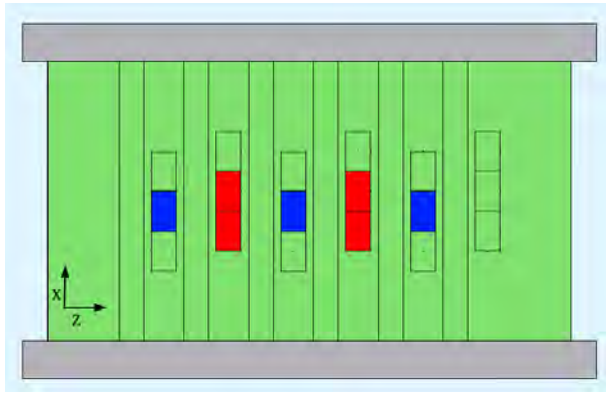

Figure 4.5: A schematic view of the hit detection efficiency method: if each of the blue cells contains a hit, the event is marked as pivot. Then, if the event contains also one or two hits in the red cells, it is marked also as probe.

event, the MST track is extrapolated into the BM detector and all the cells crossed by the track are counted as "pivots". Then, if a pivot-cell contains a BM hit, it is counted also as a "probe". As before, the efficiency is evaluated as the ratio of the "probes" over the "pivots". In addition with respect to the previous method, in this case the efficiency can be evaluated as a function of the drift distance, since each pivot-cell can be associated with a space measurement defined as the distance between the cell center and the MST track. The result is shown in the right panel of Fig.(4.6). The efficiency is higher then 0.98 if the drift distance is ≤ 0.45 cm and it drops below 0.93 if the particle crosses the cell at a distance ≥ 0.6 cm. The accuracy of the pivots drift distance evaluations is of the order of 0.034 cm in the worst case scenario of 80 MeV protons with the maximization of the multiple Coulomb scattering. Thus, the effect of the detectors misalignment and the MST track reconstruction precision are negligible and the efficiency drop at the cell border must be attributed to a physics effect rather than a geometrical or track inaccuracy effect. Indeed, as shown in Fig.(3.14) presented in Sec.(3.3.2), the electric field generated in the BM cell has different minima of few hundreds of kV/cm placed at about 0.6 cm from the cell center. This electric field drop can lead to an incomplete charge collection that worsens the detector efficiency. The staggering of the BM planes partially compensate the inefficiency since a cell border on one plane corresponds to the centers of the cells placed in the two adjacent planes.

4.2.3 Spatial and angular resolution

As in the previous efficiency analysis, also in this case two different methods have been developed to measure the BM spatial resolution.

- **BM track method:** the first method adopts only the BM hits and tracks. In details, the residuals between the BM reconstructed track and the measured drift distances are computed and fitted by a Gaussian. The sigma of the distribution is considered as the detector spatial resolution. The results for the 228 MeV and the 80 MeV protons are shown by the black dots in Fig.(4.7). In both cases, the spatial resolution in the central part of the cell is of about 60-100 µm while the mean spatial resolution is of about 130 µm.

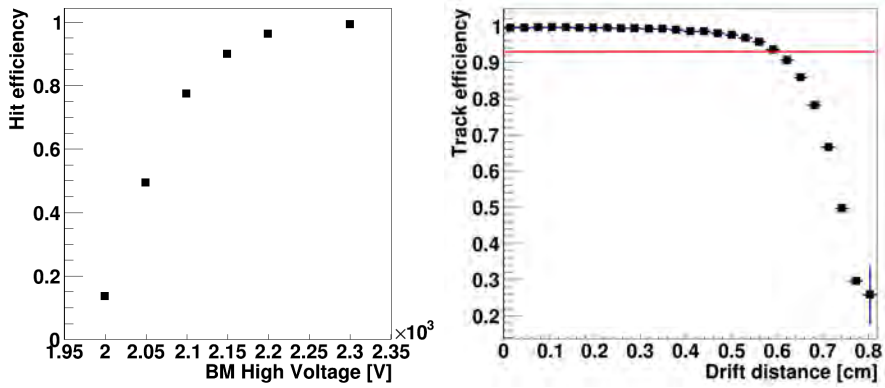

Figure 4.6: On the left, the BM hit detection efficiency as a function of the HV measured with a beam of protons at 80 MeV. On the right, the BM efficiency as a function of the drift distance measured by means of the MST tracks. The red line is placed at 0.929 and it represents the hit detection efficiency for the data taken with the HV set at 2200 V.

The BM resolution gets worse at the cell center and at the border of the cell, as described in Sec.(3.2.5). In the former case, the worsening is mainly given by the primary ionization statistics. In addition, in this case also the fixed time resolution Δt, derived from the TDC of the acquisition chain, has to be taken into account. Indeed, since the derivative of the space-time relations adopted for the BM is higher close to the cell center with respect to the cell border, the ΔX that represents the spatial measurement uncertainty corresponding to the time resolution Δt is enhanced if the track is close to the anode wire. On the contrary, the worsening of the spatial resolution at the cell border is given by the diffusion effect enhanced by the electric field reduction. No relevant differences have been found among the results obtained from the two beam energies.

- **MST track method:** the second method adopted to measure the BM spatial resolution employs the tracks reconstructed from the MST instead of the BM detector. As in the previous case, the track is extrapolated into the BM cells and the residual distribution between the track and the BM measured drift distances is computed and fitted. In this case, the sigma of the Gaussian fit is subtracted in quadrature with the MST track mean resolution (45 µm) in order to eliminate the contribution of the MST detector.

  The results of this method are shown by the red dots of Fig.(4.7). Contrarily to the BM track method, in this case the spatial resolutions measured from the data collected with the two proton beam energies are different. In particular, the mean spatial resolution extrapolated for the 228 MeV protons is of the order of $200 \pm 60\,\mu m$ with a precision in the central part of the cell of about $150 \pm 10\,\mu m$. The corresponding values for the 80 MeV protons are $340 \pm 60\,\mu m$ and $300 \pm 10\,\mu m$. Also in this case, a worsening of the performances is present close to the cell center and at the cell border due to the same motivations previously illustrated.

In order to analyze and discern the physics effects underlying the two methods, different MC simulations of the whole experimental setup have been performed by means of the FLUKA code with different primary beams (i.e.: protons at 80 MeV, 228 MeV and 10 GeV and oxygen ions at 400 MeV/u). In the SHOE reconstruction software the BM

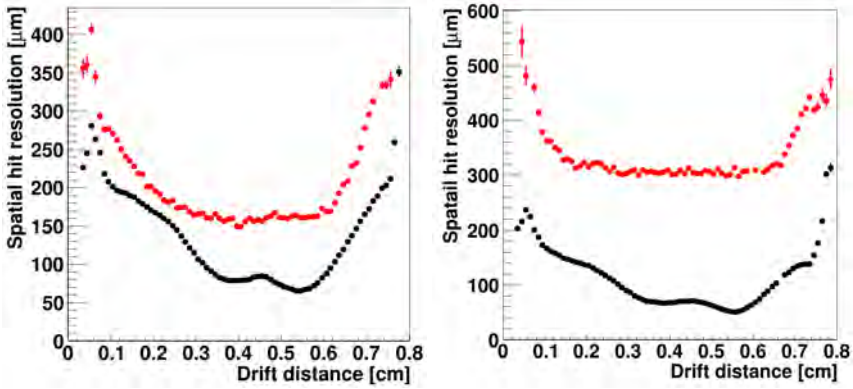

Figure 4.7: The BM spatial resolution as a function of the drift distance evaluated with the BM tracks (black) and the MST tracks (red) for the 228 MeV (left) and the 80 MeV (right) protons.

spatial resolution is the one derived from experimental data using the BM track method. Applying both the resolution evaluation methods on the simulated data, the physics phenomena included in the two methods are revealed. In details, the BM track method allows to estimate the detector spatial resolution avoiding the multiple Coulomb scattering contribution. Indeed, the black and the blue curves shown in Fig.(4.8) are substantially identical, even if they indicate the spatial resolutions calculated by the BM track method on the simulations performed with protons at 80 MeV and oxygen ions at 400 MeV/u. The same resolution curve is obtained also in the other simulations, as the results obtained from the experimental data.

On the contrary, the MST track method allows to measure the detector spatial resolution independently from the BM reconstruction algorithm, but including the multiple Coulomb scattering effect in addition to the BM intrinsic resolution. As an example, the results of the MST track method for the simulations performed with protons at 80 MeV and oxygen ions at 400 MeV/u are shown by the red and the green points of Fig.(4.8), respectively. In this case, as described in the Eq.(1.12) explained in Sec.(1.2.3), the simulated protons have lower charge and lower energy with respect to the oxygen ions, thus the spatial resolution calculated with the MST tracks for the protons is higher since the multiple Coulomb scattering effect is enhanced. On the contrary, the scattering is limited for the oxygen ions and, for this simulation, the results obtained by the MST track method are only slightly worse with respect to the results given by the BM track method. Applying both resolution evaluation methods on a simulation performed with a proton beam at 10 GeV, the two results are identical since the multiple Coulomb scattering effect is negligible. Also the results coming from the experimental data confirm the inclusion of the multiple Coulomb scattering effect in the outcome provided by the MST track method. Indeed, as illustrated in Fig.(4.7), the spatial resolutions from the 80 MeV proton data are higher with respect to the spatial resolutions calculated from the 228 MeV proton data.

In conclusion, the outcome of the BM track method depends on the space-time relations and on the BM reconstruction algorithm. If both of them are optimized, this method allows to estimate the detector spatial resolution upper limit, since no other contributions except the detector intrinsic resolution is present. Instead, the MST track method depends only on the space-time relations avoiding the use of the BM reconstruction algorithm, but the result includes the multiple Coulomb scattering effect. However,

if the incident particle charge and energy are high enough, the multiple Coulomb scattering could be negligible and the detector intrinsic resolution can be estimated also with this method.

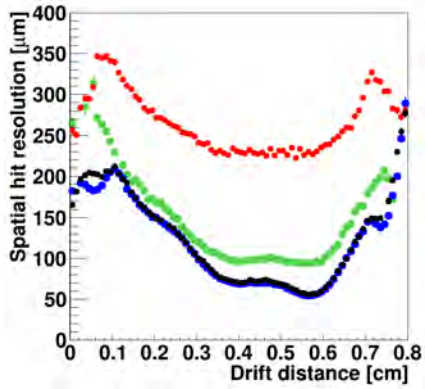

Figure 4.8: BM spatial resolutions as a function of the drift distance evaluated from MC simulations. In details, the results obtained with the BM track method for the protons at 80 MeV and the oxygen ions at 400 MeV/u are respectively shown by the black and the blue dots. The corresponding spatial resolutions calculated by the MST track method are represented by the red and the green dots.

Angular resolution

In order to evaluate the BM angular resolution, the difference between the BM track slope and the MST track slope on the two views perpendicular with respect to the beam direction is computed for each event. Then, the resulting residual distribution is fitted with a Gaussian and the sigma of the Gaussian can be considered as the BM angular resolution. The results for the experimental data taken with the 228 and 80 MeV protons indicates an angular resolution of 1.62 ± 0.16 mrad and 2.1 ± 0.4 mrad, respectively. Since the distance along the beam direction between the first and the last layer of parallel sense wires is of 13 cm, the angular resolution results are compatible with the spatial resolutions measured with the MST track method.

4.2.4 Beam transverse profile measurement

One of the goal of the BM is to measure the beam transverse profile during the data acquisition campaigns conducted with both the FOOT spectrometers. This operation is fundamental since the FOOT experiment needs to acquire the data with a low intensity beam of the order of few kHz and, at such low rate, the beam monitoring systems often available at accelerator facilities usually cannot measure the beam properties.

An example of the beam transverse profile reconstructed by the BM on the Trento proton beam with 80 MeV/u of kinetic energy is shown in the left panel of Fig.(4.9). As one can notice, the profile contains different empty straight lines arranged as a regular grid. This lines corresponds to the BM wire positions. Indeed, given the detector geometry, all the BM sense and field wires are aligned along the longitudinal coordinate. Thus, if the BM is placed along the beam line without any tilt, a primary particle that is ejected corresponding to a BM wire position will cross different wires until it is deviated from its straight path due to the multiple Coulomb scattering effect or to a nuclear interaction. As described by Eq.(1.12) in Sec.(1.2.3) and by the models

illustrated in Sec.(1.2.4), both the multiple Coulomb scattering and the nuclear interactions are enhanced if the target material density is higher. Since the wire material density ($\rho_{Al} \sim 2.6989\,g/cm^3$, $\rho_W \sim 19.3\,g/cm^3$) is much higher then the gas mixture density ($\rho_{Ar/CO_2} \sim 0.001662\,g/cm^3$), the two phenomena are enhanced for the particle that crosses the BM wires. The resulting effect is the generation of an empty area arranged as a grid in the beam transverse profile. Similar profiles have been measured also by the MST detector for the non tilted datasets acquired during the calibration test, confirming the cause of the empty zones. In addition, also the drop of efficiency at the cell border of the BM contributes to the creation of the blank areas in the beam transverse profile measured by the BM.

However, despite all these effects, the beam transverse profile can be measured without any inconvenience. In order to to check the BM performances, a study of the Trento beam spot size has been conducted to compare the BM outcomes with the results obtained by a characterization performed by other detectors [126]. In details, different datasets of 10^5 events have been acquired varying the beam energy from the minimum (70 MeV) to the maximum (228 MeV) with a step of about 20 MeV. For each dataset, the beam transverse profile has been reconstructed and fitted with a Gaussian. Then, the beam spot size is evaluated as the standard deviation of the distribution. The results obtained from the BM and the reference values are shown in the right panel of Fig.(4.9). In general, the BM estimates of the beam spot size are larger with respect to the reference values. The difference can be caused by different effects such as the multiple Coulomb scattering introduced by the FSC detector or the Gaussian fitting difficulties due to the blank areas. However, the general trend is reproduced and compared to the existing reference measurements [126], the differences are only of the order of 0.1 mm.

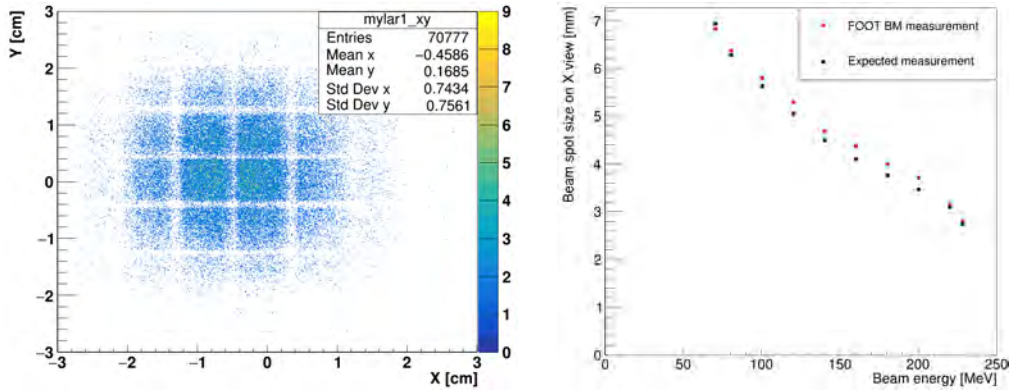

Figure 4.9: On the left, the beam profile of a 80 MeV proton beam measured by the BM. On the right, the spot size of the Trento protontherapy beam as a function of the incident particle energy measured by the BM and expected from [126]. The error bars are too small to be visualized.

4.2.5 Beam Monitor active area measurement

In principle, the BM active area is of $5.6 \times 5.6\,cm^2$, but the area in which all the twelve layers of cells are overlapped is of the order of $4 \times 4\,cm^2$. Due to the cell staggering, the outer border of the active area is covered only by three planes of cells. Since the minimum number of hits required to reconstruct a track is three per view and given the detector inefficiency at the cell border, a dataset with protons at 80 MeV with an extended

beam spot size has been taken to experimentally verify the BM total active area. This measurement is useful also for the emulsion spectrometer data taking, since the BM is adopted to measure the FOOT ECC irradiation pattern that has an extension typically of few square centimeters. In order to enlarge the beam spot, a layer of tantalum 2.5 mm thick has been placed at the nozzle exit. In this way, the beam is spread due to the MCS effect up to different square centimeters, exceeding the BM maximum active area. The beam profile measured by the detector is shown in Fig.(4.10). Thus, the detector active area is of about $4 \times 4\,\mathrm{cm}^2$. As one can notice from the y axis projection profile, outside this area, the number of tracks reconstructed by the BM drops drastically leading to a non reliable measurement.

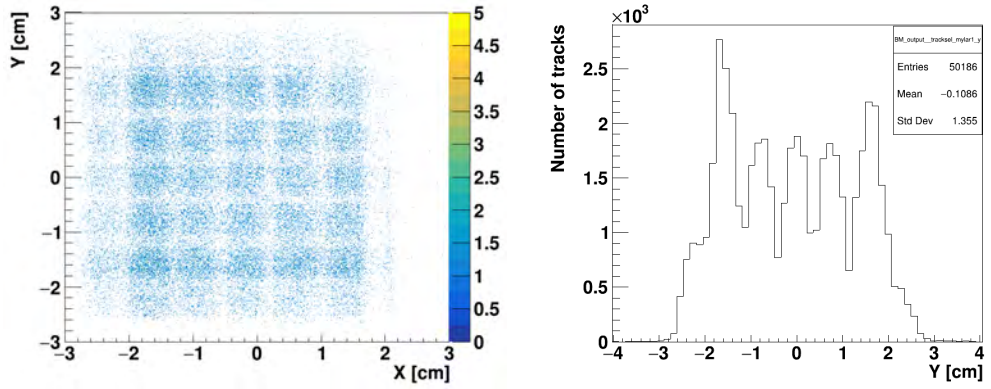

Figure 4.10: The two dimensional (left) and the y coordinate (right) beam profile measured by the BM on a dataset collected at the Trento protontherapy center with a 80 MeV proton beam spread by a layer of tantalum of 2.5 mm.

4.2.6 Calibration on the space-time relations by means of the Micro-strip Silicon detector

As described in Sec.(3.2.4), the BM track reconstruction precision completely relies on the space-time relations. If they are not properly estimated, the detector spatial resolution is heavily degraded. For this reason, a calibration of the BM space-time relations has been conducted by means of the MST detector using proton beams at 228 MeV and 80 MeV of kinetic energies.

In order to perform the calibration, each MST track is extrapolated into the BM cells calculating the drift distances that are defined as the distance of the tracks with respect to the center of the cells. If for the same event and the same cell there is a timestamp detected by the BM, the two measurements from the two detectors are coupled and they are adopted to fill a two dimensional plot that represents the distribution of the drift distances as a function of the time measurements. Then, a profiling procedure is performed: the MST drift distance plot associated to each time bin is fitted with a Gaussian distribution and the mean value is considered as the best estimate of the drift distance associated to the given time interval. Finally, the new space-time relations are obtained fitting all the drift distance best values. The two dimensional time-distance measurements plot and the result of the space-time relations calibration procedure are shown in the left panel of Fig.(4.11).

Since the FOOT experiment will collect data detecting particles more ionizing than

228 MeV protons, the entire calibration procedure has been repeated on the data collected with protons at 80 MeV to evaluate possible changes in the space-time relations. The difference between the relations measured with the 80 MeV and the 228 MeV protons is shown in the right panel of Fig.(4.11). Considering the same time interval, the drift distances measured for the low energy protons are larger with respect to the distances measured in the case of high energy protons. This effect can be explained by the different ionization density provided by the particles at different energies. As described by the Eq.(3.4) explained in Sec.(3.2.1), the number of ionization clusters produced by a particle in the gas medium is proportional to the particle dE/dx. For this reason, the 80 MeV protons have a higher number of ionization clusters and the mean distance between them is reduced with respect to the protons at higher energy. Thus, considering two particles with the same properties but different energies that cross a cell with the same track, the distance between the cell center and the closest ionizing cluster is shorter for the projectile with the lower energy. For this reason, the drift distance associated to a given time measurement is larger for the low energy-high ionizing particles. This effect is enhanced at the BM cell border where the electric field is reduced. In addition, also time-walk and time-jitter effects on the wire signal can play a role. However, the difference between the drift distances resulting from the space-time relations obtained at the two different proton energies is of the order of 35 ± 10 µm and 100 ± 13 µm for t$\leq$270 ns and t$>$270 ns, respectively. In both cases, considering also the BM inefficiency at the cell border, the difference is negligible for the BM track reconstruction purpose.

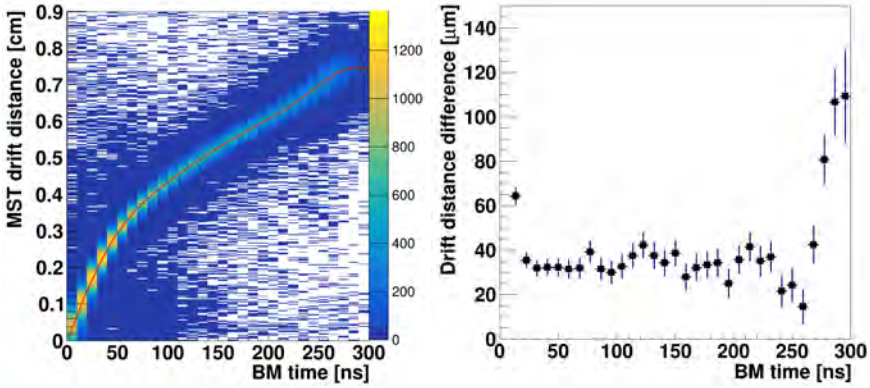

Figure 4.11: On the left, the two dimensional time-distance measurements plot obtained from the data collected with the 228 MeV protons. The new space-time relations fitted from this distribution is shown by the red curve. On the right, the difference between the space-time relations calculated from the data collected with protons at 80 MeV and 228 MeV. For each time bin, the error bar is given by the squared sum of the standard error of the mean of the two underlying space distributions.

4.2.7 Self calibration algorithm

Because of the electron drift velocity dependence on the reduced electric field as shown in Sec.(3.2.2), each BM dataset of measurements taken with a given HV value is related to a specific set of space-time relations. Since a proper calibration of the space-time relations by means of an external tracking detector is not always feasible, a self calibration algorithm has been developed to estimate the relations directly from the BM measurements. The methods, the performances and the limits of this algorithm are illustrated in the following paragraphs.

Self calibration method
The self calibration algorithm is an iterative method developed to optimize the space-time relations. As input, it requires only the BM time measurements of a dataset and a reasonable initial hypothesis of the relations. At each iteration, the method starts with the initial space-time relations converting the time measurements into a *measured drift distance* and performing the track reconstruction on the whole dataset. Then, for each hit selected by the Legendre polynomial method to fit a track, the algorithm proceeds calculating the distance between the track and the cell center, defining a *fitted drift distance*. In this way, it is possible to define a *residual* as the difference between the measured and the fitted drift distances. A drawing of a drift chamber hit, a fitted particle track and the residual between them is shown in the left panel of Fig.(4.12). Then, considering all the hits associated to a track and dividing them into different subsets of data depending on the time measurements, a plot of the residuals related to a given time interval can be filled. If the space-time relations are optimized, the residual distribution is symmetric and centered in zero. Otherwise, if the drift velocity is underestimated, the drift distance related to a given time measurement is underestimated and the residual distribution is centered towards negative values, since the fitted drift distances are larger then the measured ones. On the other hand, if the drift velocity is overestimated, also the measured drift distance is overestimated and the residual distribution is centered towards positive values. Thus, for each time interval, the sign of the mean value of the residual distribution indicates if the corresponding drift distance is underestimated or overestimated. The module of the mean value suggest the entity of the correction that has to be added or subtracted to the drift distance initial estimate. In addition, the standard deviation of the residual distribution measures the spatial resolution of the detector. An example of a residual distribution for a given time interval is shown on the right panel of Fig.(4.12). In this case, the measured drift distances are overestimated since the mean of the distribution is positive. A drawing of a hit with a positive residual is shown on the left panel of the same Fig.(4.12). After the fit of the residual distributions, taking into account their mean and standard deviation values, the algorithm provides a new set of space-time relations as output and evaluates the detector spatial resolution. Considering the new relations as input, a new iteration can be computed until the detector spatial resolution continues to improve.

The calibration algorithm is included in the SHOE reconstruction software and different tests have been conducted both on MC simulations and on experimental data. The results of this studies are illustrated in the following paragraphs.

Performances of the self calibration algorithm on MC simulations
In order to assess the performance of the algorithm, an appropriate mechanism has been developed within the SHOE software to include the possibility to calibrate the space-time relations also with the MC simulated data. Considering a set of space-time relations as the correct one (STC_{right}), the self calibration algorithm has been executed on the simulated data assuming two different initial hypothesis of space-time relations. In the first case, the initial hypothesis STR_{nc} has been set to be completely different from STR_{right}, as respectively shown by the magenta and the green curves of Fig.(4.13). In this case, the calibration algorithm does not converge since the reconstructed tracks are too different from the correct ones. In particular, the residual distributions show different peaks not correlated to the correct drift distance values and the fitting procedure can not be properly performed.

Instead, in the second case, the initial STR_0 hypothesis has been obtained modifying the STC_{right} with a transformation that maintains the shape of the correct relations. After

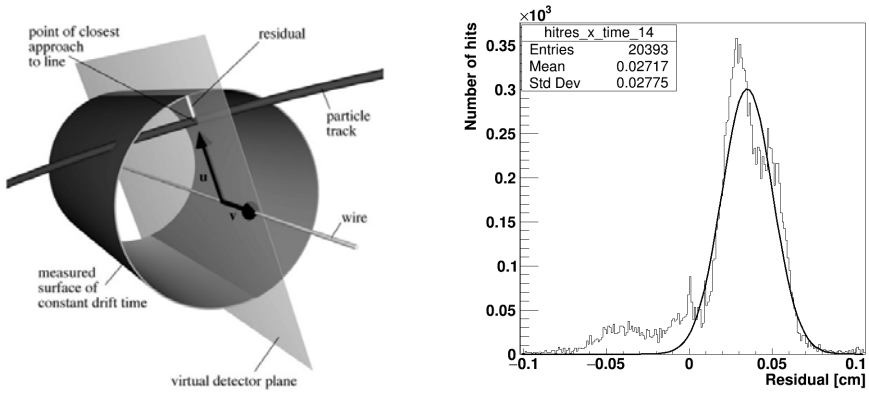

Figure 4.12: On the left, a picture of a drift chamber drift distance measurement with a fitted track and the corresponding residual. In this case the residual is positive since the measured drift distance is larger than the fitted drift distance extrapolated from the particle track. The picture is taken from [104]. On the right, an example of the residual distribution of the hits with a time measurement between 84 and 90 ns obtained using a set of space-time relations that needs to be calibrated. Also in this case, the mean value of the residual is positive indicating an overestimate of the drift distance associated to the given time interval.

few iterations, the output of the self calibration algorithm STR_5 approaches STR_{right} and, as shown in Fig.(4.13), further iterations (STR_{15}) does not change significantly the results. Even if STR_5 is similar to STR_{right} for almost all the time bins, at high time values the self calibration algorithm does not work properly and it underestimates the correct STR_{right}. This is particularly evident in the residual distributions of STR_5 presented in Fig.(4.14). The left panel of the figure shows the residuals associated to the hits with an intermediate drift distance. As one can notice, the mean value of the distribution is compatible with 0, meaning that the space-time relation is correct for this time bin. On the contrary, the right plot of Fig.(4.14) shows two distinct distributions both centered at values higher with respect to the correct one, that in this case has been estimated to be about -0.05 cm. This effect is an artifact introduced by the self calibration algorithm itself and, unfortunately, it is not avoidable. In particular, this is caused by the fact that the BM resolution at the cell border is worse with respect to the resolution in the central part of the cell, due to the diffusion effect illustrated in Sec.(3.2.5). Thus, the track reconstruction algorithm can provide a better estimate of the track parameters if the hits associated to the track do not have a high drift distance and, equally, a high time measurement. For this reason, the self calibration algorithm tends to assign to these hits a wrong value of drift distance. In this way, the hits are rejected by the track reconstruction and they cannot populate the residual distributions correctly. In addition, without the hits at the cell border, the resulting detector resolution is also apparently better. In principle, the same effect could happen also to the hits with a small drift distance since, as discussed in Sec.(3.2.5), the primary ionization statistics plays a non negligible role in the worsening of the spatial resolution close to the anode wire. However, since the space-time relations are bounded to start from the (0,0) point, this constraint helps to avoid the replication of the artifact also for the hits with a low time measurement. As a further verification, applying a fixed detector resolution instead of the real one that depends on the drift distance, the resulted STR_5 does not show the underestimate of drift distances at high time values. In addition, also the residual distribution associated to the hits with a high time value shows only one Gaussian distribution as the residuals associated to the other time intervals.

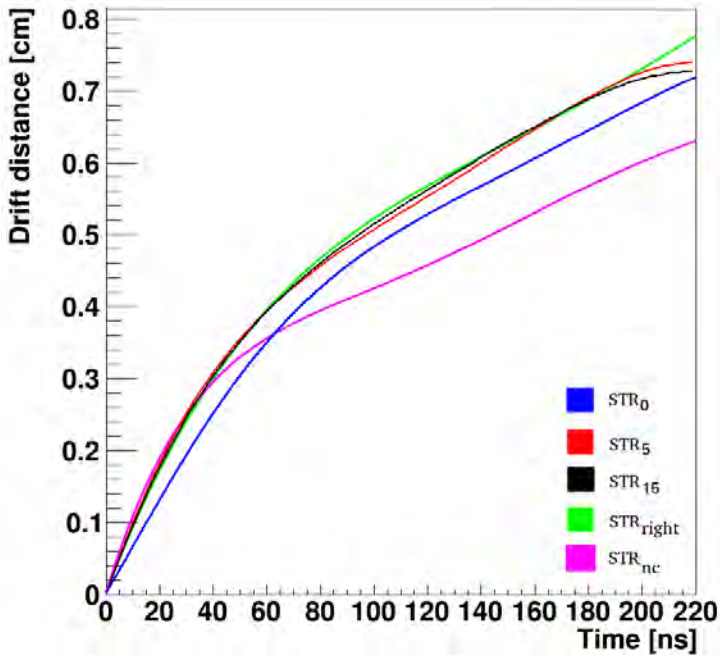

Figure 4.13: The STR curves adopted for the studies of the self calibration algorithm performed on MC simulated data.

Performance of the self calibration algorithm on experimental data
Given the properties of the self calibration algorithm studied by means of MC simulations, the algorithm has been adopted also on the experimental data collected in the calibration of the space-time relations by means of the MST detector, in order to compare the two results. As previously, the calibration procedure has been executed with two different starting STR hypothesis (STR_A and STR_B) that are shown in Fig.(4.15). In this case, both the calibration processes lead to the same result (STR_{CAL}). In both cases, the iteration stop is given when the detector mean spatial resolution starts to get worse rather than better. Indeed, after the optimal number of iterations, the artifacts explained in the previous paragraph start to increase significantly leading to the same effects presented during the MC studies. However, in this case the detector mean resolution starts to get worse after the correct number of iterations. In Fig.(4.15), also the space-time relations obtained from the calibration conducted by an external tracking detector is shown in red (STR_{MST}). The two curves associated to the two calibration methods are very similar since they are almost overlapped. The main differences are presented at the high time values, that correspond to the region in which the artifacts of the self calibration algorithm cannot be avoided.

Eventually, it is possible to conclude that the self calibration algorithm can be adopted to optimize the space-time relations directly from the BM experimental data, assuming that a reasonable initial hypothesis is provided. The algorithm performances are satisfactory, but different artifacts are present in the iteration procedure leading to an effect above all for the hits associated with a high time measurement. A calibration conducted by an external tracking detector is always preferable with respect to the use of the self calibration algorithm, but since it is not always feasible, this algorithm provides a valid

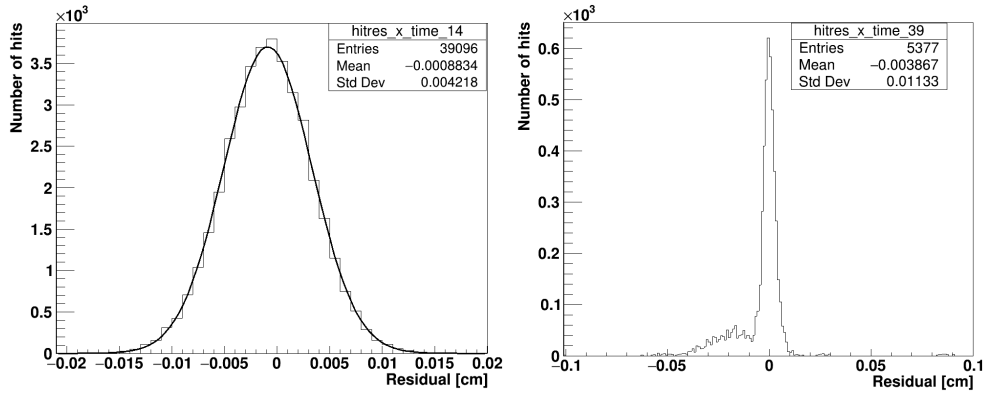

Figure 4.14: Residual distributions of the hits associated with a time interval of $70\,\text{ns} < T < 75\,\text{ns}$ (left) and $T > 200\,\text{ns}$ for the STR_5 evaluated on simulated data.

alternative.

4.3 Data taking for physics at GSI

The GSI is an international accelerator facility that can deliver beams of different ions, including unstable nuclei produced by fragmentation or fission of heavy projectiles. The field of research at GSI includes plasma physics, nuclear physics, biophysics and medical physics.

In the last few years, different data takings and test beams had been conducted by the FOOT experiment in the GSI facility using beams accelerated by the SIS-18 synchrotron both with the emulsion and with the electronic spectrometer. In the former case, the emulsion detector has been exposed to an oxygen ion beam at 200 and 400 MeV/u of kinetic energy, and a carbon ion beam with an initial kinetic energy of 700 MeV/u. In all the cases, the BM has been adopted to check the irradiation pattern prior and during the ECC exposure. The methods and the results of the BM and FSC measurements obtained during the oxygen ion campaign are illustrated in Sec.(4.3.1). In the latter case, the BM has been tested with different other detectors within the FOOT global DAQ with a 400 MeV/u oxygen ion beam. Details about the first FOOT electronic spectrometer test can be found in (4.3.2).

In addition, the BM has also been adopted to characterize the GSI 700 MeV/u carbon ion beam. The results about the beam transverse spot size and the beam rate has been published in a FOOT internal note [127] and are presented in Sec.(4.3.3).

4.3.1 Analysis for the emulsion spectrometer data taking

The emulsion spectrometer is the first FOOT detector that performed a data taking, starting to fulfill the experimental program shown in Sec.(2.2.1). As described in Sec.(2.3.2), the ECC detector is composed of different emulsion and passive material layers. The exposure of the ECC needs to be performed with a given total number of particles and a dedicated irradiation pattern. During the GSI data taking performed with oxygen ion beams at 200 and 400 MeV/u, the expected irradiation pattern consists of 25×25 spots delivered with a step of 1 mm, covering a total irradiated area of $2.4 \times 2.4\,\text{cm}^2$. The overall expected number of delivered particles is about 20000 and 15000, respectively for the

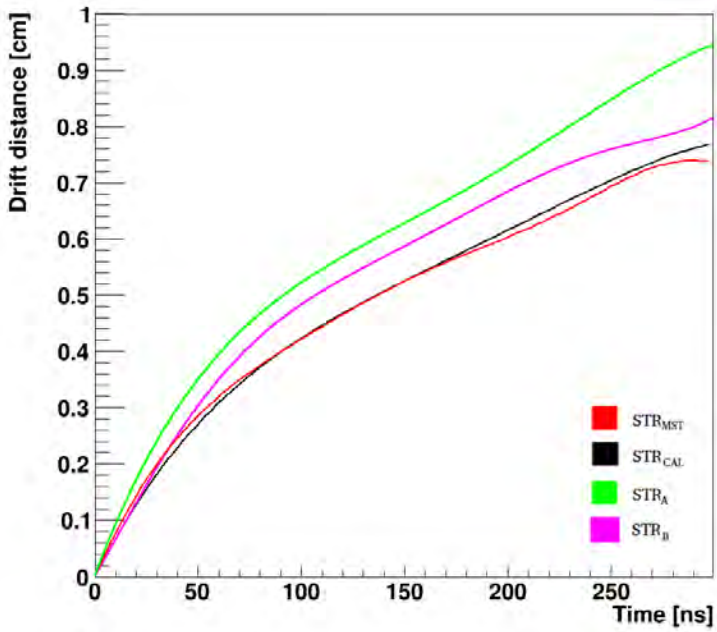

Figure 4.15: The STR curves related to the self calibration algorithm performed on the experimental data collected with 80 MeV protons.

two beam energies. Since the GSI beam monitoring system cannot measure precisely all the required characteristics of the irradiation pattern at the low intensity required by FOOT, the BM and the FSC detectors have been employed to verify the properties of the delivered beam prior the ECC exposure. A picture of the experimental setup is shown in Fig.(2.22).

First Start Counter and Beam Monitor acquisition preparation

In order to find a proper working point both for the FSC and the BM detector, different operations have been conducted prior the data acquisition. At first, the thresholds of the constant fraction discriminator adopted for the FSC readout channels have been set to a reasonable level over the background (few mV/50 Ω) and not beyond the signal peak values (up to hundreds of mV/50 Ω) exploiting the oscilloscope. In details, three channels have been set at 20 mV/50 Ω and one more noisy channel at 50 mV/50 Ω. Then, the trigger of the event has been set to be the majority of three out of four FSC signals to reject the background to a negligible level, as verified with the oscilloscope. Regarding the BM detector, the GSI gas distribution system provided a continuous flux of Ar/CO_2 gas mixture at 80/20%, with a flow rate of about 1 l/h and at a pressure of about 1 atm over the normal atmospheric condition. The threshold of the BM channels has been set to 20 mV/50 Ω, exploiting the oscilloscope as done with the FSC. The optimal HV setting has been found to be 1850 V.

Once the detectors working point has been fixed, the whole irradiation pattern has been delivered many times without the ECC detector. After the verification of the pattern correctness and the beam stability, the ECC bricks have been placed on the beam line and they have been irradiated. After the exposure, the emulsion layers have been transported to the laboratory to start the scanning and the analysis procedure illustrated

in Sec.(2.3.2).

Number of particles measurement
In order to count the total number of delivered particles, the FSC detector is connected to a scaler (CAEN V830) and a QDC (Charge to Digital Converter, CAEN V792). As described in Sec.(2.3.2), the former is adopted to count the number of trigger signals and the latter measures the total charge distribution of the particles detected by the FSC. Indeed, in principle there is the possibility that two or more particles cross simultaneously the detector generating only one trigger signal. The QDC measurement can identify these events and avoid miscalculations, since two or more particles would release a higher signal and a higher QDC measurement with respect to the single particle signal. However, as shown on the left panel of Fig.(4.16), the QDC measurements present only one clear distribution. Similar results are obtained also with the other FSC readout channels both for the 400 and the 200 MeV/u data. Thus, there is no multiple-counting effect in the fired triggers and the scaler measurement represents the total number of emitted primaries. The irradiation pattern has been delivered different times before the actual ECC exposure. The total counting measurements among the repetitions are shown in the right panel of Fig.(4.16). The expected total number of primaries was about 15000 and the measured particles is of about 14400 oxygen ions in most cases and about 15000 in the second to last repetition. In all the cases, the measured values satisfy the emulsion spectrometer requirements and the ECC has been exposed to the correct number of particles.

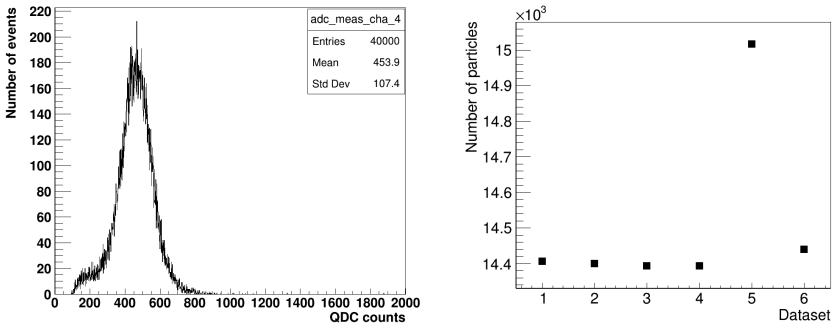

Figure 4.16: On the left, the charge distribution in arbitrary units of one of the four FSC readout channel measured by the QDC on a 400 MeV/u oxygen beam. On the right, the measurement of the total number of delivered particles among different irradiation pattern repetitions for the same particle beam.

Irradiation pattern measurement
While the FSC measures the total number of delivered particles, the BM is exploited to measure the extension and the overall spatial distribution of the irradiation pattern. The expected beam profile has an overall square area of about $2.4 \times 2.4\,\mathrm{cm}^2$. The irradiation pattern is expected to be delivered from the center of the square to the external following a spiral path, as drawn in Fig.(4.17) The BM measured beam profile projected on the ECC entrance window is shown on the left panel of Fig.(4.18). The mean X position of the distribution is not centered in zero due to a slight BM tilt on the vertical axis. On the contrary, the ECC detector has been carefully aligned along the beam line avoiding any kind of tilt or shift as much as possible. However, the total area of the delivered particles is of about $2.5 \times 2.5\,\mathrm{cm}^2$, fulfilling the ECC requirements. In addition, the beam

delivery has been completed starting from the center towards the external ring following the expected spiral pattern, as shown in the right panel of Fig.(4.18).

After the verification of the beam properties, the ECC detector has been exposed to the irradiation pattern and transported to the emulsion laboratory in Naples for the data analysis. A publication about the data collected in 2019 is in preparation.

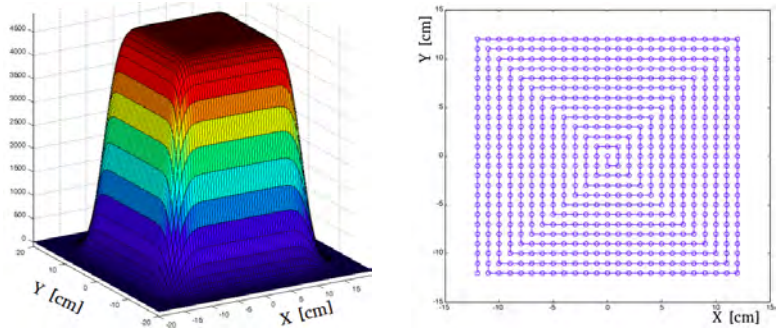

Figure 4.17: The designed irradiation pattern for the ECC data taking conducted at GSI with oxygen ions in three (left) and two (right) dimensions.

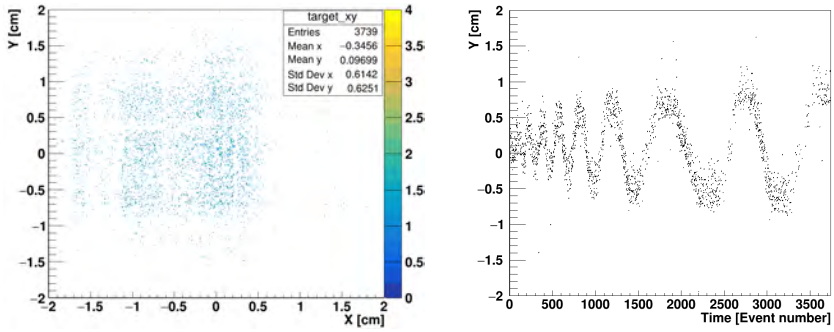

Figure 4.18: On the left, the profile of the 400 MeV/u oxygen ion beam irradiation pattern reconstructed by the BM and projected on the ECC detector entrance window. On the right, the same irradiation pattern position projected on the BM entrance window along an axis perpendicular to the beam as a function of the time.

4.3.2 Beam Monitor performances in the electronic spectrometer test

During the FOOT data taking campaign conducted at GSI, the first test of the electronic spectrometer has been completed with half of the whole experimental setup. In details, the experiment global DAQ and the trigger system described in Sec.(2.3.1) have been tested with a 400 MeV/u oxygen ion beam with the SC, BM, VTX and TW detectors. In addition, also a crystal of the calorimeter has been tested in a stand alone acquisition mode. Different datasets have been collected with and without a 5 mm thick target composed of graphite (0.915 g/cm^2).

A general scheme of the electronic setup adopted in this data taking is shown in Fig.(4.19). As one can notice, the BM has been tilted around the horizontal axis because a wedge with a thickness of 6 mm has been added under the detector structure, close to the entrance window. The rationale of this peculiar choice is given by the possibility

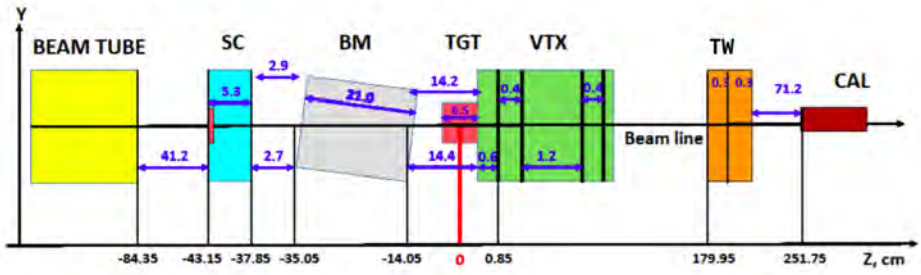

Figure 4.19: Scheme of the experimental setup adopted by the FOOT electronic spectrometer during the GSI 2019 test.

to calibrate the space-time relations with the VTX tracks as previously performed with the MST detector and, consequently, by the necessity to tilt the BM to spread the active area crossed by the beam. However, since the trigger signal derived from the SC and the TW WaveDAQ system was sampled by the general DAQ with a frequency of 100 Mhz, a time jitter of 10 ns has been introduced in the DAQ time resolution and, consequently, in the BM time measurements. Furthermore, due to a wrong firmware configuration of the VTX detector, the VTX track reconstruction efficiency was heavily reduced and no correlation has been found between the BM and the VTX tracks. Since the space-time resolution calibration with the VTX tracks is not possible, as a consequence of the time jitter issue, the BM performances obtained with the electronic setup are degraded. Indeed, the detector intrinsic resolution shown in the left panel of Fig.(4.20) is worse with respect to the results obtained during the performance assessment conducted in Trento and illustrated in Fig.(4.7). However, the BM is still able to reconstruct the beam profile that is shown on the right panel of Fig.(4.20).

On the contrary, the SC and the TW detector worked properly. Indeed, as shown in Fig.(2.24), the charge identification procedure is successfully achieved on the data collected with the target and a publication about integral cross section measurements is in preparation.

At present, all the issues related to the VTX functioning and the general DAQ time jitter should be resolved. In particular, the VTX has updated the right version of the firmware and it has already been successfully tested in a stand alone data acquisition test. Instead, the DAQ time jitter is reduced by sampling the trigger signal with a higher rate of 1 Ghz. In this way, the time resolution is of the order of 1 ns and it should be enough for the BM purposes. Both the BM and the VTX detectors will be tested in the next FOOT data acquisition campaign.

4.3.3 Characterization of the 700 MeV/u C beam at GSI

During the different data taking and test beams conducted at GSI, the FSC and the BM have also been adopted to characterize the 700 MeV/u carbon ion beam available at GSI. In this occasion, some of the BM channels experienced few difficulties. The main issue was given by one of the X view channels that has been damaged during a maintenance operation conducted few weeks before the data acquisition campaign. However, the damaged cell is placed in a very side position and it does not influence the detector performances. Indeed, considering a dataset collected in Trento with protons at 80 MeV, the number of hits detected in this cell is more than 20 times smaller then the hits read by a central cell. Moreover, the detector redundancy of layers further compensate the

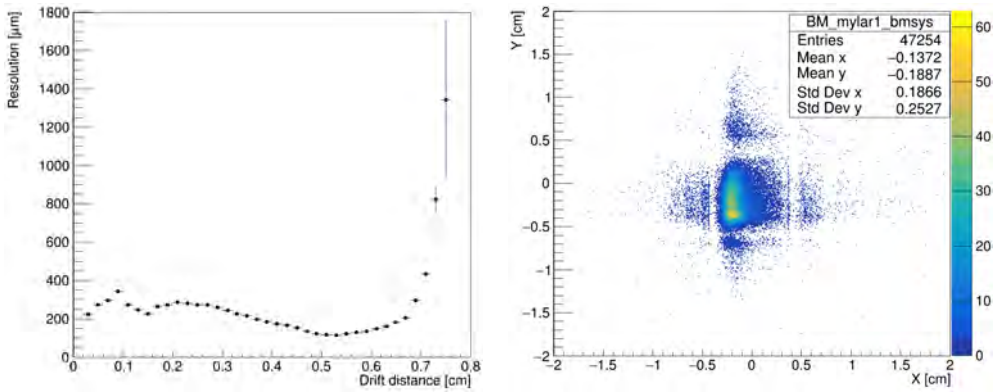

Figure 4.20: BM spatial resolution as a function of the drift distance (left) and the beam profile reconstructed by the BM (right) on the data collected with the electronic spectrometer DAQ system at GSI in 2019. The spatial resolution has been calculated with the BM track method, as described in Sec.(4.2.3).

deficiency. Since the recovery operation would take time and considering the almost negligible side effect of the accident, the replacement procedure has been postponed after the data taking.

The experimental setup consist of the FSC and the BM detectors as in the emulsion spectrometer setup shown in Fig.(2.22). The detectors has been placed in order to have the FSC centered on the beam isocenter position. The BM gas parameters were the same as the other data taking (Ar/CO_2 mixture at 80/20% flushed at about 1 l/h and with an over-pressure of 0.9 atm). The detector working point has been found to be at 1900 V. The corresponding hit distribution is peaked at 12 and the mean of the hit distribution is of about 11.84, as shown in Fig.(4.21).

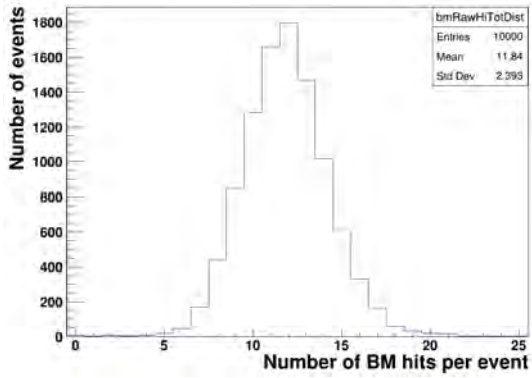

Figure 4.21: The BM hit distribution of the events collected in the data taking performed at GSI with a carbon ion beam at 700 MeV/u of kinetic energy.

In order to be prepared to a possible future data taking conducted by the FOOT electronic spectrometer in the same facility with similar beam requests, a low beam rate of few kHz has been asked to the beam delivery system to match the FOOT acquisition rate requirements. In addition, this beam rate matches also the BM acquisition rate of few kHz. The measurement of the beam rate distribution and the beam stability has been performed with the FSC detector. The results are shown in Fig.(4.22). In particular, the

mean beam rate is of about 2.4 kHz, but at such low intensity, different fluctuations in the beam rate has been detected. Figure (4.23) shows the beam transverse profile and the track angle distribution. Almost all the hits are measured by the BM central cells. The beam transverse spot size has a width of less than 0.2 mm of standard deviation and it is almost entirely contained in a cone of about $0.2°$, which matches the VTX detector active area.

In conclusion, all the beam parameters satisfy the FOOT electronic setup requirements. Indeed, GSI is one of the facility in which the FOOT experiment is expected to perform different data taking campaigns to fulfil the experimental program.

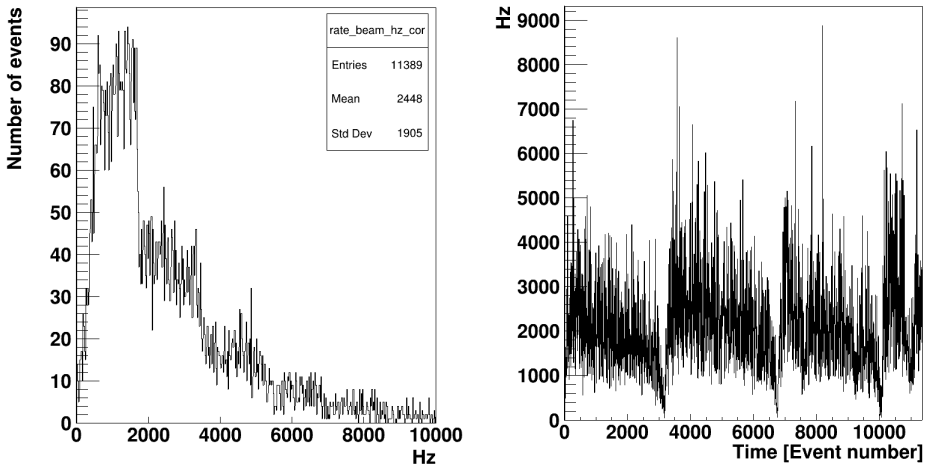

Figure 4.22: Beam rate distribution (left) and beam rate measurements as a function of the time (right) for the GSI 700 MeV/u carbon ion beam.

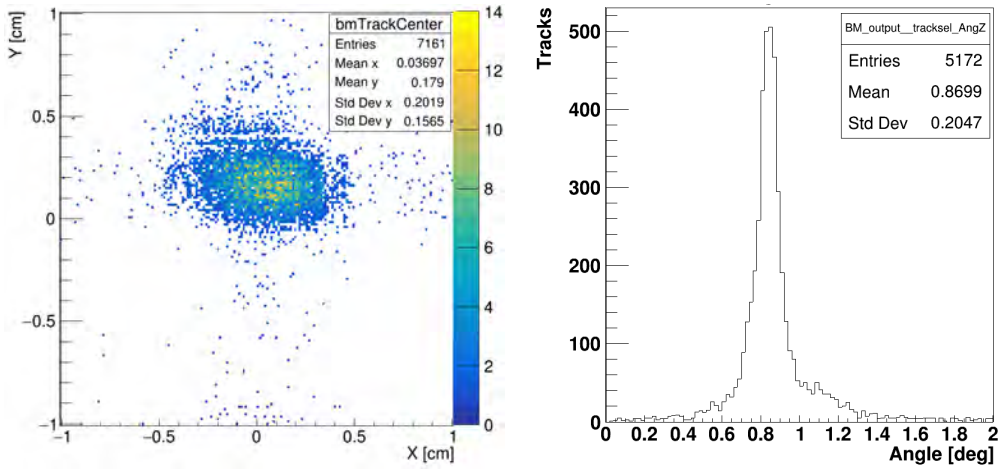

Figure 4.23: Beam transverse profile extrapolated on the BM entrance window (left) and track polar angles distribution (right) for the tracks reconstructed by the BM from the GSI 700 MeV/u carbon ion beam dataset.

CHAPTER 5

Analysis of the Beam Monitor performances

5.1 Introduction

In this chapter, the performances of the BM detector measured in different experimental data takings (see Sec.(4.2)) are studied to verify if they fulfil the FOOT experiment goals. Indeed, the BM is a fundamental detector of both the FOOT experimental setups. In particular, the beam monitoring system in the emulsion spectrometer setup is adopted to count the number of projectiles and measure the irradiation pattern distribution, as shown in Sec.(4.3). Instead, in the framework of the electronic spectrometer experimental setup, the BM has the goal to identify the pre-target fragmentation events and to measure the incident particle direction and impinging position within the target volume.

In the former case, the events with a nuclear inelastic interaction of the projectile in the SC or the BM represent a background since they can be misidentified as target fragmentation events. For this reason, they have to be rejected and different selection criteria have been studied to reach the purpose. The explanation and the performance assessment of the selection criteria are illustrated in the next section.

In the latter case, the BM track is used to match the VTX tracks in order to identify the position of the nuclear inelastic interaction of the projectile within the target material. In addition, the parameters of the track reconstructed by the BM are fundamental in the framework of the particle therapy target fragmentation measurements. Indeed, as explained in Sec.(2.2), in this case FOOT adopts an inversion of the kinematic approach to perform the cross section measurements. Since the parameters of the Lorentz transformation are derived from the direction of the projectile measured by the BM, the accuracy of the BM track reconstruction capability measured in Sec.(4.2) are propagated into the final cross section measurement. For this reason, a MC study has been conducted to analyze the impact of the BM spatial resolution on the cross section evaluations.

The theoretical aspects of the cross section and of the inverse kinematic approach is shown in Sec.(5.3), together with the results about the resolution of the cross section measurements given by the BM detector performances.

5.2 Rejection of the fragmented primaries before the target material effectiveness

One of the goal of the BM in the electronic spectrometer setup is to recognize and reject the events is which the primary particle fragmented before the target. Such events can occur when the projectile undergoes a nuclear inelastic interaction in the SC, in the BM itself or even in the different air gaps present between the nozzle and the target. In

order to estimate the fragmentation rates and to determine the proper selection criterion to flag these events with the BM measurements, a MC study has been performed on the data provided by means of the FLUKA simulation code. The MC estimates for the fragmentation rates are shown in the next subsection, followed by the description of the methods and the performances of the selection criteria conducted in Sec.(5.2.2)

5.2.1 Fragmentation rates

In order to evaluate the fragmentation rates of the primary particles in the FOOT upstream detectors, a MC simulation with a primary beam of carbon ion at 200 MeV/u has been performed by means of the FLUKA code with the SC, the BM and the target placed as in the FOOT electronic setup. In particular, the target has been designed as a 0.915 g/cm^2 thick disk composed of graphite. The results about the fragmentation rate of the primaries are shown in Tab.(5.1). The ratio between the number of events with a fragmentation before the target and the number of events with an inelastic interaction within the target is about $7.76 \pm 0.13\%$. Among the undesired fragmentation events, the SC and the BM give about the same contribution, while the inelastic interaction due to the air gaps is lower and it depends on the actual distance of the experimental setup with the beam nozzle. For this reason, the subsequent analysis is performed focusing on the events in which the projectile undergoes a nuclear inelastic interaction in the SC or in the BM. Different draws of pre-target fragmentation events are shown in Fig.(5.1) and Fig.(5.2), respectively for the interactions happened in the SC and in the BM. In addition, two examples of events in which the projectile interacts inelastically within the target volume are illustrated in Fig.(5.3).

Table 5.1: Material, density and projectile fragmentation rate of the FOOT upstream region detectors. The results are obtained from a simulation of carbon ions at 200 MeV/u impinging on a 0.915 g/cm^2 thick target composed of graphite. The errors are calculated assuming a Poisson statistics.

FOOT component	Material	Density (g/cm^3)	Fragmentation rate (10^{-4})
Start Counter	EJ228	1.023	12.37 ± 0.02
BM windows	mylar	1.4	3.01 ± 0.12
BM gas mixture	Ar/CO_2	0.0017	8.9 ± 0.2
BM wires	Al and W	2.7 (Al); 19.3 (W)	0.55 ± 0.05
BM overall			12.4 ± 0.2
Air gaps	atmospheric air	0.00129	3.45 ± 0.13
Target	C	1.83	364 ± 1

5.2.2 Selection criteria

In order to recognize the pre-target fragmentation events with the FOOT electronic spectrometer detectors, different selection criteria has been studied exploiting the BM measurements and the VTX tracks. The effectiveness and the performance of each selection criteria has been evaluated both on experimental data and MC simulations.

Number of Beam Monitor hits

A clean event in which the projectile reaches the target without any prior nuclear inelastic interaction leaves about 12-13 hits in the BM, depending on the detector working point and the projectile charge, mass and energy. As an example, the left panel of

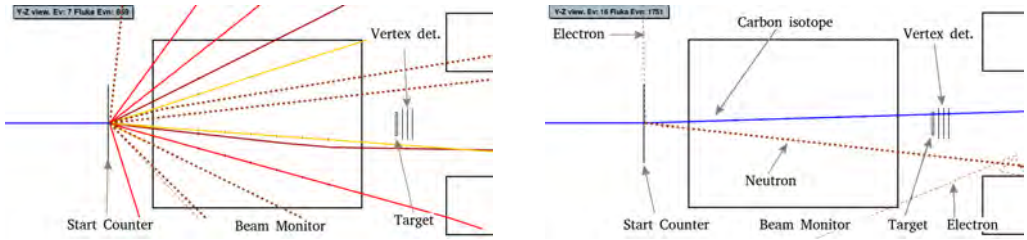

Figure 5.1: Two examples of events in which an incident carbon ion undergoes a nuclear inelastic interaction within the SC. In the first case on the left, the projectile fragmented in different protons (red), deuterons (dark red), helium ions (yellow) and neutrons (dotted), leaving a clear signature in the BM detector. In the second case on the right, the projectile emitted a neutron becoming a carbon isotope, leaving a signature in the BM and in the VTX detector similar to that of a non fragmented projectile. Both the pictures are derived from a FLUKA simulation output.

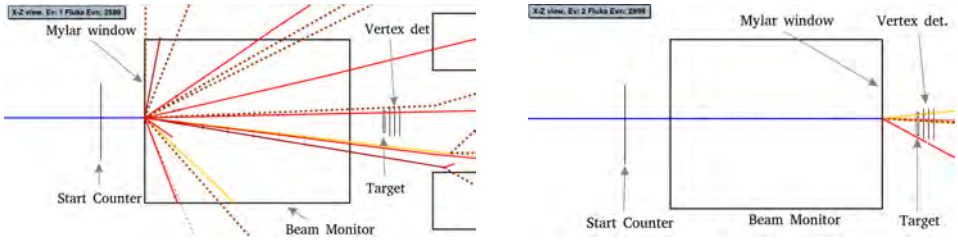

Figure 5.2: Two examples of events in which an incident carbon ion undergoes a nuclear inelastic interaction in the entrance and exit mylar window of the BM. In both cases the projectile fragmented generating different protons (red), deuterons (dark red), helium ions (yellow), and neutrons (dotted). Both the pictures are derived from a FLUKA simulation output.

Fig.(4.4) shows the hit distribution of a dataset collected from a proton beam at 80 MeV with the HV at 2200 V. In that case, since protons cannot break due to the low energy, the selection applied on the number of hits $10 \leq N_{\text{hits}} \leq 14$ was made to reject the events with δ-rays and cross talks. Considering the case of more ionizing particles such as oxygen ions, the sigma of the hit distribution is higher with respect to the case of protons due to the enhanced production of δ-rays. The number of hit distribution of the data collected at GSI with oxygen ions at 400 MeV/u is shown in the left panel of Fig.(5.4). In this case, a reasonable selection on the oxygen events is $8 \leq N_{\text{hits}} \leq 18$.

In case of events with the fragmentation of the projectiles in the SC or in the BM, the hit distribution is much more spread towards high values, due to the hits provided by the different particles generated by the primary. Both cases are illustrated in Fig.(5.4) obtained analysing MC simulations. In particular, a BM hit is counted if a charged ion crosses a BM cell with a track of at least 1 mm. In addition, also the BM TDC time resolution has been reproduced: for each event, a single cell can count multi-hits only if the time differences between hits is larger than 200 ps. Otherwise, only the hit with the smaller time measurement is counted. Both the MC distributions shown in Fig.(5.4) present a clear peak at 12 hits followed by a large amount of events characterized by a high number of hits detected by the BM. Thus, a selection criterion based on the number of BM hits can identify and reject a good part of the pre-target fragmentation events. Examples of these cases are shown on the left panel of Fig.(5.1) and Fig.(5.2).

Defining the *survival rate* as the fraction of events that passes a given selection criterion, the results obtained from the application of a cut with $8 \leq N_{\text{hits}} \leq 18$ on the

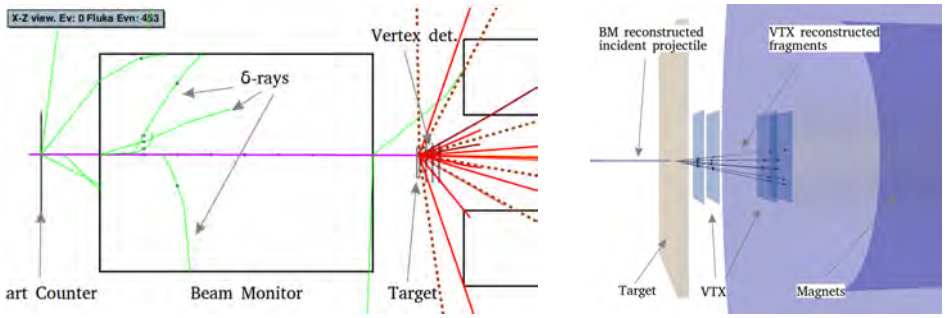

Figure 5.3: Two examples of events in which an incident projectile undergoes a nuclear inelastic interaction in the target. The former picture on the left is directly derived from the FLUKA simulation output. In this case, the incident oxygen ion produces different δ-rays (green) within the BM prior to be fragmented in the target, generating protons (red), deuterons (dark red) and neutrons (dotted). The latter case on the right is taken from the SHOE event display output of an other simulated event. In this case the BM reconstructed track is matched with the VTX fitted tracks identifying the fragmentation position inside the target volume.

different datasets are shown in Tab.(5.2). The impact of this selection on the experimental data is limited to a loss of about 5% of the events. Instead, the effectiveness of the cut on the SC and BM fragmentation simulations is much more relevant, respectively leading to a rejection of about 78% and 64% of the events.

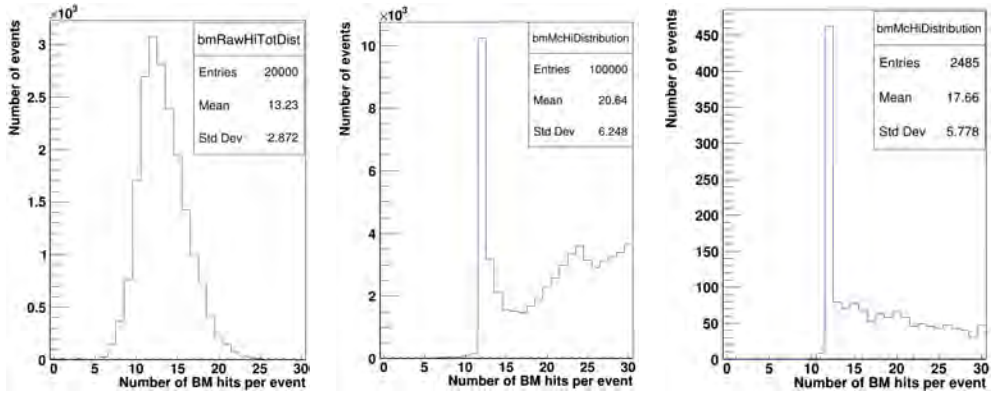

Figure 5.4: Hit distribution from a data taking conducted at GSI with a 400 MeV/u oxygen ion beam (left) and from MC simulations with the fragmentation of the projectile in the SC (center) or in the BM (right). The simulations are performed by means of the FLUKA simulation tool with an incident carbon ion beam at 200 MeV/u.

Number of Beam Monitor tracks

As described in Sec.(3.3.3), the fitting algorithm developed for the BM provides the multi-track reconstruction capability. Thus, a suitable selection criterion is given by the possibility to choose the events with only one track reconstructed by the BM ($N_{\mathrm{BMtracks}} = 1$). Indeed, if the BM reconstructs more than one track, it could be caused by the particles produced from the fragmentation of the projectile in the SC or the BM, by the detection of one or more δ-rays, by the presence of random aligned background hits or by a wrong set of space-time relations that divides the projectile hits into two distinct clusters in the Legendre space. The former case is the target of the selection criterion and it is one of

Table 5.2: Survival rates of the selection criteria applied on experimental data and MC simulations. MC data are simulated with a carbon ion beam at 200 MeV/u. The errors are calculated assuming a Poisson distribution.

Dataset	$8 \leq N_{\text{hits}} \leq 18$	$8 \leq N_{\text{hits}} \leq 18$ + one BM track	$8 \leq N_{\text{hits}} \leq 18$ + one BM-VTX track
80 MeV Protons (experimental data)	0.963 ± 0.007	0.927 ± 0.007	no data
400 MeV/u Oxygen ions (experimental data)	0.945 ± 0.007	0.790 ± 0.006	no data
SC fragmentation (MC simulation)	0.2204 ± 0.0015	0.1771 ± 0.0013	0.1548 ± 0.0012
BM fragmentation (MC simulation)	0.356 ± 0.012	0.322 ± 0.011	0.124 ± 0.007

the reason for the development of a multi-track reconstruction algorithm. All the other cases represent a loss of efficiency in the application of the selection criterion. However, as illustrated in Sec.(3.2.1), δ-rays are produced mainly perpendicularly with respect to the incident particle track and their directions are completely randomized after just few collisions. For this reason, considering also the low ionization density of the electrons and the BM geometry developed to detect longitudinal tracks, it is very difficult for the BM to reconstruct a δ-ray. Also the combinatorial background derived from the presence of aligned background hits is at a negligible level, if a proper cut on the number of hits has been previously applied. Regarding the space-time relations, if they are not properly calibrated, they could prejudice all the detector performances, including the spatial resolution and the track reconstruction capability. However, as illustrated in Sec.(4.2.7), the BM self-calibration algorithm or a calibration performed by means of an external detector should provide a reliable set of space-time relations. The overall survival rates given by the application of both the selection criteria on the experimental and simulated data are shown in Tab.(5.2).

The overall efficiency of the N_{hits} and N_{BMtracks} selection criteria evaluated on the proton data is of about 93%. Only 3% of the events has been eliminated by the cut on the number of BM tracks. On the contrary, the percentage of the surviving events for the oxygen data collected at GSI is about 79%. In this case, the N_{BMtracks} reduced the dataset of about $\sim$15.5%. The reason of the diversity between the results obtained on the two experimental datasets can be found in the efficiency loss mechanisms aforementioned. Indeed, the number of δ-rays generated by an oxygen ion is higher with respect to the number of δ-rays produced by a proton due to the energy loss contribution of Eq.(3.4) that is combined with Eq.(3.5). The enhancement of δ-rays production in the oxygen ion events leads to an increase of the BM background hits and, consequently, also to an increment of the combinatorial background. In addition, the tracks reconstructed from the proton data take advantage of the space-time relations calibration performed by means of an external tracking detector.

The rejection of the events with a projectile fragmentation in the SC and in the BM is respectively of the order of 82% and 68%. The latter result is worse with respect to the former case due to the fact that the fragmentation of the projectile can occur in the final part of the BM, leaving in the detector the same signature of the non-fragmentation events. An example is shown in the right panel of Fig.(5.2). However, in such cases, the VTX detector placed beyond the target can identify and reject the event.

Beam Monitor and Vertex detector tracks matching
Considering the events in which the projectile undergoes a nuclear inelastic interaction in the SC, the charge and angular distributions of the secondaries emitted from the SC is shown in Fig.(5.5). As one can notice, light fragments are emitted with a wider angular spread with respect to heavy particles, having a higher probability of not being detected by the BM due to the detector angular acceptance. The beam transverse profile and the charge distribution of the events that pass all the BM selection criteria are shown in Fig.(5.6). The main amount of particles are represented by the carbon and boron isotopes. As shown in Fig.(5.5), these fragments are emitted with a small tilt with respect to the initial beam direction, due to their high mass values. For this reason, also the beam profile and the signature of these events in the BM are almost identical to those of the non fragmented projectiles.

In order to further reject these events, an other selection criterion can be applied exploiting the VTX detector. In particular, an event can be rejected if the VTX cannot reconstruct a track due to the detector sensitive area, or if it reconstructs two or more tracks that do not point to the same position in the target material. In this case, considering the number of SC fragmentation events in which $8 \leq N_{hits} \leq 18$ and only one track is reconstructed both by the BM and the VTX detector, the fraction of passing events decreases from 0.1771 ± 0.0013 to 0.1548 ± 0.0012. This fraction represents the amount of events in which the projectile undergoes a nuclear inelastic interaction in the SC and that cannot be identified neither by the BM nor the VTX. An example of these events is shown in the right panel of Fig.(5.1).

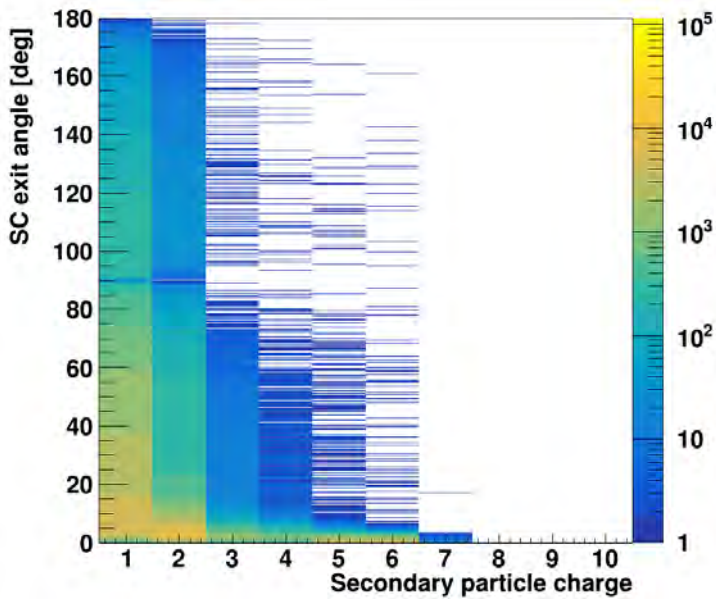

Figure 5.5: Charge and angular distribution of the secondaries emitted from the SC. Data generated from a MC simulation performed with a carbon ion beam at 200 MeV/u of initial kinetic energy.

The left panel of Fig.(5.7) shows the charge distribution of the particles generated from the fragmentation of the projectile in the BM, for the events that pass all the BM selection criteria. Differently with respect to the previous SC fragmentation events, in this case there is a large contribution derived from protons and helium ions. This is

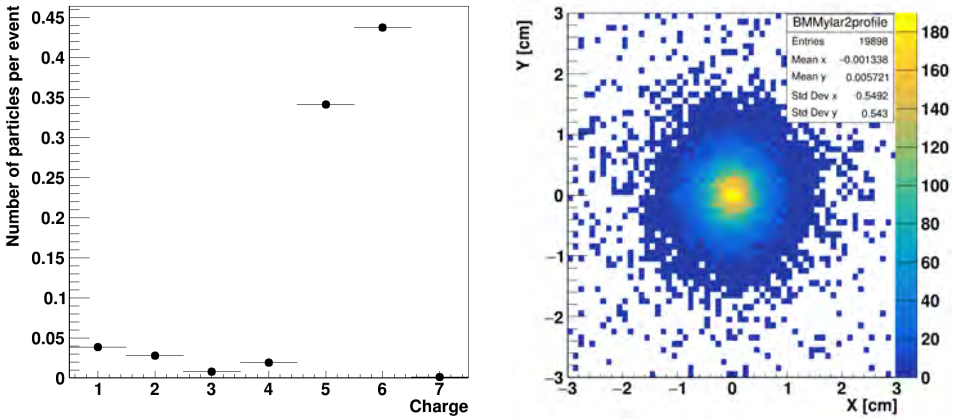

Figure 5.6: Secondary particle charge distribution (left) and beam profile projected on the BM exit window (right) of the events in which the projectile fragmented in the SC and the BM reconstructed only one track passing all the BM selection criteria. The events are derived from a MC simulation with an initial carbon ion beam at 200 MeV/u.

because they can be produced in the final part of the BM without leaving any signature in the detector. However, as in the previous case, also in this case it is possible to apply an additional selection criterion accepting the events with only one track in the VTX detector. In this way, a good fraction of events with the generation of light fragments are rejected, since a good amount of protons and helium ions can be detected by the VTX. The charge distribution of the secondaries that cross the VTX after the application of the BM and the VTX selection criteria is shown in the right panel of Fig.(5.7). After the cut on the number of VTX tracks, the fraction of events with a nuclear inelastic interaction of the primary in the BM that cannot be recognized drops from the previous 0.322 ± 0.011 up to 0.124 ± 0.007.

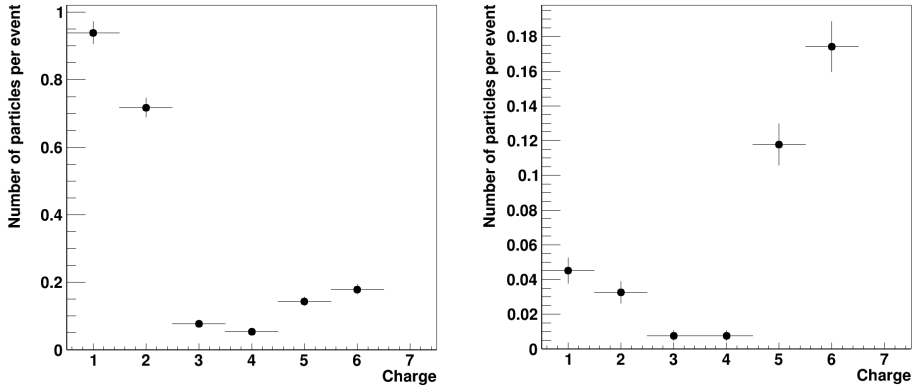

Figure 5.7: Charge distribution of the particles that cross the VTX detector and pass the BM selection criteria with (left) and without (right) the requirement of a single track in the VTX. The events are derived from a MC simulation with an initial carbon ion beam at 200 MeV/u.

The overall background contribution of the SC and BM fragmentation events can be evaluated combining the fragmentation rates illustrated in Tab.(5.1) with the results about the pre-target fragmentation rejection capability shown in Tab.(5.2). Considering

the events in which the projectile undergoes a nuclear inelastic interaction in the SC, the multiplication of the SC fragmentation rate ($12.37 \pm 0.02 \cdot 10^{-4}$) with the rate of the events that pass all the selection criteria (0.1548 ± 0.0012) represents the amount of SC fragmentation events that can be misidentified as target fragmentation events ($1.91487 \pm 0.018 \cdot 10^{-4}$). The same calculation performed on the events with a nuclear inelastic interaction in the BM gives as result $1.54 \pm 0.11 \cdot 10^{-4}$. Finally, the relative contribution of the pre-target fragmentation background can be evaluated as the ratio of the misidentified events over the total number of selected events.

In conclusion, about $0.493 \pm 0.006\%$ and $0.40 \pm 0.03\%$ of the fragmentation data collected by the FOOT electronic spectrometer are derived from events in which the projectile has fragmented respectively in the SC and in the BM instead of the target. Since the required accuracy of the FOOT differential cross section measurement is of the order of 5% and 10% respectively for the particle therapy projectile and target fragmentation effects, the obtained results are satisfactory for the FOOT goals.

5.3 Impact of the Beam Monitor performances on the inverse kinematic reconstruction

The BM is a detector adopted in all the FOOT data measurements, both for the emulsion and for the electronic spectrometers. However, among the different data taking campaigns planned over the years, the precision of the BM reconstructed tracks is relevant above all for the measurements related to the proton therapy target fragmentation effect. Indeed, in this case the FOOT experiment have to adopt an inverse kinematic approach to overcome the difficulties related to the detection of the fragments. As described in Sec.(2.2), the differential cross section measurements can be evaluated switching the role of the projectile and the target material atoms. In this way, the fragments derived from the interactions of oxygen or carbon ions on C or C_2H_4 targets are produced with a higher kinetic energy with respect to the previous direct kinematic approach, allowing the measurement of the fragments by means of the FOOT detectors. Since the inversion of kinematics completely rely on the track reconstructed by the BM, the main requirements on the BM performances are derived from this set of measurements. The performance assessment of the BM has been completed in a test beam conducted at the Trento protontherapy facility employing an external tracking detector, as illustrated in Sec.(4.2). The impact of the BM measured performances on the FOOT final cross section measurements are investigated in this section using a simulated dataset provided by means of the FLUKA MC code. In this way, the systematic uncertainty present in the FOOT measurements and derived from the BM has been estimated.

In particular, the methods adopted by the FOOT experiment to measure the differential cross sections are presented in the next subsection. Then, the mathematical formulation of the Lorentz transformation and the measurements involved in the particular case of the FOOT experiment is shown in Sec.(5.3.2). Finally, the evaluation of the impact of the BM spatial resolution on the cross section measurement accuracy are illustrated in Sec.(5.3.3)

5.3.1 Cross section measurement method

Given a particle species, the mathematical expression of the differential cross section measurement as a function of the energy ($d\sigma/dE$) is:

$$\frac{d\sigma}{dE} = \frac{\Delta\Omega}{4\pi} \cdot \frac{Y(E)}{N_p \cdot N_t \cdot \Delta\mathrm{E} \cdot \epsilon_{\mathrm{reco}} \cdot \epsilon_{\mathrm{id}} \cdot \epsilon_{\mathrm{phy}}} \tag{5.1}$$

Details about the meaning and the methods adopted by the FOOT experiment to measure all the terms contained in Eq.(5.1) are listed:

- $\boldsymbol{\Delta\Omega}$: is the angular acceptance considered for the cross section measurement.
- $\boldsymbol{Y(E)}$ **:** is the fragment yield as a function of the energy. Since the measurement of the particle energy is subject to the effects arisen by the detectors and the reconstruction algorithm, an *unfoldig* procedure is conducted to take into account and correct the measured values in order to extract the right ones. In details, the particle energy measurements **y** can be correlated to the real energy values **x** with the correction matrix **A**:

  $$\mathbf{y=Ax} \tag{5.2}$$

  The **A** matrix contains all the information about the experimental effects present within the measured data. It can be evaluated by means of MC simulations if all the parameters of the detectors (resolution, threshold etc.) are taken into account in the simulated data. Indeed, this is what is performed within the FOOT reconstruction software SHOE, as described in Sec.(2.5.2). Thus, ones the correction matrix **A** is evaluated associating the simulation true values with the SHOE reconstructed output, the unfolding matrix **A** of Eq.(5.2) can be inverted and the real values **x** can be extrapolated from the measurements **y**:

  $$\mathbf{x=A^{-1}y} \tag{5.3}$$

  However, the calculation and the inversion of the unfolding matrix is a complex operation that requires the use of different advanced statistics tools. Further details about the unfolding procedure can be found in [128].

- $\boldsymbol{N_p}$ **:** is the number of incident primary particles. In the FOOT electronic spectrometer setup, the data collected with the minimum bias trigger shown in Sec.(2.3.1) are adopted to calculate the particle fragmentation rate and, hence, to evaluate N_p. Instead, for the emulsion spectrometer setup, N_p is simply the number of particles delivered by the accelerator with the irradiation pattern. This value is measured by the FSC detector, as shown in (4.3.1). However, in both cases there are different sources of systematic uncertainties that have to be considered and evaluated (e.g.: the efficiency of the minimum bias trigger and the efficiency of the FSC detector).
- $\boldsymbol{N_t}$ **:** represents the number of particles per unit surface within the target. It can be calculated with the target parameters as following:

  $$N_t = \frac{\rho \cdot N_A \cdot \delta z}{A} \tag{5.4}$$

  where ρ is the target density, N_A is the Avogadro's number, δz is the target thickness and A is the mass number of the target material.

- $\boldsymbol{\Delta E}$ **:** is the energy phase space factor, defined as the width of the yield distribution bin associated to the given cross section bin.

- ϵ_{reco} **:** is the track reconstruction efficiency. As described in Sec.(2.5.2), at the moment there are two distinct algorithms, both based on Kalman filter, in development within the FOOT analysis software SHOE to reconstruct the whole track of a fragment. The performances and the efficiencies of these algorithms are evaluated by means of MC simulations.

- ϵ_{id} **:** is the particle charge and mass identification efficiency. In order to estimate this quantity, a full MC simulation is adopted to compare the "MC truth" with the reconstructed particle properties. The latter is derived from the charge and mass identification methods described in Sec.(2.4.2) that take as input the single detector reconstructed quantity. In this way, a *mixing matrix* can be computed and ϵ_{id} can be extrapolated.

- ϵ_{phy} **:** is the efficiency related to the physics effects that prevent a correct reconstruction of the fragments. As an example, it takes into account the geometrical acceptance of the FOOT apparatus, considering the fraction of particles emitted and deviated by the magnetic field outside the angular acceptance of the detectors. It includes also the cases in which a fragment undergoes a secondary nuclear inelastic interaction before the calorimeter.

  As for the previous efficiency factors, also in this case ϵ_{phy} is evaluated by means of MC simulations. In particular, given a fragment charge and mass for which the cross section needs to be calculated, an ad-hoc simulation is performed with the particle emitted from the target material towards the FOOT downstream detectors with different initial angles and energies. Then, an efficiency matrix can be computed filling each energy-angle bin with the ratio of the number of particles that reaches the scintillator and the calorimeter over the number of emitted particles with the given energy and angle. Once the matrix is filled, each bin of the fragment yield $Y(E)$ measured on the experimental data can be weighted with the associated bin of the efficiency matrix in order to calculate the correct cross section value.

Considering the methods adopted to estimate all the efficiencies included in Eq.(5.1), it is clear that both the detector simulation and the MC total cross section evaluation must be reliable to obtain solid results. Indeed, in the former case, all the detector performance assessment parameters collected in the different dedicated data taking campaigns are included within the SHOE reconstruction software. As an example, the BM efficiency, spatial resolution, hit distribution and all the other measured parameters shown in Sec.(4.2) are reproduced in the simulated data, as described in Sec.(2.5.2). This is necessary to ensure a reliable measurement of ϵ_{reco} and ϵ_{id}. In the latter case, the accuracy of the MC simulated data is necessary to measure ϵ_{phy}. The benchmark of the FLUKA total cross section estimates has been completed with different data takings conducted over the years. As shown in Fig.(5.8), the experimental values of the total cross section measurements for the particles at the energies involved in the particle therapy are compatible with the FLUKA simulations. Indeed, the goal of the FOOT experiment is to perform the measurement not of the total, but of the differential cross sections that are not sufficient for the current medical and physics applications.

In addition to the measurement of the efficiency terms, also their systematic uncertainties have to be estimated. As an example, the particle charge identification depends

on the parameters of the function expressed in Eq.(2.3) and shown in the left panel of Fig.(2.24). Thus, the uncertainty on the parameters of the function represents a systematic uncertainty on the final cross section measurement. An other example is provided by the mixing matrix adopted to measure ϵ_{id}. Indeed, since the matrix is computed with a limited statistics, also this statistical uncertainty have to be propagated as a systematic uncertainty on the final cross section measurement. Further examples about the systematic uncertainties and the methods adopted to estimate them can be found in [129].

The main component of the cross section formula shown in Eq.(5.1) is the fragment yield $Y(E)$. In the case of the target fragmentation cross section measurement, the yield of the particles needs to be estimated in the system of reference of the projectile. Thus, at first the energy of the fragments are measured in the laboratory frame. Then, the inversion of the kinematics is performed with the BM measurement of the projectile direction. The mathematical aspects involved in the inversion of the kinematics and the specific case of the FOOT measurements are illustrated in the next subsection.

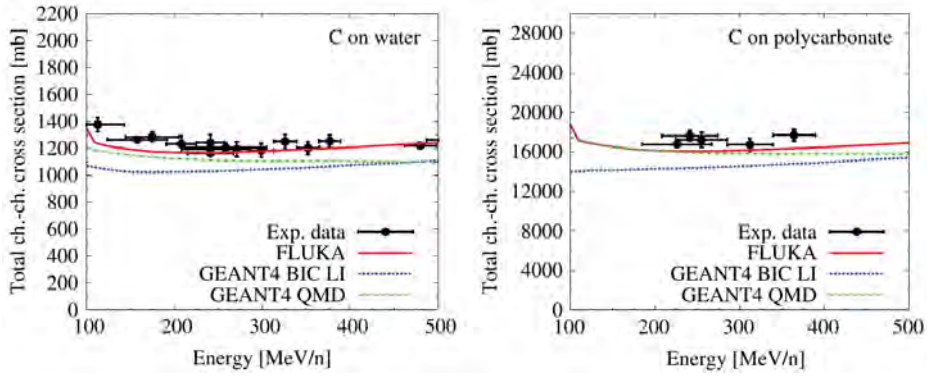

Figure 5.8: Total charge changing cross sections of carbon ions interacting with water (left) and polycarbonate ($C_{16}H_{14}O_3$, right) evaluated both from experimental measurements and MC simulations performed by means of different MC codes [130].

5.3.2 Mathematical formulation and application of the inverse kinematic approach in the framework of the FOOT experiment

The inversion of kinematics approach adopted in the FOOT experiment consists in the change of the system of reference from the laboratory frame to the projectile (or patient) frame. Given the relativistic velocity of the incident particles, the theoretical formulation is derived by the *Lorentz transformation*.

Lorentz transformation

Considering $A^{\mu}=[a^0, a^1, a^2, a^3] = [a^0, \vec{a}]$ as a generic Lorentz covariant four-vector measured in the laboratory frame S, where a^0 is the temporal component and $\vec{a}$ represents the three-component space vector, the Lorentz transformation is defined as the transformation that allows to retrieve the four-vector A'^{ν} measured in a different inertial system of reference S':

$$A'^{\nu} = \Lambda^{\nu}_{\mu} A^{\mu} \tag{5.5}$$

where Λ^{ν}_{μ} is defined as the *Lorentz tensor*. The Einstein notation is adopted to sum over the repeated indices and each tensor index run over 0, 1, 2 and 3. Considering the case

of a general boost $\vec{\beta} = (\beta_1, \beta_2, \beta_3)$ of the frame S' with respect to the frame S, the explicit form of the Lorentz tensor can be calculated applying the Lie theory and the result is [131]:

$$\Lambda(\vec{\beta}) = \begin{pmatrix} \gamma & -\gamma\beta_1 & -\gamma\beta_2 & -\gamma\beta_3 \\ -\gamma\beta_1 & 1 + \frac{(\gamma-1)\beta_1^2}{\beta^2} & \frac{(\gamma-1)\beta_1\beta_2}{\beta^2} & \frac{(\gamma-1)\beta_1\beta_3}{\beta^2} \\ -\gamma\beta_2 & \frac{(\gamma-1)\beta_1\beta_2}{\beta^2} & 1 + \frac{(\gamma-1)\beta_2^2}{\beta^2} & \frac{(\gamma-1)\beta_2\beta_3}{\beta^2} \\ -\gamma\beta_3 & \frac{(\gamma-1)\beta_1\beta_3}{\beta^2} & \frac{(\gamma-1)\beta_2\beta_3}{\beta^2} & 1 + \frac{(\gamma-1)\beta_3^2}{\beta^2} \end{pmatrix} \tag{5.6}$$

where $\gamma = \frac{1}{1-\beta^2}$ and $\beta^2 = \beta_1^2 + \beta_2^2 + \beta_3^2$.

The inverse kinematic approach applied to the FOOT experiment

The goal of the FOOT experiment is to detect and reconstruct the four momenta of the fragments in the laboratory frame and convert the measurements into the projectile frame, using the formula expressed in Eq.(5.5). In order to complete the task, the boost $\vec{\beta}$ of the projectile frame presented in Eq.(5.6) have to be estimated event per event. The BM detector can measure the direction of the incident particles, providing two out of three of the required parameters. Indeed, the module of the boost cannot be measured event per event neither by the BM nor by one of the other FOOT detectors. However, the projectile mass (m) and the particle initial total energy (E) are controlled by the accelerator facility and they are known parameters. Thus, all the components of the projectile four momentum $P = (E/c, \vec{p}) = (E/c, m\gamma\vec{\beta}c)$ can be reconstructed using also the conservation law $E^2 - p^2 = mc^2$. Once the boost $\vec{\beta}$ of the projectile is retrieved, the inversion of the kinematics can be applied on the fragments four momenta with the Eq.(5.5) and $\Lambda(-\vec{\beta})$.

As an example, considering a simulation with a primary beam of oxygen ions at 200 MeV/u of initial kinetic energy ejected along the z axis direction, the corresponding boost between the projectile and the laboratory frame is of the order of $\vec{\beta} \sim (10^{-3}, 10^{-3}, 0.6)$. The energy distribution of the fragments produced in the laboratory and the projectile frame is respectively shown in Fig.(5.9) and Fig.(5.10). As expected, in the former case the energy distributions have a peak around the projectile initial kinetic energy. Instead, in the latter projectile frame case, all the fragments have a kinetic energy of the order of few MeV/u. This is the reason why the angular dependence of the particles is not investigated: the particle range associated to such small values of kinetic energy is of the order of few µm, thus the effect of the angular spread of the fragments on the dose deposition calculation is negligible.

5.3.3 Impact of the Beam Monitor performances on the cross section measurements

Since the inversion of the kinematics depends on the accuracy of the projectile direction measurement, the results of the BM performance assessment conducted at the Trento protontherapy facility and shown in Sec.(4.2) can be adopted to estimate the resolution of the final cross section measurement due to the BM track reconstruction precision. In order to achieve this goal, a full FOOT simulation has been conducted by means of the FLUKA software with an initial oxygen ion beam at 200 MeV/u impinging on a target of graphite. The differential cross section has been estimated for the ^{12}C fragments emitted with $\theta \leq 0.186$, which is the angular acceptance of the TW detector. The inversion of the kinematics has been performed using both the "MC truth" and the BM reconstructed

track to check the differences obtained on the results. Applying the expression illustrated in Eq.(5.1), the track reconstruction efficiency (ϵ_{reco}) and the particle identification efficiency (ϵ_{id}) has been set to 1, since the aim of this study is to evaluate the accuracy of the cross section measurement given only the BM spatial resolution contribution. For the same reason, also the unfolding procedure that should be performed on the fragments yield has not been executed. Thus, all the parameters related to the fragments (energy, charge, mass and track direction) are directly taken from the "MC truth". All the other terms necessary to evaluate the differential cross section have been estimated as described in Sec.(5.3.1). The final cross section measurement is shown in the left panel of Fig.(5.11). The results obtained with the inversion of the kinematics performed applying the "MC truth" and the BM reconstructed track are compatible. No relevant differences between the two curves is found. Indeed, as shown in the right panel of Fig.(5.11), the difference between the two cross section measurements is of the order of few percent. The discrepancy is enhanced for the high energy values mainly due to the low number of particles and, hence, the low statistics. Considering the FOOT goal to measure the target fragmentation differential cross sections with an accuracy of about 10%, the BM performances satisfy the requirement and the primary direction measured by the BM can be safely used to perform the inversion of the kinematics.

However, in this study the contribution of the FOOT global track reconstruction precision, the particle identification efficiency and the energy resolution of the calorimeter have not been considered. At the moment, the FOOT global reconstruction based on the Kalman filter is in a development phase and it will be completed soon.

The particle identification analysis is ongoing with the first data collected at GSI and the calorimeter have conducted different data takings with proton and carbon ion beams and other data takings are foreseen in 2021 to complete the performance assessment. Thus, once the global reconstruction based on the Kalman filter algorithm and the particle identification performance analysis will be finalized, when the characterization of the calorimeter will be concluded, it will be possible to estimate the overall accuracy of the FOOT experiment evaluation of the final cross section measurement.

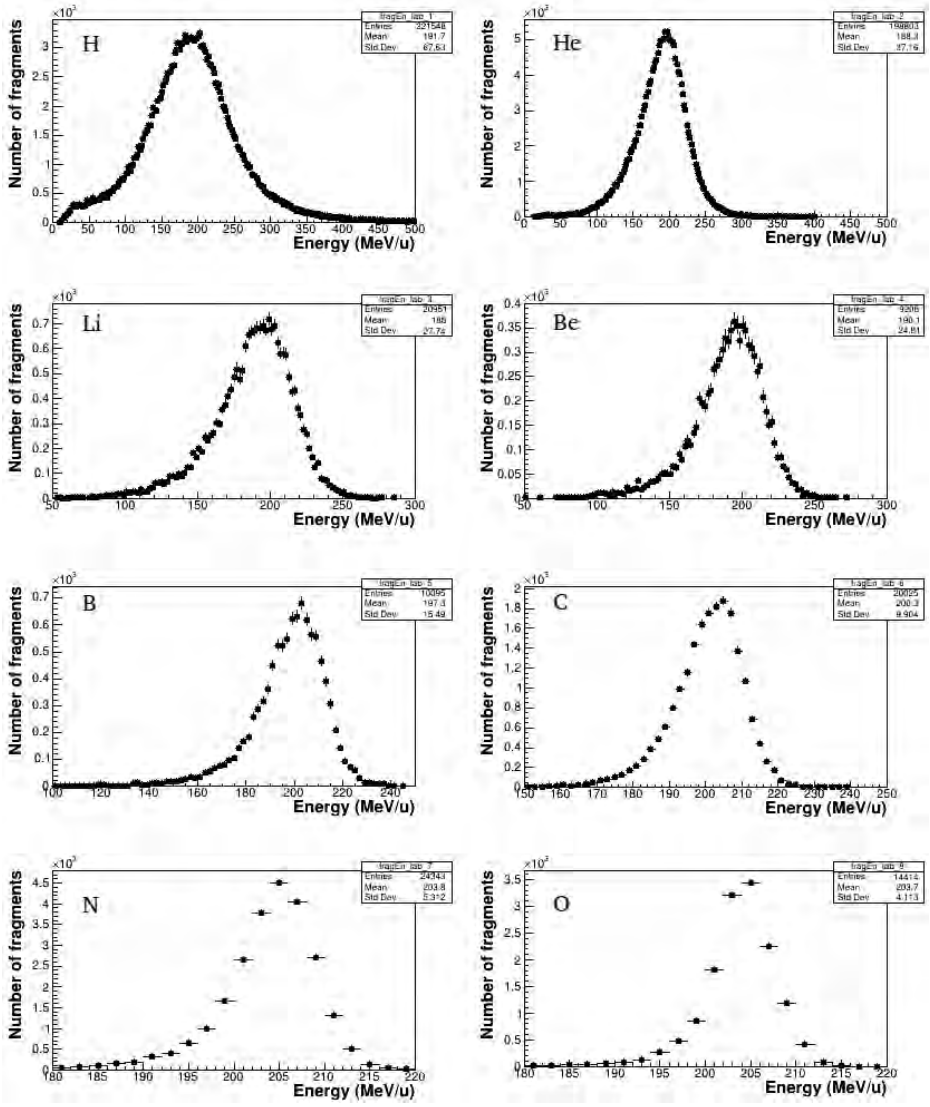

Figure 5.9: Kinetic energy distribution in the laboratory frame of the fragments produced by a simulated beam of oxygen ions with an initial kinetic energy of 200 MeV/u impinging on a graphite target. Each plot corresponds to the distribution for a given charge of the fragments.

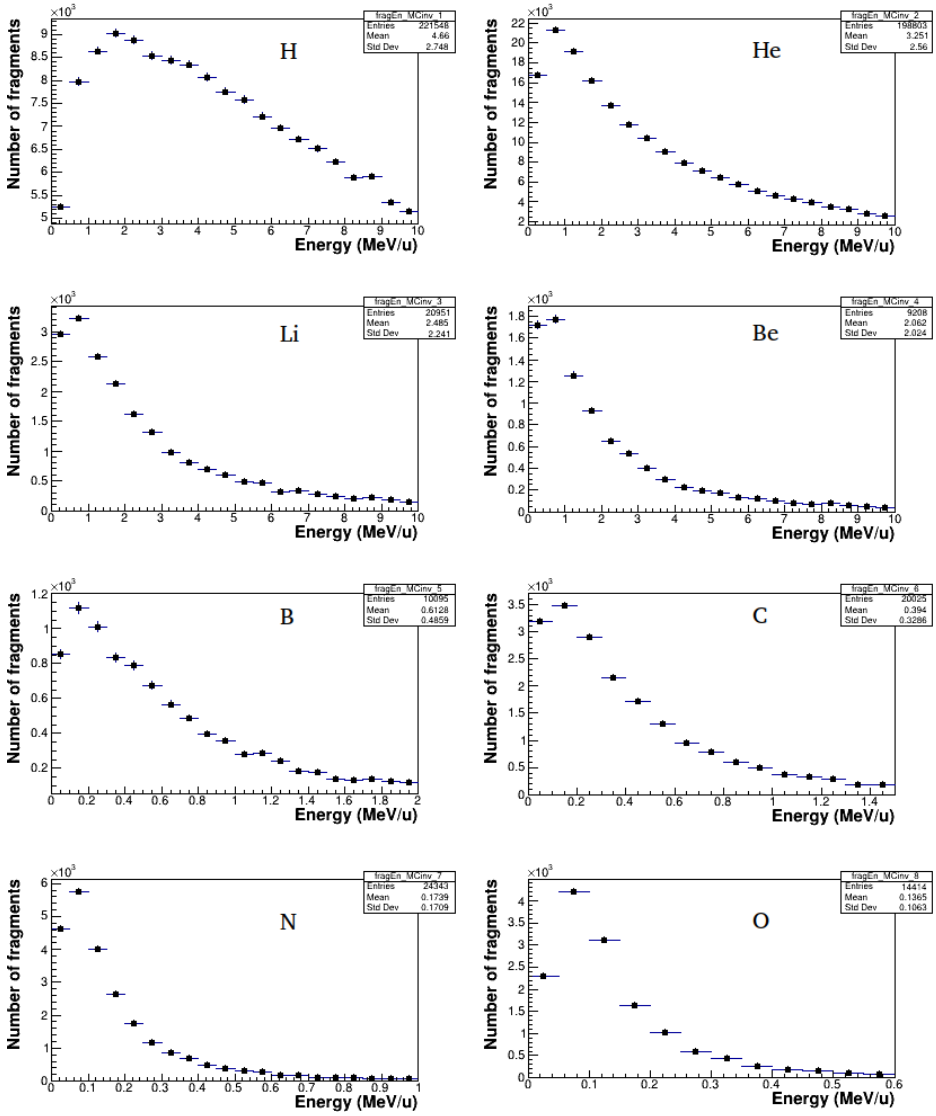

Figure 5.10: Kinetic energy distribution in the projectile frame of the fragments produced by a simulated beam of oxygen ions with an initial kinetic energy of 200 MeV/u impinging on a graphite target. Each plot corresponds to the distribution for a given charge of the fragments.

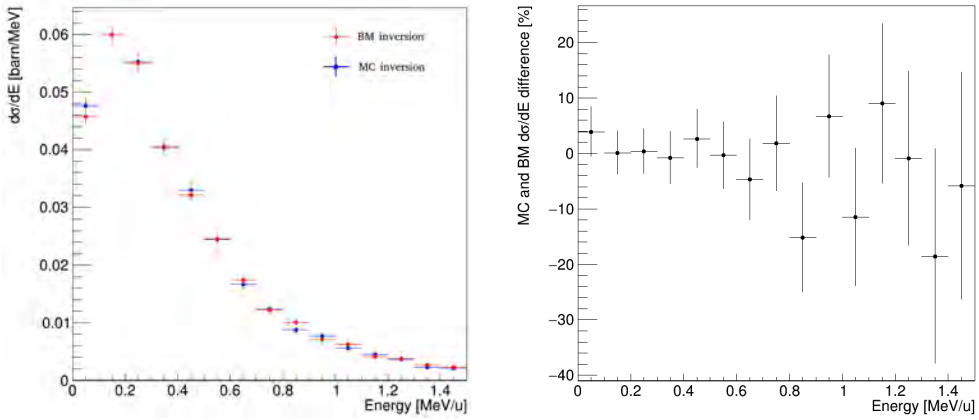

Figure 5.11: On the left, differential cross section of the ^{12}C fragments produced by a beam of oxygen ions at 200 MeV/u impinging on a C target measured in the system of reference of the projectile. The inversion of the kinematics has been performed with the BM reconstructed track (red) and the "MC truth" (blue). On the right, relative difference between the cross section values estimated with the kinematic inversion performed with the MC parameters and the BM reconstructed track.

Conclusions

The FOOT project is a nuclear physics experiment that aims to measure the differential cross sections ($d^2\sigma/d\Omega \cdot dE$) of the nuclear interactions involved in particle therapy and space radioprotection. The final experimental data will be adopted as benchmark for the MC simulation tools, to improve the current particle therapy treatment planning systems and to develop a new shielding design suitable for the future space missions. The FOOT project consists of two different experimental setups. One of the setups is an emulsion spectrometer based on the nuclear emulsion technology developed to measure the light fragments ($Z \leq 3$). The second setup is an electronic setup composed of different sub-detectors optimized for the detection of heavy fragments ($Z \geq 3$). In both the apparata a drift chamber is adopted as Beam Monitor. It is employed to measure the projectile direction and position, to count the total number of delivered particles and to reject the pre-target fragmentation events.

In this Ph. D. project, which has contributed to the construction and start of the FOOT experiment, the drift chamber has been finalized, tested, calibrated and operated in the experiment. A multi-track reconstruction algorithm has been developed taking advantages of the Legendre polynomials properties combined with a χ^2 minimization algorithm. The software has been tested and optimized both on experimental and on MC simulated data. Then, it has been included within the FOOT global reconstruction code.

The detector has been used in different tests and data takings. In particular, an extensive calibration and performance assessment has been conducted with protons at 228 and 80 MeV, employing an external telescope composed of layers of micro-strip silicon detectors. In this occasion, the overall Beam Monitor efficiency has been measured to be of 0.929 ± 0.008. However, a consistent drop of efficiency has been detected at the cell border due to a lowering of the electric field, as verified by calculations performed with the Garfield++ software.

The detector intrinsic spatial resolution has been measured to be of about 60-100 µm in the central part of the cell, considering the residual distributions derived from the Beam Monitor tracks and hits. An alternative method to measure the drift chamber spatial resolution has been applied employing the micro-strip detector tracks instead of the Beam Monitor tracks. In this case, on one hand one can obtain the results avoiding the use of the drift chamber reconstruction algorithm. On the other hand, the outcome includes the multiple Coulomb scattering effect, as verified by MC simulation studies. The spatial resolution in the central part of the cell obtained with the second method is of about 150 ± 10 µm and 300 ± 10 µm respectively for the 228 MeV and 80 MeV protons.

The two corresponding angular resolutions have been measured to be of 1.62 ± 0.16 mrad and 2.1 ± 0.4 mrad.

The Beam Monitor has also been allowed to measure the transverse profile of the incoming proton beam, varying the projectile energy and the associated beam spot size. The results have been compared with the nominal values obtained from an independent experiment. The Beam Monitor measurements constantly overestimate the reference values and the difference between them is of the order of 0.1 mm. The discrepancy can be caused by the multiple Coulomb scattering effect due to a plastic scintillator placed along the beam line, prior the drift chamber. However, the general trend of the beam spot size as a function of the beam energy is well reproduced and the difference with the reference value is of the order of $\leq 5\%$. Then, the active area of the Beam Monitor has been measured with a broadened proton beam and the result is of about $4 \times 4\,\mathrm{cm}^2$.

Finally, the space-time relations of the drift chamber have been measured combining the micro-strip detector tracks with the Beam Monitor hits. The results have been adopted as benchmark for a self calibration method developed to estimate the space-time relations using only the Beam Monitor hits and tracks. The functioning and the limits of the algorithm have been verified. This algorithm can be now used to optimize the drift chamber space-time relations in the test beams in which an external calibration is not feasible.

The detector has been successfully operated in the FOOT data takings performed with both the experimental setups. In particular, in the framework of the emulsion spectrometer measurements, the Beam Monitor has been employed to measure the profile of the irradiation pattern and to count the total number of delivered particles. Then, during the test performed with the electronic spectrometer, the drift chamber has been used with the FOOT general DAQ system to measure the incoming beam direction and position. In addition, the Beam Monitor has performed a characterization of the GSI 700 MeV/u carbon ion beam, measuring the transverse spot size, the rate and the angular spread of the incoming beam.

The final part of the project has been devoted to a detailed study of the performances of the detector in view of the work for the data analysis of the FOOT experiment. In particular, different selection criteria have been studied to identify and reject the pre-target fragmentation events. The fundamental selection criteria on the Beam Monitor are given by the number of hits ($8 \leq N_{\text{hits}} \leq 18$) and tracks ($N_{\text{BMtracks}} = 1$). An additional cut consists in the request of a matching between the Vertex detector tracks and the Beam Monitor track position. In this way, analyzing the MC simulations, it turns out that it is possible to successfully reject about 85% and 88% of the events in which projectile fragmentation occurred in the Start Counter and in the Beam Monitor respectively. In the case of the electronic spectrometer, considering a realistic scenario with a simulation performed with a 200 MeV/u carbon ion beam impinging on a 0.915 $\mathrm{g/cm}^2$ thick graphite target, about 0.5% and 0.4% of primaries interact in the Start Counter and in the Beam Monitor, respectively. These numbers will be considered in the estimation of the systematic uncertainties of the physics measurements.

Since target fragmentation cross section measurements in FOOT rely on the Beam Monitor tracks to perform the inversion of the kinematics, the impact of the drift chamber spatial resolution on the cross section accuracy has been estimated by means of MC simulations. In particular, $\mathrm{d}\sigma/\mathrm{dE}$ has been evaluated with the inversion of the kinematics performed both with the Beam Monitor track and the "MC truth". The discrepancy between the two values has been found to be of the order of few percent. Since FOOT is required to measure the target fragmentation cross sections with a precision of about 10%, the projectile direction measured by the Beam Monitor can be safely adopted to

perform the inversion of the kinematics.

Bibliography

[1] Particle therapy co-operative group. https://www.ptcog.ch. Accessed: 2020-11-19.

[2] Marco Durante and Francesco Tommasino. Proton radiobiology. *Cancers (Basel)*, 7, 02 2015.

[3] K Gunzert-Marx, H Iwase, D Schardt, and R S Simon. Secondary beam fragments produced by 200 MeV u-112c ions in water and their dose contributions in carbon ion radiotherapy. *New Journal of Physics*, 10(7):075003, jul 2008.

[4] Francesco Tommasino, Emanuele Scifoni, and Marco Durante. New ions for therapy. *International Journal of Particle Therapy*, 2(3):428–438, 2015.

[5] What's next for nasa. https://www.nasa.gov/about/whats_next.html. Accessed: 2020-05-03.

[6] L Arrabito, C Bozza, S Buontempo, L Consiglio, M Cozzi, N D'Ambrosio, G De Lellis, M De Serio, F Di Capua, D Di Ferdinando, N Di Marco, A Ereditato, L S Esposito, R A Fini, G Giacomelli, M Giorgini, G Grella, M Ieva, J Janicsko Csathy, F Juget, I Kreslo, I Laktineh, K Manai, G Mandrioli, A Marotta, P Migliozzi, P Monacelli, U Moser, M T Muciaccia, A Pastore, L Patrizii, Y Petukhov, C Pistillo, M Pozzato, G Romano, G Rosa, A Russo, N Savvinov, A Schembri, L Scotto Lavina, S Simone, M Sioli, C Sirignano, G Sirri, P Strolin, V Tioukov, and T Waelchli. Track reconstruction in the emulsion-lead target of the OPERA experiment using the ESS microscope. *Journal of Instrumentation*, 2(05):P05004–P05004, may 2007.

[7] Leo W.R. *Techniques for nuclear and particle physics experiments*. Springer-Verlag, 1987.

[8] M. Tanabashi et all. Review of particle physics. *Phys. Rev. D*, 98:030001, Aug 2018.

[9] E.V. Benton and R.P. Henke. Heavy particle range-energy relations for dielectric nuclear track detectors. *Nuclear Instruments and Methods*, 67(1):87 – 92, 1969.

[10] Aafke Christine Kraan. Range verification methods in particle therapy: Underlying physics and monte carlo modeling. *Frontiers in Oncology*, 5:150, 2015.

[11] G. Kraft. Tumor therapy with heavy charged particles. *Progress in Particle and Nuclear Physics*, 45, 12 2001.

[12] James F. Ziegler and Jochen P. Biersack. *The Stopping and Range of Ions in Matter*, pages 93–129. Springer US, Boston, MA, 1985.

[13] Barkas W.H. *Nuclear research emulsions. Vol.1: Techniques and theory*. Academic Press, 1963.

[14] J. Lindhard, V. Nielsen, M. Scharff, and P.V. Thomsen. Integral equations governing radiation effects. (notes on atomic collisions, iii). *Kgl. Danske Videnskab., Selskab. Mat. Fys. Medd.*, 33.10, 1 1963.

[15] T Elsässer, A Gemmel, M Scholz, D Schardt, and M Krämer. The relevance of very low energy ions for heavy-ion therapy. *Physics in Medicine and Biology*, 54(7):N101–N106, mar 2009.

[16] John Sabin, Jens Oddershede, and Stephan P. A. Sauer. On the determination of the mean excitation energy of water. *Advances in Quantum Chemistry*, 65:63–77, 12 2013.

[17] Helmut Paul. Chapter two - on the accuracy of stopping power codes and ion ranges used for hadron therapy. In Dževad Belkić, editor, *Theory of Heavy Ion Collision Physics in Hadron Therapy*, volume 65 of *Advances in Quantum Chemistry*, pages 39 – 61. Academic Press, 2013.

[18] Marco Durante and Harald Paganetti. Nuclear physics in particle therapy: a review. *Reports on Progress in Physics*, 79(9):096702, aug 2016.

[19] Thomas Bortfeld. An analytical approximation of the bragg curve for therapeutic proton beams. *Medical Physics*, 24(12):2024–2033, 1997.

[20] Dieter Schardt, Thilo Elsässer, and Daniela Schulz-Ertner. Heavy-ion tumor therapy: Physical and radiobiological benefits. *Rev. Mod. Phys.*, 82:383–425, Feb 2010.

[21] M. J. Berger, M. Inokuti, H. H. Andersen, H. Bichsel, D. Powers, S . M. Seltzer, D . Thwaites, and D. E. Watt. Report 49. *Journal of the International Commission on Radiation Units and Measurements*, os25(2):NP–NP, 04 2016.

[22] Vavilov P.V. Ionization losses of high energy heavy particles. *Soviet Phisics JEPT*, 5(4), 1957.

[23] Joseph F. Janni. Energy loss, range, path length, time-of-flight, straggling, multiple scattering, and nuclear interaction probability: In two parts. part 1. for 63 compounds part 2. for elements 1 z 92. *Atomic Data and Nuclear Data Tables*, 27(2):147 – 339, 1982.

[24] Moliére G. Theorie der streuung schneller geladener teilchen ii. mehrfach- und vielfachstreuung. *Zeitschrift für Naturforschung A*, 3(2):78–97, 1948.

[25] Virgil L. Highland. Some practical remarks on multiple scattering. *Nuclear Instruments and Methods*, 129(2):497 – 499, 1975.

[26] Yung-Su Tsai. Pair production and bremsstrahlung of charged leptons. *Rev. Mod. Phys.*, 46:815–851, Oct 1974.

[27] B. Gottschalk, A.M. Koehler, R.J. Schneider, J.M. Sisterson, and M.S. Wagner. Multiple coulomb scattering of 160 mev protons. *Nuclear Instruments and Methods in Physics Research Section B: Beam Interactions with Materials and Atoms*, 74(4):467 – 490, 1993.

[28] Martin Soukup, Matthias Fippel, and Markus Alber. A pencil beam algorithm for intensity modulated proton therapy derived from monte carlo simulations. *Physics in Medicine and Biology*, 50(21):5089–5104, oct 2005.

[29] Yupeng Li, Ronald X Zhu, Narayan Sahoo, Aman Anand, and Xiaodong Zhang. Beyond gaussians: a study of single-spot modeling for scanning proton dose calculation. *Physics in Medicine and Biology*, 57(4):983–997, feb 2012.

[30] H. W. Lewis. Multiple scattering in an infinite medium. *Phys. Rev.*, 78:526–529, Jun 1950.

[31] Bernard Gottschalk. Radiotherapy proton interactions in matter. 03 2018.

[32] H. L. Bradt and B. Peters. The heavy nuclei of the primary cosmic radiation. *Phys.*

Rev., 77:54–70, Jan 1950.

[33] Marco Durante and Francis A. Cucinotta. Physical basis of radiation protection in space travel. *Rev. Mod. Phys.*, 83:1245–1281, Nov 2011.

[34] John Wilson, Sang Chun, Forooz Badavi, Lawrence Townsend, and Stanley Lamkin. Hzetrn: A heavy ion/nucleon transport code for space radiations. 01 1992.

[35] Ram Tripathi, Francis Cucinotta, and John Wilson. Nasa technical paper 3621. 02 1997.

[36] R.K. Tripathi, F.A. Cucinotta, and J.W. Wilson. Accurate universal parameterization of absorption cross sections iii – light systems. *Nuclear Instruments and Methods in Physics Research Section B: Beam Interactions with Materials and Atoms*, 155(4):349 – 356, 1999.

[37] Lembit Sihver and Davide Mancusi. Present status and validation of hibrac. *Radiation Measurements*, 44:38–46, 01 2009.

[38] J. Hüfner, K. Schäfer, and B. Schürmann. Abrasion-ablation in reactions between relativistic heavy ions. *Phys. Rev. C*, 12:1888–1898, Dec 1975.

[39] R. Serber. Nuclear reactions at high energies. *Phys. Rev.*, 72:1114–1115, Dec 1947.

[40] H. W. Bertini, T. A. Gabriel, R. T. Santoro, O. W. Hermann, N. M. Larson, and J. M. Hunt. Hic-1: a first approach to the calculation of heavy-ion reactions at energies greater than or equal to 50 mev/nucleon. 1 1974.

[41] Jörg Aichelin. "quantum" molecular dynamics—a dynamical microscopic n-body approach to investigate fragment formation and the nuclear equation of state in heavy ion collisions. *Physics Reports*, 202(5):233 – 360, 1991.

[42] G.F. Bertsch and S. [Das Gupta]. A guide to microscopic models for intermediate energy heavy ion collisions. *Physics Reports*, 160(4):189 – 233, 1988.

[43] M. Cavinato, E. Fabrici, E. Gadioli, E. Gadioli Erba, M. Galmarini, A. Gritti, and P. Vergani. *Boltzmann Master Equation Theory of Nuclear Reactions: From Nucleons to Heavy Ions*, pages 25–41. Springer US, Boston, MA, 1994.

[44] J. J. Griffin. Statistical model of intermediate structure. *Phys. Rev. Lett.*, 17:478–481, Aug 1966.

[45] M. Blann. Precompound analyses of spectra and yields following nuclear capture of stopped π^-. *Phys. Rev. C*, 28:1648–1662, Oct 1983.

[46] Michael Joiner and Albert Van der Kogel. *Basic Clinical Radiobiology*. 03 2009.

[47] R. L. Warters and K. G. Hofer. Radionuclide toxicity in cultured mammalian cells: Elucidation of the primary site for radiation-induced division delay. *Radiation Research*, 69(2):348–358, 1977.

[48] Anthony Tubbs and André Nussenzweig. Endogenous dna damage as a source of genomic instability in cancer. *Cell*, 168(4):644 – 656, 2017.

[49] Jac Nickoloff, Neelam Sharma, and Taylor. Clustered dna double-strand breaks: Biological effects and relevance to cancer radiotherapy. *Genes*, 11:99, 01 2020.

[50] Michael F. L'Annunziata. Chapter 1 - radiation physics and radionuclide decay. In Michael F. L'Annunziata, editor, *Handbook of Radioactivity Analysis (Third Edition)*, pages 1 – 162. Academic Press, Amsterdam, third edition edition, 2012.

[51] Mario Carante and Francesca Ballarini. Modelling cell death for cancer hadrontherapy. *AIMS Biophysics*, 4:465–490, 07 2017.

[52] M Scholz and G Kraft. Calculation of heavy ion inactivation probabilities based on track structure, x-ray sensitivity and target size, Jan 1994.

[53] Thilo Elsässer, Wilma Weyrather, Thomas Friedrich, Marco Durante, Gheorghe

Iancu, Michael Krämer, Gabriele Kragl, Stephan Brons, Marcus Winter, Klaus Weber, and Michael Scholz. Quantification of the relative biological effectiveness for ion beam radiotherapy: Direct experimental comparison of proton and carbon ion beams and a novel approach for treatment planning. *International journal of radiation oncology, biology, physics*, 78:1177–83, 11 2010.

[54] Roland B. Hawkins. A statistical theory of cell killing by radiation of varying linear energy transfer. *Radiation Research*, 140(3):366–374, 1994.

[55] Roland B. Hawkins. A microdosimetric-kinetic model for the effect of non-poisson distribution of lethal lesions on the variation of rbe with let. *Radiation Research*, 160(1):61–69, 2003.

[56] Albrecht M. Kellerer and Harald H. Rossi. A Generalized Formulation of Dual Radiation Action. *Radiation Research*, 178(2), 2012.

[57] Tatsuaki Kanai, Yoshiya Furusawa, Kumiko Fukutsu, Hiromi Itsukaichi, Kiyomi Eguchi-Kasai, and Hiroshi Ohara. Irradiation of Mixed Beam and Design of Spread-Out Bragg Peak for Heavy-Ion Radiotherapy. *Radiation Research*, 147(1):78, January 1997.

[58] P Howard-Flanders and A Pirie. The effect of breathing oxygen on the radiosensitivity of the rabbit lens and use of oxygen in x-ray therapy. *Radiation Research*, 7, 10 1957.

[59] World Health Organization. *WHO report on cancer: setting priorities, investing wisely and providing care for all*. World Health Organization, 2020.

[60] James Slater. From x-rays to ion beams: A short history of radiation therapy. *Ion Beam Therapy: Fundamentals, Technology, Clinical Applications, Biological and Medical Physics, Biomedical Engineering*, 320:3–642, 01 2012.

[61] Alexandra Taylor and M Powell. Intensity-modulated radiotherapy - what is it? *Cancer imaging : the official publication of the International Cancer Imaging Society*, 4:68–73, 02 2004.

[62] Nuclear physics for medicine. Report, Nuclear Physics European Collaboration Committee (NuPECC), 2014.

[63] Francesco Dionisi, Stephen Avery, John Lukens, Xuanfeng Ding, John Kralik, M. Kirk, Robert Roses, James Metz, and John Plastaras. Proton therapy in adjuvant treatment of gastric cancer: Planning comparison with advanced x-ray therapy and feasibility report. *Acta oncologica (Stockholm, Sweden)*, 53, 05 2014.

[64] Michele M Kim, Peyton Irmen, Khayrullo Shoniyozov, Ioannis I Verginadis, Keith A Cengel, Costantinos Koumenis, James M Metz, Lei Dong, and Eric S Diffenderfer. Design and commissioning of an image-guided small animal radiation platform and quality assurance protocol for integrated proton and x-ray radiobiology research. *Physics in Medicine & Biology*, 64(13):135013, jul 2019.

[65] Harald Paganetti. Range uncertainties in proton therapy and the role of monte carlo simulations. *Physics in Medicine and Biology*, 57(11):R99–R117, may 2012.

[66] G. Traini, I. Mattei, G. Battistoni, M.G. Bisogni, M. [De Simoni], Y. Dong, A. Embriaco, M. Fischetti, M. Magi, C. Mancini-Terracciano, M. Marafini, R. Mirabelli, S. Muraro, V. Patera, A. Schiavi, A. Sciubba, E. [Solfaroli Camillocci], S.M. Valle, and A. Sarti. Review and performance of the dose profiler, a particle therapy treatments online monitor. *Physica Medica*, 65:84 – 93, 2019.

[67] M Krämer and M Scholz. Treatment planning for heavy-ion radiotherapy: calculation and optimization of biologically effective dose. *Physics in Medicine and Biology*, 45(11):3319–3330, oct 2000.

[68] E Haettner, H Iwase, M Krämer, G Kraft, and D Schardt. Experimental study of nuclear fragmentation of 200 and 400 MeV/u12c ions in water for applications in particle therapy. *Physics in Medicine and Biology*, 58(23):8265–8279, nov 2013.

[69] Satoshi Kodaira, Hisashi Kitamura, Mieko Kurano, Hajime Kawashima, and Eric Benton. Contribution to dose in healthy tissue from secondary target fragments in therapeutic proton, he and c beams measured with cr-39 plastic nuclear track detectors. *Scientific Reports*, 9, 12 2019.

[70] Mirko Boezio and Emiliano Mocchiutti. Chemical composition of galactic cosmic rays with space experiments. *Astroparticle Physics*, s 39–40, 08 2012.

[71] Cary Zeitlin and Chiara Tessa. The role of nuclear fragmentation in particle therapy and space radiation protection. *Frontiers in Oncology*, 6, 03 2016.

[72] Stephen Guetersloh, Cary Zeitlin, L.H. Heilbronn, Jack Miller, T. Komiyama, A. Fukumura, Y. Iwata, T. Murakami, and Manojeet Bhattacharya. Polyethylene as a radiation shielding standard in simulated cosmic-ray environments. *Nuclear Instruments and Methods in Physics Research Section B: Beam Interactions with Materials and Atoms*, 252:319–332, 11 2006.

[73] B. Blau, S.M. Harrison, H. Hofer, S.R. Milward, G. Kaiser, John [S.H. Ross], S.C.C. Ting, and J. Ulbricht. The superconducting magnet system of the alpha magnetic spectrometer ams-02. *Nuclear Instruments and Methods in Physics Research Section A: Accelerators, Spectrometers, Detectors and Associated Equipment*, 518(1):139 – 142, 2004. Frontier Detectors for Frontier Physics: Proceedin.

[74] J. Dudouet, D. Juliani, M. Labalme, D. Cussol, J. Angélique, B. Braunn, Jose Colin, Christian Finck, jean-marc Fontbonne, H. Guérin, P. Henriquet, J. Krimmer, Marc Rousseau, M. Saint-Laurent, and Samuel Salvador. Double differential fragmentation cross-section measurements of 95 mev/u 12c on thin targets for hadrontherapy. *Physical Review C*, 88, 08 2013.

[75] C. Divay, J. Colin, D. Cussol, Ch. Finck, Y. Karakaya, M. Labalme, M. Rousseau, S. Salvador, and M. Vanstalle. Differential cross section measurements for hadron therapy: 50 mev/nucleon ^{12}C reactions on h, c, o, al, and $^{\mathrm{nat}}$Ti targets. *Phys. Rev. C*, 95:044602, Apr 2017.

[76] Move-it project site. `https://www.tifpa.infn.it/projects/move-it/`. Accessed: 2020-08-06.

[77] Chapter 1 - human body composition and muscle mass. In Jerzy A. Zoladz, editor, *Muscle and Exercise Physiology*, pages 3 – 26. Academic Press, 2019.

[78] R.A. Weldon, J.M. Mueller, P. Barbeau, and J. Mattingly. Measurement of ej-228 plastic scintillator proton light output using a coincident neutron scatter technique. *Nuclear Instruments and Methods in Physics Research Section A: Accelerators, Spectrometers, Detectors and Associated Equipment*, 953:163192, 2020.

[79] Eljen plastic scintillator. `https://eljentechnology.com/products/plastic-scintillators`. Accessed: 2020-08-06.

[80] L. Galli, A.M. Baldini, Fabrizio Cei, Marco Chiappini, M. Francesconi, Marco Grassi, U. Hartmann, Manuel Meucci, F. Morsani, Donato Nicolo, Angela Papa, Stefan Ritt, E. Schmid, and Giovanni Signorelli. Wavedaq: An highly integrated trigger and data acquisition system. *Nuclear Instruments and Methods in Physics Research Section A: Accelerators, Spectrometers, Detectors and Associated Equipment*, 936, 07 2018.

[81] M Toppi et al. Measurement of fragmentation cross sections of ^{12}C ions on a thin gold target with the FIRST apparatus. *Phys. Rev. C*, 93(06):064601, 2016.

[82] Eleuterio Spiriti, Christian Finck, Jérôme Baudot, Clovis Divay, Didier Juliani,

M. Labalme, Marc Rousseau, Samuel Salvador, Marie Vanstalle, Clementina Agodi, Giacomo Cuttone, M. Napoli, and F. Romano. Cmos active pixel sensors response to low energy light ions. *Nuclear Instruments and Methods in Physics Research Section A Accelerators Spectrometers Detectors and Associated Equipment*, 875, 09 2017.

[83] Bartsch V Bol J Dierlamm A Grigoriev E Hauler F Herz O Jungermann L Koppenhoefer M Sopczak A Boer, W de and Th Schneider. Measurements with a cmos pixel sensor in magnetic fields, Jul 2002.

[84] Plume project. `http://www.iphc.cnrs.fr/PLUME.html`.

[85] Morrocchi Matteo, Esther Ciarrocchi, Andrey Alexandrov, Behcet Alpat, Ambrosi Giovanni, Argirò Stefano, Arteche Raul, Bartosik Nazar, Giuseppe Battistoni, Belcari Nicola, Matteo Bertazzoni, Biondi Silvia, Graziano Bruni, Niccolò Camarlinghi, Carra Pietro, Piergiorgio Cerello, Clozza Alberto, Sofia Colombi, De Giovanni, and Maria Giuseppina. Development and characterization of a e-tof detector prototype for the foot experiment. *Nuclear Instruments and Methods in Physics Research Section A: Accelerators, Spectrometers, Detectors and Associated Equipment*, 916, 10 2018.

[86] B. Adeva et al. The construction of the l3 experiment. *Nuclear Instruments and Methods in Physics Research Section A: Accelerators, Spectrometers, Detectors and Associated Equipment*, 289(1):35 – 102, 1990.

[87] M.C. Montesi et al. Ion charge separation with new generation of nuclear emulsion films. *Open Physics*, 17(1):233 – 240, 2019.

[88] M. Kaplon, B. Peters, and D. M. Ritson. Emulsion cloud-chamber study of a high energy interaction in the cosmic radiation. *Phys. Rev.*, 85:900–903, Mar 1952.

[89] K Kodama et al. Detection and analysis of tau–neutrino interactions in donut emulsion target. *Nuclear Instruments and Methods in Physics Research Section A: Accelerators, Spectrometers, Detectors and Associated Equipment*, 493(1):45 – 66, 2002.

[90] E. Eskut et al. The chorus experiment to search for $\rightarrow$ oscillation. *Nuclear Instruments and Methods in Physics Research Section A: Accelerators, Spectrometers, Detectors and Associated Equipment*, 401(1):7 – 44, 1997.

[91] Taku Nakamura et al. The opera film: New nuclear emulsion for large-scale, high-precision experiments. *Nuclear Instruments and Methods in Physics Research Section A: Accelerators, Spectrometers, Detectors and Associated Equipment*, 556(1):80 – 86, 2006.

[92] Z Abou-Haidar et al. Performance of upstream interaction region detectors for the FIRST experiment at GSI. *Journal of Instrumentation*, 7(02):P02006–P02006, feb 2012.

[93] T.T. Böhlen, F. Cerutti, M.P.W. Chin, A. Fassò, A. Ferrari, P.G. Ortega, A. Mairani, P.G. Sala, P.G. Smirnov, and V. Vlachoudis. The FLUKA Code: Developments and Challenges for High Energy and Medical Applications. *Nuclear Data Sheets*, 120:211, 2014.

[94] Alfredo Ferrari, Paola R Sala, Alberto Fassò, and Johannes Ranft. FLUKA: A Multi-Particle Transport Code. Technical Report CERN-2005-10, INFN/TC_05/11, SLAC-R-773, CERN, INFN, SLAC, 2005.

[95] G. Battistoni et al. The FLUKA Code: An Accurate Simulation Tool For Particle Therapy. *Front. Oncol.*, 6:116, 2016.

[96] `https://www.fluka.org`.

[97] Stephen M. Seltzer and Martin J. Berger. Bremsstrahlung spectra from electron interactions with screened atomic nuclei and orbital electrons. *Nuclear Instruments*

and Methods in Physics Research Section B: Beam Interactions with Materials and Atoms, 12(1):95 – 134, 1985.

[98] Stephen M. Seltzer and Martin J. Berger. Bremsstrahlung energy spectra from electrons with kinetic energy 1 kev–10 gev incident on screened nuclei and orbital electrons of neutral atoms with z = 1–100. *Atomic Data and Nuclear Data Tables*, 35(3):345 – 418, 1986.

[99] Lev Davidovich Landau and I I Pomeranchuk. The limits of applicability of the theory of Bremsstrahlung by electrons and of the creation of pairs at large energies. *Dokl. Akad. Nauk SSSR*, 92:535, 1953.

[100] Ter-Mikaelyan M.L. Bremsstrahlung radiation spectrum in a medium. *Dokl. Akad. Nauk SSSR*, 94:1033, 1954.

[101] A. Capella, U. Sukhatme, C.-I. Tan, and J. [Tran Thanh Van]. Dual parton model. *Physics Reports*, 236(4):225 – 329, 1994.

[102] R.J. Glauber and G. Matthiae. High-energy scattering of protons by nuclei. *Nuclear Physics B*, 21(2):135 – 157, 1970.

[103] The fluka code for space applications: recent developments. *Advances in Space Research*, 34(6):1302 – 1310, 2004. Space Life Sciences: Radiation Risk Assessment and Radiation Measurements in Low Earth Orbit.

[104] C. Höppner, S. Neubert, B. Ketzer, and S. Paul. A novel generic framework for track fitting in complex detector systems. *Nuclear Instruments and Methods in Physics Research Section A: Accelerators, Spectrometers, Detectors and Associated Equipment*, 620(2):518 – 525, 2010.

[105] Rutherford E. and Geiger H. An electrical method of counting the number of α-particles from radio-active substances. *The royal society A: mathematical, physical and engineering sciences*, 81:141 – 161, 1908.

[106] G. Charpak, R. Bouclier, T. Bressani, J. Favier, and Č. Zupančič. The use of multiwire proportional counters to select and localize charged particles. *Nuclear Instruments and Methods*, 62(3):262 – 268, 1968.

[107] A.H. Walenta, J. Heintze, and B. Schürlein. The multiwire drift chamber a new type of proportional wire chamber. *Nuclear Instruments and Methods*, 92(3):373 – 380, 1971.

[108] Jay N. Marx and David R. Nygren. The Time Projection Chamber. *Phys. Today*, 31N10:46–53, 1978.

[109] A. Oed. Position-sensitive detector with microstrip anode for electron multiplication with gases. *Nuclear Instruments and Methods in Physics Research Section A: Accelerators, Spectrometers, Detectors and Associated Equipment*, 263(2):351 – 359, 1988.

[110] F. Sauli. Gem: A new concept for electron amplification in gas detectors. *Nuclear Instruments and Methods in Physics Research Section A: Accelerators, Spectrometers, Detectors and Associated Equipment*, 386(2):531 – 534, 1997.

[111] Y. Giomataris, Ph. Rebourgeard, J.P. Robert, and G. Charpak. Micromegas: a high-granularity position-sensitive gaseous detector for high particle-flux environments. *Nuclear Instruments and Methods in Physics Research Section A: Accelerators, Spectrometers, Detectors and Associated Equipment*, 376(1):29 – 35, 1996.

[112] Maxim P. Titov. Gaseous Detectors: Recent developments and applications. 8 2010.

[113] Walter Blum, Werner Riegler, and Luigi Rolandi. *Particle detection with drift chambers; 2nd ed.* Springer, Berlin, 2008.

[114] Korff S.A. *Electron and nuclear counters*. Van Nostrand, 1946.

[115] Francesco Tommasino. *Caratterizzazione di un monitor di fascio per adroterapia con ioni*

carbonio. PhD thesis, Universitá sapienza di Roma, Facoltá di ingegneria biomedica, 2010. unpublished thesis.

[116] Fabio Sauli. *Drift chambers*, page 264–291. Cambridge Monographs on Particle Physics, Nuclear Physics and Cosmology. Cambridge University Press, 2014.

[117] Garfield++. `http://garfieldpp.web.cern.ch/garfieldpp/`. Accessed: 2020-08-11.

[118] Cern. `https://home.cern/`. Accessed: 2020-08-10.

[119] Kalman R. E. A new approach to linear filtering and prediction problems. *Transactions of the ASME–Journal of Basic Engineering*, 82(series D):35–45, 1960.

[120] Rene Brun and Fons Rademakers. Root — an object oriented data analysis framework. *Nuclear Instruments and Methods in Physics Research Section A: Accelerators, Spectrometers, Detectors and Associated Equipment*, 389(1):81 – 86, 1997. New Computing Techniques in Physics Research V.

[121] F. James and M. Roos. Minuit - a system for function minimization and analysis of the parameter errors and correlations. *Computer Physics Communications*, 10(6):343 – 367, 1975.

[122] R. K. P. Zia, Edward F. Redish, and Susan R. McKay. Making sense of the legendre transform. *American Journal of Physics*, 77(7):614–622, Jul 2009.

[123] A. Paoloni, M. Anelli, E. Iarocci, V. Patera, L. Piersanti, A. Sarti, and A. Sciubba. The upstream detectors of the first experiment at gsi. *Physics Procedia*, 37:1466 – 1472, 2012. Proceedings of the 2nd International Conference on Technology and Instrumentation in Particle Physics (TIPP 2011).

[124] Y. Dong et al. The drift chamber detector of the foot experiment: Performance analysis and external calibration. *Nuclear Instruments and Methods in Physics Research Section A: Accelerators, Spectrometers, Detectors and Associated Equipment*, 986:164756, 2021.

[125] J. Alcaraz et al. The alpha magnetic spectrometer silicon tracker: Performance results with protons and helium nuclei. *Nuclear Inst. and Methods in Physics Research, A*, 593(3):376 – 398, 2008.

[126] F. Tommasino et al. Proton beam characterization in the experimental room of the Trento Proton Therapy facility. *Nuclear Inst. and Methods in Physics Research, A*, 869:15–20, 2017.

[127] G. Battistoni et al. Characterization of the 12C beam at 700 MeV/u at GSI using the FOOT Beam Monitor. *FOOT internal note*, (1), 2020.

[128] M. Matzke. Unfolding procedures. *Radiation Protection Dosimetry*, 107(1-3):155–174, 11 2003.

[129] I. Mattei et all. Measurement of 12 c fragmentation cross sections on c, o, and h in the energy range of interest for particle therapy applications. *IEEE Transactions on Radiation and Plasma Medical Sciences*, PP:1–1, 02 2020.

[130] T T Böhlen, F Cerutti, M Dosanjh, A Ferrari, I Gudowska, A Mairani, and J M Quesada. Benchmarking nuclear models of FLUKA and GEANT4 for carbon ion therapy. *Physics in Medicine and Biology*, 55(19):5833–5847, sep 2010.

[131] John David Jackson. *Classical electrodynamics*. Wiley, New York, NY, 3rd ed. edition, 1999.

List of Publications

Refereed publications

- Y. Dong et all., "The Drift Chamber detector of the FOOT experiment: Performance analysis and external calibration", *Nuclear Inst. and Methods in Physics Research, A: Accelerators, Spectrometers, Detectors and Associated Equipment*, 986:164756, 2021, doi:10.1016/j.nima.2020.164756

- I. Mattei et all., "Measurement of ^{12}C Fragmentation Cross Sections on C, O and H in the Energy Range of interest for Particle Therapy Applications", *IEEE Transactions on Radiation and Plasma Medical Sciences*, vol. 4, no. 2, pp. 269-282, 2020, doi:10.1109/TRPMS.2020.2972197

- M. Morrocchi et all., "Development and characterization of a ΔE-TOF detector prototype for the FOOT experiment", *Nuclear Inst. and Methods in Physics Research, A: Accelerators, Spectrometers, Detectors and Associated Equipment*, 911:0–8, 2018, doi:10.1016/j.nima.2018.09.086

- M.C. Montesi et all., "Ion charge separation with new generation of nuclear emulsion films", *Open Physics*, 17(1):233 – 240, 2019, doi:10.1515/phys-2019-0024

- E. Gioscio et all., "Development of a novel neutron tracker for the characterisation of secondary neutrons emitted in Particle Therapy", *Nuclear Inst. and Methods in Physics Research, A: Accelerators, Spectrometers, Detectors and Associated Equipment*, 958:162862, 2020, doi:10.1016/j.nima.2019.162862

- V. Giacometti et all., "Characterisation of the MONDO detector response to neutrons by means of a FLUKA Monte Carlo simulation", *Radiation Measurements*, 119:144-149, 2018, doi:10.1016/j.radmeas.2018.10.006

- G. Traini et all., "Review and performance of the Dose Profiler, a particle therapy treatments online monitor", *Physica Medica*, 65:84-93, 2019, doi:10.1016/j.ejmp.2019.07.010

- A. Rucinski et all., "Secondary radiation measurements for particle therapy applications: Charged secondaries produced by ^{16}O ion beams in a PMMA target at large angles", *Physica Medica*, 64:45-53,2019, doi:10.1016/j.ejmp.2019.06.001

Publications under review

- M. Toppi et all., "Measuring the impact of Nuclear Interaction in Particle Therapy and in Radio Protection in Space: the FOOT experiment", submitted to *Frontiers*
- G. Galati et all. , "Charge identification of fragments with the emulsion spectrometer of the FOOT experiment", submitted to *Open physics*
- E. Fiorina et all., "Detection of inter-fractional morphological changes in proton therapy: a simulation and in-vivo study with the INSIDE in-beam PET", submitted to *Frontiers*.
- M. Toppi et all., "Monitoring carbon ion beams transverse position detecting charged secondary fragments: results from patient treatment performed at CNAO", submitted to *Frontiers*.
- M. Toppi et all., "PAPRICA: the PAir PRoduction Imaging ChAmber - Proof Of Principle", submitted to *Frontiers*
- M. Toppi et all., "The MONDO tracker: characterisation and study of secondary ultra-fast neutrons production in Carbon Ion Radio-Therapy", submitted to *Frontiers*.
- A. Embriaco et all., "FLUKA simulation of target fragmentation in proton therapy", submitted to *Physica Medica*.

Publications in conference proceedings

- Y. Dong et all. ,"Study of the performance of the FOOT experiment", *ALKU Journal of Science*, NSP2018 special issue, 86-92, 2019
- I. Mattei et all., "Scintillating Fiber Devices for Particle Therapy Applications", *IEEE Transactions on Nuclear Science*, 65:8, 2054-2060, 2018, doi:10.1109/TNS.2018.2843179
- M. De Simoni et all., "In-room test results at CNAO of an innovative PT treatments online monitor (Dose Profiler)", *Il nuovo cimento C*, 41:209, 2018, doi:10.1393/ncc/i2018-18209-2
- M. Fischetti et all., "Characterisation of the secondary-neutron production in particle therapy treatments with the MONDO tracking detector", *Il nuovo cimento C*, 41:206, 2018, doi:10.1393/ncc/i2018-18206-5
- A. Alexandrov et all., "The FOOT experiment: fragmentation measurements in particle therapy", *Radiation and Applications*, vol 3, issue 3, 190-196, 2018, doi:10.21175/RadJ.2018.03.032
- E. Manuzzato et all., "A 16×8 digital-sipm array with distributed trigger generator for low snr particle tracking", *IEEE Solid-State Circuits Letters*, 2(9):75-78, 2019, doi:10.1109/ESSCIRC.2019.8902571

- G. Traini et all., "Performance of the ToF detectors in the FOOT experiment", *Il nuovo cimento C*, 43:16, 2020, doi:10.1393/ncc/i2020-20016-5
- I. Mattei et all., "Charged particles and neutron trackers: Applications to particle therapy", *Nuclear Inst. and Methods in Physics Research, A: Accelerators, Spectrometers, Detectors and Associated Equipment*, 954:161229, 2020, doi:10.1016/j.nima.2018.09.064
- G. Silvestre et all. "Evaluation of double-sided silicon microstrip sensor for the FOOT experiment", *Nuclear Instruments and Methods in Physics Research Section A: Accelerators, Spectrometers, Detectors and Associated Equipment*, 936:36-38, 2019, doi:10.1016/j.nima.2018.10.190

Acknowledgments

Alla fine di questo mio percorso, vorrei ringraziarti Giuseppe per avermi accolto nel tuo gruppo di ricerca, permettendomi di svolgere sia la tesi magistrale che il progetto di dottorato. In particolare, ti ringrazio per avermi insegnato così tanto durante tutti questi anni, spaziando dall'oscillazione dei neutrini alle basi di elettronica, il tutto passando per fisica medica e nucleare. Più di ogni altra cosa, ti vorrei ringraziare per aver sempre trovato il tempo da dedicarmi, nonostante tutti gli impegni e gli incarichi che hai avuto e che hai tuttora. Mi hai sempre risposto celermente a qualsiasi domanda e ti sei sempre preoccupato di come procedeva la mia attività di ricerca. A distanza di cinque anni, posso affermare con sicurezza che non avrei potuto immaginare un mentore migliore.

Care Ilaria, Serena e Silvia, se sono riuscito a terminare questo percorso accademico è ovviamente anche merito vostro. Vi ringrazio per tutte le volte che avete risposto ai dubbi da matricola che ogni tanto mi assalgono, per essere sempre presenti sia nei momenti di necessità che in quelli di svago e per tutti i preziosi consigli che mi avete dato nel tempo. In particolar modo, vi ringrazio per avermi dimostrato che nessun ostacolo è insormontabile. In questi ultimi anni, ognuno di voi è riuscito in un'impresa che io, in simili condizioni, non sarei riuscito a portare a termine. C'è chi è riuscito a vincere e portare avanti un progetto di ricerca gestendo anche una bambino, chi si è fatto una famiglia giá durante l'ultimo anno di dottorato e chi è arrivato persino al consiglio di stato per far valere i propri diritti. Sappiate che ammiro molto voi e Giuseppe.

Inoltre, vorrei ringraziare il prof. Franco Camera per la disponibilità che ha sempre mostrato nei miei confronti. Vorrei ringraziare Alessia per tutte le volte che ha pazientemente risposto alle mie domande e per tutti i consigli che mi ha dato. Ringrazio molto Francesco e Sofia per tutto l'aiuto ed il supporto che mi hanno dato sia durante i test beam che nell'analisi dati. È stato bello lavorare insieme con "la cameretta" affrontando sia i momenti più difficili, che quelli più luminosi. Vorrei inoltre ringraziare Alessio, Giacomo, Michela, Vincenzo ed in generale tutto il gruppo di Roma con cui ho condiviso molte esperienze e a cui devo molto per avermi insegnato le basi per svolgere l'attività di dottorato.

Infine, come negli articoli scientifici, voglio ringraziare la persona più importante, cioè te Ilaria. Ti ringrazio per essere sempre al mio fianco e per aver lottato con me anche nei momenti di maggior difficoltà. Senza il tuo costante incoraggiamento, senza tutto l'amore che mi dimostri quotidianamente sarei perso. Come la volta scorsa, anche la fine di questa mia tesi porta ad un nuovo inizio per noi. Sarà l'inizio di un qualcosa ancora migliore di quello che già abbiamo. Perciò spero tu non me ne voglia se stavolta dedico questa tesi a B.